

AFRL-AFOSR-VA-TR-2023-0119

Dynamics of Unsteady Flow past Bluff Bodies with Lofted Bases

Gaitonede, Datta
OHIO STATE UNIVERSITY
1960 KENNY RD
COUMBUS, OH,
US

10/31/2022
Final Technical Report

DISTRIBUTION A: Distribution approved for public release.

Air Force Research Laboratory
Air Force Office of Scientific Research
Arlington, Virginia 22203
Air Force Materiel Command

DISTRIBUTION A: Distribution approved for public release.

REPORT DOCUMENTATION PAGE

PLEASE DO NOT RETURN YOUR FORM TO THE ABOVE ORGANIZATION.

1. REPORT DATE	2. REPORT TYPE	3. DATES COVERED	
20221031	Final	START DATE 20170501	END DATE 20210430

4. TITLE AND SUBTITLE
Dynamics of Unsteady Flow past Bluff Bodies with Lofted Bases

5a. CONTRACT NUMBER	5b. GRANT NUMBER	5c. PROGRAM ELEMENT NUMBER
	FA9550-17-1-0228	61102F
5d. PROJECT NUMBER	**5e. TASK NUMBER**	**5f. WORK UNIT NUMBER**

6. AUTHOR(S)
Datta Gaitonede

7. PERFORMING ORGANIZATION NAME(S) AND ADDRESS(ES)
OHIO STATE UNIVERSITY
1960 KENNY RD
COUMBUS, OH
US

8. PERFORMING ORGANIZATION REPORT NUMBER

9. SPONSORING/MONITORING AGENCY NAME(S) AND ADDRESS(ES)	10. SPONSOR/MONITOR'S ACRONYM(S)	11. SPONSOR/MONITOR'S REPORT NUMBER(S)
Air Force Office of Scientific Research 875 N. Randolph St. Room 3112 Arlington, VA 22203	AFRL/AFOSR RTA1	AFRL-AFOSR-VA-TR-2023-0119

12. DISTRIBUTION/AVAILABILITY STATEMENT
A Distribution Unlimited: PB Public Release

13. SUPPLEMENTARY NOTES

14. ABSTRACT
This report describes a comprehensive four-year effort to characterize the wake downstream of a surrogate cargo aircraft fuselage. The specific configuration is a cylinder with freestream flow-aligned axis, and a base at various upsweep angles. A tightly-integrated experimentalcomputational campaign was conducted. Experiments included high-fidelity point-, planar and volume measurements, while simulations employed very high-order Large-Eddy Simulations. Key findings of the efforts cover the physical three-dimensional mean structure of the wake, unsteadiness associated with vortex meandering and the phenomenon of hysteresis. The effects of Reynolds number and upsweep angle on these features were examined in detail. The primary vortical structure emerging due to separation around the periphery of the base rolls up into a horse-shoe structure which ultimately separates from the base to form a generally streamwise oriented vortex pair. The development of the turbulent flow is characterized by numerous instabilities. The vortices downstream meander at characteristic frequencies designated by their Strouhal numbers based on cylinder diameter. A reduced model shows however, that far downstream, the complex motion can be represented with only a few modes obtained from Proper Orthogonal Decomposition. Hysteresis is observed with Reynolds number as well as upsweep angle varied independently with the two states corresponding to the above described vortex regime, and a separate wake regime characterized by a turbulent

15. SUBJECT TERMS

16. SECURITY CLASSIFICATION OF:			17. LIMITATION OF ABSTRACT	18. NUMBER OF PAGES
a. REPORT U	b. ABSTRACT U	c. THIS PAGE U	UU	127

19a. NAME OF RESPONSIBLE PERSON	19b. PHONE NUMBER *(Include area code)*
GREGG ABATE	425-1779

DISTRIBUTION A: Distribution approved for public release.

Final Report
Grant number: FA9550-17-1-0228

Dynamics of unsteady flow past bluff bodies with lofted bases

Program Officer: **Gregg Abate, Ph.D.**
Program Officer, Air Force Office of Scientific Research
AFRL/AFOSR/RTA-1
gregg.abate@us.af.mil

Datta V. Gaitonde
Mechanical and Aerospace Engineering
The Ohio State University
Columbus, OH 43210
gaitonde.3@osu.edu

Farrukh S. Alvi and **Rajan Kumar**
Mechanical Engineering
Florida State University
Tallahassee, FL 32310
alvi@eng.famu.fsu.edu

Sponsored Program Officer: Molly Wilson
Senior Sponsored Program Officer
The Ohio State University
College Of Engineering Engineering Sponsored Program Services
2nd Floor Bevis Hall, 1080 Carmack Rd Columbus, Ohio 43210
614-688-1478, wilson.940@osu.edu

Period of performance: 05/01/2017 – 04/30/2021

DISTRIBUTION A: Distribution approved for public release.

Dynamics of unsteady flow past bluff bodies with lofted bases

Datta V. Gaitonde
The Ohio State University, Columbus, OH 43210

Farrukh S. Alvi and Rajan Kumar
Florida State University, Tallahassee, FL 32310

Table of Contents

1 Abstract **4**

2 Introduction **4**

3 Data acquisition and generation techniques **9**
3.1 Experimental methods . . . 9
3.1.1 Facility and model details . . . 9
3.1.2 Particle Image Velocimetry (PIV) . . . 10
3.1.3 Surface pressure measurements . . . 11
3.1.4 Stall hysteresis experimental procedure . . . 12
3.2 Numerical methods . . . 14
3.2.1 Numerical Scheme . . . 15
3.2.2 Computational Domain and Mesh . . . 16
3.2.3 Simulation Parameters and Boundary Conditions . . . 16

4 Flow Description **17**
4.1 Experimental investigation . . . 17
4.1.1 Surface flow features . . . 17
4.1.2 Trends in surface pressure . . . 20
4.1.3 Three-dimensional flow topology of the near-wake . . . 23
4.1.4 Separation bubble and wake transition . . . 30
4.2 Simulation investigation . . . 32
4.2.1 Baseline vortex structure . . . 32
4.2.2 Overview of Unsteady Flowfield . . . 34
4.2.3 Characterization of Mean Vortex Pair . . . 36
4.2.4 Evolution of the vorticity field . . . 42
4.3 Summary . . . 54

5 Hysteresis **55**
5.1 Experimental investigation . . . 55
5.1.1 Mean flow observations of wake stall and its hysteresis . . . 55
5.1.2 Hysteresis of the wake stall at $\phi = 45^\circ$ . . . 59
5.1.3 Proposed flow regime map for the slanted cylinder wake at zero pitch . . . 65
5.1.4 Dynamic behavior of the wake in the hysteresis window . . . 67

DISTRIBUTION A: Distribution approved for public release.

5.2 Computational Investigation 76
5.2.1 Hysteresis Simulation Procedure 77
5.2.2 Kinematics of Vortex and Wake Regimes 79
5.2.3 Upsweep Surface Flowfield and Drag Considerations 82
5.2.4 Turbulence and Spectra 85
5.3 Summary 90

6 Unsteady Vortex Motion **92**
6.1 Meandering of Streamwise Vortices 93
6.1.1 Phenomenology 93
6.1.2 Coherent Structures 95
6.2 Linear Stability Analysis 99
6.2.1 Theoretical Vortex Model 100
6.2.2 Stability Approach 101
6.2.3 Stability Analysis of Afterbody Vortices 104
6.3 Governing linear stability equations 105

7 Reduced Model of Vortex Pair **112**
7.1 Low-rank Representation 112
7.2 Summary 118

8 Overall Summary **119**

9 List of Publications from this Work **120**

Bibliography **120**

DISTRIBUTION A: Distribution approved for public release.

1 Abstract

This report describes a comprehensive four-year effort to characterize the wake downstream of a surrogate cargo aircraft fuselage. The specific configuration is a cylinder with freestream flow-aligned axis, and a base at various upsweep angles. A tightly-integrated experimental-computational campaign was conducted. Experiments included high-fidelity point-, planar and volume measurements, while simulations employed very high-order Large-Eddy Simulations. Key findings of the efforts cover the physical three-dimensional mean structure of the wake, unsteadiness associated with vortex meandering and the phenomenon of hysteresis. The effects of Reynolds number and upsweep angle on these features were examined in detail. The primary vortical structure emerging due to separation around the periphery of the base rolls up into a horse-shoe structure which ultimately separates from the base to form a generally streamwise oriented vortex pair. The development of the turbulent flow is characterized by numerous instabilities. The vortices downstream meander at characteristic frequencies designated by their Strouhal numbers based on cylinder diameter. A reduced model shows however, that far downstream, the complex motion can be represented with only a few modes obtained from Proper Orthogonal Decomposition. Hysteresis is observed with Reynolds number as well as upsweep angle varied independently with the two states corresponding to the above described vortex regime, and a separate wake regime characterized by a turbulent wake without large scale coherent features. The research resulted in numerous conference and journal publications which describe these findings in further detail.

2 Introduction

Aft sections of cargo aircraft fuselages are characterized by relatively large upsweep angles to accommodate loading doors and facilitate drop operations. Typical cargo aircraft upsweep angles are larger than those employed in passenger aircraft, and can range between $7\,\mathrm{deg}$ and $28\,\mathrm{deg}$ – some examples are illustrated in Fig. 1. For example, whereas the Boeing 777 has an upsweep of only $14\,\mathrm{deg}$, that for the C-130 is $28\,\mathrm{deg}$.

Under these conditions, the flow separates around the periphery of the base surface, yielding a complicated turbulent wake, which is the focus of this work. The implications of the wake on mission performance and operations can be substantial, since the wake contains many unfavorable flow characteristics. Large inboard and vertical induced velocities raise the likelihood of parachute collisions, tail strikes, and inaccurate cargo drops. Additionally, the low-pressure footprint on the base adversely affects drag and reduces aircraft fuel efficiency. For example, the footprint on the C-130 Hercules has been estimated to contribute as much as 11% to the total drag Smith, Yagle, et al., 2013.

Configurations with such upswept afterbodies, where streamwise vortices adversely affect overall drag, are also common in automobiles (Lienhart, Stoots, et al., 2002), high speed trains (Bell, Burton, et al., 2016), and helicopters (Stepanov, Zherekhov, et al., 2016). The present study is thus relevant to flows beyond the cargo aircraft of current interest. Furthermore, the dynamical characteristics of afterbody vortices are similar to streamwise vortices found in wing-tip vortices (Yeung and Lee, 1999) and delta wings (Gursul, 2005). In blunt-nose bodies of revolution such as missiles and projectiles, streamwise vortices are formed at the forebody (near the nose)

DISTRIBUTION A: Distribution approved for public release.

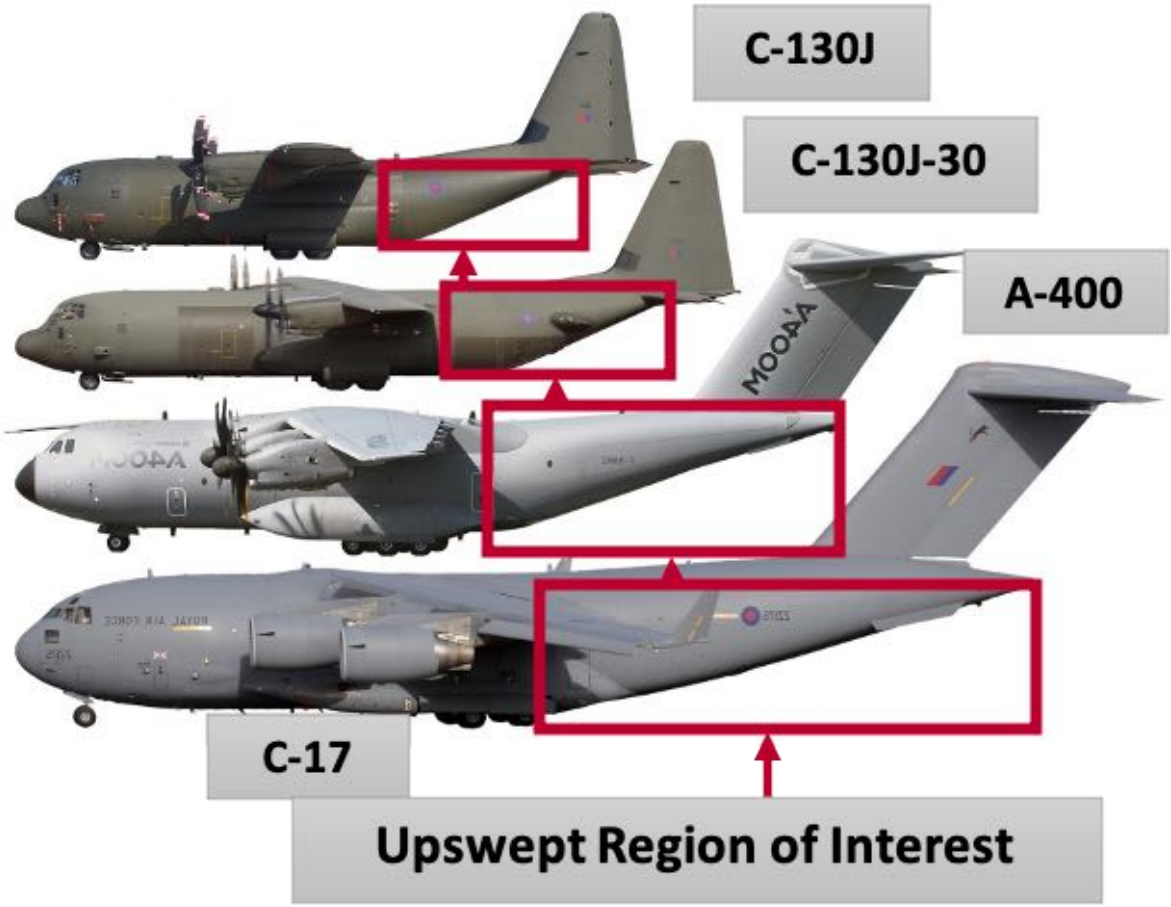


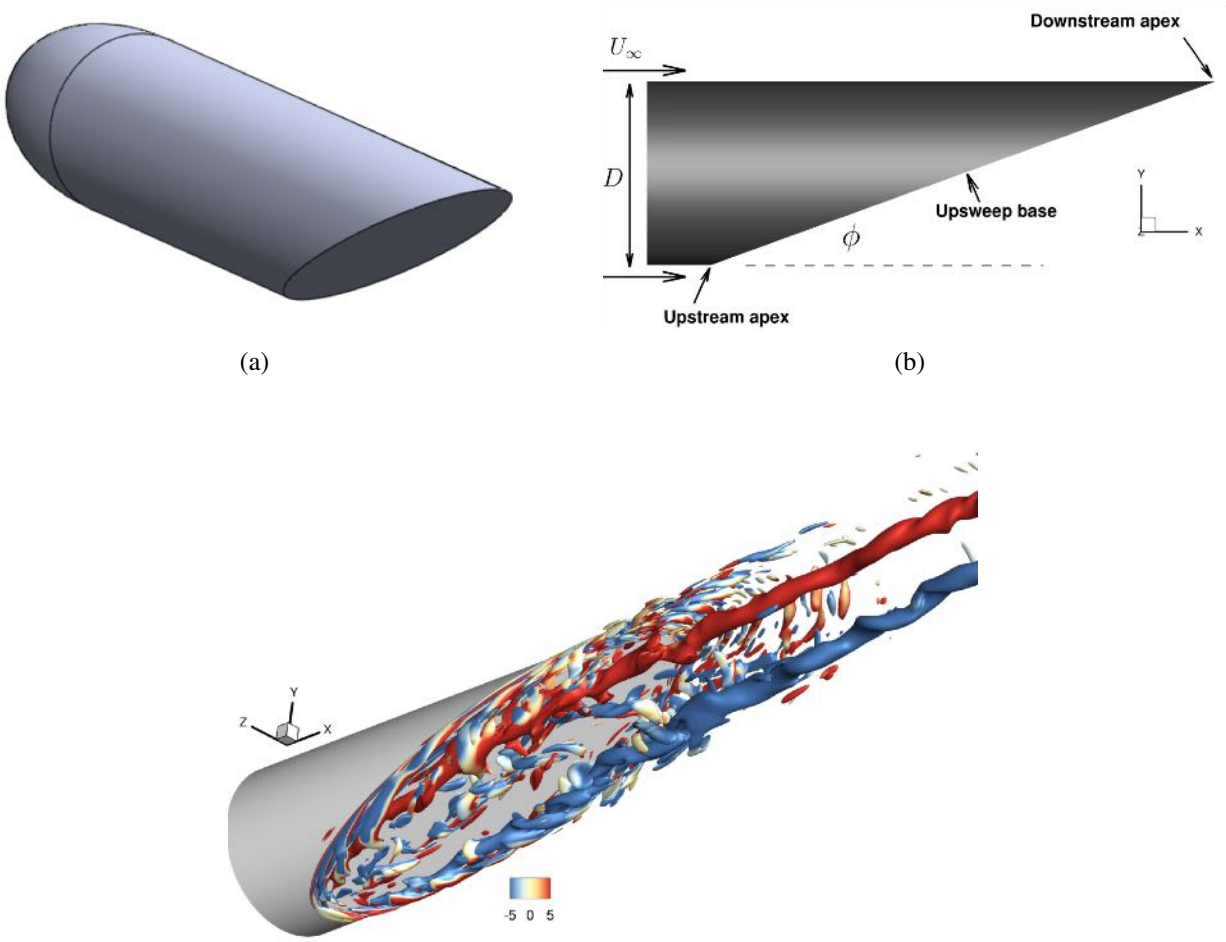
Figure 1: Aftbodies of typical cargo aircraft

instead of afterbody under suitable conditions (Lopera, Ng, et al., 2007), thus affecting the flow downstream.

The flow behind a cargo fuselage-like geometry has been the subject of several test campaigns: Table 1 lists some of the relevant experimental studies conducted on scale models of aircraft or simplified geometries with different forebody configurations. These span a range of upsweep angles and Reynolds numbers. One of the earliest studies was performed by Morel (1978) (Table 1), who considered both axisymmetric as well as rectangular configurations, this latter being representative of sedan cars. For the axisymmetric configuration, drag increases with upsweep angle until a critical angle, beyond which a sudden drop is observed. This drop was attributed to the transition of the flow from a streamwise vortex regime, similar to the one shown in Fig. 2c, to one representing a turbulent wake regime. Xia and Bearman (1983) subsequently conducted experiments with an ellipsoidal nose forebody configuration, and made similar observations as Morel (1978) regarding the change in drag. However, they found that the change in flow regime could be sensitive to aspects of the experimental setup and procedure.

Britcher and Alcorn (1991) further examined the change from vortex to wake flow using ogive cylinders. They report that at upsweep angle $\phi = 45°$, the flow behind the configuration is a

DISTRIBUTION A: Distribution approved for public release.



(a) (b)

(c)

Figure 2: (a) Canonical representation of a cargo aircraft fuselage. (b) Base region and nomenclature employed. (c) Instantaneous solution illustrating the vortex pair, with iso-surfaces using Q-criterion and colored with the streamwise vorticity component, ω_x.

Table 1: Experimental studies on slanted base afterbody flows

Ref.	$\phi(^\circ)$	$Re_D \times 10^{-4}$	**Forebody Configuration**
Morel (1978)	[20 90]	9.4	-
Xia and Bearman (1983)	[20 90]	[18 29]	Ellipsoidal nose
Britcher and Alcorn (1991)	[20 90]	[3 12]	Ogive cylinder
Epstein, Carbonaro, et al. (1994)	28	[8.3 23.7]	C-130
Bury, Jardin, et al. (2013)	28	[35 70]	C-130
Bulathsinghala, Jackson, et al. (2017)	[24 32]	2,20	Ellipsoidal nose
Zigunov, Sellappan, et al. (2019)	20,32,45	[2.5 50]	Ellipsoidal nose

DISTRIBUTION A: Distribution approved for public release.

turbulent wake when the Re_D is below the critical value. As Re_D is increased, while keeping upsweep angle constant, the flow transitions to one containing a streamwise vortex pair. These vortices are observed to be robust, in the sense that they do not transition back to a wake flow when Re_D is reduced *i.e.,* the flow exhibits hysteresis.

A few studies have also been published on more realistic configurations; these have helped establish that the simplified configuration of Fig. 2 is a reasonable surrogate for cargo aircraft. Epstein, Carbonaro, et al. (1994) performed wind tunnel tests on a simplified $1:32$ scale model of a *C-130* fuselage at lower Reynolds numbers than flight conditions. Oil flow visualizations discerned multiple lines of separation and reattachment in the base region. In particular, regions of large crossflow were observed in conjunction with bifurcation lines, indicating the development of streamwise vortices along the fuselage. Base pressure measurements along the center revealed that the pressure increases with distance from the upstream apex (see Fig. 2b for nomenclature), and spanwise pressure minima arise due to the footprints of the streamwise vortices. One of the key findings was that though the experiments were performed at low Re_D, the results corresponded well with those obtained from actual flight Reynolds numbers. Bury, Jardin, et al. (2013) developed a further understanding of the flow by using Particle Image Velocimetry (PIV) to examine flow structures developing around the same model as Epstein, Carbonaro, et al. (1994) but at slightly higher Reynolds numbers. The PIV measurements were obtained for both closed and the opened cargo-door and ramp configurations. Apart from noticing primary longitudinal vortex pair as found in other studies, they also reported formation of induced vortices due to interaction of primary vortices with the empennage. Further, in an open bay configuration, they found occurrence of two new pairs of counter-rotating vortices that originate from the cargo ramp and the beaver-tail. Another noteworthy effort is that of Coustols, Prudhomme, et al. (1995) who examined the effect of the horizontal stabilizer and concluded that the boundary-layer development in this region is primarily dictated by the fuselage geometry (particularly the upsweep) and not by the presence of the horizontal tail.

Several recent experimental studies on the simplified configuration of Fig. 2a have used high-resolution diagnostics to generate a better understanding of the key flow features. Bulathsinghala, Jackson, et al. (2017) performed several experiments in a closed-return wind tunnel using various diagnostics including PIV and pressure transducers. They comprehensively document the features of the streamwise vortex pair in a broad range of upsweep angles ($24^\circ \leq \phi \leq 32^\circ$). In addition to the development of the vortices from the rollup of a vorticity sheet emerging due to separation around the periphery of the upswept base, they also describe the factors associated with increase in vortex strength (circulation) with upsweep angle; these are elaborated on further in the results below.

In addition to the campaigns to understand the baseline flow, many efforts have examined control techniques. Carter (2017) describe active and passive control devices in a practical setting, with the goal of reducing the drag penalty due to streamwise vortices. Large vortex generators in the fuselage models of Boeing 747 and Lockheed C-5 have achieved reductions of 1% and 2% in total drag for these aircraft (Wortman, 1999). Light weight microvanes in the upswept region of C-130 have also achieved significant drag reduction (Smith, Yagle, et al., 2013).

DISTRIBUTION A: Distribution approved for public release.

Simulation-based efforts have been relatively rarer than experiment; many have had more practical goals and have thus chosen more realistic configurations. Because of limitations of Reynolds-Averaged Navier-Stokes (RANS) methods in predicting separated flow physics, several efforts have used more advanced techniques such as Detached-Eddy Simulation (DES; Claus, Morton, et al. (2005) and Morton, Vignes, et al. (2006)) , and Delayed Detached-Eddy Simulations (DDES; Bergeron, Cassez, et al. (2009) and Pang, Ng, et al. (2012)). In general, these studies successfully predict pairs of streamwise vortices as found in experimental studies. However, uncertainties have persisted regarding the nature of separation and vortex strength variations. Bergeron, Cassez, et al. (2009) associated the discrepancy with experiments to the sensitivity of the turbulence model employed – the Spalart–Allmaras model with rotation and curvature correction (SARC) – in regions of large pressure gradients. Pang, Ng, et al. (2012) used the shear-stress transport (SST) model in DDES to improve predictions. Overall, these efforts have greatly facilitated analysis of more practical configurations, but the geometric complexity has inhibited a more fundamental elucidation of the dynamics, since the required resolution for fine-scale unsteadiness is not affordable for the chosen configurations .

Since the inception of this project, several contemporary efforts have explored the flowfield as well as its control. Bulathsinghala, Wang, et al. (2018) used minispoilers near the downstream apex to achieve a drag reduction of about 5% through displacement of the vortices from the surface by the presence of spoilers. These minispoilers act in a similar fashion as Gurney flaps used in delta wings for flow control(Li and Wang, 2003). More recently, Jackson, Wang, et al. (2019) investigated active flow control techniques on these vortices through continuous and pulsed blowing to achieve a maximum of 9% drag reduction. Bulathsinghala, Wang, et al. (2019) measured the effects of splitter-plates, cavities, and flaps on the afterbody vortices and separated flow with surface pressure and PIV measurements. The goal of this work, however, was not drag reduction but to study the transport aircraft configurations with open door and airdrops. An interesting finding was that the splitter-plate and cavity cases display increased unsteadiness in the separated flow region near the upstream apex.

Contemporary efforts have also featured higher-fidelity three-dimensional base flow simulations, at the Large-Eddy Simulation (LES) level, which are challenging because of the required resources. Garmann and Visbal (2019) achieved a breakthrough by using high-order techniques and overset mesh methodology to successfully perform an LES on one of the configurations examined experimentally by Bulathsinghala, Jackson, et al. (2017). The results, obtained at the same Reynolds number as experiment ($Re_D = 2 \times 10^5$), also consider the forebody configuration to obtain a suitable state of the boundary layer entering the base region. The simulation predicts the transitional process of an incoming laminar boundary layer on the fuselage through the formation of Tollmein-Schlichting waves. After separation from the base edge, the simulations display fine-scale features of the streamwise vortex pair expected at this upsweep angle. The predictions compare very well with the corresponding experiments of Bulathsinghala, Jackson, et al. (2017), and facilitate a detailed analysis of important aspects of the flow structure. Key findings include a highly unsteady and turbulent flow near the upstream apex, and meandering of vortices in the wake region that decrease with streamwise distance.

DISTRIBUTION A: Distribution approved for public release.

In the present effort, we performed a systematic, joint experimental and computational study of this flowfield. The synergy between simulation and measurements has been crucial to the rapid advances achieved during this project. Both thrusts have brought to bear the most advanced techniques available, including time-accurate volume measurements and wall-resolved simulations: these are detailed in Section 3. The high-accuracy data obtained has been subjected to state-of-the-art processing techniques and has facilitated exploration of features that are difficult achieve with either one of the thrusts. Only highlights are presented in this report, with details deferred to the numerous publications that have appeared in the literature or are under consideration. Specifically, this work has:

- Elaborated the mean flow structure of the flow with increasing angle (Section 4)
- Examined the phenomenon of hysteresis by considering change in Reynolds number (experiment) and upsweep angle (simulation) (Section 5).
- Clarified the nature of wake unsteadiness and its effects (Section 6), including the stability properties of the downstream vortex pair.
- Developed a reduced-order model by examining the rankedness of the system and isolating key modes (Section 7)

Where possible and necessary, the results are assimilated into the prior and concurrent body of literature.

3 Data acquisition and generation techniques

3.1 Experimental methods

3.1.1 Facility and model details

The experiments conducted in this study were performed at the Florida Center for Advanced Aero-Propulsion (FCAAP) Low-Speed Wind Tunnel (LSWT), an open-loop Eiffel-type facility capable of free stream velocities of $V_\infty = 2.5 - 70$ m/s. The facility has a square test section of 762 mm side and 1564 mm streamwise length. The test section has optical access on all four sides, allowing for advanced flow diagnostics such as Particle Image Velocimetry (PIV), Pressure Sensitive Paint (PSP), and surface oil flow visualization. At the nominal operational range, the facility has a free

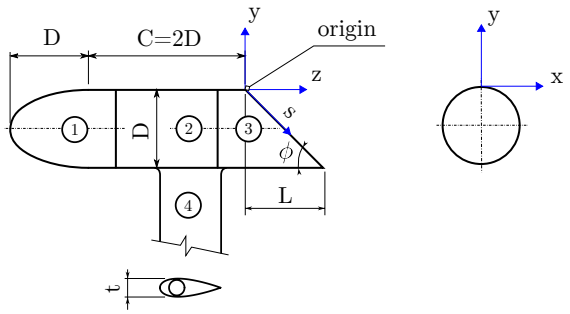


Figure 3: Sectioned model used in the experiments with coordinate system origin and directions used highlighted

DISTRIBUTION A: Distribution approved for public release.

stream turbulence $Tu = u_i'/V_\infty < 0.3\%$.

The slanted cylinder model used in this study is the same used in Zigunov, Sellappan, et al. (2020b), consisting of three tubular sections of external diameter $D = 146$ mm as displayed in figure 3. The Reynolds number per unit freestream velocity, based on the cylinder diameter, is $Re_D/V_\infty = 9736/\frac{m}{s}$. The front section (1) possesses an ellipsoidal nose of a 2:1 ratio, connected to a middle cylindrical section (2) with a mounting strut (4) attached to it. The rear section (3) has the geometry of interest - a truncated cylindrical body with a planar slanted surface. The slanted surface, in the context of aircraft fuselages, represents the afterbody shape that is known to produce a counter-rotating pair of vortices at its rear. In the case of the simplified geometry studied, the connection between the cylindrical main body and the slanted surface is a sharp edge, which ensures the formation of a shear layer.

A few different angles of the slanted afterbody section were manufactured, namely $\phi = 20°$, $32°$, $45°$, $50°$. The latter two slant angles were manufactured with the intent of examining the hysteresis behavior first noted by Britcher and Alcorn (1991) at the slant angle of $\phi = 45°$. The slant angle of $\phi = 50°$, has only been observed to form the fully separated wake regime and was considered to be an important benchmark comparison. The slant angles of $\phi = 20°, 32°$ were examined to understand the typical regime of this wake, which forms a counter-rotating vortex pair.

It is important to note the presence of the mounting apparatus shown in figure 3 (4), since its wake could affect the Reynolds number values observed for the transitions seen in this experiment. The strut mount is a cylindrical tube shrouded with a NACA0020 airfoil shape of thickness $t = 22$ mm. The strut was positioned under the cylindrical section due to the weight of the model, with the model made of aluminum to withstand the high heat loads produced by the high-power laser used in the PIV experiments.

3.1.2 Particle Image Velocimetry (PIV)

The main diagnostic technique employed in this study to characterize the details of this flow was PIV, due to its powerful ability to perform non-intrusive, full-field, quantitative measurements in almost arbitrary regions of the flow field. Due to the intensive and frequent usage of the technique throughout this study, the general details will be described in the narrative and the specifics of each setup are discussed in detail in Zigunov, 2020. PIV measurements were performed along multiple planes of interest around the model, as shown in Figure 4.

The various PIV setups utilized during this multi-year study fell under three distinct categories. In all cases the image acquisition, post-processing and cross-correlation with PIV were performed with the commercial PIV system provided by LaVision (DaVis 8.4.0).

1. **Low Frame Rate PIV:** For the low frame rate PIV, the acquisition setups could be either Planar PIV (PPIV), with a single LaVision sCMOS camera, capturing at 2560×2160 pixels, or Stereoscopic PIV (SPIV) using two sCMOS cameras. Scheimpflug adaptors were employed in the SPIV setup to ensure the entire interrogation plane is in focus. In both types of setups, a 200mJ/pulse, double-pulse Quantel Evergreen laser was employed to provide hthe required illumination. The pulse delay was varied as necessary to achieve about 8-10 px of

DISTRIBUTION A: Distribution approved for public release.

mean particle displacement in the region of interest. Typical correlation uncertainties with the PPIV setup were of $\sim 1\%$ in regions of high shear and $<0.1\%$ in the free stream. For the SPIV, the typical correlation uncertainties were higher, $\sim 5\%$ of the local value in high-shear regions and 1% in the free stream. Additional information on the uncertainty quantification methods is given by Wieneke (2015) and Neal, Sciacchitano, et al. (2015).

2. **Time-Resolved PIV:** In specific cases, a time-resolved PIV setup was necessary to examine the unsteady characteristics of the flow field. One Phantom v2512 camera was employed in PPIV setups, and two high-speed cameras were utilized for SPIV setups. The cameras were only used at their full spatial resolution, 1280×800 px, at frame rates varying between 5,000 fps and 22,600 fps. The light source used was a Photonics Industries DM150-532-DH high repetition rate laser. The laser provided nominally 20 mJ/pulse. The vector uncertainty of time-resolved SPIV was higher ($\sim 10\%$) in relation to the other experiments presented in this work, due to the difficulty in illuminating the particles with a sufficiently large signal-to-noise ratio. PPIV runs had less difficulty with illumination, with typically lower uncertainty values ($\sim 3-5\%$).
3. **Volumetric Reconstruction (Stacked Stereoscopic PIV or S-SPIV)**: The volumetric reconstruction of the mean flow fields was accomplished by using a low frame rate PIV setup (as described in item 1). The volumetric reconstruction was possible with the attachment of a precision traversing mechanism to move the laser and its optics synchronously with another linear motion device attached to the cameras (two linear traverses were needed, as the cameras were positioned far from the laser). This setup is visually depicted in Figure 4. The cameras and laser plane, moving together, allowed for the automated capture of multiple PIV planes along the traversing line without the necessity for camera re-alignment and calibration. This approach makes the experiment much less time consuming and enables volumetric flow visualization without a tomographic PIV setup. The advantages and disadvantages of each setup are also described in Sellappan, McNally, et al., 2018 for the interested reader.

3.1.3 Surface pressure measurements

Average static pressure measurements were performed on the rear slanted surface at 143 pressure ports for each model slant angle, which were laid out as displayed in Figure 5. The pressure ports were scanned using a 48-channel Scanivalve valve scanner connected to an Omega PX653 pressure transducer. The transducer range used was a function of freestream velocity, as detailed in Table 2. The maximum uncertainty in the pressure coefficients displayed in the results was $\Delta C_p = 0.03$ for the $Re_D = 2.5 \times 10^4$ case. The transducer ranges utilized for each freestream velocity are detailed in Table 2 along with the uncertainty values ΔC_p related to the sensors used. The measurements were averaged over 30 seconds for each port. Four runs were necessary to cover the full pressure port count, which involved stopping the tunnel fan and reconnecting the pressure tubing inside the model due to limitations in the number of pressure tubes that could be routed through the support strut. The pressure ports at the centerline remained connected throughout the pressure survey, ensuring the experiment was repeatable to within sensor uncertainty. Out of the 143 ports, 22 ports were placed at mirrored locations with respect to the YZ plane to validate that the mean flow

DISTRIBUTION A: Distribution approved for public release.

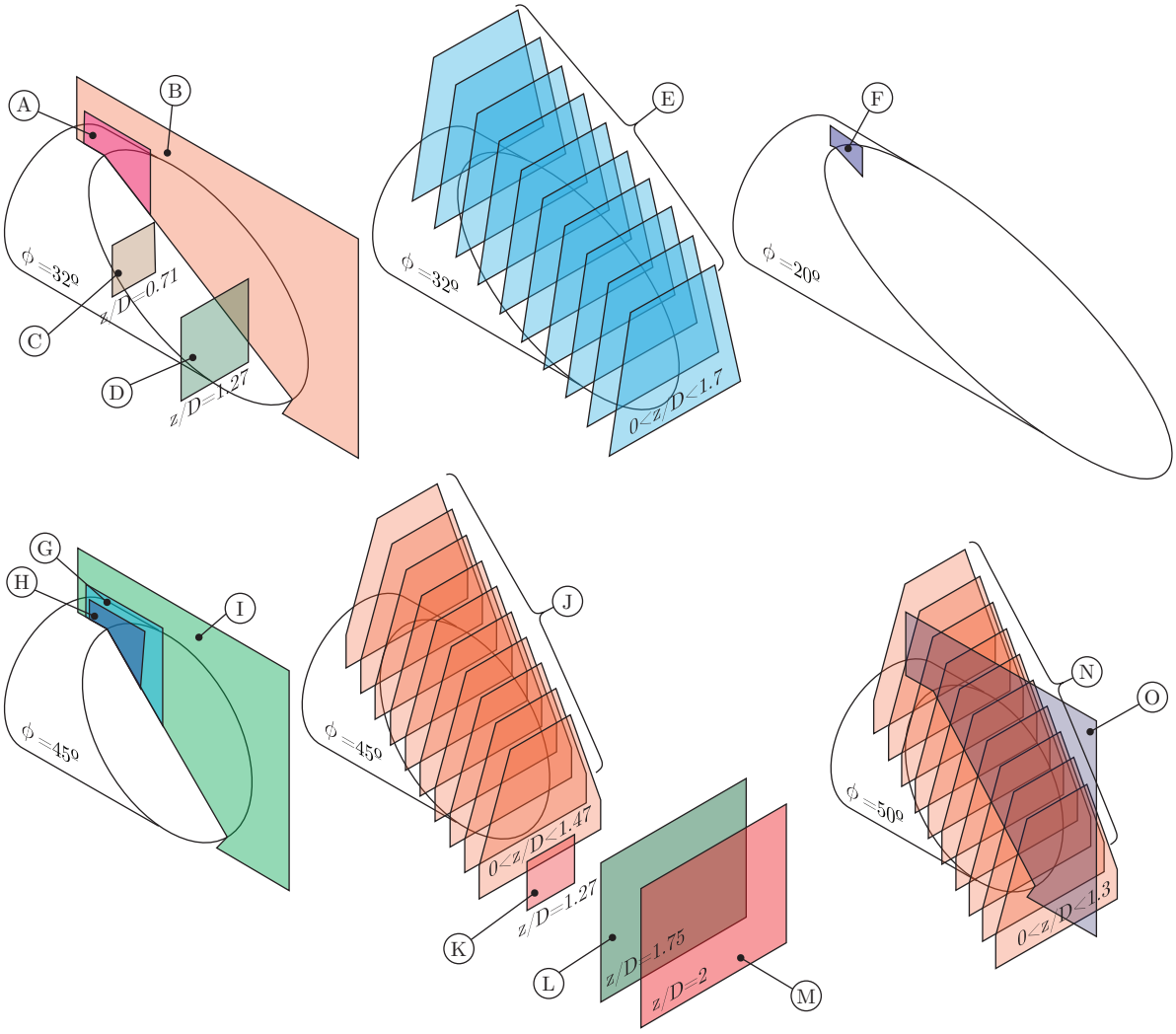


Figure 4: PIV Planes employed in this study. S-SPIV stacks (E), (J), (N) have many more planes than represented in the illustration.

was symmetric across the center plane. Within the pressure sensor uncertainty, the same pressure values were measured in the mirrored locations for all conditions tested.

3.1.4 Stall hysteresis experimental procedure

In order to capture the flow evolution for the study of hysteresis, in particular the changes when the flow field transitions from one state to another, very precise control of the free stream velocity was implemented. In order to minimize the effects related to free stream acceleration transients, the ramping up of the free stream was performed with the minimum rate possible in the LSWT facility. The rate of acceleration/deceleration was measured to be approximately constant as a function of free stream velocity, and was kept below $dV_\infty/dt < 0.1$ m/s^2.

DISTRIBUTION A: Distribution approved for public release.

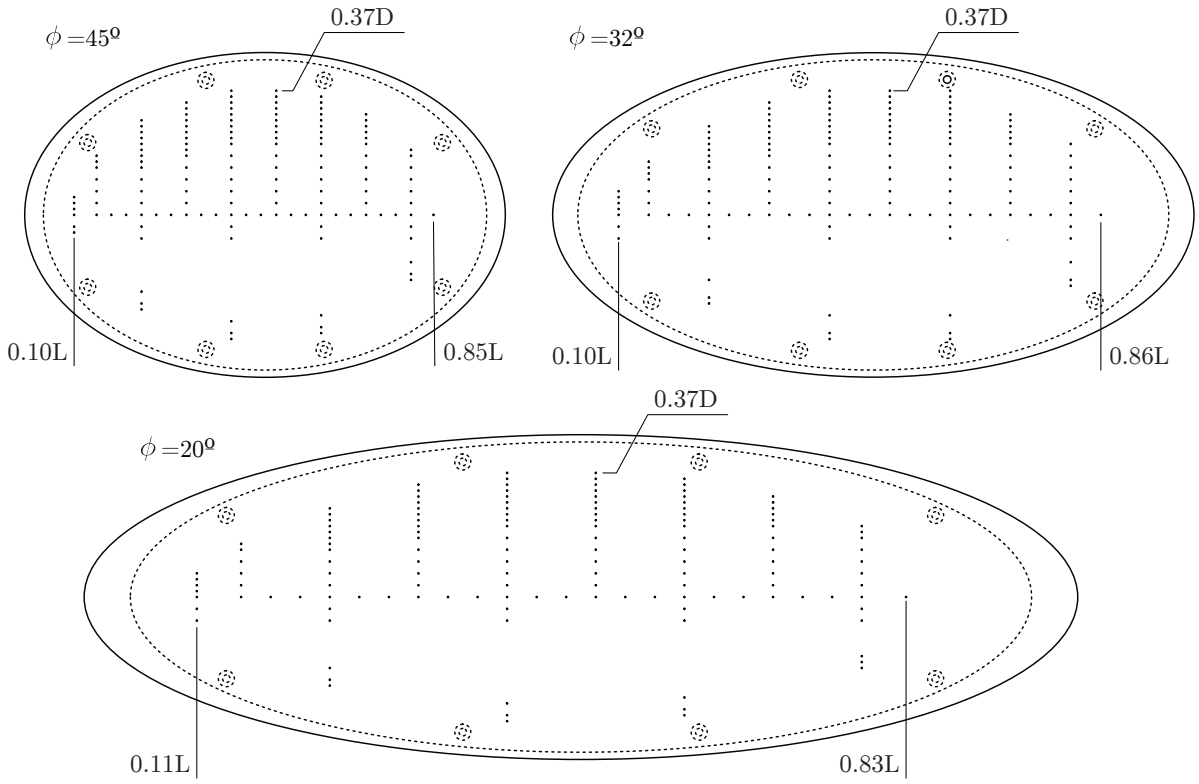


Figure 5: Position of all pressure ports used in this study, to scale.

Table 2: Pressure transducer ranges utilized for each freestream Reynolds number and the corresponding measurement uncertainty normalized by dynamic pressure

Re_D	Transducer Range [Pa]	ΔC_p
2.5×10^4	0 to 24.88	0.031
4×10^4	0 to 24.88	0.012
2×10^5	0 to 248.84	0.005
5×10^5	0 to 2488.4	0.008

The wind tunnel free stream velocity was increased in a stair-step pattern, as indicated in figure 6, traversing in approximately uniform increments in Re_D. Guided by previous experiments, the approximate values of the transition Reynolds numbers $Re_{t,upper}$ and $Re_{t,lower}$ were known *a priori* and the grid was therefore highly refined close to the threshold values. The flow was kept at a fixed free stream velocity for variable periods, since the convective times are longer for the lower Reynolds number cases. The minimum number of convective times allowed for flow stabilization prior to PIV capture was $\tau = tV_\infty/D > 2 \times 10^3$. When the flow was observed to transition from the stalled wake regime to the vortex pair regime ($Re_{t,upper}$) through examination of the raw PIV images, the free stream was slowly decreased in the same stair-step pattern until the stall of the

DISTRIBUTION A: Distribution approved for public release.

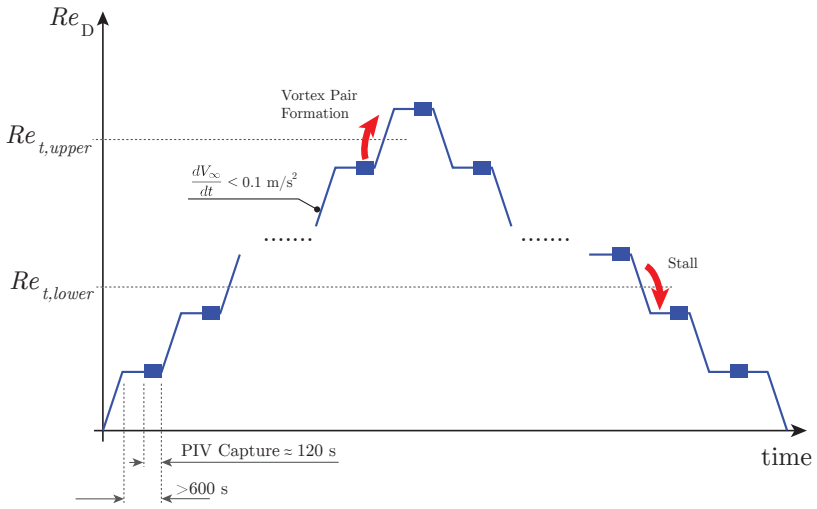


Figure 6: Graphical description of the experimental procedure employed to observe the flow progression as the wake goes through the stall hysteresis process. Red arrows indicate the abrupt transition of the wake

wake was observed at $Re_{t,lower}$.

3.2 Numerical methods

The governing equations are the full 3D compressible Navier-Stokes equations for a generalized curvilinear coordinate system:

$$\frac{\partial}{\partial\tau}\left(\frac{\mathbf{U}}{J}\right)+\frac{\partial\mathbf{F}}{\partial\xi}+\frac{\partial\mathbf{G}}{\partial\eta}+\frac{\partial\mathbf{H}}{\partial\zeta}=\frac{1}{Re}\left[\frac{\partial\mathbf{F}_v}{\partial\xi}+\frac{\partial\mathbf{G}_v}{\partial\eta}+\frac{\partial\mathbf{H}_v}{\partial\zeta}\right]+\mathbf{S} \tag{1}$$

where **U** is the conserved variable vector, **F**, **G**, and **H** are the inviscid flux vectors represented by:

$$\mathbf{U}=\begin{pmatrix}\rho\\ \rho u\\ \rho v\\ \rho w\\ \rho E\end{pmatrix},\mathbf{F}=\frac{1}{J}\begin{pmatrix}\rho U\\ \rho uU+\xi_x p\\ \rho vU+\xi_y p\\ \rho wU+\xi_z p\\ (\rho E+p)U-\xi_t p\end{pmatrix},\mathbf{G}=\frac{1}{J}\begin{pmatrix}\rho V\\ \rho uV+\eta_x p\\ \rho vV+\eta_y p\\ \rho wV+\eta_z p\\ (\rho E+p)V-\eta_t p\end{pmatrix} \tag{2}$$

$$\mathbf{H}=\frac{1}{J}\begin{pmatrix}\rho W\\ \rho uW+\zeta_x p\\ \rho vW+\zeta_y p\\ \rho wW+\zeta_z p\\ (\rho E+p)W-\zeta_t p\end{pmatrix} \tag{3}$$

where J is the Jacobian matrix transformation from Cartesian coordinates and dimensional time (x,y,z,t) to curvilinear coordinates and non-dimensional time (ξ,η,ζ,τ). With the contravariant

DISTRIBUTION A: Distribution approved for public release.

velocities U, V, W given by:

$$U = \xi_t + \xi_x u + \xi_y v + \xi_z w \tag{4}$$

$$U = \eta_t + \eta_x u + \eta_y v + \eta_z w \tag{5}$$

$$U = \zeta_t + \zeta_x u + \zeta_y v + \zeta_z w \tag{6}$$

The viscous flux vectors $\mathbf{F}_v$,$\mathbf{G}_v$,$\mathbf{H}_v$ are represented as:

$$\mathbf{F}_v = \frac{1}{J}\begin{pmatrix} 0 \\ \xi_x\tau_{xx} + \xi_y\tau_{xy} + \xi_z\tau_{xz} \\ \xi_x\tau_{xy} + \xi_y\tau_{yy} + \xi_z\tau_{yz} \\ \xi_x\tau_{xz} + \xi_y\tau_{yz} + \xi_z\tau_{zz} \\ \xi_x b_x + \xi_y b_y + \xi_z b_z \end{pmatrix}, \mathbf{G}_v = \frac{1}{J}\begin{pmatrix} 0 \\ \eta_x\tau_{xx} + \eta_y\tau_{xy} + \eta_z\tau_{xz} \\ \eta_x\tau_{xy} + \eta_y\tau_{yy} + \eta_z\tau_{yz} \\ \eta_x\tau_{xz} + \eta_y\tau_{yz} + \eta_z\tau_{zz} \\ \eta_x b_x + \eta_y b_y + \eta_z b_z \end{pmatrix}, \tag{7}$$

$$\mathbf{H}_v = \frac{1}{J}\begin{pmatrix} 0 \\ \zeta_x\tau_{xx} + \zeta_y\tau_{xy} + \zeta_z\tau_{xz} \\ \zeta_x\tau_{xy} + \zeta_y\tau_{yy} + \zeta_z\tau_{yz} \\ \zeta_x\tau_{xz} + \zeta_y\tau_{yz} + \zeta_z\tau_{zz} \\ \zeta_x b_x + \zeta_y b_y + \zeta_z b_z \end{pmatrix} \tag{8}$$

where τ_{ij} is the stress tensor and $\dot{q}_i$ is the heat flux vector as a function of local Mach number M:

$$\tau_{ij} = M\left[\mu\left(\frac{\partial u_i}{\partial x_j} + \frac{\partial u_j}{\partial x_i}\right) + \lambda_b \frac{\partial u_k}{\partial x_k}\delta_{ij}\right] \tag{9}$$

$$\dot{q}_i = -\left[\frac{M\mu}{Pr(\gamma - 1)}\right]\frac{\partial c^2}{\partial x_i} \tag{10}$$

$$b_i = u_j\tau_{ij} - \dot{q}_i \tag{11}$$

The dynamic viscosity μ is temperature dependent and is obtained from Sutherland's law. The bulk viscosity is assumed to be $\lambda_b = -2/3\mu$, and a perfect gas assumption with a constant Prandtl number of Pr=0.72 is used.

3.2.1 Numerical Scheme

The simulations primarily use 4^{th}-order compact-differencing spatial discretization (Lele, 1992; Gaitonde and Visbal, 1998) with a 6^{th}-order filter (Gaitonde and Visbal, 2000). However, numerical convergence is examined through p-refinement Lockard, Brentner, et al., 1995; Wake and Choi, 1996 by also repeating a sample simulation with a 6^{th}-order scheme and 8^{th}-order filter. A 2^{nd}-order implicit diagonalized Beam and Warming scheme Beam and Warming, 1978 is used for the temporal discretization. A timestep Δt, non-dimensionalized by D and U_∞ of 2.5×10^{-4} is found to be sufficient to obtain time-resolved results. The mean flow results represent time-averaged data over $500{,}000$ iterations or 125 characteristic times based on U_∞ and D. Other details pertinent to statistics gathering and specific simulations are described later in proper context.

DISTRIBUTION A: Distribution approved for public release.

3.2.2 Computational Domain and Mesh

The specific configuration employed is based on the concurrent experimental effort performed at Florida State University (FSU) as described in Zigunov, Sellappan, et al. (2019), and is comprised of a cylinder with streamwise-aligned axis with a slanted base (Fig. 2b). The computational domain and mesh are shown in Fig. 7. For computational convenience and efficiency, the nose region is not computed; further justification for this choice is presented below with the boundary conditions. An axisymmetric, structured grid is used of streamwise and radial extents of $12D$ and $14D$ respectively. A near-field view of the mesh near the cylinder surface is shown in Fig. 7. The mesh density is selected based on the results of Garmann and Visbal (2019), who use a similar numerical scheme and demonstrate mesh independence. The resulting grid has $485 \times 418 \times 285$ nodes in the streamwise, radial, and azimuthal directions respectively.

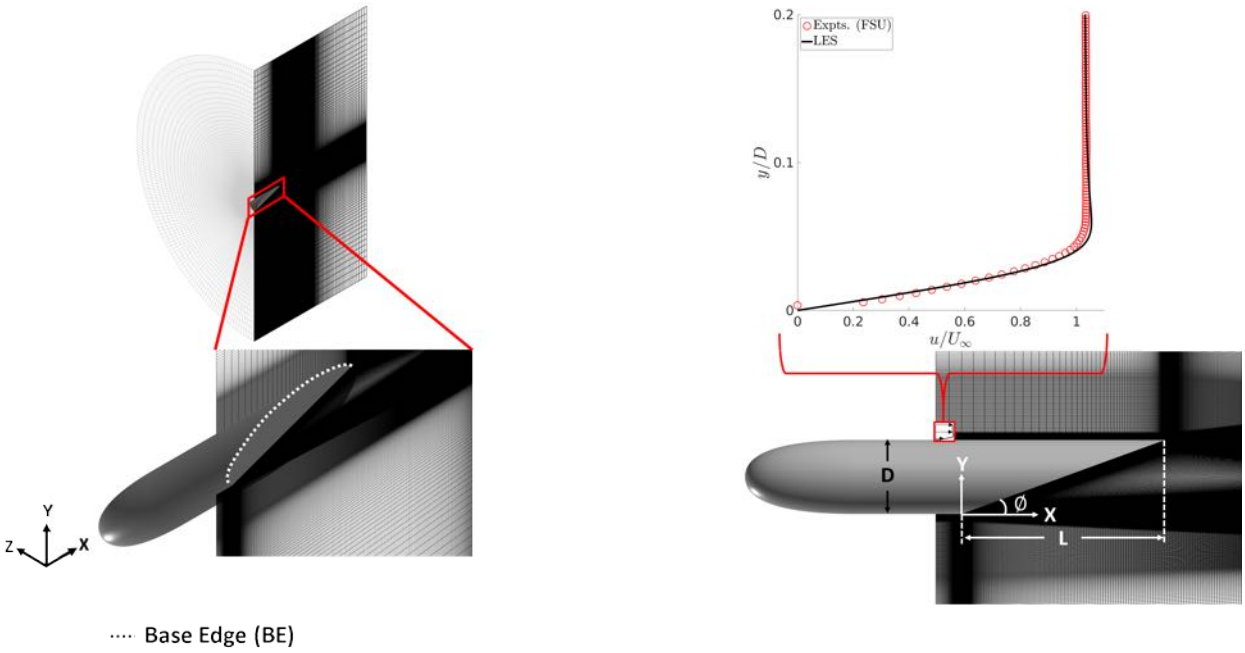
3.2.3 Simulation Parameters and Boundary Conditions

Most of the simulations were conducted on three upsweep angles, $20°$, $32°$, $45°$, all at the nominal Reynolds number of $Re_D = 2.5 \times 10^4$, which is the lowest value at which some experimental data is available from Zigunov, Sellappan, et al. (2019). Each of these three upsweep angles display the streamwise vortex pair ("vortex regime"); a higher $55°$ upsweep angle case is also simulated to illustrate some features of the turbulent "wake regime". Several experimental studies Epstein, Carbonaro, et al., 1994; Bury, Jardin, et al., 2013; Bulathsinghala, Jackson, et al., 2017 have noted the relatively weak dependence on Reynolds number in the range listed in Table 1. Further evidence for this observation is shown in this work using simulations at $Re_D = 5 \times 10^4$, as well as through comparisons with measurements at the same and higher Reynolds numbers. Other campaigns, such as to study hysteresis, are presented later.

No-slip and zero normal pressure gradient are specified on the cylinder surface. A five-point overlap is used in the azimuthal direction to enforce periodicity. The freestream condition is specified at the radial farfield boundary. Since the nose region is not considered, experimental data is employed to generate the inflow data at a location upstream of the slanted base. An auxiliary simulation at the same Reynolds number is performed on an infinite axisymmetric body corresponding to the cylinder with axis parallel to the flow. A boundary layer profile from this simulation is extracted so that it matches that provided by the experiments performed at Florida State University.

The boundary layer thus obtained is shown in Fig. 7b, which compares the simulated inflow and the experimental data. The simulated profile clearly agrees quite well with the measured profile and facilitates the restriction of the domain to exclude the forebody region. Lastly, the mesh structure chosen results in a singularity along the axis, which is addressed by enforcing solution continuity Speth and Gaitonde, 2013. For reference, the upstream apex (UA) and a downstream apex (DA) are extreme endpoints on the base.

DISTRIBUTION A: Distribution approved for public release.



(a) (b)

Figure 7: Computational mesh. (a) isometric view of the base and corresponding closeup of the cylinder and (b) sideview with the inflow boundary layer profile used for LES.

4 Flow Description

4.1 Experimental investigation

4.1.1 Surface flow features

A representative oil flow image describing the salient flow features as observed on the surface of the slanted cylinder is displayed in Fig. 8. A time-lapse sequence is provided as supplementary material in Zigunov, Sellappan, et al., 2020a. These features will be further characterized and confirmed by the PIV results presented in the following sections and are common between the observations made in this study.

The side view shows the oil flow tracer dragged upwards at the upwash region due to the strong suction on the slanted surface. The fluid, bounded by the cylindrical surface, collects towards the centerline and accelerates towards the slant edge along the upper portion of the cylinder. The same effect is observed in the top view of the model at the cylindrical surface close to the slant edge, where the oil flow lines converge towards the center plane. Due to the sharp edge of the slanted surface, the shear layer location is fixed geometrically and the flow separates around the slant edge perimeter. However, the low pressure on the slanted surface causes the fluid to reattach to the surface, forming a three-dimensional, open separation bubble. The oil flow lines in the separation bubble region move upstream, as indicated by the white arrows pointing left in fig. 8. The separation bubble imprints on the surface a “source point” feature, where the oil flows

DISTRIBUTION A: Distribution approved for public release.

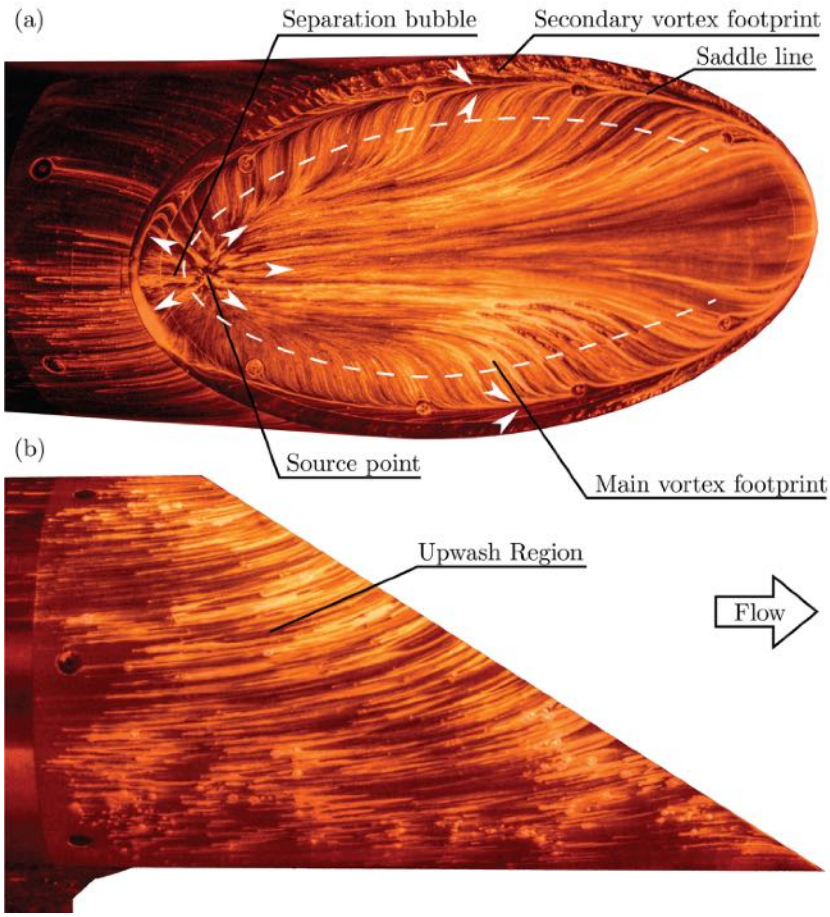


Figure 8: Representative oil flow image for the case $\phi = 32°$ and $Re_D = 5 \times 10^5$. Labels indicate salient flow features. White arrowheads indicate direction of oil flow. Dashed line highlights main vortex footprint. (a) Top view. (b) Side view.

outwards in all directions. The term "source point" here will be used to refer to this particular feature observed at the reattachment of the separation bubble, however it is to be interpreted as a typical saddle line feature observed in separation bubbles that, due to the three-dimensionality of this wake flow, is confined to a small region in space, thus appearing visually as a "source point" in the oil flow images.

As previously described in the work of Bulathsinghala, Jackson, et al. (2017) and other researchers, this geometry's flow topology is characterized by the presence of a strong counter-rotating vortex pair, which leaves a footprint on the slanted surface as a strong sideways oil flow motion that is directed outwards from the symmetry plane and is highlighted as a dashed line in the top view of Fig. 8. The transition from the separation bubble to the vortex footprint is smooth. Furthermore, a secondary footprint due to a secondary vortex, which will be discussed further in section 4.1.3, can also be identified closer to the slant edge. These two footprints have opposite shear directions, leading to a convergence line where the oil accumulates and forms a rivulet along

DISTRIBUTION A: Distribution approved for public release.

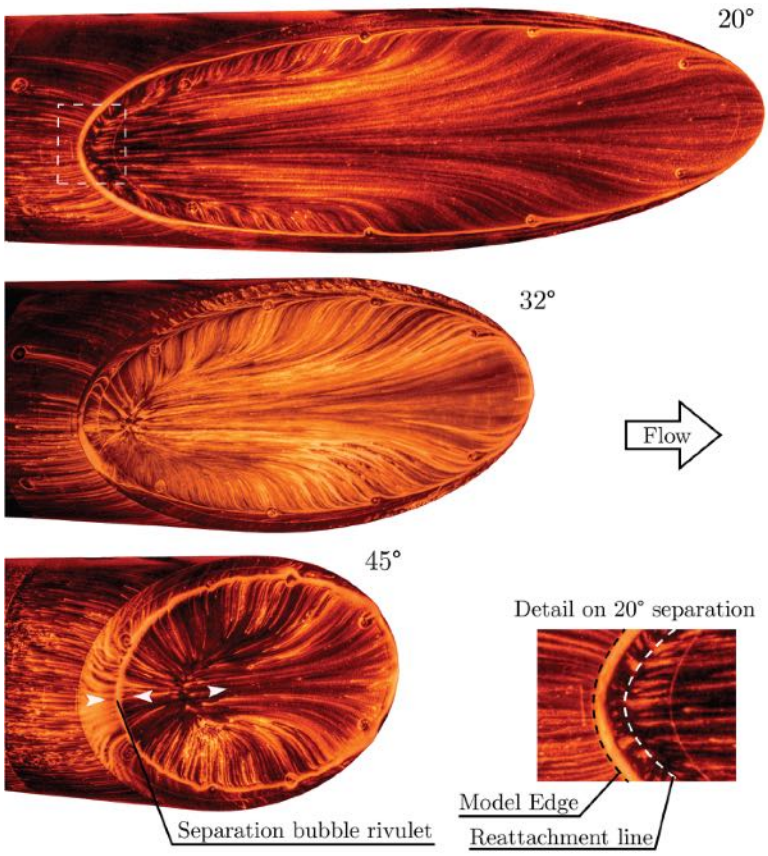


Figure 9: Impact of slant angle on oil flow features for $\phi = 20°$, $32°$ and $45°$. For all cases $Re_D = 5 \times 10^5$. Images show the slanted surface. Detail on $\phi = 20°$ separation bubble provided, identifying region of reversed flow (between black and white dashed lines). Time-lapse surface pattern evolution available in movies 1-3

a line, which is labeled in Fig. 8 as "Saddle Line". A similar feature was also observed in oil flow studies performed by Epstein, Carbonaro, et al. (1994) on more realistic aircraft fuselage afterbodies, which was associated with the presence of surface curvature and its effect on the vortex pair. For the slanted cylinder geometry, however, this feature can be regarded as a "corner vortex", as it is the result of the interaction of a vortex and a shear layer at a sharp corner.

Important trends in the flow features are observed in the oil flow images shown in Fig. 9 as the slant angle ϕ is increased. The leading slant edge is aligned at the left side of the images to facilitate comparison of the flow feature locations. The "source point" clearly moves downstream as the slant angle is increased, indicating a longer separation bubble. The time-lapse image sequence (movie 2) that shows the flow evolution of the $\phi = 20°$ case reveals the presence of upstream-moving oil traces, and is highlighted in the detail in Fig. 9. The curvature of the oil flow lines near the main vortex pair footprint location becomes more pronounced as the slant angle is increased, indicating a stronger sideways motion related to the presence of a stronger vortex. It is also observed that the spanwise extent to which the vortex footprint influences the oil flow streamlines increases with

DISTRIBUTION A: Distribution approved for public release.

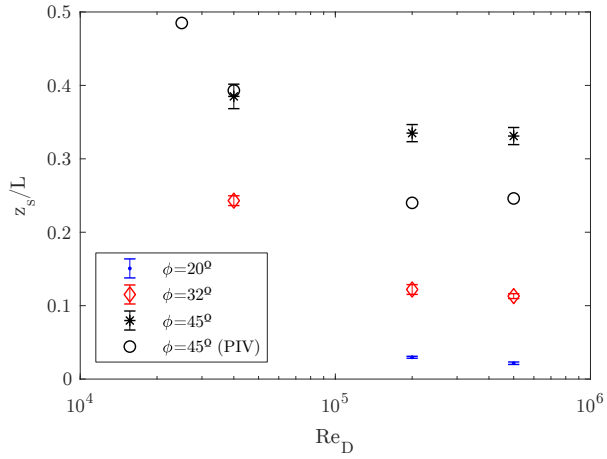


Figure 10: Streamwise location of the "source point" feature as identified in the surface flow experiments as a function of Re_D and ϕ. Black circles indicate results from planar PIV for comparison

slant angle ϕ, which in conjunction with the increased size of the separation bubble indicates a general trend of growth in size of relative flow features with increased slant angle.

The $\phi = 45°$ case presents an anomalous behavior between the leading edge of the slanted surface at the centerline and the "source point", where the surface lines formed a steady oil rivulet that streamed outwards towards the saddle line. The feature is labeled in Fig. 9 as "Separation Bubble Rivulet" and the directionality of the oil flow lines is indicated with white arrows. Although it is possible that this feature could be associated with a limitation of the oil flow technique, which depends on the balance between the shear forces produced by the flow and the gravitational force acting on the oil, the PIV measurements confirm that this feature is indeed present in the mean flow field as will be discussed in Section 4.1.4. This flow feature can be a product of the complex interaction between the separating shear layer and the reversed flow inside the separation bubble, which forms a highly unsteady flow pattern, resulting in this unusual mean downstream flow in that region.

For the 8 cases where oil flow visualization was successfully performed, it was possible to identify the reattachment point ("source point", refer to Fig. 8) location, z_s, measured from the origin. This quantity is plotted in Fig. 10, normalized by the slant length L. As can be observed in Fig. 10, the measured separation bubble lengthens (its reattachment point z_s/L moves downstream) as the Reynolds number Re_D is decreased, and the changes are significant across the order-of-magnitude changes in Re_D examined in this study. The same trend of downstream movement of the reattachment point is observed as the slant angle ϕ is increased. A comparison is provided against measured PIV reattachment locations for the $\phi = 45°$ case, and further discussion on the discrepancies observed is given in Section 4.1.4.

4.1.2 Trends in surface pressure

Mean pressure measurements were performed at 143 pressure ports as described in Section 3.1.3 for the 12 cases examined in this study. The trends in pressure distribution were monotonic in the

DISTRIBUTION A: Distribution approved for public release.

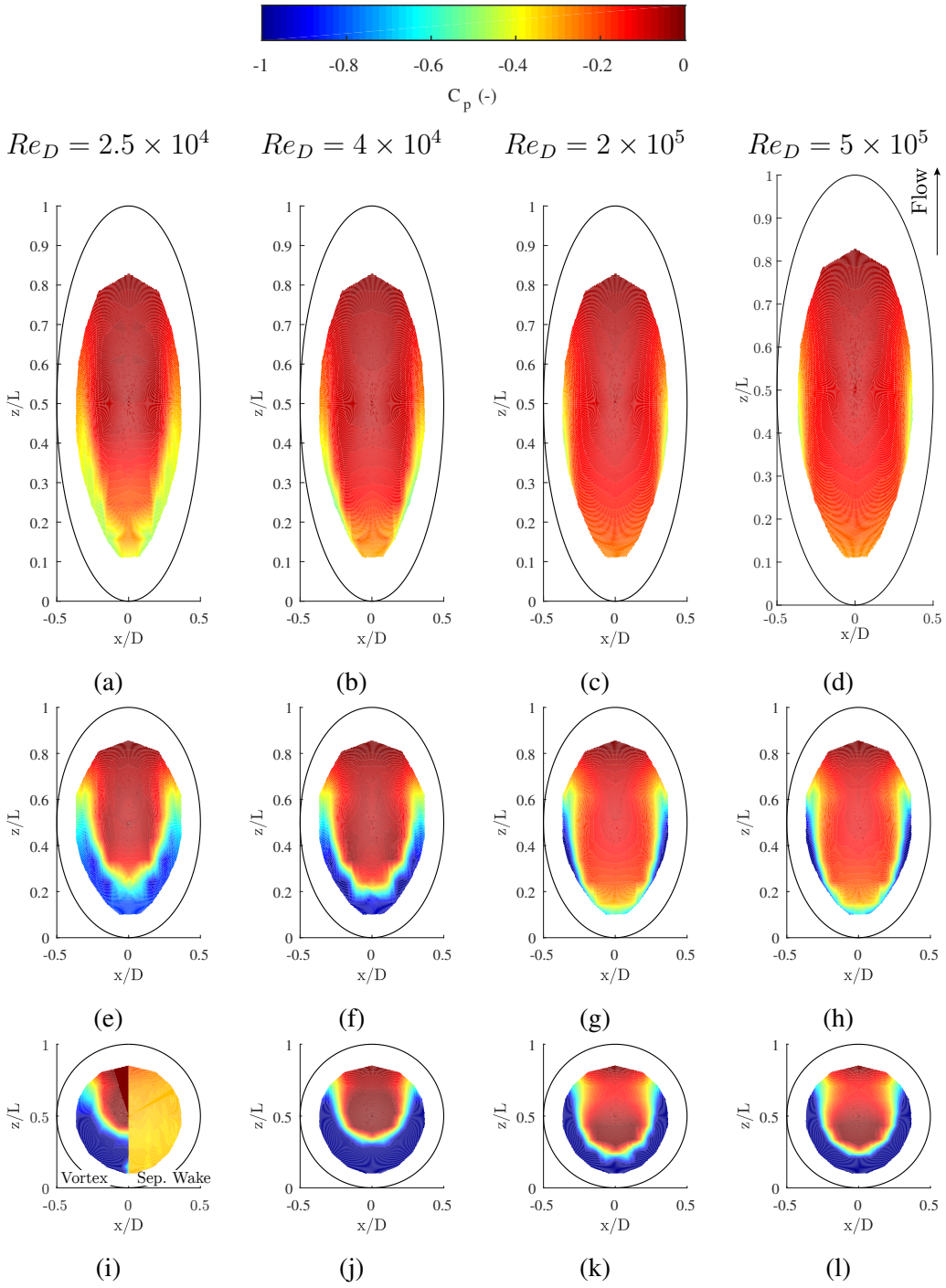


Figure 11: Top view showing the effect of Reynolds number and slant angle on the pressure distribution over the slanted surface for the cases studied. (a) - (d) $\phi = 20°$, (e) - (h) $\phi = 32°$, (i) - (l) $\phi = 45°$. Reynolds number indicated on the top of each column. Flow is from bottom to top

DISTRIBUTION A: Distribution approved for public release.

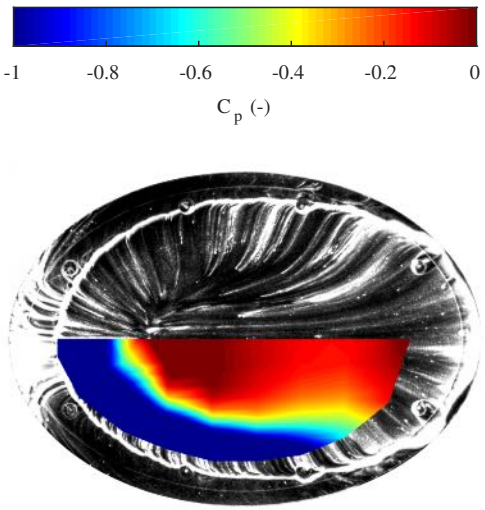


Figure 12: Pressure measurements plotted against grayscale oil flow image for the $\phi = 45°$, $Re_D = 5 \times 10^5$ case, showing relative location of features. Colormap is consistent with previous figures, however $C_{p,min} = -1.75$ exceeds color scale

vortex-dominated regime and are summarized in fig. 11. The horseshoe-shaped vortex footprint described in the previous section is also observed in the pressure plots as an "U" shape in all cases. The case shown in fig. 11 (i), which corresponds to $\phi = 45°$ and $Re_D = 2.5 \times 10^4$, is split in two sub-cases. This lower Reynolds number value is notable in that two different pressure signatures were possible depending on the start-up transient of the tunnel. The results for these two flow patterns observed are on either side of fig. 11 (i). The vastly different pressure signature indicates that this case suffered a flow pattern transition, similar to that reported by Britcher and Alcorn (1991) based on drag measurements, which were also a function of Reynolds number for this slant angle. The pressure signature shown in the right of fig. 11 (i) is believed to correspond to the separated wake flow pattern, whereas the left-half pressure field corresponds to the vortex pair flow pattern. Details about how the two flow patterns were obtained will be further discussed in Section 4.1.4.

Apart from the transitional case shown in fig. 11 (i), the surface pressure trends are consistent with the surface flow observations. As the Reynolds number is increased, the separation bubble extent, which imparts its signature as a very low pressure region in the surface, seems to shrink. The vortex footprint also moves towards the edges of the slant, confining the extents of its influence. Due to physical construction limitations it was not possible to perform surface pressure measurements near the slanted surface edge to observe the entire vortex footprint in the pressure distribution. The inverse trend is observed when the slant angle ϕ is increased, that is, as ϕ is increased the separation bubble lengthens and the vortex footprint influences a larger portion of the slanted surface area. These trends are consistent with the observed increase in the drag coefficient C_D as the slant angle is increased as reported in past studies (Morel, 1980; Xia and Bearman, 1983). Since the opposite trend was observed with respect to Reynolds number, it is reasonable to

DISTRIBUTION A: Distribution approved for public release.

$\phi = 32°$		
z_{start} [mm]	z_{end} [mm]	Δz [mm]
-1	47	3
47	112	5
112	140	7
140	180	10
180	210	15
210	250	20

$\phi = 45°$		
z_{start} [mm]	z_{end} [mm]	Δz [mm]
1	40	3
40	120	5
120	170	10
170	215	15

Table 3: Resolution of the S-SPIV reconstruction performed for the $Re_D = 2 \times 10^5$ cases. Block delimiters z_{start} and z_{end} define the vector z resolution Δz within a range of z planes used for the reconstruction of the three-dimensional flow field

speculate that the drag coefficient will also increase with decreasing Re along order of magnitude changes.

The oil flow images at the slanted surface were dewarped using a simple perspective projection based on the location of the center of the mounting screws. The dewarped images were plotted together with the C_p measurements in fig. 12 for the case $\phi = 45°$ and $Re_D = 5 \times 10^5$. The view is normal to the slanted surface. This case was specifically chosen because the "source point" appears inside of the measurement extent of the pressure distribution. The relative position of surface flow features and their pressure signature can be correlated and it becomes evident that the recirculation region is formed due to the strong adverse pressure gradient present on the surface. The form of a horseshoe shape over the surface is consistent between the oil traces and pressure distribution.

4.1.3 Three-dimensional flow topology of the near-wake

A volumetric reconstruction of the average flow field over the slant was performed for two representative cases at $Re_D = 2 \times 10^5$, with slant angles of $\phi = 32°$ and $\phi = 45°$, where optical access was favorable for the automated capture of multiple planes. The z-planes used for the reconstruction are detailed in Table 3; a variable plane spacing was used to capture the fine-scale details of the flow close to the separation bubble while avoiding the capture of an unnecessary amount of data in regions where the gradients of the quantities of interest are not as steep. Isosurfaces of dimensionless Q criterion computed from the reconstructed mean velocity field are displayed in fig. 13 to highlight the vortical structures present in the mean flow. The results presented correspond to averages of 300 PIV fields for each plane.

The isosurfaces of dimensionless Q criterion clearly highlight the dominant vortex pair in this flow, as well as the transition of the separation bubble into the vortical structures. This transition of the separation bubble into a pair of vortex tubes is directly measured experimentally for the first time with a high density of vectors close to the separation bubble, allowing for the adequately fine resolution of the derivative quantities necessary for computing Q in the presence of steep gradients.

The streamlines, generated from arbitrarily selected points on the isosurfaces, also reveal the vortex structure by wrapping around the isosurfaces through the measurement domain. Both slant

DISTRIBUTION A: Distribution approved for public release.

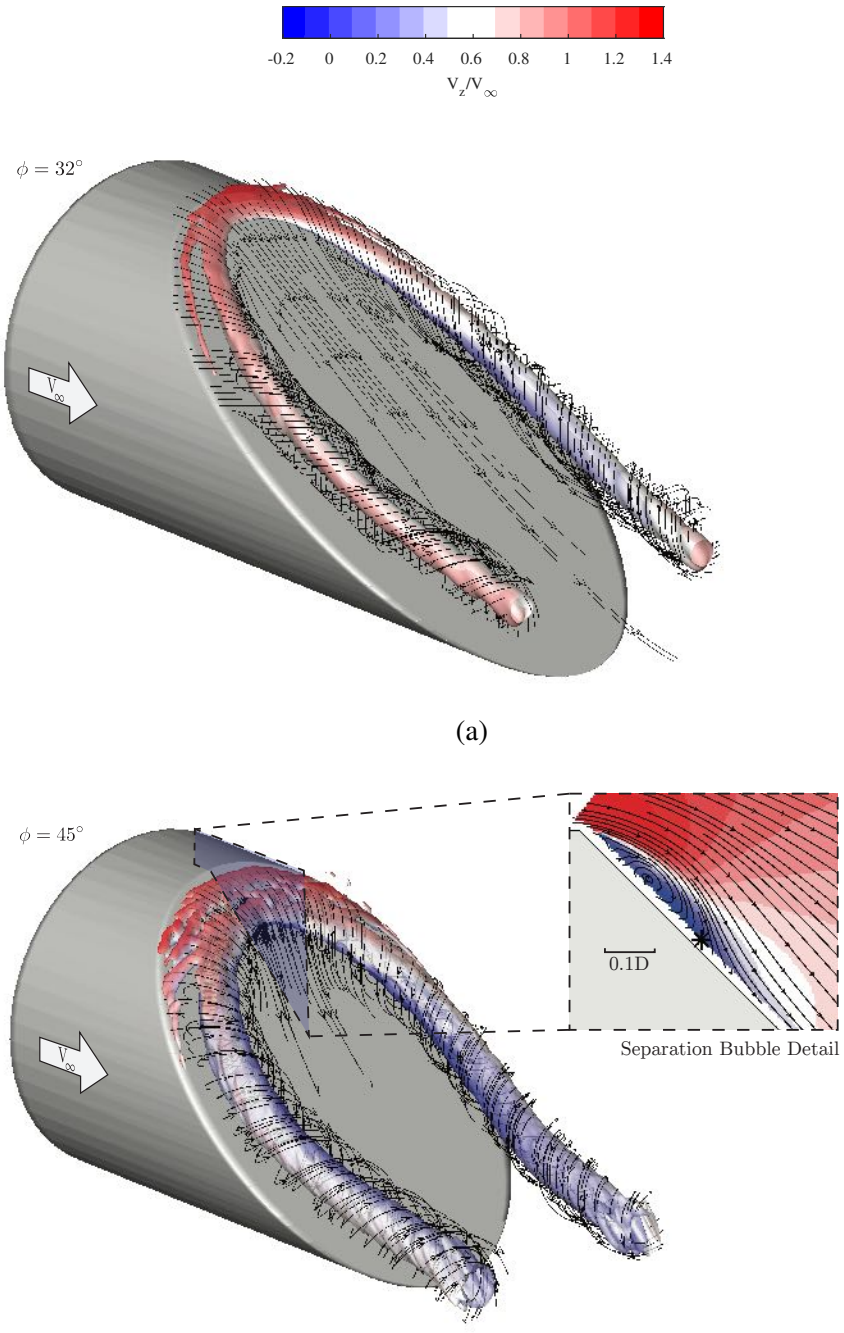


Figure 13: S-SPIV volumetric reconstruction of the mean flow for slant angles (a) $\phi = 32°$ and (b) $\phi = 45°$, both at $Re_D = 2 \times 10^5$. Isosurfaces highlight $Q(D/V_\infty)^2 = 180$ and are colored by non-dimensional velocity (V_z/V_∞). Streamlines seeded at approximately equally spaced points on isosurfaces of $Q(D/V_\infty)^2 = 90$ (not shown). Last plane at $z/L = 1.06$ in (a) and at $z/L = 1.47$ in (b). Inset figure show a detail of the separation bubble recirculation zone as seen by a high-magnification planar PIV experiment.

DISTRIBUTION A: Distribution approved for public release.

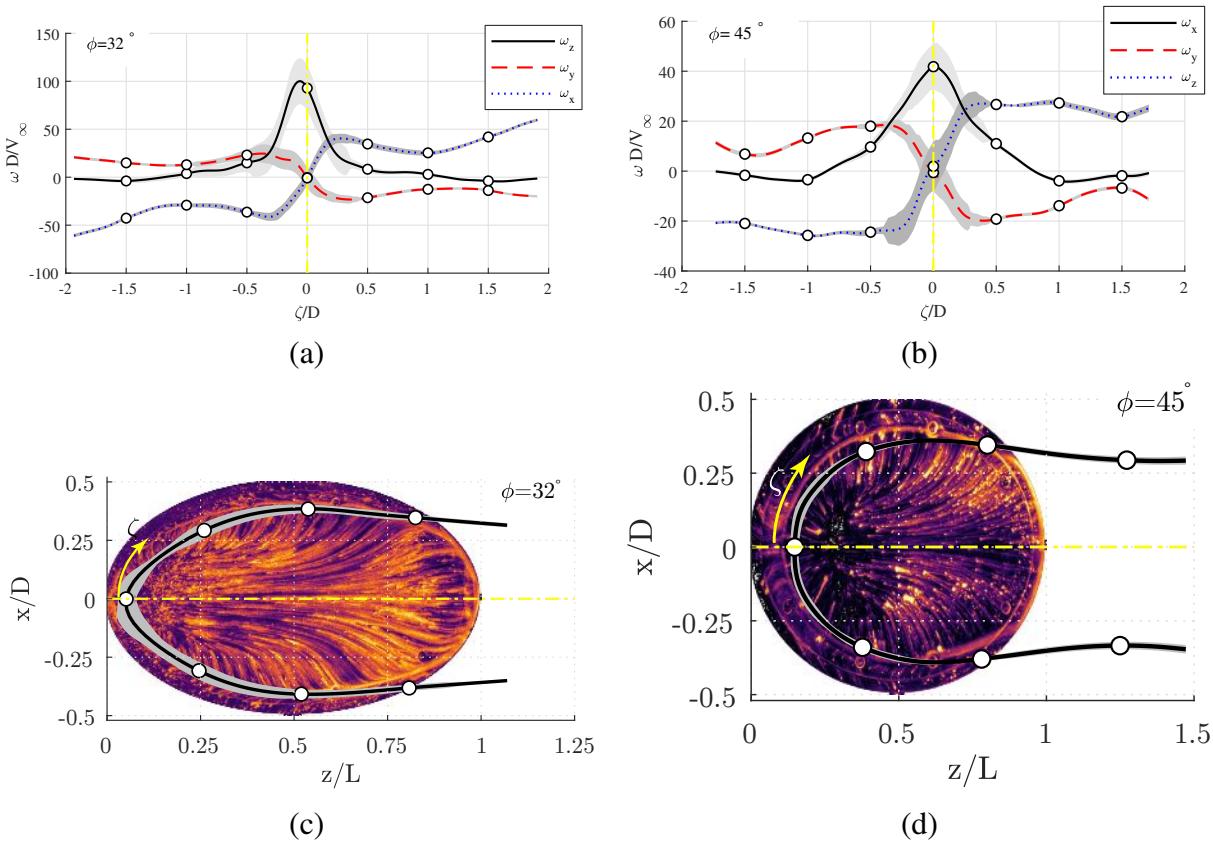


Figure 14: (a,b) Evolution of magnitude and direction of the vorticity vector components $[\omega_x, \omega_y, \omega_z]$ against the coordinate-transformed vortex core location ζ, as detected from the reconstructed fields of fig. 13. All figures refer to $Re = 2 \times 10^5$. Mean vortex core tracking shown in (c,d) from local peaks of Q criterion. White circles represent matching locations in the coordinate along the vortex core ζ between left and right figures, and centerline is marked as a yellow dashed line. Corresponding oil flow photographs shown in (c,d) to illustrate flow pattern observed. Shaded zones represent 2σ uncertainty bounds in both vorticity quantities and vortex core location.

angles reconstructed by the use of this technique present this striking transition from the inner circulation region at the separation bubble location to a free vortex pair, which indicates a very strong connection between the formation of the two structures. The lengthening of the separation bubble is also evident for the $\phi = 45°$ case. The separation feature is shown magnified in the inset figure of fig. 13 (b), showing data from the planar PIV experiment described in section 4.1.4. It was not possible to observe, however, a region of reversed flow for the case $\phi = 32°$ at $Re_D = 2 \times 10^5$ due to the limitations of the PIV technique close to the wall. However, based on the oil flow patterns indicating the presence of reversed flow in the surface footprint, it is reasonable to assume that the same separation bubble feature also forms for this case.

In order to quantify the connection between the separation bubble and the vortex pair, a line that goes through the local peaks in Q value was defined in the reconstructed 3D vector field. This line is plotted for $\phi = 32°$ in fig. 14 (c) and $\phi = 45°$ in fig. 14 (d). A coordinate along this line, ζ, is

DISTRIBUTION A: Distribution approved for public release.

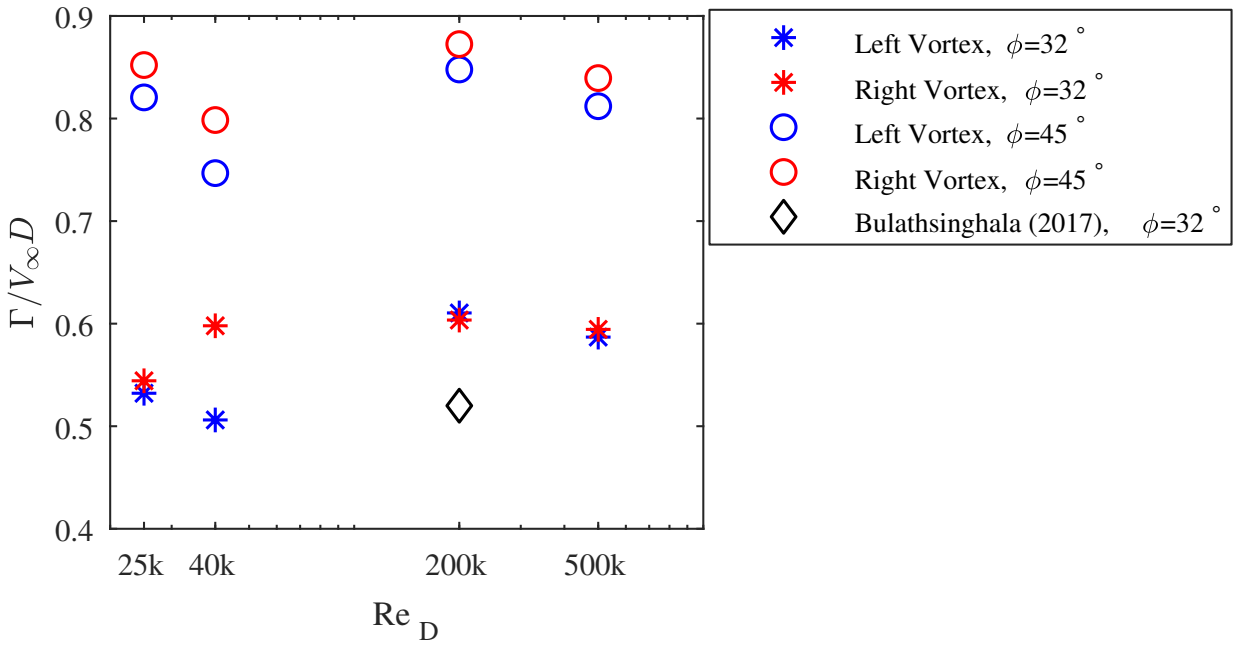


Figure 15: Effect of Reynolds number and slant angle ϕ on the average vortex circulation at the plane $z/L = 1.0$. Left and right vortex highlighted to show possible biases in the flow. A matching result from Bulathsinghala, Jackson, et al., 2017 is also shown for reference

then defined to track the vorticity quantities and their evolution as the horseshoe structure evolves downstream. The origin of this coordinate system is defined as $\zeta = 0$ when the line of local peak Q crosses the center plane. The spanwise vorticity ω_x inside the separation bubble can then be plotted against this coordinate ζ and shown to be smoothly redirected into streamwise vorticity ω_z, as is quantitatively shown in fig. 14 (a,b) for the same cases shown in fig. 13. Matching points between the vorticity charts (a,b) and the vortex core (c,d) are displayed as white circles to facilitate interpretation. The oil flow images corresponding to the same conditions display the patterns formed on the surface under the vortex core. For both slant angles examined, the center plane location $\zeta/D = 0$ shows the peak value of spanwise vorticity ω_x and near-zero vertical and streamwise vorticity $[\omega_y, \omega_z]$ at the recirculation zone core. These $[\omega_y, \omega_z]$ values increase in magnitude as the vorticity vector turns streamwise and in the direction of the slanted surface. At approximately $\zeta/D = 1$, the streamwise vortex pair is fully formed, possessing non-zero $[\omega_y, \omega_z]$ as it points in the direction of the slanted surface. The extent of the interrogation volume was not sufficient to observe the free vortex pair interact ($\zeta/D > 1.5$), but it is expected that the vortices evolve asymptotically to a parallel vortex pair and eventually break down far downstream due to the Crow instability (C. Crow, 1970).

Trends in vortex circulation at the plane $z/L = 1.0$ are displayed in fig. 15, where the normalized circulation of a single vortex is plotted for the eight cases analyzed, against Reynolds number. The circulation was obtained by integrating the streamwise vorticity ω_z in circular areas of increasing radius around the peak point, until the changes in the quantity calculated were less than 2%.

DISTRIBUTION A: Distribution approved for public release.

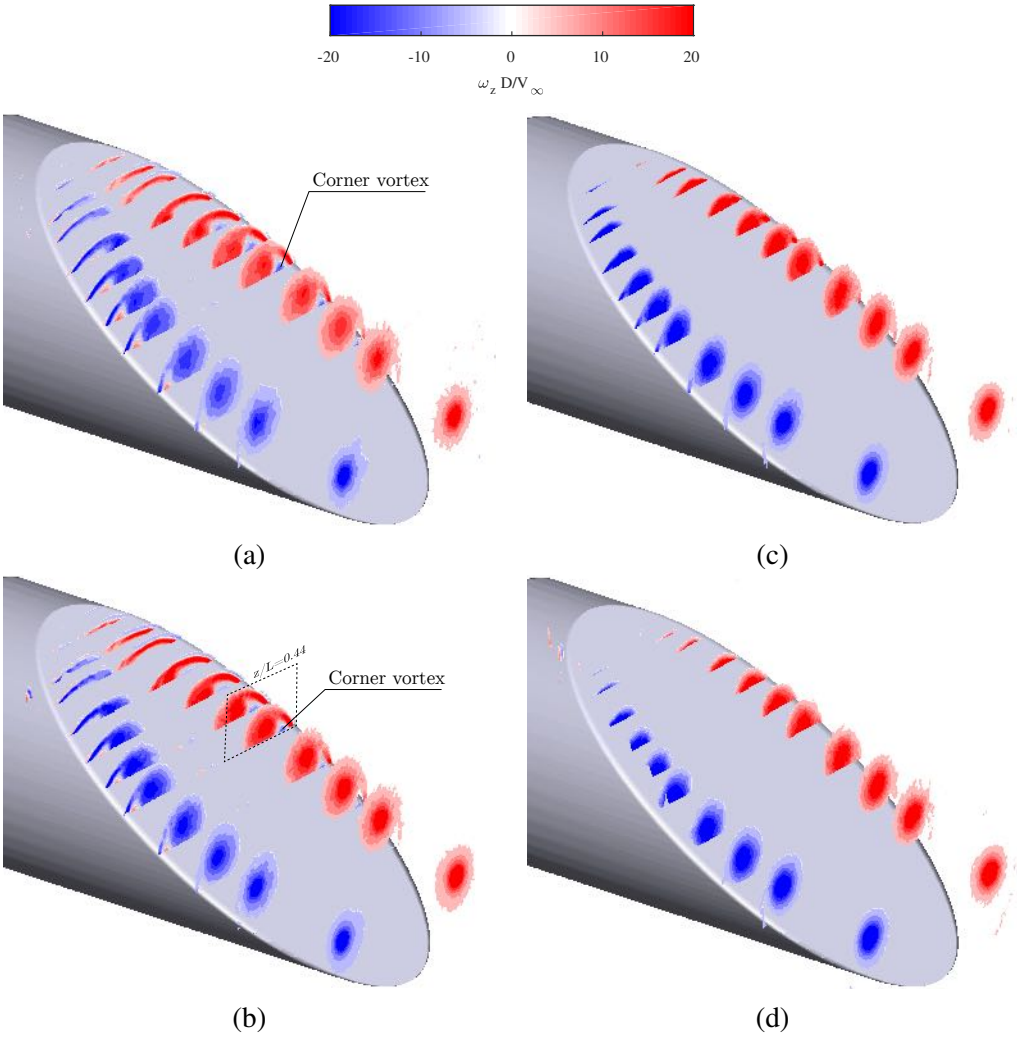


Figure 16: Effect of Reynolds number on the z vorticity field as observed by multiple SPIV planes. (a) $Re_D = 2.5 \times 10^4$, (b) $Re_D = 4 \times 10^4$ and (c) $Re_D = 2 \times 10^5$ and (d) $Re_D = 5 \times 10^5$ for the $\phi = 32°$ case. Absolute vorticity values $|\omega_z D/V_\infty|$ occluded to highlight the important structures. Planes displayed: $z/L = 0.05, 0.085, 0.135, 0.175, 0.25, 0.3, 0.37, 0.44, 0.54, 0.64, 0.75, 1.0$

In all cases, the radius of the interrogation area was less than half the distance between the vortex cores. The circles in fig. 15 point to a larger circulation for the $\phi = 45°$ case, which is on average 44% stronger than the $\phi = 32°$ case. Comparing with fig. 14 (a,b), it is possible to observe that the $\phi = 32°$ case has a greater peak vorticity at the most downstream location ($\omega_z D/V_\infty > 50$) when compared with the $\phi = 45°$ case ($\omega_z D/V_\infty \approx 25$). Since the vortex with greater circulation ($\phi = 45°$) has a lower peak vorticity, it is possible to assume the case with the larger slant angle generates a less coherent vortex core, which might point to an increased wandering in relation to the $\phi = 32°$ case. Furthermore, there seems to be a slight strengthening of the vortex pair as Re_D is increased, however the number of data points is insufficient to draw a conclusion.

The circulation of the left vortex of the $\phi = 45°$ case seems to be slightly (on average, 5%)

DISTRIBUTION A: Distribution approved for public release.

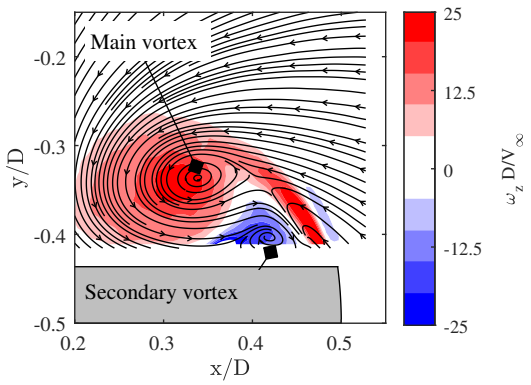


Figure 17: Interaction of the shear layer and the vortex, showing a counter-rotating vorticity pocket, for the $\phi = 32°$, $Re_D = 4 \times 10^4$ case. Plane at $z/L = 0.44$. Viewing axis aligned with freestream.

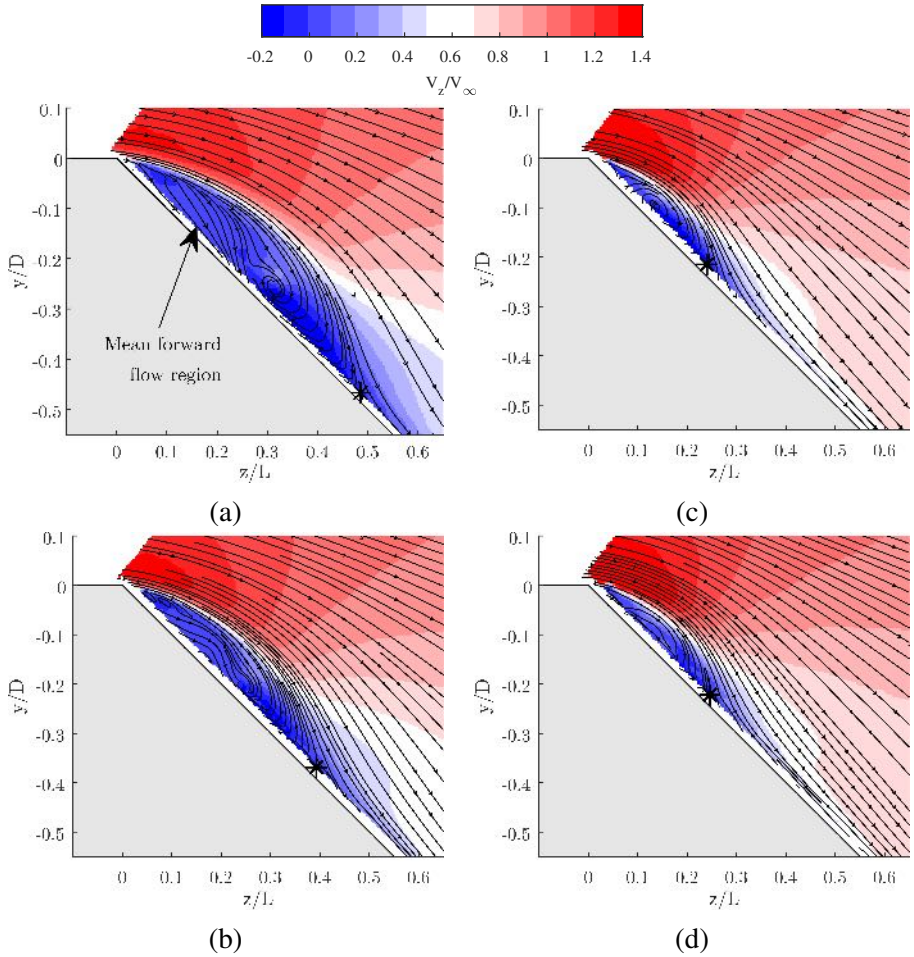


Figure 18: Effect of Re_D on the separation bubble shape as seen through contours of normalized streamwise velocity calculated from the mean of 500 planar PIV fields at $x/D = 0.0$ for $\phi = 45°$ and (a) $Re_D = 2.5 \times 10^4$, (b) $Re_D = 4.1 \times 10^4$, (c) $Re_D = 2 \times 10^5$, (d) $Re_D = 5 \times 10^5$. Black star shows the reattachment point computed as $V_s = 0$

DISTRIBUTION A: Distribution approved for public release.

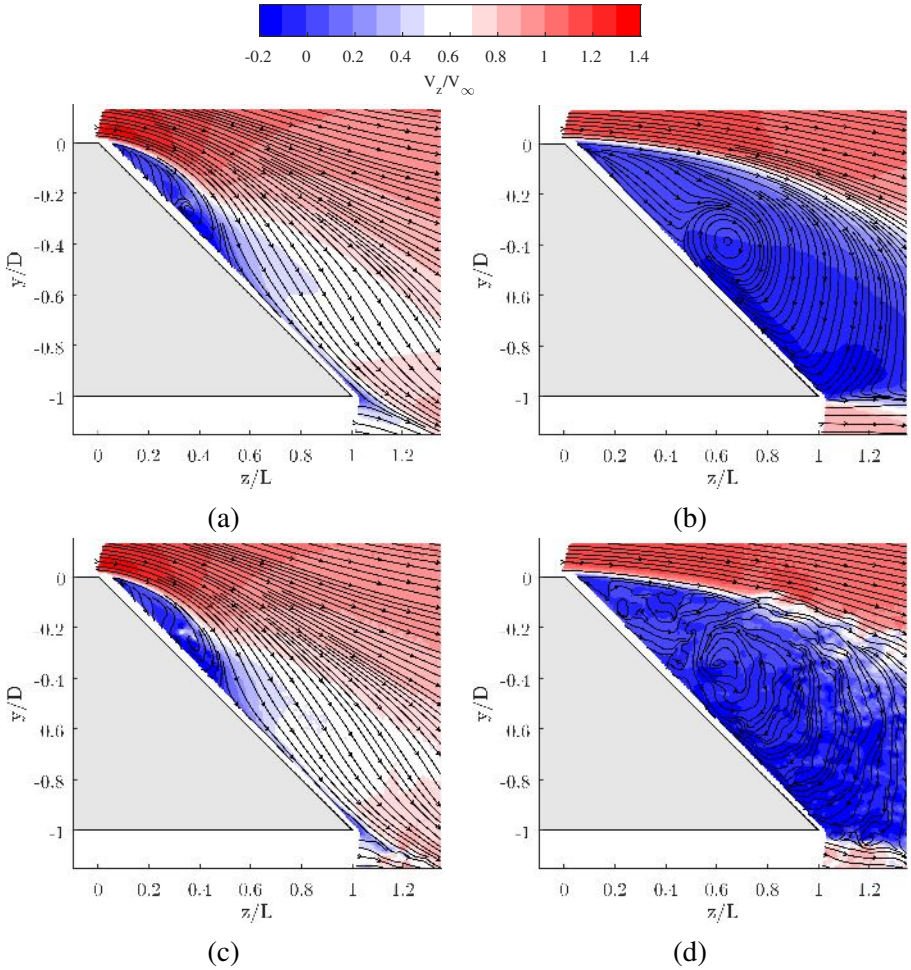


Figure 19: Steady-state bi-stability of the case $Re_D = 2.5 \times 10^4$ and $\phi = 45°$ at center plane ($x/D = 0.00$). In (a) the separation bubble closes inside the slanted surface, which is related to the formation of a counter-rotating vortex pair. In (b) the open separation pattern is related to a more unsteady wake. (c) and (d) show representative instantaneous snapshots of the corresponding cases (a) and (b).

weaker than the right vortex, despite the experimental efforts to ensure the model was free of any yaw angle. The model centerline yaw angle was measured against the wind tunnel reference wall to be within $\pm 0.1°$ and maintained undisturbed during the entirety of this study. Asymmetry in the vector fields is also apparent in the work by Epstein, Carbonaro, et al. (1994), indicating this geometry may be particularly sensitive to very small changes in yaw angles with regards to the symmetry in circulation strength within the vortex flow field. The black diamond shown in the plot displays a matching case from Bulathsinghala, Jackson, et al., 2017, at $\phi = 32°$ and $Re_D = 2 \times 10^5$. Although there is disagreement in the circulation values obtained to some extent, it is not clear how the facility effect and the presence of obstacles downstream of the model will change the vortex circulation for this particular configuration. As the experiments performed in this study only employed external optical components for the PIV measurements, the effect of

DISTRIBUTION A: Distribution approved for public release.

downstream blockage was eliminated.

A closer examination of the development of the z component of the vorticity vector, ω_z, is presented for the $\phi = 32°$ case in fig. 16 for four Reynolds numbers. The lower two Reynolds number cases, (a,b), possess a noticeably different vortex shape closer to the separation bubble region in comparison to the higher Reynolds number cases (c,d), which are indistinguishable from one another. The more elongated vorticity contours reveal a more defined shear layer at lower Re_D. By focusing on the planes around $z/L = 0.44$ (highlighted in fig. 16b), a small secondary vortex (of opposite sign, labeled "corner vortex" in fig. 16) close to the slant edge can be noticed, which is also evident in the oil flow images and characterized as a "secondary vortex". This secondary vorticity region seems to be related to the interaction of the main vortex and the wall, and seems to be more detectable in the lower Reynolds number cases, where the flow features are physically larger .

A detailed view of the shear layer is presented in fig. 17 for the case $\phi = 32°$ and $Re = 4 \times 10^4$. The streamlines provide a means to observe the main vortex (in red) and the small counter-rotating secondary vortex (in blue). This provides evidence that this feature might be a general feature of the slanted cylinder flow topology, however it was not possible to observe it for the higher Reynolds numbers due to the challenges related to surface reflections. However, the presence of this region at higher Reynolds numbers would explain the presence of the "saddle line" presented in the oil flow results in Figs. 8 and 9, since the opposing spanwise direction of the flow over the surface forces the oil to collect in a stream. Similar evidence has been provided by Garmann and Visbal, 2019 in LES simulations for $Re_D = 2 \times 10^5$ and $\phi = 28°$.

4.1.4 Separation bubble and wake transition

Planar PIV planes in the streamwise direction were captured to observe details that spanwise planes could not resolve with sufficient detail. For the $\phi = 45°$ slant angle the separation bubble was large enough to allow for the observation of its flow topology for all Reynolds numbers studied. The velocity fields obtained at the center plane are displayed in fig. 18, along with streamlines and a reattachment point location that was obtained by finding the point where the velocity parallel to the slanted surface V_s, defined in Eq. 12, was equal to zero.

$$V_s = V_z \cos(\phi) - V_y \sin(\phi) \tag{12}$$

Fig. 18 also displays the trends in the separation bubble shape as Re_D is increased. The reattachment point, shown as a black star in the plots, moves upstream as Re_D is increased, following the trend observed in oil flow, as shown in fig. 10. It is worth noting that although the locations z_s/L do not match, there is very good agreement on the trends observed. The oil flow measurements, due to the gravity forces acting on the oil, should be slightly biased downstream. Conversely, the reattachment location based on the PIV velocity fields by finding $V_s = 0$ should be biased upstream, especially for the higher Re_D, as the reflections from the laser sheet do not allow for observation close to the surface, and a proxy for V_s is used at the closest point measured in the field. For reference, the closest point to the surface measured from PIV is $0.015D$ from the slanted surface. Nevertheless, the very rapid growth of the separation bubble length as Re_D is decreased

DISTRIBUTION A: Distribution approved for public release.

is a potential explanation for the transition of this flow to a fully separated wake pattern at lower Reynolds numbers.

The flow topology within the separation bubble, however, is complex. It is more evident in the lower Reynolds number cases in fig. 18 (a) and (b), for which the larger physical size of the separation bubble allowed for the observation of the details of the flow. The streamlines separate first at the sharp edge as expected, however, a mean forward flow is observed close to the surface. This "mean forward flow region" indicated in fig. 18 (a) has a very low velocity magnitude but also very low shear stresses. The mean velocity gradients remain concentrated in the shear layer. The reattachment pattern seems to separate once again, which happens at $z/L = 0.24$ for the $Re_D = 2.5 \times 10^4$ case, this time forming a recirculation zone. The flow then reattaches for the last time where the black star is plotted. This unusual separation bubble pattern seems to be corroborated by the surface flow pattern discussed in Section 4.1.1.

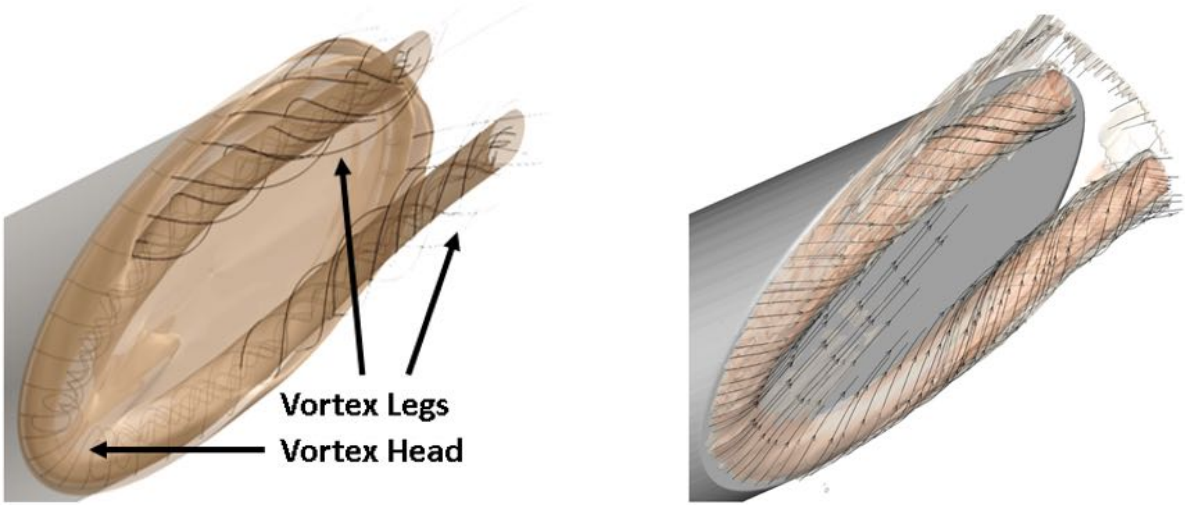
It is conjectured here that this unusual separation feature shape is a product of a highly three-dimensional interaction in the flow field. The oil flow pattern between the sharp edge and the "Separation Bubble Rivulet" feature shown in fig. 9 suggests that there is average flow towards the center plane, indicating the mean streamlines sharply deflect from the sides of the cylindrical surface towards the center plane as soon as they reach the slanted edge, potentially due to a very steep pressure gradient. Future studies of the topology details in this region might lead to a clearer picture of the global flow pattern transitional characteristics and its connection with the incoming boundary layer characteristics. This separation bubble feature has not been identified in the $\phi = 20°$ and $\phi = 32°$ cases due to limitations in the spatial resolution of the optical equipment used, and therefore require a specially-designed experiment to achieve the necessary magnification levels.

The flow topology at the lower Reynolds number for the $\phi = 45°$ case proved to be bi-stable in steady-state. As can be observed in fig. 19, there are two possible flow states for the same Reynolds number of $Re_D = 2.5 \times 10^4$. The transition is apparently related to the hysteresis effect first related by Britcher and Alcorn (1991) in a model with the same slant angle based on drag and base pressure measurements. The flow state in fig. 19(a) shows a closed separation bubble and is believed to be related to the formation of the pair of counter-rotating vortices over the slanted surface given the S-SPIV results presented for the higher Reynolds number cases.

The flow state shown in fig. 19(b) corresponds to what is regarded in the literature as a fully separated wake pattern. The two flow fields possess the same freestream velocity as measured by a Pitot-static probe upstream of the model. The vortex flow state in fig. 19 (a) can be attained, with consistent repeatability, by letting the freestream velocity overshoot to a higher value (in this experiment, to $Re_D = 4 \times 10^4$ or $V_\infty = 4.1$ m/s) and then reducing it to the corresponding 2.6 m/s ($Re_D = 2.5 \times 10^4$). The wake flow state in (b), however, can only be obtained if the freestream velocity is slowly increased to 2.6 m/s without overshoot. The maximum acceleration rates were limited by the facility control systems to 0.7 m/s^2.

The instantaneous snapshots shown in fig. 19(c) and (d) reveal the finer-scale flow structures that compose both flow states. The wake state observed in fig. 19(d) shares similarities with the flow visualization photographs shown by Xia and Bearman (1983) for $\phi = 70°$, potentially indicating the slant angle of $\phi = 45°$ would also display a low-frequency shedding mode when

DISTRIBUTION A: Distribution approved for public release.



(a) 32° (LES) (b) 32° (PIV)

Figure 20: Depiction of horseshoe-shaped vortex with $|\omega|D/U_\infty = 10$ iso-surface and streamlines for (a) LES (b) experiments performed at FSU

transitioned to the wake state. It is clear, however, that the fluctuations in the vortex state in fig. 19(c) are much lower in magnitude with respect to the mean when compared to the wake state of fig. 19(d).

Based on these observations, it is proposed herein that the vortex flow pattern is the preferred flow state in this bi-stable wake. Both flow states persisted for as long as the experiments lasted (10 minutes, or $V_\infty t/D > 10^4$), providing strong indication that both states are stable indefinitely, even though the wake state might present strong shedding dynamics. Once a coherent vortex pair is formed through the overshoot of freestream velocity, their net induced velocity at the center plane deflects the freestream streamlines towards the slanted surface and enables the separation bubble to reattach in the slanted surface. This deflection of the freestream enables the vortex dominated wake to persist even after the Reynolds number has been lowered.

4.2 Simulation investigation

The complementary simulation campaign also obtains the principal features described above, which serve for validation. The results are also analyzed for features not easily accessible in the experiments, such as the far downstream region. For completeness, these results are presented in a self contained manner, with repetition limited to the extent possible.

4.2.1 Baseline vortex structure

The main features observed in the experiment are successfully reproduced in the simulations. Figure 20 shows the primary mean coherent structure observed in the baseline 32° case, which is very close to the upsweep angle of Lockheed C-130 Hercules ($\phi \approx 28^\circ$). These structures are visualized using iso-surfaces of total vorticity ($|\omega|D/U_\infty$) and are compared with corresponding results from experiments (above) performed at a higher $Re_D = 2 \times 10^5$. Despite the differences

DISTRIBUTION A: Distribution approved for public release.

in Reynolds number, the vortical structure obtained from simulations (Fig. 20a) and experiments (Fig. 20b) are strikingly similar. The principal feature again may be described in terms similar to those used earlier with the experimental data *i.e.,* the clearly observable large horseshoe-shaped vortex, whose head and legs have been marked in Fig. 20a. Similar structures have been observed in studies of other flows past bluff bodies Morgan and Visbal, 2019; Singha and Balachandar, 2011 These three-dimensional formations patterns are related to the "U"-type structures characterized by Dallmann (1983), discussed further below.

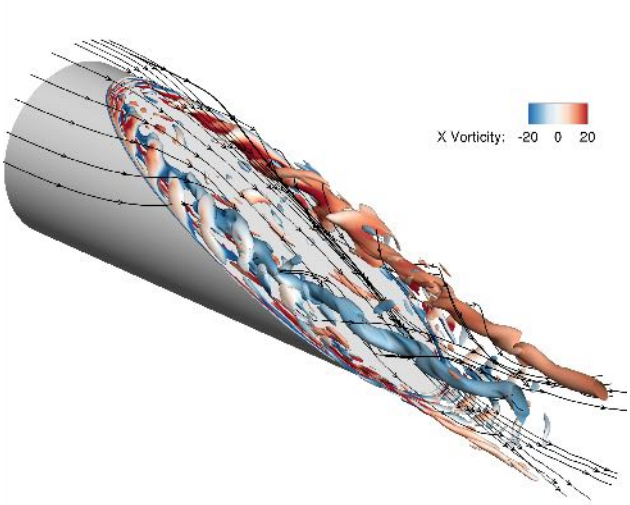
The connection between the streamline paths and the formation of the horseshoe structure is evident from Fig. 20. To reiterate, the shear layer separates from the cylinder surface along the entire periphery of the sharp base-edge. At the upstream apex, the flow curls back towards the base to form the vortex head. The head region remains in close proximity to upstream apex as it grows around the periphery, changing orientation so that its core follows the general contour of the base edge, while entraining fluid from the shear layer separating from the periphery. At a certain peripheral location that depends on the base angle, the vortex lifts away from the surface, and orients the two legs symmetrically in a more streamwise direction, to form the features commonly described as a streamwise vortex pair.

These observations allow reiteration of the fact that the dominant feature arising from flow separation around the periphery of the base region is a streamwise-oriented vortex pair downstream (Bulathsinghala, Jackson, et al., 2017; Garmann and Visbal, 2019), similar to the results described in this report (Zigunov, Sellappan, et al., 2020a; Ranjan, Aultman, et al., 2020). For reference, visualizations from the current Large Eddy Simulations (LES) are shown in figure 21. In figure 21(a), a Q-criterion (Haller, 2005) iso-level ($Q = 30$) is depicted, colored by streamwise vorticity, ω_x, together with select superposed streamlines to provide an indication of the swirling motion in the instantaneous flow. The counter-rotating streamwise vortex pair as well as the twisting motion of each vortex in the pair, are clearly evident. Figure 21(b) displays the mean flowfield using the same flow variables. In the mean sense, each vortex in the pair gradually assumes an axisymmetric form in the region outside of the immediate vicinity of the upstream apex. § 4.2.2 and § 4.2.3 provide further insights into the mean structure of the flowfield and lay the foundation to examine the spatio-temporal features of the vortex pair as influenced by a breakdown of the separated shear layer, fluid entrainment, potential vortex-vortex interactions and meandering.

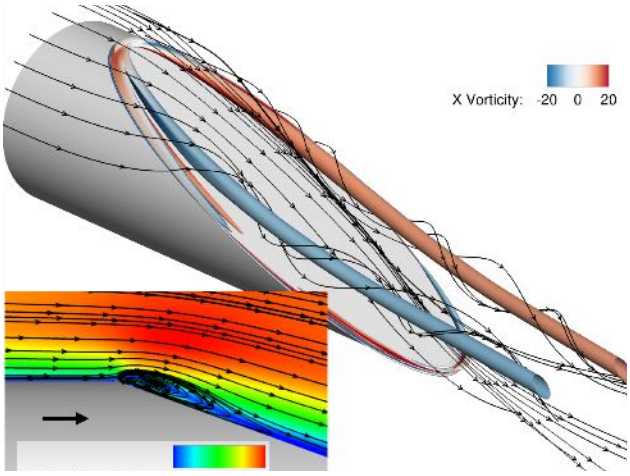
Depending on the Reynolds number, this structure persists in a range of $\phi \leq 45°$; descriptions at other upsweep angles in $24° \leq \phi \leq 45°$ may be found earlier as well as in Bulathsinghala, Jackson, et al. (2017), Garmann and Visbal (2019), and Zigunov, Sellappan, et al. (2020a) and Ranjan, Aultman, et al. (2020).

From a practical point of view, the presence of the vortex pair results in higher drag and significant unsteadiness for long distances downstream due to the meandering (or wandering) of vortices, both of which are major concerns for designers. For example, the unsteadiness and meandering motion can affect payload accuracy and paratrooper safety, as well as impose constraints on distance from trailing aircraft and airport operations (Holzäpfel, Strauss, et al., 2019). The simulations explore: 1) describe the phenomenology of streamwise-oriented vortex pair dynamics, including meandering, 2) place this phenomenology in the context of stability mechanisms, and 3) examine

DISTRIBUTION A: Distribution approved for public release.



(a) Instantaneous flow



(b) Mean flow

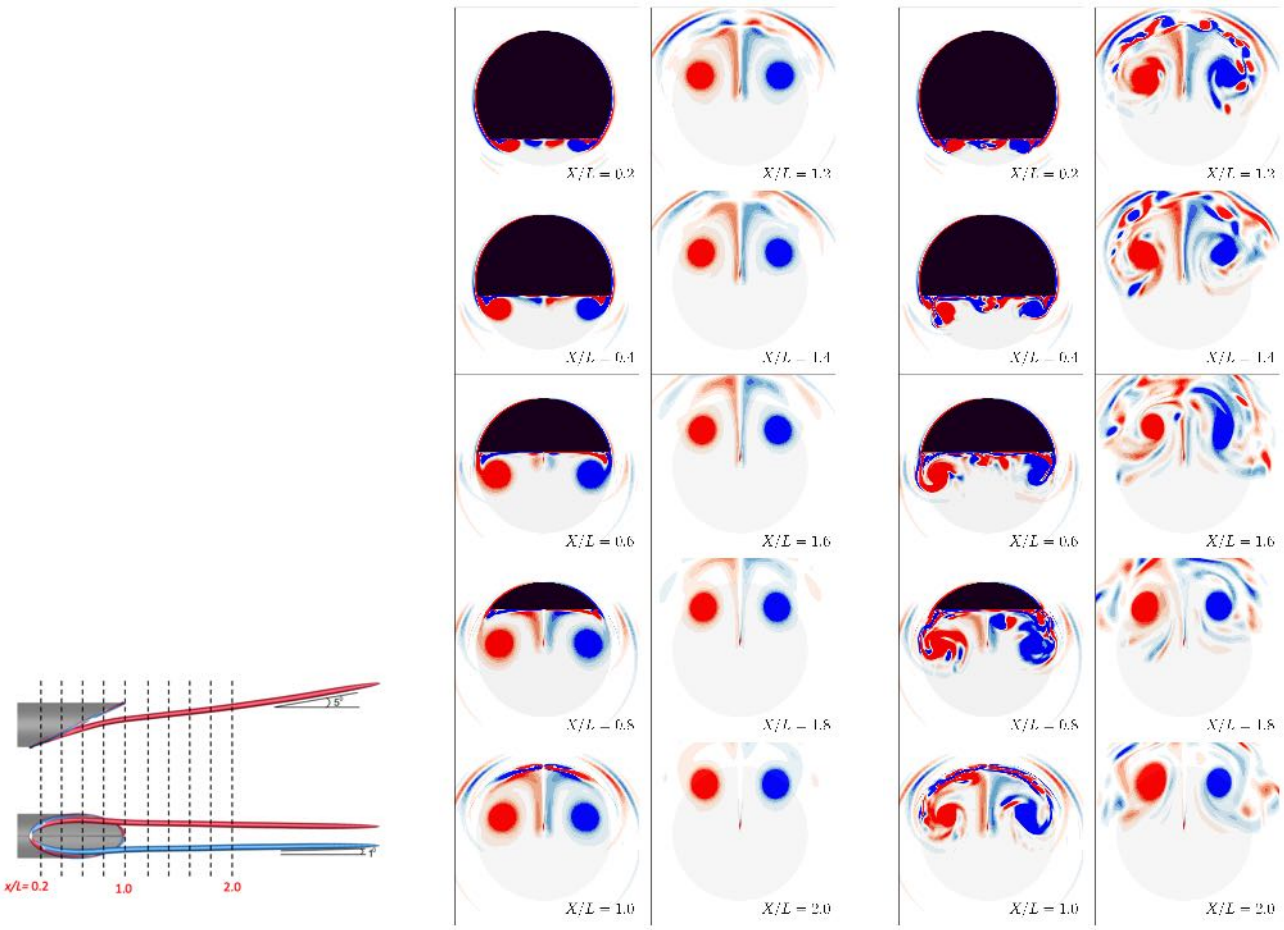
Figure 21: Longitudinal vortices behind the slanted body. An iso-surface of $Q = 30$ is plotted, colored by streamwise vorticity ω_x. The mean separation bubble near the upstream apex is shown in inset (b). The configuration is inverted with positive y-axis pointing downward for display purposes.

the low-rank behavior of the complex flowfield for potential model-order reduction.

4.2.2 Overview of Unsteady Flowfield

The representative three-dimensional instantaneous and mean flow structures were shown earlier in figure 21. The latter was obtained by computing the time average over $700{,}000$ snapshots encompassing total non-dimensional time of $T_c \equiv tU_\infty/D = 175$. The turbulent flowfield arises as a result of the strong interaction between the separating shear layer and vortices in the region adjacent to the upswept base. Looking downstream, the left and right vortices have dominantly

DISTRIBUTION A: Distribution approved for public release.



(a) Streamwise vortices (b) Mean (c) Instantaneous

Figure 22: Evolution of streamwise vortex along the base of the upswept surface through ω_x contours at 11 levels between -3 and 3. Crossflows in the intervals for 0.2 between $X/L = 0.2$ and 2.0 for the mean (b) and a representative instantaneous snapshot (c) are shown. (a) shows the locations in front and top view of vortices visualized using Q-criterion.

positive and negative streamwise vorticity components respectively. In the instantaneous flow, figure 21(a), there are smaller convecting structures that are washed out in the time-averaged sense (figure 21(b)).

A granular description of the formation of the vortex pair is now provided for reference. The mean trajectory of the vortices is displayed using side and bottom views in figure 22(a), again with the same isolevels as in figure 21. The side view indicates that after a streamwise turn immediately after lifting off from the base, the vortex remains inclined to the freestream at an approximate angle of $5°$ even far downstream. The bottom view shows that the two mean vortices approach each other at a very small angle of approximately $1°$ towards the symmetry plane.

Figures 22(b) and (c) show the mean and instantaneous streamwise vorticity components, respectively, using cross-sectional contours at ten different locations between $0.2 \leq X/L \leq 2.0$,

DISTRIBUTION A: Distribution approved for public release.

marked by dotted lines in figure 22(a). The mean vorticity field at $X/L = 0.2$ displays a teardrop-shaped structure, with opposing signs in the dominant lobes, which are located symmetrically about the mid-plane, $z = 0$. For future reference, the two vortices in the pair are designated as **L** and **R** vortex based on whether, looking downstream, they are located to the left or right of the symmetry plane respectively. Each vortex in the pair on the base is fed by the shear layer and gradually evolves into an axisymmetric structure at about $X/L \sim 0.6$. As evident from (a), the vortex detaches from the surface; thus the connection with the feeding sheet is clearly weaker at $X/L = 0.8$.

At the downstream apex of the upswept base ($X/L = 1.0$), the vortices are completely detached from the surface and the direct effect of the base shear layer on the fully developed mean vortex pair gradually diminishes. The process continues with streamwise distance with the vortices becoming essentially independent from the immediate effects of the base. Secondary and tertiary vortices are also present beneath the primary vortex, as clearly evident in planes intersecting the base. These have opposite and same signs, respectively, as the corresponding primary vortex in the pair and their influence far downstream of the base appears to be a higher-order effect. Further details of these mean flow features for ϕ values of $20°$, $32°$ and $45°$, together with various aspects of the flow on the base plane, such as surface oil flow and pressure patterns, as well as drag, have been discussed extensively in Ranjan, Aultman, et al. (2020).

Instantaneous structures of the vortices, as well as their meandering downstream, are shown in figure 22(c) on the same planes as in (b) for a representative snapshot. Although the flow is unsteady and turbulent along the entire base region, the instantaneous flow displays the dominant signature of primary vortices, consistent with figure 21(a). However, the axisymmetric nature is not evident, and the meandering of vortices is discernible in the streamwise vorticity field from $X/L = 0.8$ downstream as a result of interactions with the shear layer. Animations indicate a swirling motion of the vortex center with time, as discussed further in § 6.1.1.

Each vortex contains some regions of opposite-signed (secondary) vorticity field, these have some similarity to the "vortical substructures" described in Gordnier and Visbal (2005), who note their presence around the primary cores of delta-wing vortices. Their genesis is associated with the vortex-surface interaction and eruptions from the boundary layer on the upswept base surface. Their influence on the unsteady motion is significant near the base of the bluff body, as they interact with the primary vortices (Yaniktepe and Rockwell, 2004; Gursul, Gordnier, et al., 2005). Downstream of the base, these interactions diminish, and between $X/L = 1.2$ and $X/L = 2.0$, a perceptible decrease of intensity in the meandering is evident. The entrainment of flow separating at the downstream apex into the central region between the vortex cores continues until further downstream. These observations are generally consistent with those of Garmann and Visbal (2019), who performed LES of the entire configuration (including forebody) at a higher Reynolds number of $Re_D = 2.0 \times 10^5$.

4.2.3 Characterization of Mean Vortex Pair

The mean vortex pair is discussed in a canonical sense to identify key parameters of interest; this also sets the stage for subsequent examination of underlying instability mechanisms. The

DISTRIBUTION A: Distribution approved for public release.

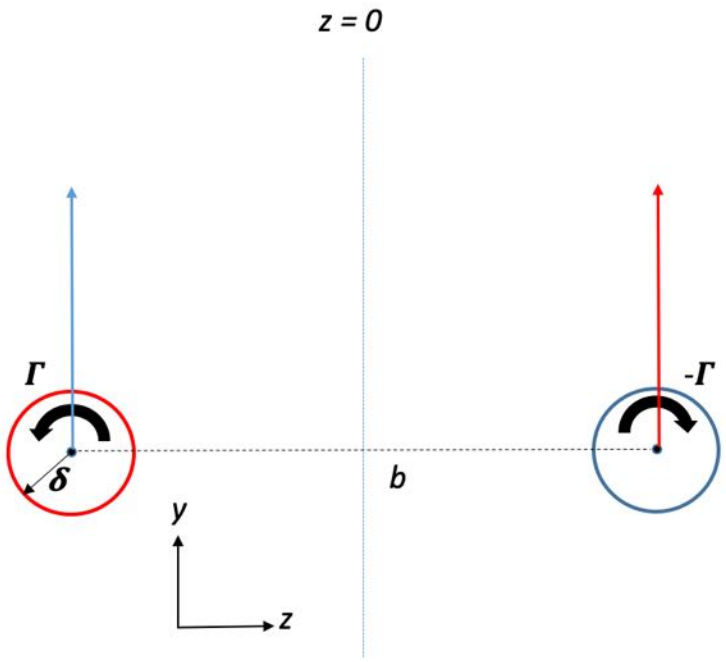


Figure 23: Pair of counter-rotating vortices at a streamwise location. δ-radius and $|\Gamma|$-circulation of vortex. b-separation distance between vortices.

afterbody flow on the slanted cylinder presents a classical counter-rotating vortex pair of equal strength, shown schematically in figure 23. The main parameters of interest are the radius of the vortex core, δ, the distance between the centroids of the vortices, b, and the circulation of the vortices, Γ. The **L** and **R** vortices thus lie at $X_L = -b/2$ and $X_R = b/2$ symmetrically about the midplane.

The coordinates of the vortex centers are a primary quantity in the spatial evolution of the mean vortices (Lombard, Moxey, et al., 2016). In the literature on flow behind afterbodies, the maximum value of the Q-criterion (Bulathsinghala, Jackson, et al., 2017) or entropy (Garmann and Visbal, 2019) is typically used to identify the core center. In this work we use the Γ_1/Γ_2 approach proposed in Graftieaux, Michard, et al. (2001), employed previously by Bell, Burton, et al. (2016) and concurrently by Ranjan, Aultman, et al. (2020) and Zigunov, Sellappan, et al. (2020a). The method provides the center and boundary of a vortex by considering the local convection velocity field in the region of interest. Once the vortex is identified, the circulation may be computed using the area integral of vorticity.

Figure 24(a,b) respectively plot the vertical and spanwise locations of the **L** and **R** vortex cores. Figure 24(a) indicates that both vortices develop in the same manner along the streamwise distance, X/L, as anticipated, and in fact, Figure 24(b) displays symmetry about $z = 0$. A closer examination reveals that after the formation of the tear-drop shaped vortex at $X/L = 0.2$, the distance between the vortices grows until $X/L \sim 0.6$. This is consistent with the peripheral development of the 3D vortex structure shown in figure 21(b). Beyond $X/L \sim 0.6$, the centers approach each other until $X/L \sim 1.0$ as they conform to the elliptic shape of the base. Further

DISTRIBUTION A: Distribution approved for public release.

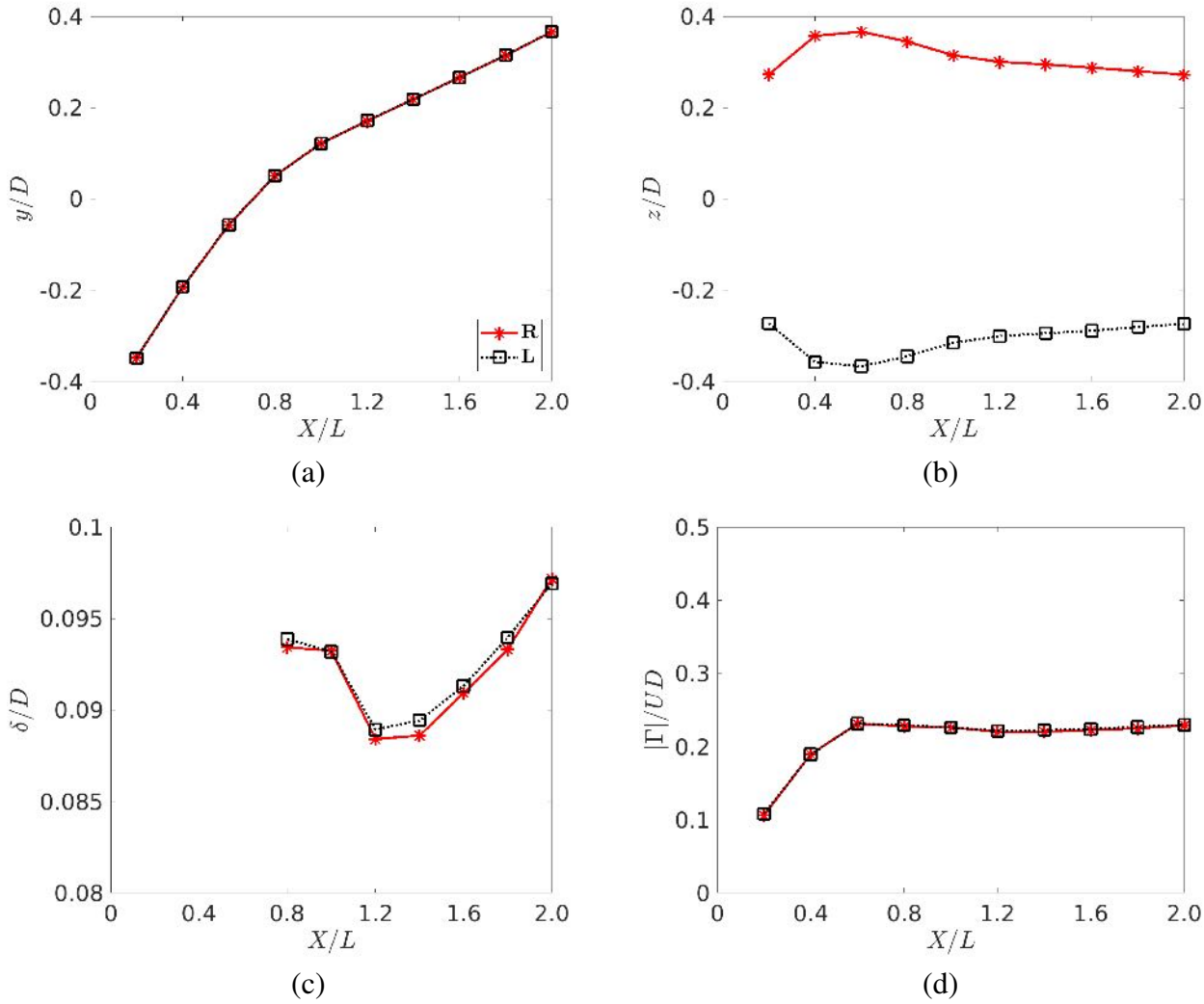


Figure 24: Mean streamwise vortex location at different X/L. (a) Vertical location, (b) Spanwise location, (c) Radius and (d) Circulation of the core.

downstream, beyond $X/L \sim 1.2$, the vortices achieve an asymptotic state inclined at about 5° to the free-stream flow (see figure 22(a)). For future reference, the precise inter-vortical separation, b, is reported as a function of X/L in Table 4, along with several other properties discussed below.

Evolution of vortex structure with base angle

Figure 25 uses the λ_2 criterion to display the vortex structure for all three upsweep angles in the vortex regime; this variable better characterizes the vortex structure than $|\omega|$ used earlier, but requires higher data resolution than is available from experiments. The structures are colored with non-dimensionalized streamwise vorticity $\dfrac{\omega_x D}{U_\infty}$ in order to identify the sense of rotation. For the

DISTRIBUTION A: Distribution approved for public release.

$\frac{X}{L}$	$\frac{\delta}{D}$	$\frac{b}{D}$	$\frac{\delta}{b}$	$\frac{\lvert\Gamma\rvert}{UD}$
0.2	-	0.5450	-	0.1070
0.4	-	0.7143	-	0.1895
0.6	-	0.7333	-	0.2315
0.8	0.0935	0.6893	0.1356	0.2288
1.0	0.0932	0.6297	0.1480	0.2262
1.2	0.0884	0.6010	0.1471	0.2210
1.4	0.0886	0.5890	0.1504	0.2218
1.6	0.0909	0.5761	0.1578	0.2234
1.8	0.0933	0.5607	0.1664	0.2255
2.0	0.0972	0.5456	0.1781	0.2295

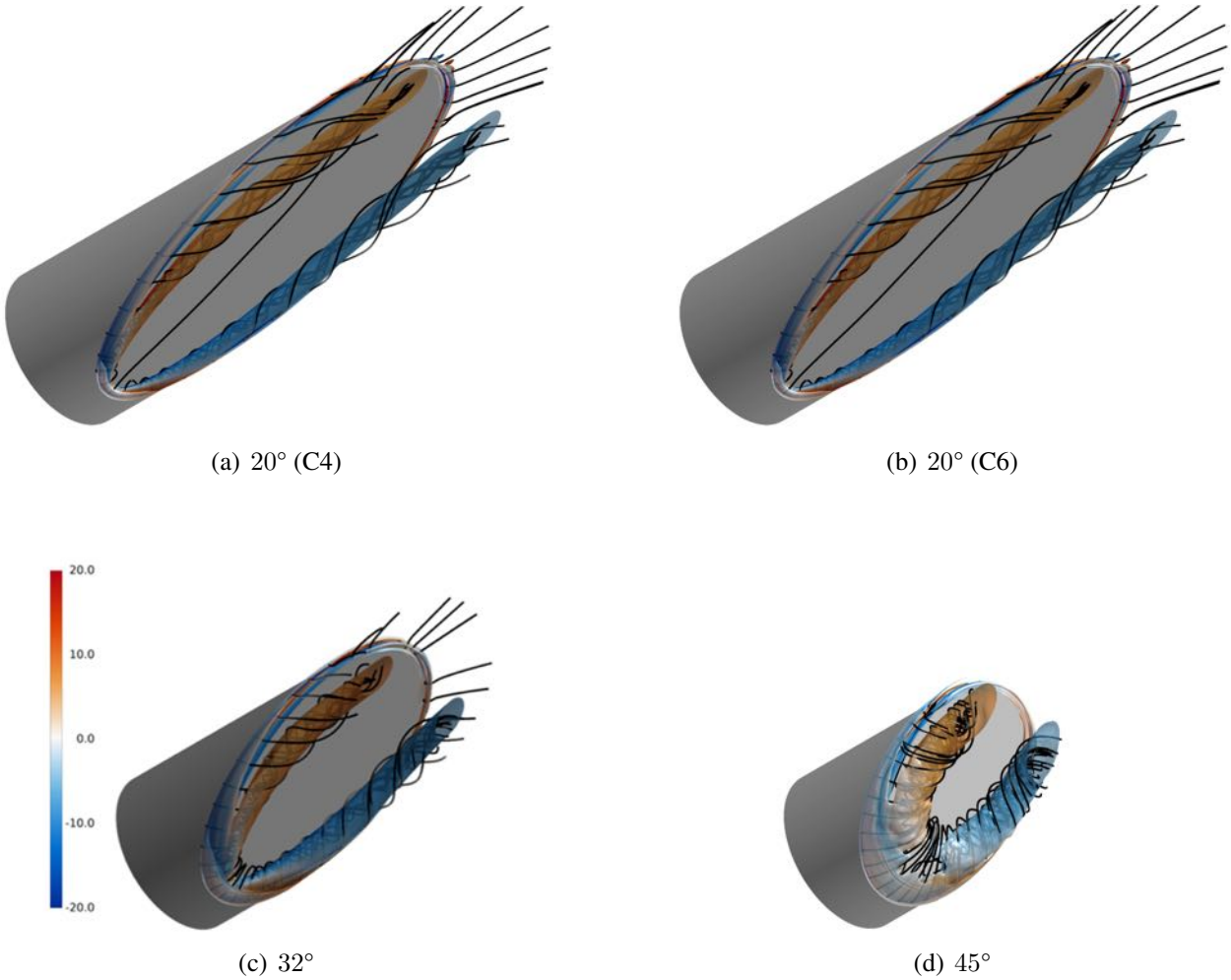
Table 4: Properties of mean vortex at different streamwise locations. Note that there is less than 1% difference between left and right vortices in computation of parameters such as δ and $|\Gamma|$. The reported quantities are thus averaged between the two. See sketch 23 for definitions of parameters.

20° case, results from both the 4^{th} and 6^{th} order schemes are shown, designated as C4 (Fig. 25a) and C6 (Fig. 25b) respectively. The size and strength of the vortical structure are similar with both schemes, and, together with other data presented below, indicate that the results are mesh resolved.

All three upsweep angles depicted in Fig. 25 display the above-described horseshoe-shaped vortex. However, the changes in several features are indicative of its evolution as discussed below. The size of the vortex, including both head and leg regions, increases with base angle. For example, when ϕ is decreased from the baseline 32° (Fig. 25c) to 20° (Fig. 25a), the structure has a smaller size near the upstream apex, and more slender legs. On the other hand, when the upsweep is increased further to 45° (Fig. 25d), these features become more prominent than at 32°. The size of these large vortices directly relate to their strength, and hence drag, as discussed below.

The simulations also facilitate analysis of the downstream development of the vortex pair, where they have the potential to affect payload trajectories as well as the unsteady loads on the horizontal tail Ghoreyshi, Bergeron, et al., 2017. The downstream trajectories of the vortices for all the three upsweep angles are shown in Fig. 26 using the Q-criterion at $Q = 5$. To enable a direct comparison, all three cases are referenced to the same point at the center of the base. The side view, Fig. 26a, indicates that the trajectories follow the edge of the upswept base prior to lifting off away from the surface *i.e.,* as ϕ increases, the vertical angle of the trajectory of the vortices also rises. Quantitative estimates indicate vertical trajectories inclined at $5^\circ, 9.5^\circ$, and 14.5° relative to the freestream with increasing upsweep angle. Further, the results indicate that though the size of the vortices increases with upsweep angle, their region of prominence downstream becomes shorter, since they also dissipate faster. This trend of shorter coherent vortex legs with increasing upsweep angle is consistent with the anticipated emergence of the wake flow regime at larger angles, for which the organized streamwise vorticity is small, as discussed further below.

DISTRIBUTION A: Distribution approved for public release.



(a) 20° (C4)

(b) 20° (C6)

(c) 32°

(d) 45°

Figure 25: Rendering of horseshoe-shaped vortex with iso-surfaces of $\lambda_2 = -10$. Vortices are colored with streamwise vorticity (ω_x). Streamlines are also shown.

The trajectories in the spanwise direction are shown in Fig. 26b. The influence of the head region increases with upsweep, consistent with the prior observations in Fig. 25. It will be shown later that the sizes of these heads at the symmetry plane are proportional to the extent of the recirculation region formed near the upstream apex. As anticipated, the legs are symmetric about the vertical mid-plane. However, a closer examination also reveals that after lifting away from the surface, the vortices in the higher upsweep case are located slightly closer to each other than when the upsweep is smaller.

A further quantification of the evolution of the vortices with base angle emerges from tracking the locations of vortex cores. This is accomplished by using the Γ_1 and Γ_2 approaches of Graftieaux, Michard, et al. (2001), which consider the streamline topology of flow near the vortex to identify the vortex center location and boundary respectively. These variables then facilitate the calculation of the circulation through the usual area integral of the vorticity field. Figure 27a shows the vertical trajectory of the vortex cores. The abscissa is the streamwise distance, x, along

DISTRIBUTION A: Distribution approved for public release.

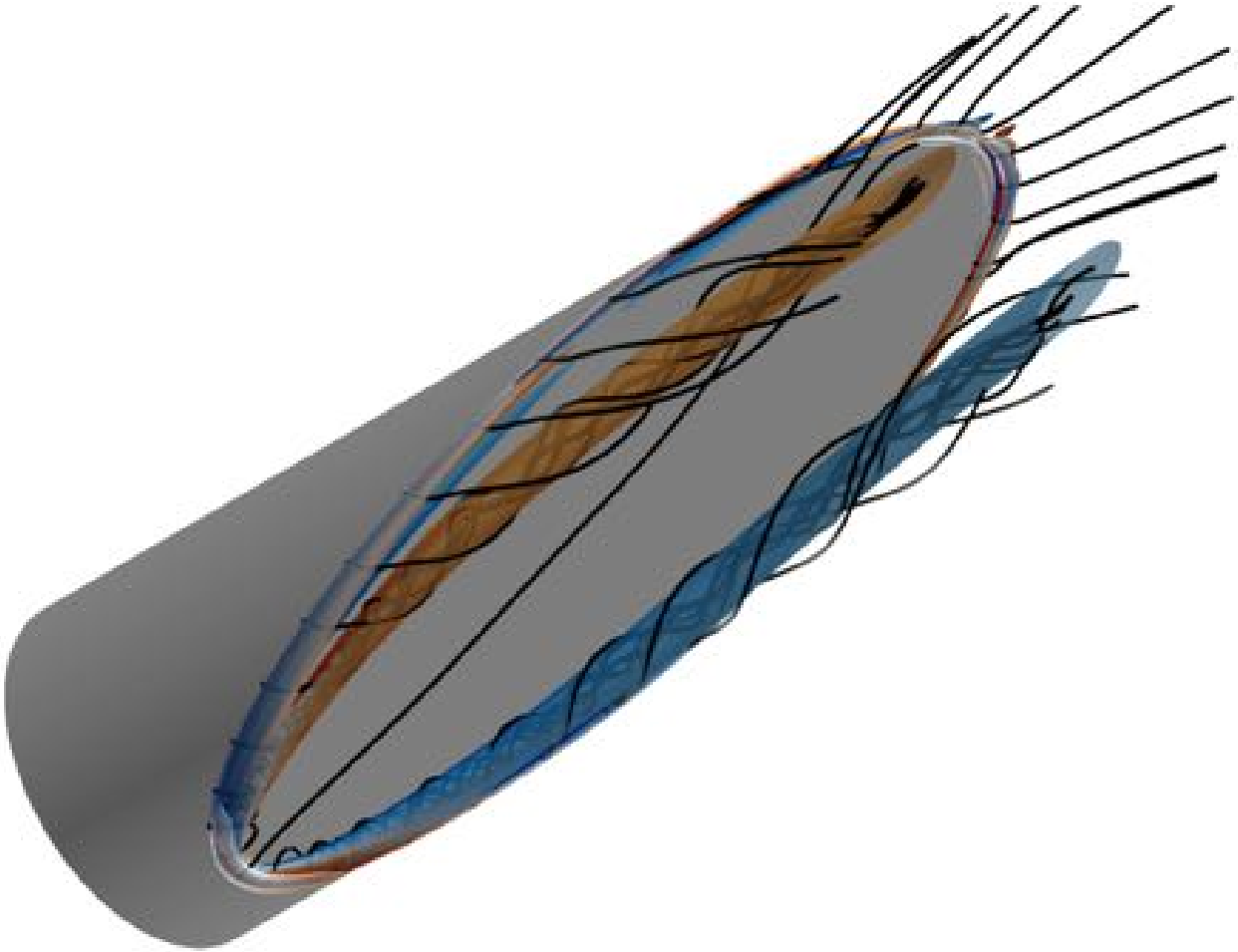
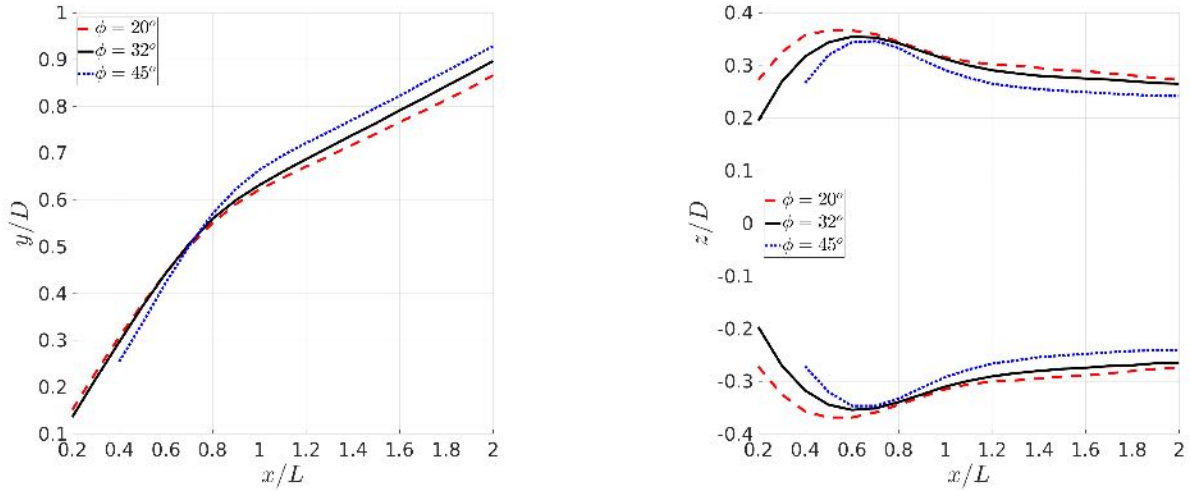


Figure 26: Vortex trajectories identified by isosurfaces of Q-criterion at $Q = 5$: (a) sideview and (b) bottom view. The structures are colored by ω_x.

the upswept base normalized by the axial base length $L \equiv D\ \cot(\phi)$, similar to the approach of Bulathsinghala, Jackson, et al. (2017). Although L itself is the largest for the smallest upsweep angle, the normalization maps upstream and downstream apexes to $x/L = 0$ and 1, respectively, for all upsweep angles. The vortex core locations on both sides of the symmetry plane are plotted; the overlap between these indicates that the left and right vortex legs are essentially the same, except for the sign of the streamwise vorticity. The vortex cores for $20°$ and $32°$ have similar vertical trajectories until $x/L \simeq 0.8$. The $45°$ case has a relatively large vortex head, whose core on the symmetry plane is only detected further downstream – as such, the $45°$ curve in Fig. 27a does not have a core prior to $x/L \sim 0.4$. This is confirmed in streamline traces discussed later. The lifting away of the vortex legs occurs just prior to the location where these trajectories show a relative reduction in slope. A key observation on comparing figures 26a and 27a is that while the vertical inclination of the vortex pair depends on the upsweep, scaling based on axial base length L shows a reasonable collapse of their trajectories for all upsweep cases.

DISTRIBUTION A: Distribution approved for public release.



(a) (b)

Figure 27: Position of vortex cores in the vertical, (a), and spanwise, (b), directions at different streamwise locations.

The spanwise evolution of the vortex core trajectories is shown in Fig. 27b. The left and right vortices develop symmetrically, further confirming the adequacy of the averaging process. Focusing first on the region near the upstream apex, the trend is for the core to occur at larger outboard locations for the smaller angles. This can be visually verified from the previously discussed Fig. 25, and represents the fact that the smaller upsweep angles result in weaker vortices which are more constrained towards the periphery of the base. Proceeding downstream however, after the cores lift away from the base surface, they exhibit inward motion (towards each other) – this feature is strongest for the $45°$ case, whose cores are closest to each other. As discussed below, they are also larger and display the greatest interactions with each other.

4.2.4 Evolution of the vorticity field

The evolution of the vortices is further examined by considering the streamwise component of vorticity (ω_x) on a series of crossflow planes shown in Fig. 28. The results are the computational counterparts of hte experimental observations shown earler. The streamwise locations for the baseline $32°$ case, Fig. 28a, are at $x/L = 0.05$, 0.085, 0.135, 0.175, 0.25, 0.3, 0.37, 0.44, 0.54, 0.64, 0.75, 1.0, to correspond with the PIV results. shown in Fig. 28b. For $20°$ also, contours are plotted at the same locations (Fig.28c), while for $45°$ in Fig. 28(d), planes are taken at $x/L = 0.23, 0.3, 0.41, 0.51, 0.69, 0.9, 1.37$ for clearer display. The experimental and simulation results for $32°$ bear close resemblance to each other: in particular, the simulations clearly capture the shape and growth of the primary vortices. At inception, the cores develop as two teardrop shaped vortices fed by the separated shear layer along the base edge. The left vortex is comprised of negative streamwise vorticity, while the right vortex is positive. As the primary vortex core evolves in the streamwise direction, it grows larger and becomes more axisymmetric, through diffusion processes and entrainment.

DISTRIBUTION A: Distribution approved for public release.

The structure on the $x/L = 0.54$ plane is boxed to highlight the fact that as the vortex lifts away from the surface in the process of forming the streamwise vortex pair, the connection between the separating shear layer feeding sheet and the core gradually weakens. The transformation to an essentially axisymmetric vortex pair is evident well before the downstream apex. These observations are generally similar to those of Bulathsinghala, Jackson, et al. (2017) at an upsweep of $\phi = 28°$, as well as the corresponding numerical results of Garmann and Visbal (2019). Since the Reynolds numbers of these different studies span a wide range, it is evident the primary vortical structures are relatively independent of this parameter.

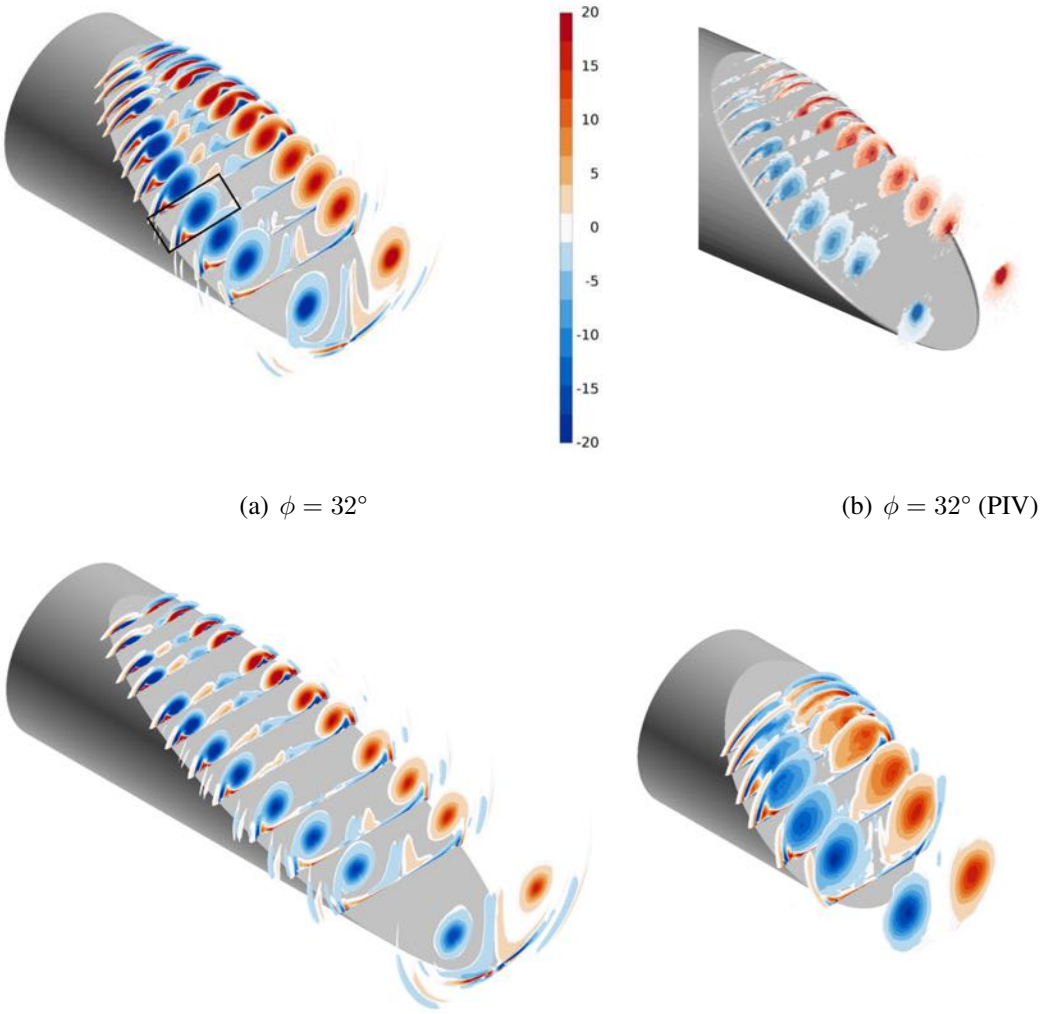
The effect of other upsweep angles on the streamwise component of the vorticity field is shown in Fig. 28c and d. The roll-up process is generally similar, but distinctions in size and strength of the vortex are evident. Figure 28c reiterates prior observations about the more outboard trajectory of the weaker $20°$ vortex (Fig. 25). At $45°$(Fig. 28d), the spatial extent of each vortex leg is much larger and appears more diffused (note that these planes are different from those at the other angles to better visualize the structure). Several efforts Morel, 1980; Xia and Bearman, 1983; Britcher and Alcorn, 1991 have noted that a wake regime may occur at $45°$ either at lower Reynolds number or due to hysteresis. In the present case, the simulation is obtained by systematically increasing the base angle; with this procedure, the vortex regime persists at $45°$.

In addition to the prominent primary vortex, each frame of Fig. 28 shows several smaller structures. The first set of structures represents the secondary vortex beneath the primary vortex, while the second set, the centerline structures, lie between the two vortex legs towards the vertical symmetry plane. Further details of the vortical structure, and the near-wall features may be obtained by highlighting details of a select crossflow plane.

Figures 29a and b respectively show enlarged views of computational and experimental streamline patterns (restricted to the $x/L = 0.44$ plane) for the $32°$ deg case, though the experimental results are obtained at slightly higher $Re_D = 4 \times 10^4$. The most prominent feature is the separated shear layer from the leading edge which forms the main vortex. However, both experiment and simulation show a secondary vortical structure beneath, essentially induced by the primary structure, with dynamics similar to those encountered in delta wings Gursul, Gordnier, et al., 2005; Gordnier, Visbal, et al., 2009. Thus, the primary and secondary features of the flow have similar scaled properties that are only weakly dependent on the Reynolds number. Secondary vortices are also seen in other upsweep cases, as shown in Figs. 29c and d for angles $20°$ and $45°$ respectively. For all the LES results, the figures also show a nascent tertiary separation, which is not immediately apparent in the experimental data. This may be a mild Reynolds number effect, or possibly more difficult to observe because of their small size and proximity to the base surface.

The simulation results of Fig. 28a also shows centerline structures between the legs of the primary vortex, near the symmetry plane. The axial vorticity signs of these are, initially, like the secondary vortices, *i.e.,* opposed to those of the primary vortex . The experimental result of Fig. 28b also shows the signature of these features, though they are not as striking, partly as a result of their proximity to the wall. These near-centerline features arise from the flow that sweeps spanwise towards the symmetry plane after primary attachment. A reversal in sign of the streamwise vorticity at larger x/L is due to the lift-off of these structures from the surface, which

DISTRIBUTION A: Distribution approved for public release.



(a) $\phi = 32°$ (b) $\phi = 32°$ (PIV)

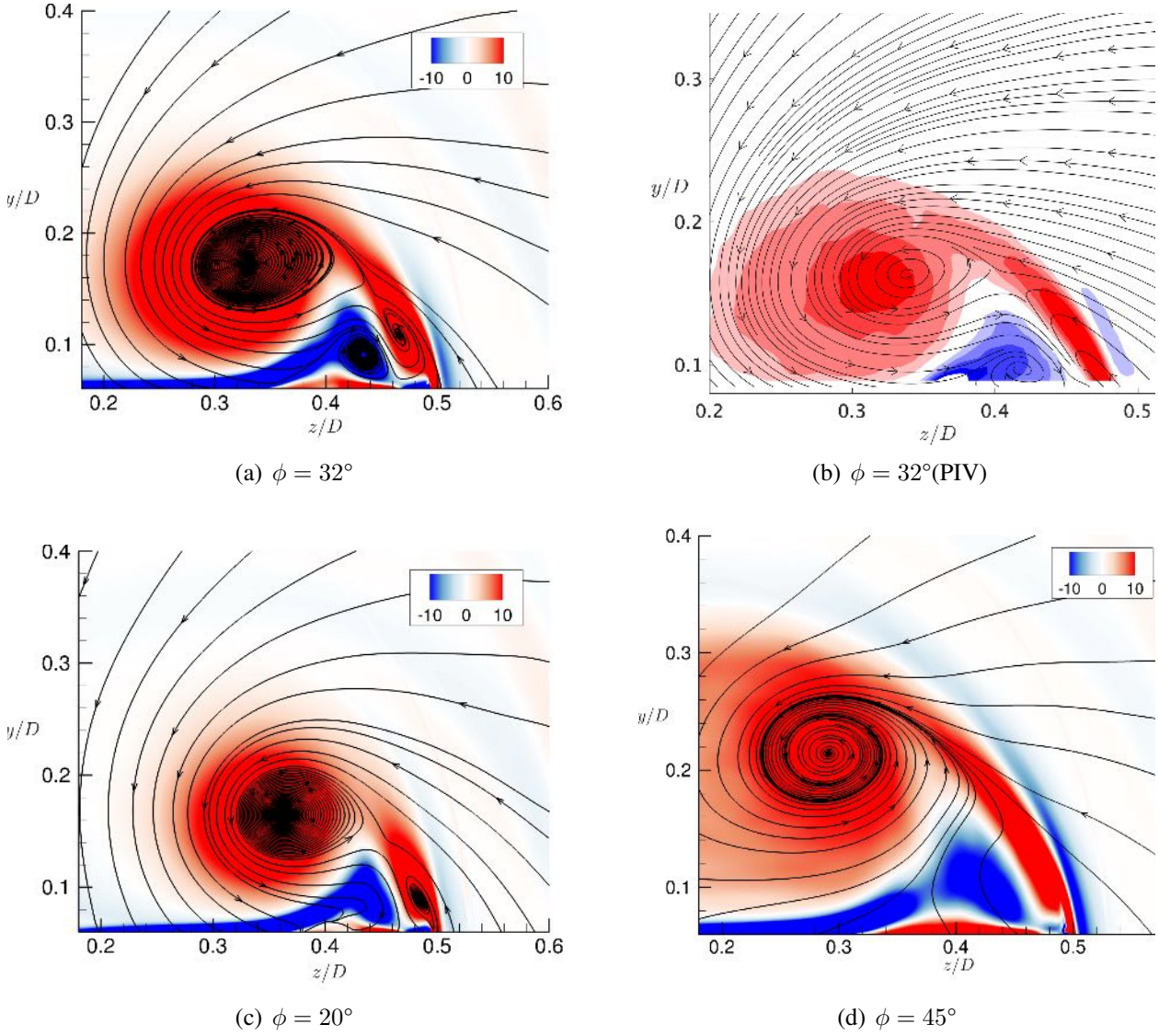
(c) $\phi = 20°$ (d) $\phi = 45°$

Figure 28: Evolution of vortex rollup captured by planes of normalized ω_x for (a) $32°$, (b) $32°$ from PIV measurements taken by Zigunov, Sellappan, et al. (2019), (c) $20°$, and (d) $45°$.

in turn induces a counter-rotating feature, similar to the phenomena described in Gaitonde (2013).

The evolution of vortex strength may be characterized by plotting the normalized circulation ($|\Gamma|/U_\infty D$). These results, obtained after identifying the vortex core using the Γ_1/Γ_2 approach of Graftieaux, Michard, et al. (2001) described earlier, are plotted in Fig. 30, with respect to x/L. The experimental results of Bulathsinghala, Jackson, et al. (2017) for $24°$ and $32°$ cases at $Re_D = 2 \times 10^5$ are also plotted for reference. For each case, the strength of the vortex increases when it is near the base surface as a consequence of shear layer entrainment, observed earlier in Fig. 28. The rise is most rapid for the $45°$ case, which also shows a prominent peak at the location where the legs have detached from the base. At higher upsweep angles, this lift-off location thus lies further

DISTRIBUTION A: Distribution approved for public release.



(a) $\phi = 32°$

(b) $\phi = 32°$(PIV)

(c) $\phi = 20°$

(d) $\phi = 45°$

Figure 29: Primary and secondary structures captured through planes of normalized ω_x and constrained streamlines at $x/L = 0.44$. Note that the experimental results in (b) are at a slightly different Reynolds number $Re_D = 4 \times 10^4$, and the contours are plotted at slightly different levels between -25 and 25 for clarity.

away from the upstream apex. Although a reexamination of Fig. 25d suggests the possibility of a conceptual extension to $90°$ where the legs potentially close upon themselves and the vorticity is essentially azimuthal as opposed to streamwise, the bifurcation to a wake regime precedes such a development – a few comments on the wake regime are presented later.

By about two base lengths downstream Fig. 30, the strengths of the vortices have stabilized at non-dimensional values of approximately 0.22, 0.38 and 0.59 for the three cases, respectively. This is indicative of the relatively long-enduring nature of these vortices. Since the vortex strength has been shown to be directly related to the drag (*e.g.,* Bulathsinghala, Jackson, et al. (2017)),

DISTRIBUTION A: Distribution approved for public release.

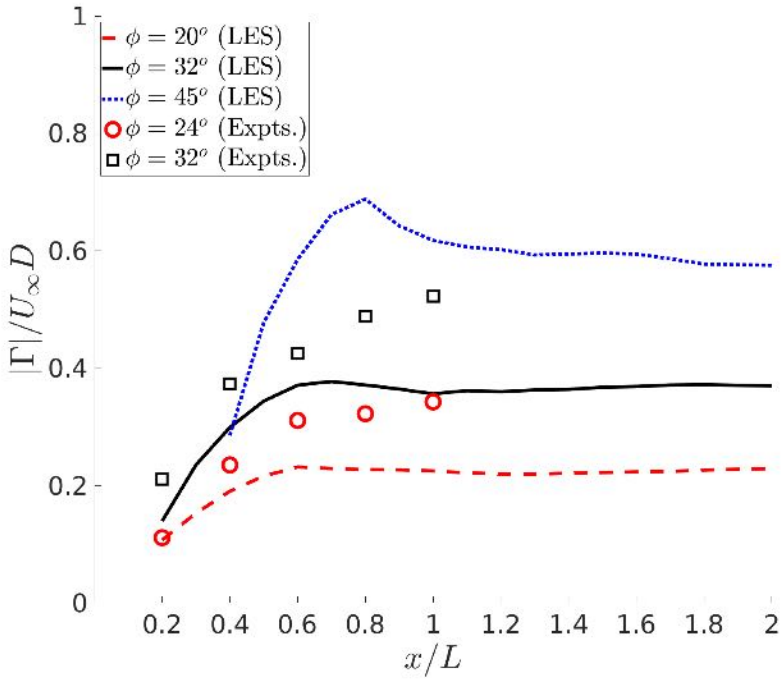
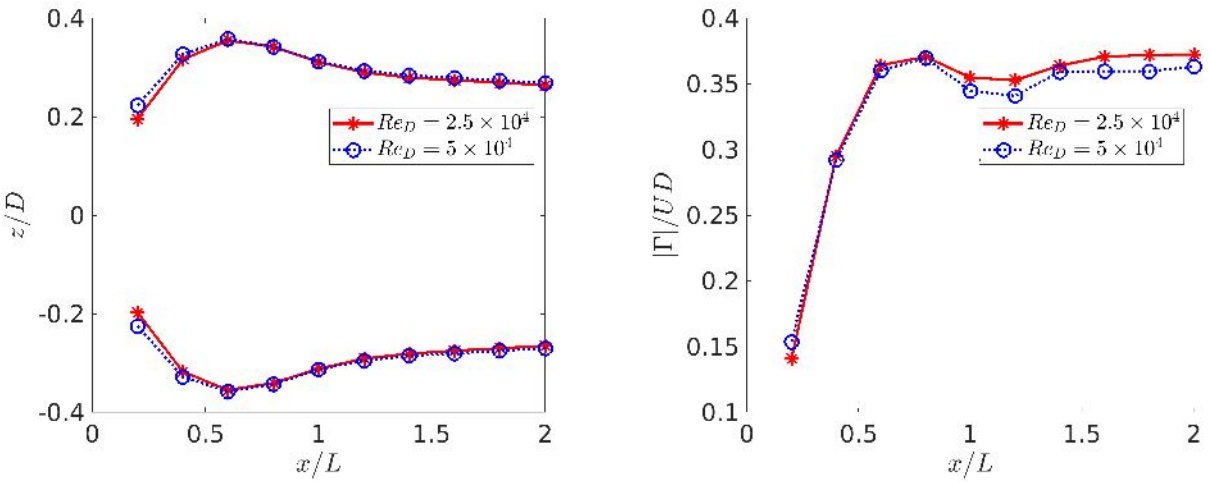


Figure 30: Evolution of vortex strength across the upswept length calculated with normalized circulation ($\frac{|\Gamma|}{U_\infty D}$). Experimental results are from Bulathsinghala, Jackson, et al. (2017).

these values quantify the penalties associated with higher base angles, as elaborated on further below through base surface pressure results. The experimental results at $24°$ and $32°$ display a monotonic increase, though some reduction in rate of growth is apparent. The simulated $32°$ results lie between the two experimental observations. These distinctions may be affected by choice of vortex identification technique, which are estimated with Q-criterion and the Γ_1/Γ_2-method in the experiments and simulations, respectively.

Several of the above results have shown that the current simulations reproduce the principal features observed at higher Reynolds number in experiments. A quantitative assessment of sensitivity to Reynolds number was performed for the $32°$ case by doubling the Reynolds number to $Re_D = 5 \times 10^4$. The three-dimensional flowfield for this case, comprised of a pair of streamwise vortices as before, remains similar (not shown). The trajectory data of the vortices, including spanwise locations and circulation, for the two Reynolds number cases are shown in Figs. 31a and b, respectively. The differences are clearly relatively small; Fig. 31a indicates that the inception of the vortices at $x/L = 0.2$ is only slightly outboard for higher Re case, and circulation values and changes with downstream distance are also relatively similar. At the downstream apex ($x/L = 1.0$), the circulation for higher Re case is slightly (3%) smaller than that for lower Re flow. This trend is consistent with the experimental observations of Bulathsinghala, Jackson, et al. (2017), who measured higher drag at lower Re due to increased circulation.

DISTRIBUTION A: Distribution approved for public release.



(a) Spanwise location

(b) Circulation

Figure 31: Development of streamwise vortices for 32° case at two Reynolds numbers.

Evolution of base surface features

As noted earlier, the upsweep angle has previously been shown to have significant implications on the drag associated with the base surface Morel, 1978; Morel, 1980; Xia and Bearman, 1983; Bulathsinghala, Jackson, et al., 2017. The dynamics on the base plane region is analyzed below to establish the connection between the base surface pressure and the vortical structure for each angle. The pressure field is the most direct variable of interest in establishing drag and is plotted in Fig. 32 as the pressure coefficient, $C_p = \dfrac{P - P_\infty}{1/2\rho_\infty U_\infty^2}$ for the three angles in the vortex regime. Across all upsweep angles, a horseshoe-shaped suction footprint is observed, similar to the experimental observations of Zigunov, Sellappan, et al. (2019) and Bulathsinghala, Jackson, et al. (2017). This suction region spans the approximate area where the corresponding three-dimensional vortical structures of Fig. 25 are close to the base surface. Several of the features noted in the three-dimensional structure are also evident here. The peripheral extent of the suction region, corresponding to that where the developing vortex is fed by the shear layer, increases with upsweep angle. Likewise, a corresponding increase in size of the suction region is also apparent. The base pressure drag-coefficient may be estimated from:

$$C_{D_B} = \frac{\int_A (P_\infty - P)\, \mathrm{d}A}{0.5\rho_\infty u_\infty^2 A_p} \tag{13}$$

where $\mathrm{d}A$ is the elemental area vector in the direction of cylinder axis and A_p is the projected base area. For upsweep angles of $20°$, $32°$ and $45°$, values of C_{D_B} are 0.11, 0.27 and 0.51 respectively. The increase in drag with angle is consistent with the stronger vortex obtained at the higher upsweep angles. As a counterpart to the connection between the surface and off-surface flow discussion in the context of experimental observations, it is instructive to connect the suction region to the "footprint" of the vortical structure for each case. This is facilitated by examining

DISTRIBUTION A: Distribution approved for public release.

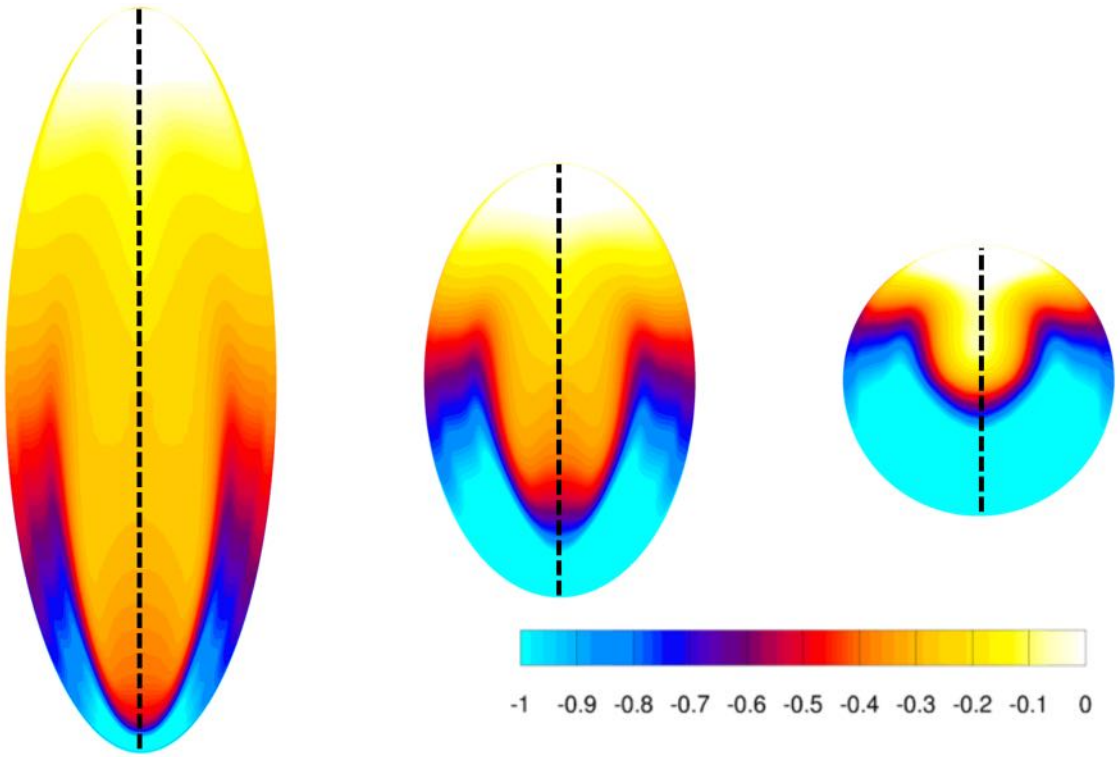


Figure 32: C_p contours on base surface; left to right correspond to $20°$, $32°$ and $45°$, upsweep angles respectively. Dashed line used for subsequent line plot.

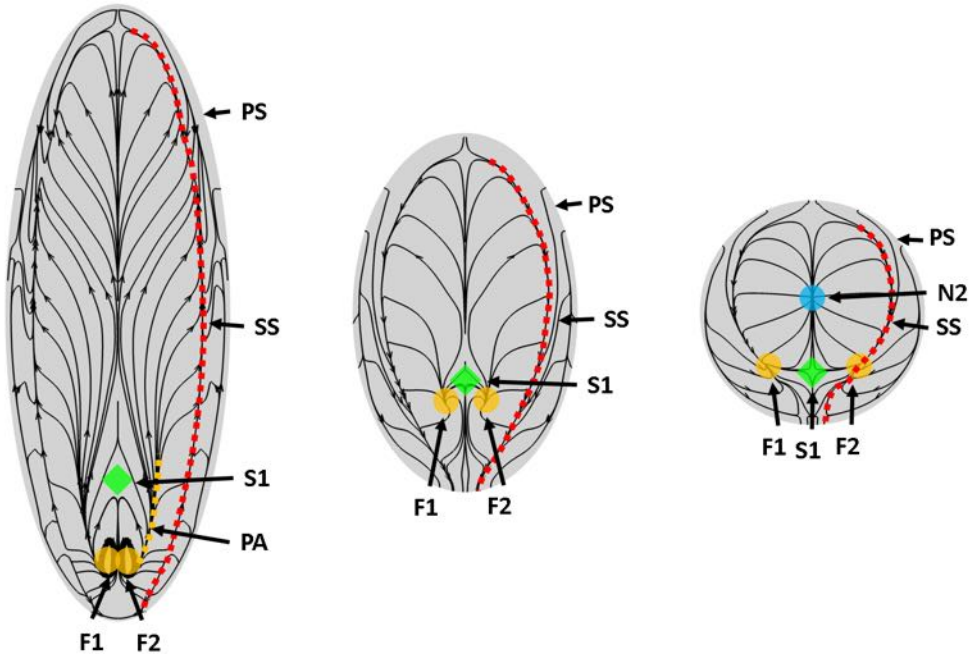


Figure 33: Vortex footprint on the upswept base captured through surface constrained streamlines; left to right correspond to $20°$, $32°$ and $45°$, upsweep angles respectively.

DISTRIBUTION A: Distribution approved for public release.

surface-constrained (or restricted) streamlines that represent the surface oil flow pattern. These streamlines on the upswept base are plotted for the three angles in Fig. 33. Such portraits are generated by releasing particle traces adjacent to the base, but with velocity vectors constrained to be parallel to the base. The patterns so obtained provide crucial insight into the behavior of the flow Perry and Chong, 1987; Tobak and Peake, 1982.

The primary features of interest are lines of coalescence and divergence, which represent locations where the flow separates and attaches, respectively (cf. Visbal (1991)). Surface streamlines also display one or more critical points *i.e.,* points in the pattern where the shear stress is zero. These can be classified as nodes or focii and saddles, and their dynamics has been discussed in literature(Perry and Chong, 1987; Dallmann, 1988). Although such points follow specific laws in the numbers and types of critical point combinations that are physically feasible, in the present study, we merely highlight the prominent features that are pertinent to the goals of the paper. Observations from the current simulations are followed by brief comments on the results presented by Garmann and Visbal (2019).

The 20° degree case is discussed first (Fig. 33a), and the effect of increasing base surface angle is discussed subsequently. For this sharp-edged configuration, the flow separates on the entire periphery of the base edge: we refer to this as primary separation (PS). The footprint of the vortex is most clearly visible in the head region of the horseshoe vortex, located near the upstream apex, since it is closest to the base surface at this point. In this region, a clear primary line of attachment (divergence) is observed (marked PA); the region between PS and PA thus encompasses the vortex head. PA becomes less distinct away from the upstream apex, as the vortex takes shape. The 20° case vortex is slender (Fig. 25) and has only a relatively small pressure footprint in the circumferential direction (Fig. 32). The flow attaching at PA sweeps spanwise in both directions, towards the edge as well as towards the symmetry plane. The former regime separates prior to reaching the edge at the line of secondary separation, 'SS'. The latter regime essentially interacts with its mirror counterpart, and separates at the symmetry plane: this region is the footprint of the centerline structures discussed in the context of Fig. 28.

The surface pattern of the 20° case contains several critical points. Although most of the primary flow features discussed in Figs. 25 and 28 are evident in the efforts of Bulathsinghala, Jackson, et al. (2017) and Garmann and Visbal (2019), these critical points are not as prominent in their results. The surface pattern detail may thus be one of the few manifestations of the relatively lower Reynolds numbers chosen in the present simulations. The pattern is nonetheless interesting especially insofar as it aids in the description of the evolution of the pattern with base surface angle. Returning to the 20° results of Fig. 33a, the prominent feature near the upstream apex is a trio of two foci (F1, F2) and a saddle (S1). The other critical points are not explicitly marked since some of these finer details are not of concern in the present work.

When the angle is increased to 32°, the principal surface oil flow features remain generally similar. Primary separation again occurs around the entire periphery of the base edge and the line of secondary separation (SS) remains prominent. The direction of flow along SS shows a subtle change in that at 32°, there is an apparent downward motion of the flow. This is not significant, since the planar-restricted velocity is extremely small; the flow essentially leaves the surface along

DISTRIBUTION A: Distribution approved for public release.

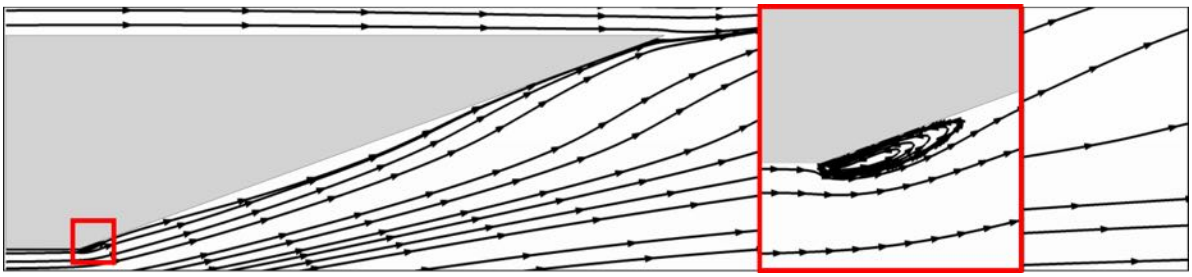
a perpendicular to the SS line. Although not shown for brevity, this is confirmed from the local in-plane and out-of-plane velocities at the point next to the base surface. The F1-F2-S1 combination moves upward along the base, and extends further in the spanwise direction, but retains its topological definition.

In the 45° case, the features take on a rather more axisymmetric form. The secondary separation line remains prominent, and the F1-F2-S1 trio extends over an even larger region in the spanwise direction. Perhaps the most prominent change is the formation of a clear critical point, the node N2, near the center of the base. The terminology N2 (rather than N1) is chosen to reflect that traditionally the node formed on the forebody (not simulated in this work) is designated N1. Note that unlike in a classical unseparated flow past a sphere, where the downstream surface oil flow node must be stable (i.e., constitutes a sink in streamlines), in the current case, N2 is unstable and is a source of streamlines. The distinction arises from the fact that flow separates around the entire periphery of the base edge, which requires a source of streamlines on the base plane. The formation of N2 is not abrupt; rather, the surface pattern emanating essentially radially from N2 is a natural progression of the convergence of lines near the symmetry plane that are evident in the lower angle cases. N2 may be viewed potentially as a precursor to the anticipated wake regime at higher angles. Indeed, as noted earlier, a wake regime is even possible at 45° itself *i.e.,* hysteresis has been observed at this angle Britcher and Alcorn, 1991, and can be reproduced numerically under suitable conditions, but is not examined here. A smooth extension to the limit of a 90° base surface angle may be postulated by noting that for axisymmetry, all critical points other than N2 weaken and disappear. Aspects of such a structure has been discussed for a 3-D supersonic base flow in Gaitonde (2010) in which also the vortex lines form a generally horseshoe shape. As a final observation, the flow attaching at N2 separates at the secondary separation line as before, which also allows for a smooth extension to the limiting 90° case.

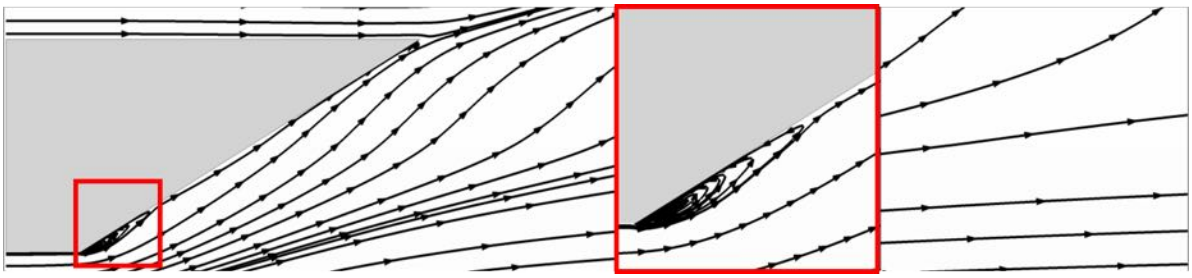
It is helpful in aiding the discussion to complement the surface streamline pattern with restricted streamlines on the symmetry plane. These portraits can also display lines of coalescence and attachment as well as critical points, though their implications differ from those in the surface streamlines. The underlying dynamics revealed by such symmetry plane streamlines have been discussed extensively in Dallmann (1983). Figure 34 shows these streamlines for the three angles. The observed features are similar in all cases, but are clearest in the largest angle case. The primary features are those corresponding to the cross-section of the head vortex, and are classically representative of features observed when flow separates at a symmetry plane. The distinction between separation on a 3-D symmetry plane and its 2-D counterpart is important (Dallmann, 1983). Unlike in the "center" type of off-surface critical point obtained in the 2-D case, here a (stable) focus (F3) is realized, together with two surface (half-)saddle points, SS1' and SS2'. F3 constitutes a sink in the symmetry plane streamlines as they evolve away from it to form the vortex head. The structure has been described by Zigunov, Sellappan, et al. (2019) as indicative of an open separation bubble. As evident from Fig. 34, the size of the separation bubble increases with the upsweep angle. The extent of these bubbles for angles ϕ =20°, 32° and 45° as a fraction of slant length, $S = \dfrac{D}{\sin(\phi)}$, are 0.0725, 0.22 and 0.456, respectively.

The connection between the head of the vortex and local surface pressure may be finalized by

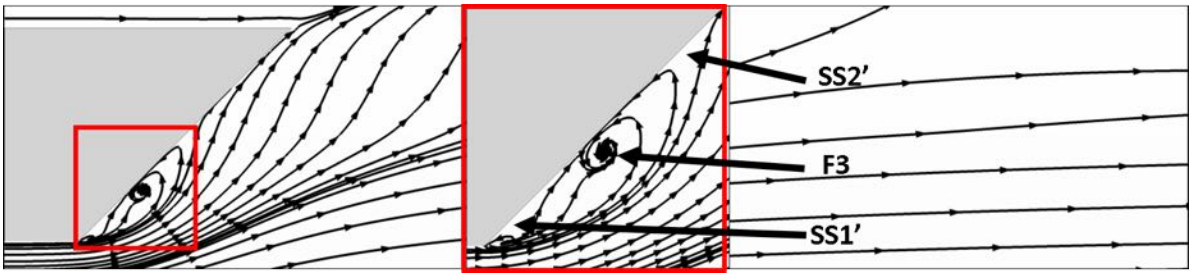
DISTRIBUTION A: Distribution approved for public release.



(a) $\phi = 20°$



(b) $\phi = 32°$

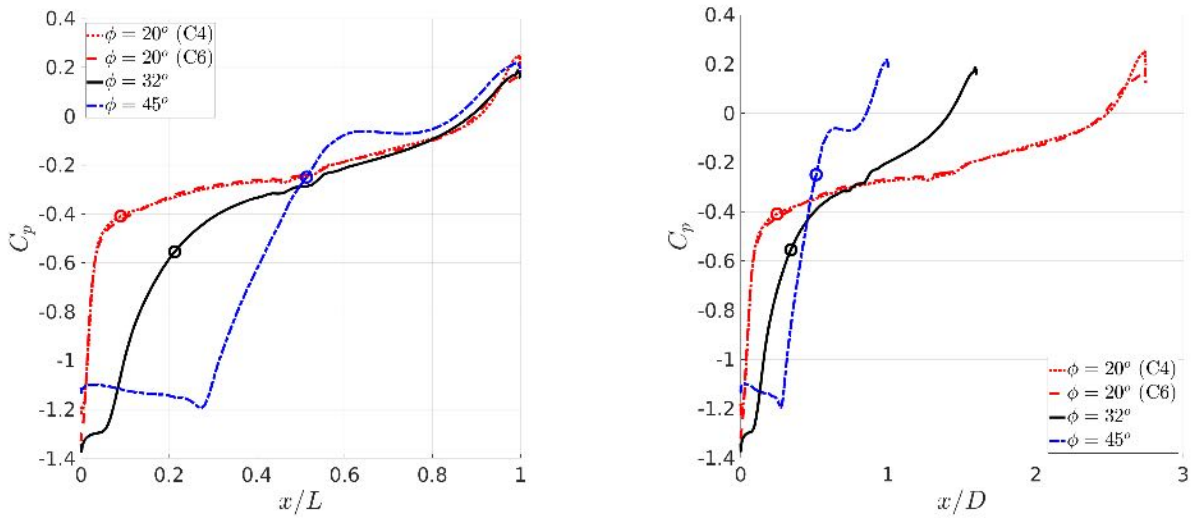


(c) $\phi = 45°$

Figure 34: Separation region on the symmetry plane with surface constrained streamlines. The zoomed-in view of the separation bubble is shown in the inset.

considering C_p values along the centerline as shown by the dashed line in Fig. 32. The results are plotted in Fig. 35a and b along x/L and x/D respectively, to highlight the variations with relative and absolute axial lengths. For the $20°$ case, results with the higher-order *C6* scheme have also been plotted; the close agreement with the *C4* case provide further confirmation about the adequacy of the numerical approach. The low-pressure region for the $20°$ case has a relatively small extent on the symmetry plane of Fig. 32. In Fig. 35a, this manifests as a rapid increase until about $x/L \sim 0.05$ after which the rise becomes more gradual. At $32°$, this rise is preceded by a small region of relatively flat C_p near the upstream apex. To connect the pressure to the surface and symmetry plane patterns, the locations of the attachment point SS2' are marked. In each case, this attachment point does not occur at the initiation of the rapid rise, but rather, near the end of the rising part of the C_p profile. The $45°$ case shows several distinct features that distinguish it from the other two cases. C_p is higher at the upstream apex than at the lower angles, and a region of relatively constant pressure is also established. The case also shows a second plateau

DISTRIBUTION A: Distribution approved for public release.



(a) (b)

Figure 35: C_p on the symmetry plane of the upswept base surface. The abscissa is x/L (a) or x/D (b). The locations of SS2' for each case are shown with round markers.

near $x/L \sim 0.65$.

The above observations allow for a clearer correspondence of the vortex head region with its surface footprint, which was difficult to achieve with surface streamline patterns because of absence of a clear attachment line. The central region of the head of the vortex in the $45°$ case may be assigned to F3. The surface oil flow immediately beneath F3 is in fact the S1 of the F1-F2-S1 combination. On the other hand, the surface pattern at SS2' corresponds to N2. As a final note, this correspondence between off-surface symmetry plane restricted streamlines and the surface pattern is not as clear in the lower angle cases, which exhibit smaller head regions.

Aspects of wake regime

The above discussion has made several references to the wake regime, which does not display the prominent streamwise vortex pair. The LES are performed at $\phi = 55°$, which is sufficiently above ϕ_{cr} so as the observe the wake regime without a significant Re dependence. Figure 36 shows key features of the wake regime. The absence of streamwise vortices is very apparent, and the wake flow now shows a large recirculation region behind the body. The iso-surfaces of total vorticity show a doughnut like structure very close to the surface, along with shear layer regions near the periphery of the base. This figure may be compared with the iso-surfaces shown in Fig. 20 for the vortex case, where the total vorticity field shows a clear horse-shoe like structure. The doughnut-shaped vorticity field in the current wake case is not formed around the center cylinder axis but is shifted towards downstream apex. This is due to the asymmetry in the flow in axial direction for $55°$ case, where the flow separates earlier at the bottom than at the top. If the upsweep angle is further increased to $\phi = 90°$ then an axisymmetric flow may be achieved. However, recent workGrandemange, Gohlke, et al., 2013 points toward a more complex nature of the flow

DISTRIBUTION A: Distribution approved for public release.

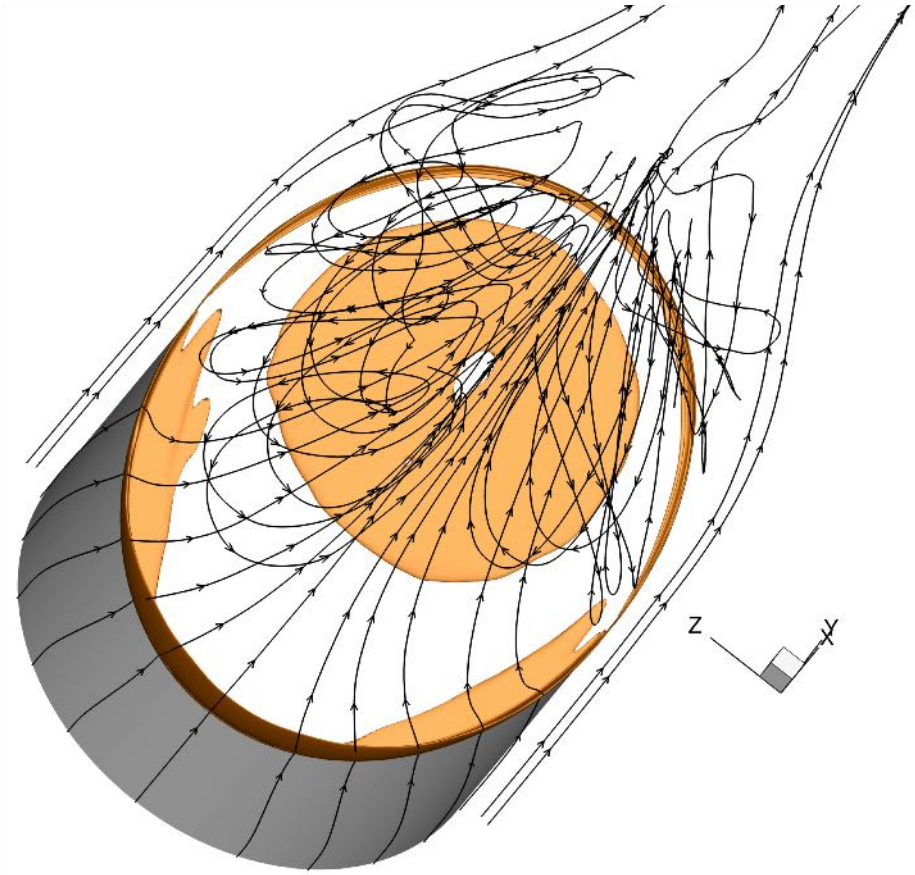
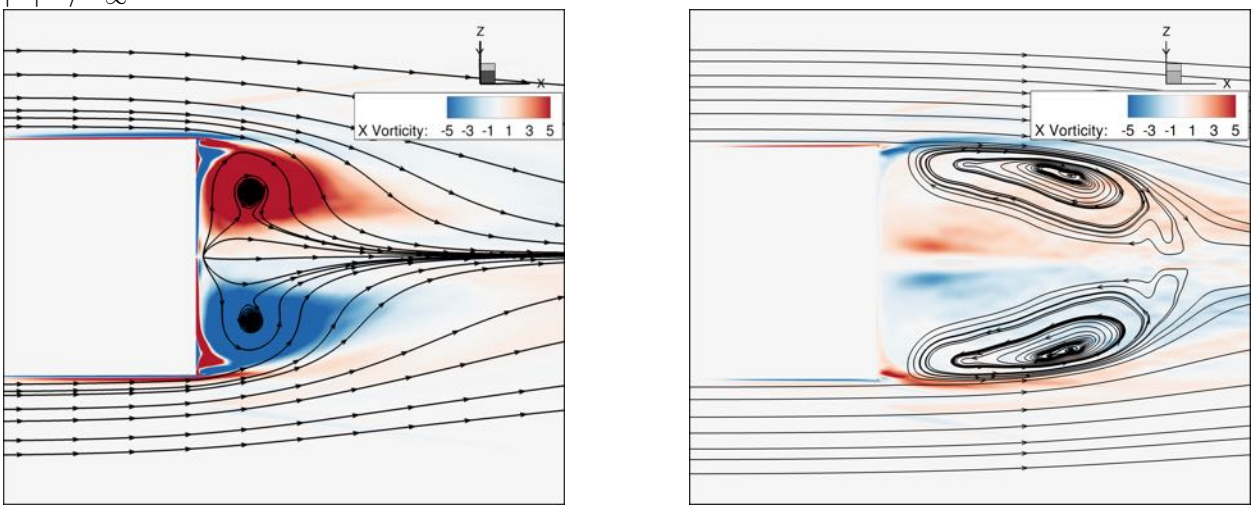


Figure 36: Wake regime at $\phi = 55°$ depicted using volume streamlines. Iso-surfaces at $|\omega|D/U_\infty = 20$ are also shown.



(a) 45° (b) 55°

Figure 37: Comparison of vortex and wake regime on xz-plane at $y = 0$. Contours of $\omega_x D/U_\infty$ are shown at same levels for both the cases. Sectional streamlines are also plotted.

DISTRIBUTION A: Distribution approved for public release.

at high Re, including the possibility of a bistable flow instantaneously, where the recirculation region repeatedly switches between two reflectional symmetry-breaking positions. The volume streamlines in Fig. 36 further indicate the presence of two lobes in the flow downstream of base, arranged symmetrically around the $z = 0$ plane. These structures are typical of bluff-body wakes as in flow past cylinders except that again, here they are not axisymmetric around the cylinder axis for the reasons noted earlier.

In order to visualize these structures in the wake, the flow is shown on a horizontal sectional cut ($y = 0$ constituting an xz-plane) in Fig. 37. To enable a direct comparison with the vortex case, the same view is also shown for 45° upsweep. As described earlier, the vortex case in Fig. 37a is characterized by concentrated vorticity fields, representing the penetration of the legs of the horseshoe through this plane. The surface streamlines show nodes at the vortex cores, and secondary vortices are also observed. Compared to this, the wake case in Fig. 37b shows a very weak vorticity field downstream of the base, though the oppositely signed regions are still segregated by the symmetry plane. Further, the streamlines show that the separation region in the wake case is significantly bigger than in the vortex case. Though not shown here for brevity, the high vorticity field in the vortex case leaves a stronger suction footprint on the base surface leading to higher drag compared to the wake case, as observed in experiments (Britcher and Alcorn, 1991).

4.3 Summary

The combined experimental and simulation campaigns have yielded a composite description of the flowfield over a wide range of Reynolds numbers and slant angles. Oil flow images, stacked SPIV flow field reconstruction and computational equivalents enable the definition of the main features. A "horseshoe vortex" feature, which is the result of a smooth transition between a separation bubble and a pair of counter-rotating vortices, is the most striking feature observed. Its presence causes a very low pressure region over the slant plane, which has an effect on the flow over the cylindrical surface that is seen as a large acceleration both towards the center plane and towards the slanted surface. The footprint of a secondary vortex was also observed, whose existence and shape was confirmed by PIV measurements.

As the slant angle is increased, the separation bubble grows in size and the vortices increase in circulation, becoming stronger. It is conjectured from these observations that when the separation bubble grows to a length comparable to the length of the slanted surface, the flow transitions to the fully separated wake state. The effect of lengthening of the separation bubble was also observed in the experiments as the Reynolds number is decreased, however it is unclear if the same trend applies to vortex strength. As far as the data points analyzed can show, the vortex strength trends are much less prominent than the trends in separation bubble length with respect to Reynolds number.

The separation bubble shape for $\phi = 45^\circ$ was also characterized. The flow pattern observed suggests the presence of a highly three-dimensional flow field inside the separation bubble, potentially indicating the presence of an inflow from off-center locations towards the center. Furthermore, a bi-stable flow pattern was observed at the lower Reynolds number $Re_D = 2.5 \times 10^4$ for the $\phi = 45^\circ$ model, related to the initial overshoot of freestream velocity. It is very likely that other means could be used to cause the switching of flow patterns, opening up the possibility for active

DISTRIBUTION A: Distribution approved for public release.

flow control studies for this geometry. A schematic summarizing the flow features over this canonical bluff body was generated by compiling the features that are common to the vortex-dominated wake flow regime of the cylinder with a slanted base.

Many of the manifestations in the current computations match experimental and other computational results at higher Reynolds numbers. These may be reiterated as follows. The Reynolds number sensitivity indicates the relatively weak dependence of this parameter on the overall structure and various non-dimensional features of interest, including the locations and circulations of the vortex pairs. The vertical inclination of the vortex pair measured from the freestream direction increases with base surface angle. However, a scaling that accounts for the sweep provides a reasonable collapse of this data indicating that this relative angle is not sensitive to upsweep. The overall strength of the vortex increases with upsweep angle, however the persistence of the vortex is larger for the smaller upsweep angles. In addition to the primary vortex, a secondary vortex is evident, as are centerline structures whose signatures are also confirmed in the experimental data. The suction region of the base pressure reflects the horseshoe shape of the adjacent vortex head, resulting in increasing drag with upsweep angle.

A detailed analysis of the flow reveals significant changes in the surface streamline pattern with upsweep angle, and yields insights into pathways by which the streamwise aligned vortex may ultimately result into a turbulent wake-type regime, elements of which are discussed using an LES solution at 55° upsweep. Finally, the data provide an avenue for an assessment of the global stability characteristics of the flow, as discussed subsequently, to aid in reduced order modeling and exploration of efficient control strategies.

5 Hysteresis

5.1 Experimental investigation

5.1.1 Mean flow observations of wake stall and its hysteresis

The mean flow topology of the fully separated wake regime ("stalled regime") outside of the hysteresis zone will be first examined in this section. This will enable the understanding of the flow topology of the "stalled regime" when the slant angle ($\phi = 50^\circ$) unambiguously defines the flow topology ($\phi > \phi_{crit}$) - at least to the extent this and previous studies have observed so far. The "stalled" flow topology presented in this section was observed until the upper limit of the free stream velocity available in this facility ($V_\infty = 70\ m/s$ or $Re_D = 6.8 \times 10^5$). The terminology proposed in this work ("stalled regime") is in contrast with that proposed by Britcher and Alcorn (1991) ("turbulent closure") for reasons discussed below.

Surface flow features

The surface flow topology of the vortex state between the slant angles of $\phi = 20^\circ$ and $\phi = 45^\circ$ were discussed above together with matching high-fidelity computational results. One of these results (also described in Zigunov, Sellappan, et al. (2020a)) at $\phi = 45^\circ$ (vortex regime) is compared with the surface flow topology obtained at $\phi = 50^\circ$, both at a Reynolds number of $Re_D = 5 \times 10^5$, in figure 38. The features listed in figure 38(a) for $\phi = 45^\circ$ are a visual summary of the discus-

DISTRIBUTION A: Distribution approved for public release.

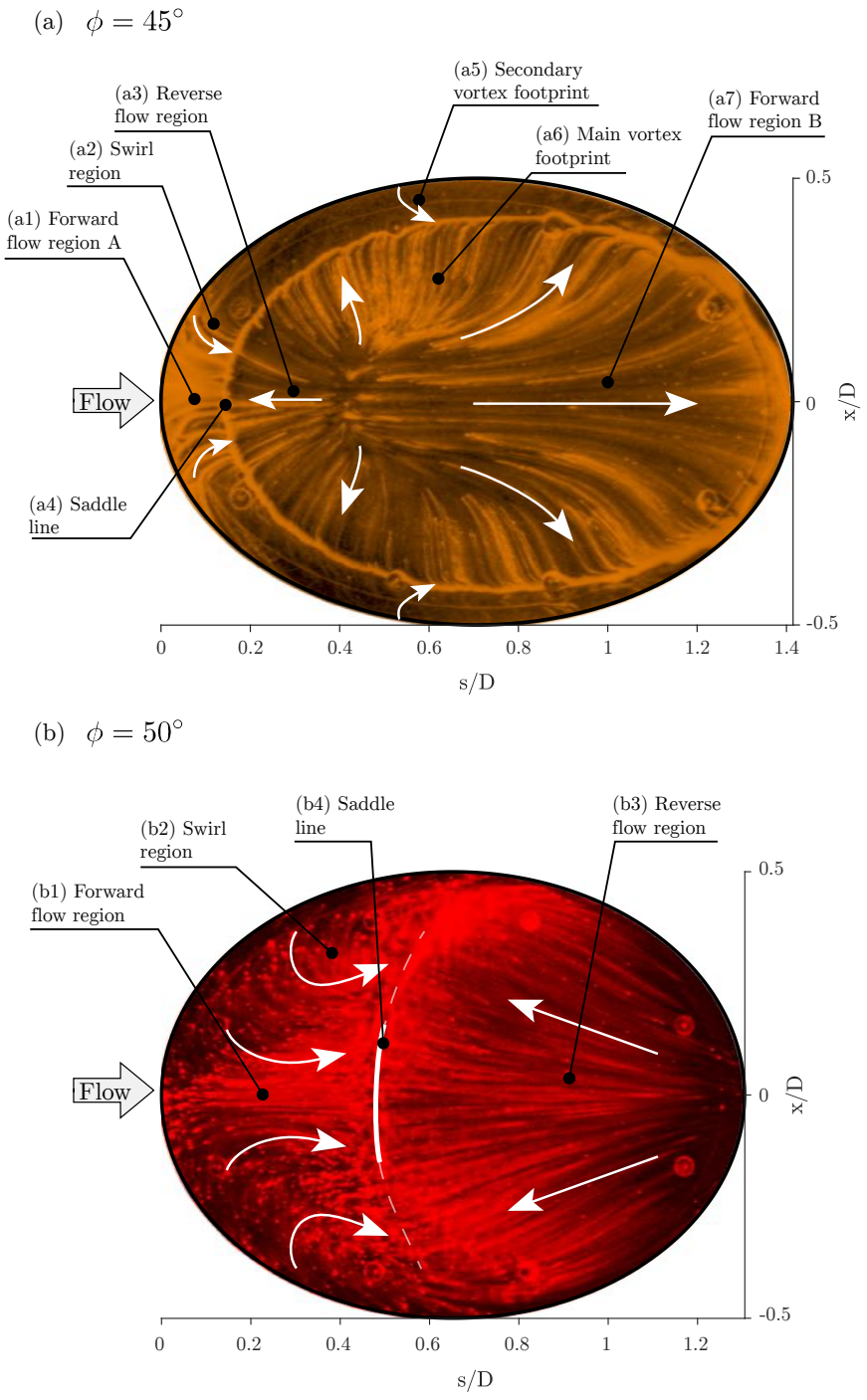


Figure 38: Dewarped oil flow photographs observing the slanted flat surface for the slant angles of (a) $\phi = 45^\circ$ (Zigunov, Sellappan, et al., 2020a) and (b) $\phi = 50^\circ$. Both cases were taken at $Re_D = 5 \times 10^5$. Surface-constrained s/D coordinate increases in the streamwise direction and has origin at the upstream leading edge of the slanted surface

DISTRIBUTION A: Distribution approved for public release.

sion presented by Zigunov, Sellappan, et al. (2020a) and greatly differ from the oil flow pattern at $\phi = 50°$, shown in figure 38(b). Movie 1 is also provided in the supplementary material to clarify the oil flow directions indicated by the arrows for figure 38(b). In the stalled regime of figure 38(b), the forward flow region (b1) extends for a longer portion of the surface (to about $s/D = 0.5$) in comparison with the vortex regime (a1), where the forward flow region only extends to about $s/D = 0.14$. This forward flow region is not due to the boundary layer from the cylindrical surface staying attached, since the sharp edge at $s/D = 0$ ensures flow separation and the formation of a shear layer. It appears that this feature is related to a highly three-dimensional flow field within this separated flow zone, which encompasses the swirl region (b2). A similar flow structure appears to also be present to a lesser extent in the $\phi = 45°$ case, as shown in figure 38 (a2). It is conjectured that the two flow structures are of the same kind, however the full stall of the $\phi = 50°$ case makes the region more readily visible in the oil surface flow.

The reverse flow region (b3) is characteristic of a typical fully-separated bluff-body wake, and a similar region is also present in (a3) for the $\phi = 45°$ case, related to the footprint of the separation bubble recirculation zone. In the $\phi = 45°$ case, however, the reattachment point on the slanted surface forms a "source point" feature, which is absent at $\phi = 50°$ - indicating the separation bubble does not find a reattachment point on the slanted surface in the stalled regime. The presence of a forward and a reverse flow region on the surface creates a surface lift-off line, denominated as "saddle line" in (b4). This "saddle line" has similar features as the "saddle line" observed in the $\phi = 45°$ case (a4). It is also important to note that the regions where these "saddle line" features form are usually of lower velocity magnitude, being prone to the generation of artifacts from the effect of gravity on the oil. In many aspects, however, the surface flow features observed in figure 38(b) seem to already be present in the vortex regime of figure 38(a), although the features are greatly magnified for the stalled regime of figure 38(b), dominating the wake.

Three-dimensional flow field at $\phi = 50^o$

By utilizing the stacked stereoscopic PIV (S-SPIV) technique described in Section 3.1.2 it was possible to reconstruct the mean flow topology of the slanted cylinder in the stalled regime. A lower Reynolds number of $Re_D = 2.5 \times 10^4$ was employed for this measurement, in order to enable direct comparison with the cases presented in Section 5.1.2 where hysteresis was observed for $\phi = 45°$. Observations performed with planar PIV at the center plane $x/D = 0$ indicate that the main features of the flow are mostly similar in the Reynolds number range $Re_D = 2.5 \times 10^4$ to $Re_D = 6.8 \times 10^5$.

Figure 39(a) presents a three-dimensional view of the mean flow topology as captured by S-SPIV. Each plane contains a mean of 500 PIV snapshots. Fifty-two evenly spaced planes were captured between $z/D = 0$ and $z/D = 1.26$, with a spacing between planes of $\Delta z/D = 0.034$. The PIV plane spacing corresponds to 5 millimeters in physical dimensions, which is about twice the PIV laser thickness used. The flow topology in this stalled regime reveals a complex interaction inside the separation bubble. As expected, the separated flow at the edge of the slanted surface forms a shear layer, highlighted in figure 39(a1), all around the cylindrical surface. Unlike the vortex regime discussed by Zigunov, Sellappan, et al. (2020a), the shear layer does not reattach

DISTRIBUTION A: Distribution approved for public release.

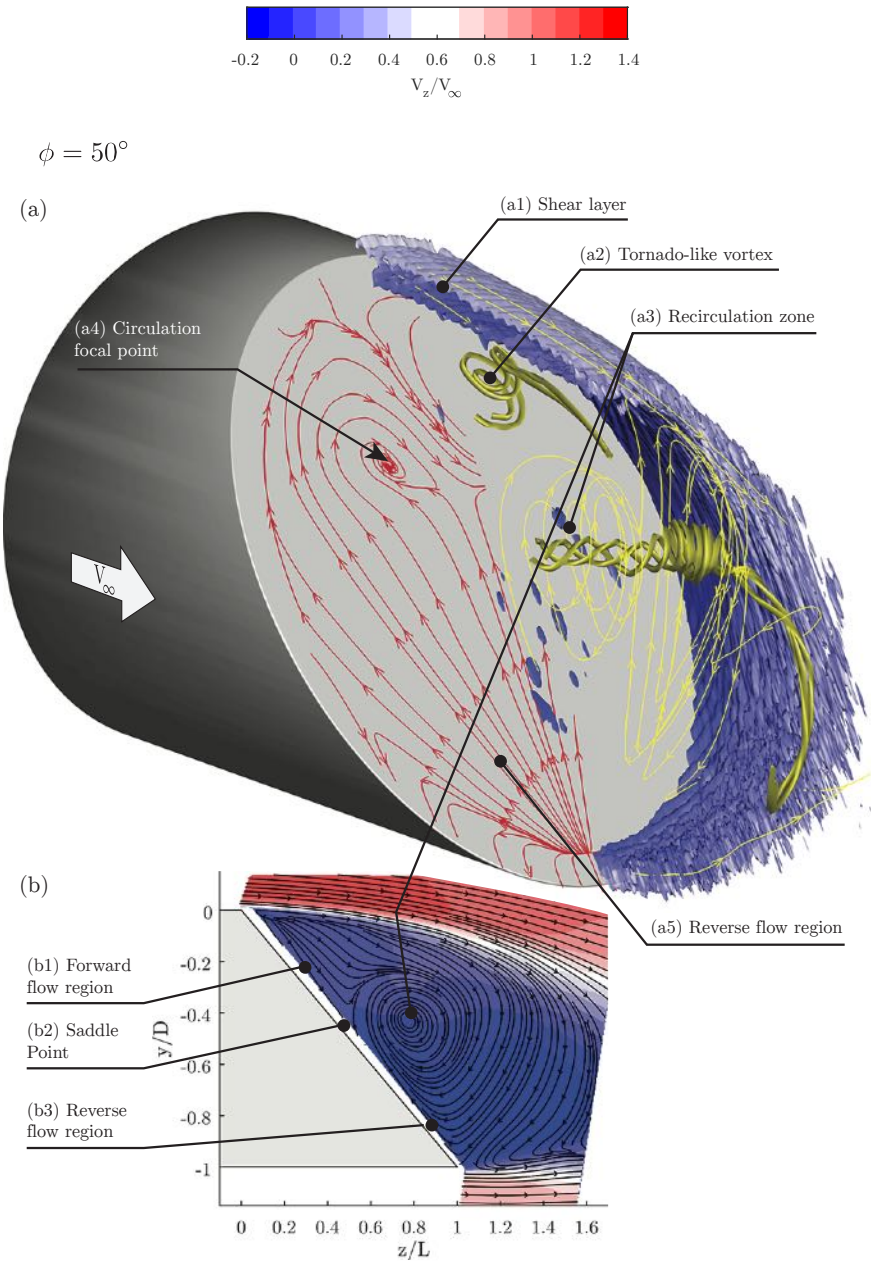


Figure 39: (a) S-SPIV three-dimensional reconstruction of the mean wake topology for $\phi = 50°$ and $Re_D = 2.5 \times 10^4$. Thin red streamlines are surface-constrained to a plane offset $0.035D$ from the slanted surface and are shown only for $x/D < 0$. Remaining features only shown for $x/D > 0$ to prevent occlusion of the flow field inside the separation zone. Isosurfaces of $|\vec{\omega}D/V_\infty| = 4$ colored by V_z/V_∞ highlight the shear layer. High frequency noise in isosurfaces due to PIV uncertainty and interpolation artifacts. Thick yellow volumetric stream-ribbons highlight the two main vortical structures identified inside the bubble. (b) Mean planar PIV flow field at $x/D = 0$ for the same case, showing the recirculation bubble more clearly

DISTRIBUTION A: Distribution approved for public release.

onto the cylindrical surface, instead forming the fully separated wake.

Inside the wake bubble, there are two main regions of interest, namely, the main recirculation zone in figure 39(a3) and the "tornado-like" vortex highlighted in figure 39(a2). The main recirculation zone (a3) seems to dominate the majority of the downstream portion of the open wake and appears to bend downstream. It is not clear due to the downstream extents of the data collected whether this vortical structure forms a closed toroidal vortex, as seen by Pavia, Varney, et al. (2019) in the blunt-end $\phi = 90°$ case, or if the vortical pair formed extends for a short downstream portion in a similar fashion as the vortex-dominated wake state does.

In the upstream portion inside the slanted surface, a vortical structure similar to a small tornado (figure 39, a2) produces a focal point in the surface-restrained streamlines, as shown in the opposite side of the symmetry plane in figure 39 (a4). It was not possible to generate isosurfaces that highlight this structure through the S-SPIV flow field reconstruction, as the sparse planes acquired and artifacts from the interpolation prevent the highlighting of weak vortical structures. Also, the surface-restrained streamlines shown in red do not display a clear saddle line feature as observed in the oil flow photographs of figure 38 (b4). The lack of this feature is believed to be associated with the fact the streamlines were restrained to a surface about $0.035D$ from the slanted plane, due to limitations related to PIV reflections at the surface. It is also possible that the saddle line shown in figure 38 (b4) occurs for only a very short spanwise extent around the centerline and appears to be wider in the oil flow photographs because the oil flow development at low velocities and a high slant angle against gravity prevents the oil from fully conforming to the surface flow topology.

It is clear, however, that a saddle line should be present in the model surface based on the examination of the cross-section at the center plane shown in figure 39(b), which shows the open separation bubble has a point of lift-off indicated in (b2). The forward flow region (b1) is produced by the "tornado-like" structure in figure 39(a2). This vortical structure should also be present in the vortex regime, since the vortex regime also presents a similar region in its surface flow (figure 38, a2). It is possible that this pair of swirling flow structures might play an important role in the dynamics of the slanted cylinder wake, both in the vortex regime and the stalled regime, however detailed time-resolved information on this feature and its connection with vortex wandering/shedding is yet to be described in detail.

5.1.2 Hysteresis of the wake stall at $\phi = 45°$

At the slant angle of $\phi = 45°$, Britcher and Alcorn (1991) reported a bi-stable behavior of the wake as a function of Reynolds number in an interference-free, magnetic levitation wind tunnel. A clearer understanding of the main flow features that constitute the stalled regime of the slanted cylinder wake presented in the previous section serves as a foundation to describe the behavior of the wake in this bi-stable Reynolds number range.

Evolution of the wake as a function of Re_D

This section will discuss the results obtained with the hysteresis experiment described in Section 3.1.4 for $\phi = 45°$. Figure 40 summarizes the observed flow fields from planar PIV at the center plane $x/D = 0$ as a function of Reynolds number; for selected cases. A total of 15 cases

DISTRIBUTION A: Distribution approved for public release.

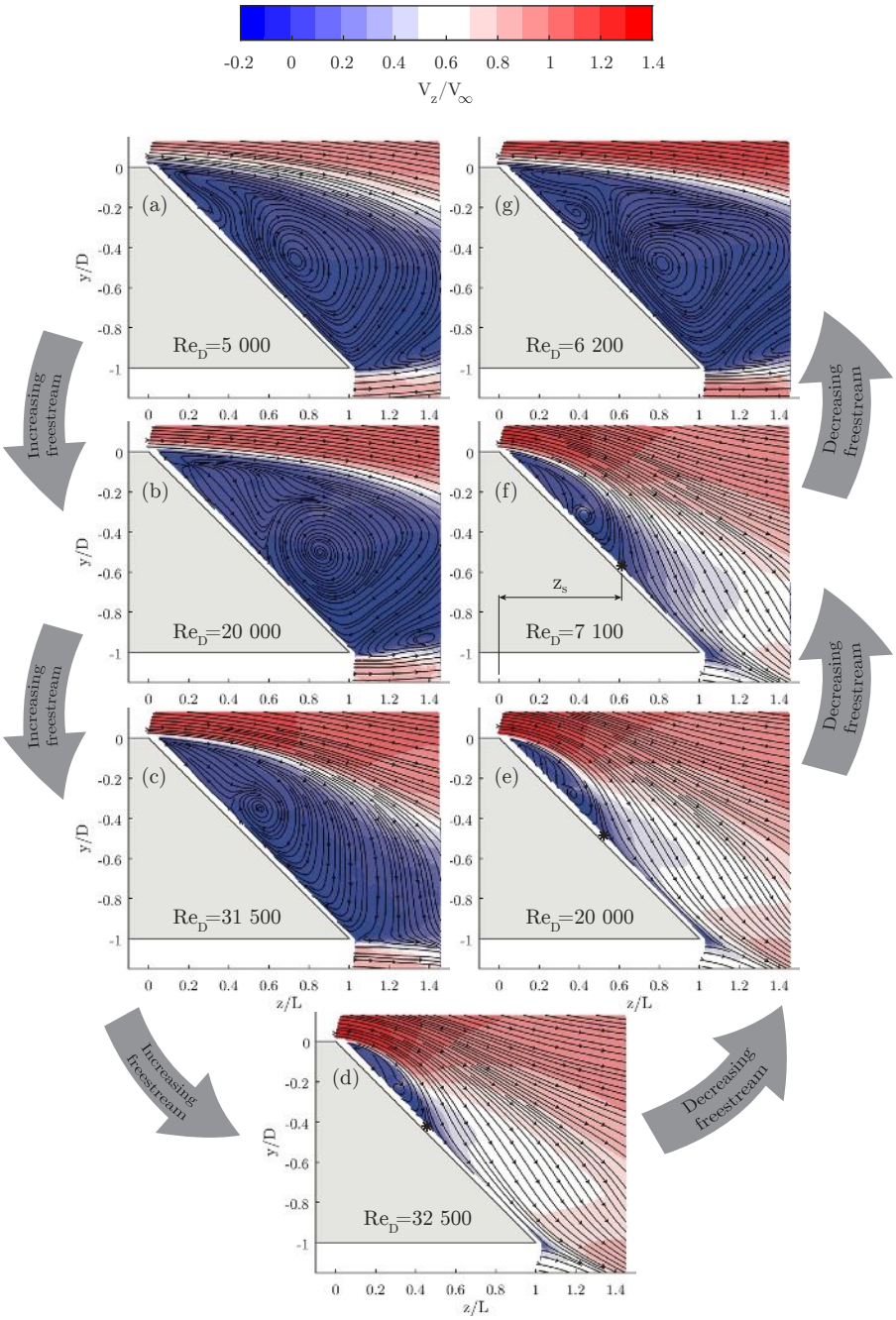


Figure 40: Mean flow fields from 500 planar PIV snapshots captured at the streamwise center plane ($x/D = 0$) as a function of Reynolds number around the stall hysteresis zone for $\phi = 45°$. Free stream velocity slowly changed between states. From (a) to (d) the Reynolds number is increased until the stalled regime at (c) transitions to a vortex pair regime (d), inferred by the presence of a closed separation bubble. Vortex regime persists as Re_D is decreased (e and f) until transition back to stalled regime occurs (g). Sequence also provided in Movie 2 with all cases examined

DISTRIBUTION A: Distribution approved for public release.

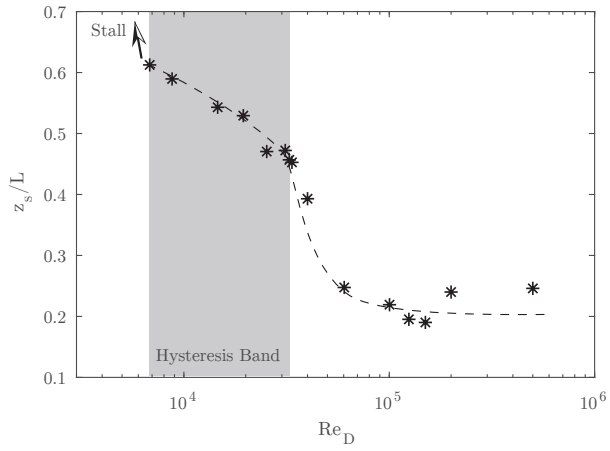


Figure 41: Observed position of the reattachment point as a function of Re_D for $\phi = 45°$ when the vortex regime is present. Reattachment point z coordinate (z_s) obtained from mean PIV fields by locating the point where the surface velocity $V_s = 0$

were acquired, and are provided in the Supplementary Material (Movie 2), showing more intermediary steps between the cases. The flow displays an open separation bubble at its wake with a very similar topology to the stalled regime presented in figure 39 (b) for a wide range of low Reynolds numbers (between figure 40 (a) and (c)). The flow features within the open separation bubble evolve as the stalled wake becomes more energized with increasing Reynolds number. Between figure 40 (c) and (d), however, a small change in Reynolds number from $Re_D = 31500$ to $Re_D = 32500$ causes a major change in the flow topology as the open separation bubble closes. The Reynolds number where this transition occurred was consistent across multiple experiments, even after disassembly and posterior re-assembly of the model in the wind tunnel.

The transitioned flow in figure 40 (d) displays a closed separation bubble, which corresponds to the formation of the vortex regime as described by Zigunov, Sellappan, et al. (2020a). The separation bubble - and by extension the vortex pair - persists when decreasing the Reynolds number after the transition to the vortex regime, as shown in the progression figure 40 (d) - (f). The bubble also systematically increases in size as the free stream speed is reduced, as the trend of reattachment point location displayed in figure 41 indicates. At Reynolds numbers higher than $Re_D \approx 60000$, the separation bubble has an approximately constant size, and below this threshold the separation bubble size increases quickly. The rate of increase in the separation bubble size is reduced when the hysteresis band is reached, and by the threshold Reynolds number $Re_D = 6200$ shown in figure 40 (g) the closed separation bubble cannot be sustained anymore and the flow topology transitions to an open separation bubble - effectively "stalling" in a similar fashion an airfoil does as a function of angle of attack. This hysteresis effect was observed in the case of airfoils at low Reynolds numbers by many researchers (Hu, Yang, et al., 2007; Hoffmann, 1991; Li, Zhang, et al., 2018) and, in the case of the airfoils, it seems to be correlated to the dynamics of the leading-edge separation bubble and appears to be successfully described by a cusp-catastrophic model (Li, Zhang, et al., 2018).

DISTRIBUTION A: Distribution approved for public release.

It is worth noting, however, that the observed transition from the stalled regime to the vortex regime occurred at $Re_D \approx 32000$ in the experiments herein presented, which is about half of the value reported by Britcher and Alcorn (1991) ($Re_D = 60000$). Differences in the experimental conditions could have triggered the early transition in the experiments reported in the current work. Most importantly, the presence of the shrouded strut in the results herein reported - in contrast to the magnetically suspended model used by Britcher and Alcorn (1991) - is the principal difference between the setups and hence the most likely reason to have caused the earlier flow regime switching observed in this work. Other possible reasons could include boundary layer characteristics at the cylindrical section and the differences in the free stream turbulence conditions between facilities. The free stream turbulence intensity was measured specifically for this experiment at the upper transition free stream velocity of $V_\infty = 3.3$ m/s in an empty test section with a Dantec 55P11 hotwire probe and was found to be 0.17% of the free stream. The results of figure 40 were obtained without any tripping device in the cylindrical surface, however another dataset was captured with a 40-grit sandpaper ring positioned at the nose of the cylinder. The transition Reynolds number values were consistent within uncertainty between the tripped and untripped cases, in both directions, which indicates that boundary layer conditions might be a secondary effect when compared with the presence of the strut, even though the observations of Britcher and Alcorn (1991) seem to suggest that the tripped boundary layer would present the stalled wake regime for a much broader range of Reynolds numbers. Finally, it is also worth noting that Britcher and Alcorn (1991) did not observe a transition back to the wake state with decreasing free stream, possibly because their experiments were limited to Reynolds numbers greater than $Re_D = 30000$.

Given the observations noted, it is believed that the presence of the shrouded strut could have a relevant impact on the wake dynamics at the lower Reynolds numbers examined. Further experimental observations with different mounting apparatuses are crucial for a clearer understanding of the hysteresis phenomenon observed in the wake of the slanted cylinder. On the other hand, the fact that the hysteresis effect is still manifested under the non-ideal conditions presented in this experimental work is a clear indicator of its robustness and relevance.

The two possible three-dimensional flow topologies at $\phi = 45°$, $Re_D = 2.5 \times 10^4$

The Reynolds number of $Re_D = 2.5 \times 10^4$ was elected for further characterization of the flow topology with the S-SPIV technique for the slant angle of $\phi = 45°$. Figure 42 shows the two possible flow topologies that can be attained depending on the hysteretic path followed by the free stream, as described in Section 5.1.2. Striking similarities can be observed between the stalled wake at $\phi = 45°$ in figure 42(a) with the $\phi = 50°$ wake of figure 39(a), and the same flow features are observed in both flows, indicating the stalled regime attainable for $\phi = 45°$ is indeed the same flow regime presented at $\phi = 50°$. It is important to reiterate that each of the S-SPIV experiments take about 4 hours of data collection with the wind tunnel at a constant free stream speed to complete all SPIV planes, which indicates that both flow states were sufficiently stable to persist during the entirety of the experiment, corresponding to $\tau_D = tV_\infty/D > 2.5 \times 10^5$ convective times. If the flow were alternating between the two flow states during the experiments, clear discontinuities in the data would be observed.

DISTRIBUTION A: Distribution approved for public release.

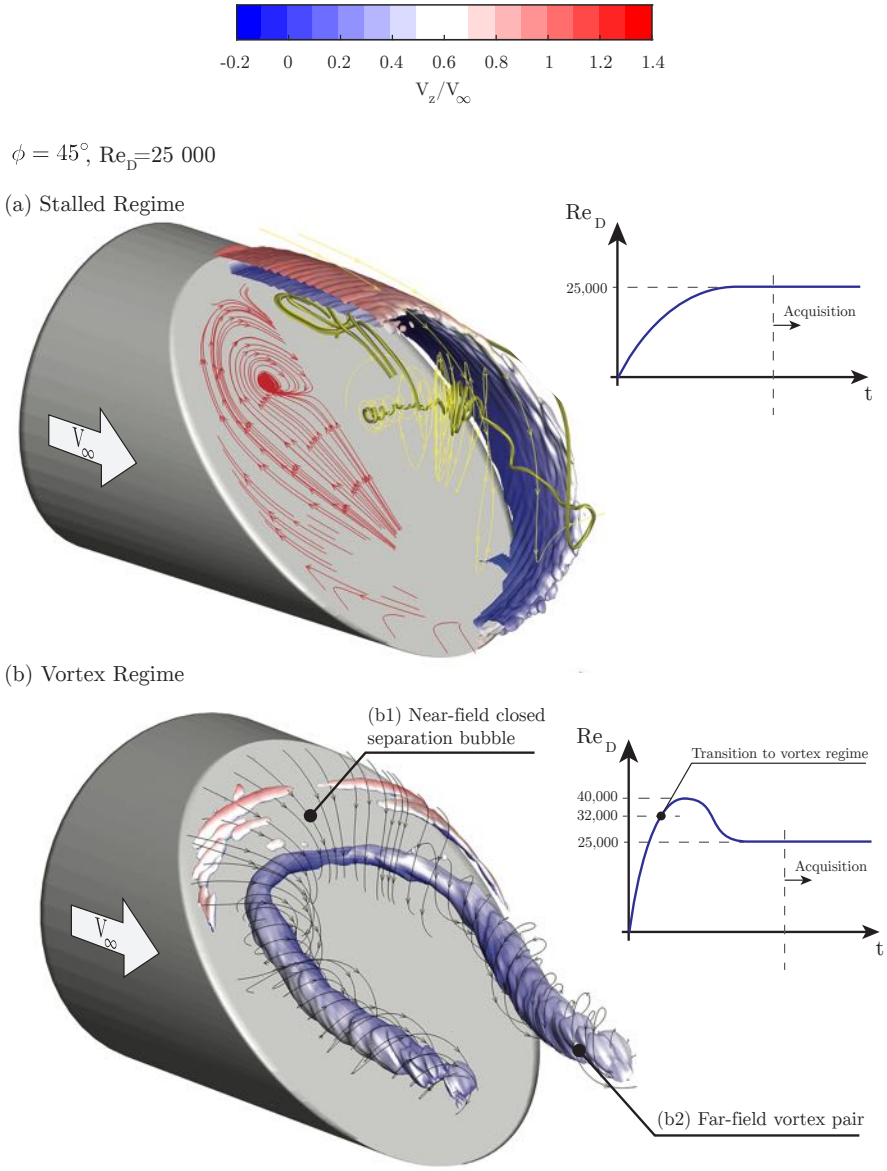


Figure 42: S-SPIV three-dimensional reconstruction of the mean wake topology for $\phi = 45°$ and $Re_D = 25000$ in the stalled regime (a) and the vortex regime (b). Representation in (a) follows the same standards and color codes described in figure 39 for qualitative comparison between the two wakes. Inset graph illustrates the free stream time history utilized to achieve each flow state. Isosurfaces in (a) of vorticity magnitude $|\vec{\omega}D/V_\infty| = 11$ colored by V_z/V_∞. Isosurfaces of Q-criterion in (b) $Q(D/V_\infty)^2 = 125$ were used to highlight the vortex pair

As indicated in the inset graph of figure 42(a), the stalled state can be obtained by slowly raising the free stream velocity of the wind tunnel until the desired Reynolds number of $Re_D = 25000$ was achieved. On the other hand, the vortex regime of figure 42(b) is attained only if the free stream velocity overshoots the transition Reynolds number identified in Section 5.1.2. The vortex

DISTRIBUTION A: Distribution approved for public release.

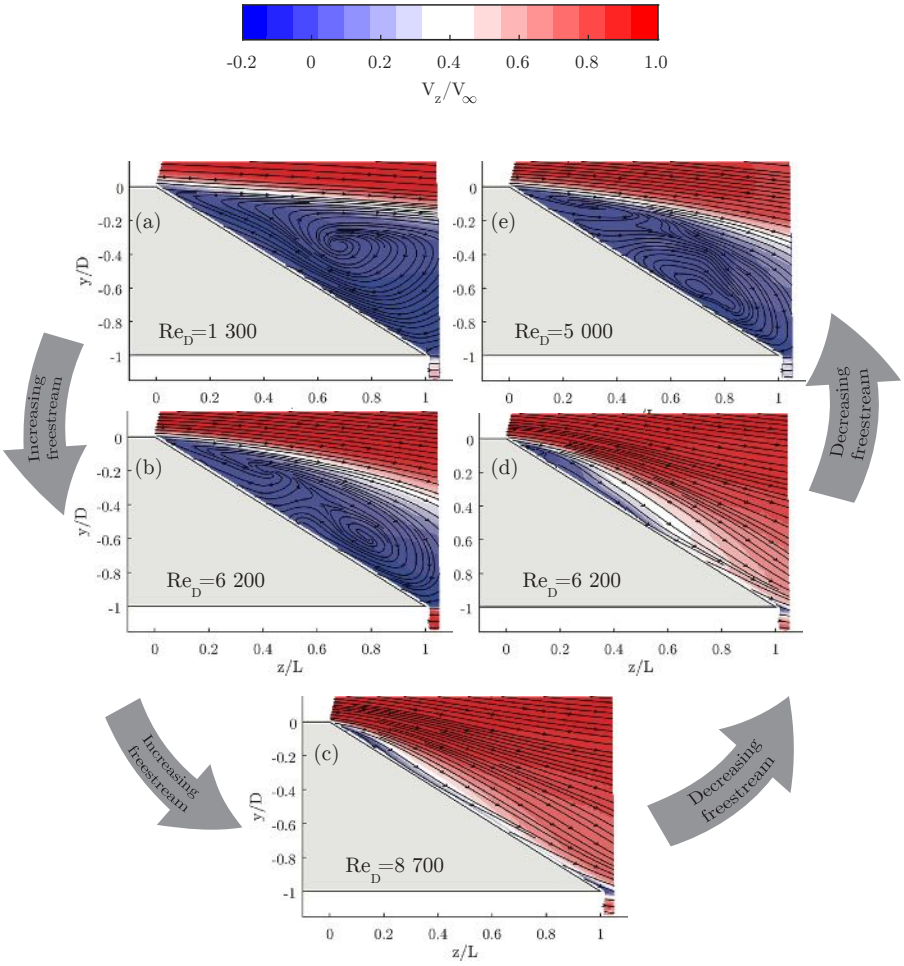


Figure 43: Mean flow fields observed from 100 planar PIV snapshots at the streamwise center plane ($x = 0$) as a function of Reynolds number around the stall hysteresis zone for $\phi = 32°$. Free stream velocity slowly changed between states. From (a) to (c) the Reynolds number is increased until the wake state at (b) transitions to a vortex pair state (c), inferred by the presence of a closed separation bubble. Vortex state persists as Re_D is decreased (d) until transition back to wake state occurs at $Re_D \approx 5000$ (e)

regime flow topology is typical of higher Reynolds numbers in this geometry and has been well described by previous researchers (Bulathsinghala, Jackson, et al., 2017; Garmann and Visbal, 2019; Zigunov, Sellappan, et al., 2020a).

Similar behavior at $\phi = 32°$

Although Morel (1980) characterized the slant angle $\phi \approx 45°$ as "transitional" due to their observations of sudden drag coefficient change as a function of slant angle for a fixed Re_D, it is reasonable to question whether this flow transition would have occurred at a different slant angle ϕ if the Reynolds number was different - especially given the evidence presented in section 5.1.2.

DISTRIBUTION A: Distribution approved for public release.

In order to explore this effect, the model slant angle was changed to $\phi = 32°$ by swapping the rear section. The facility was then started at a very low Reynolds number of $Re_D = 1300$ and planar PIV planes were captured at the center plane $x/D = 0$ following the procedure described in Section 3.1.4. Extra care was taken to ensure the flow fields were stable given the longer time scales related with the lower Reynolds numbers explored. The observed flow field at $Re_D = 1300$ was of a fully separated wake, as displayed in figure 43 (a).

Increasing the Reynolds number slowly until $Re_D = 6200$ did not trigger the transition of the flow regime, as displayed in figure 43 (b). The upper shear layer generated at the leading edge, however, was observed to approach the trailing edge with increasing Reynolds number. A similar effect is also evident at $\phi = 45°$ close to the transition Reynolds number of $Re_D = 31500$.

Increasing the Reynolds number further leads to the transition to the vortex regime, as shown in figure 43 (c). The shear layer movement towards the trailing edge in the two slant angles examined indicates that the attachment of the upper shear layer must play an important role in the establishment of the vortex flow regime by closing the recirculation zone. It is conjectured that the flow field produced by the wrapping of the vortex pair induces an extra downwash component at the center plane, which increases the stability of the now closed separation bubble in the vortex regime, possibly playing an important role in the hysteresis phenomenon observed.

It is worth noting, however, that a narrower hysteresis window was observed ($\Delta Re_D \approx 3700$) at this lower slant angle $\phi = 32°$, requiring the reduction of the Reynolds number to $Re_D = 5000$ (figure 43 (e)) to observe the stall of the wake. The narrowing of the hysteresis window with decreasing slant angle is consistent with the previously stated hypothesis, since the downwash effect caused by the vortex pair has a weaker influence upstream as the slant length is increased. This effect, combined with the lower circulation produced by the vortices in the $\phi = 32°$ case, contributes to the narrowing of the hysteresis window.

5.1.3 Proposed flow regime map for the slanted cylinder wake at zero pitch

The two data points explored so far ($\phi = 32°, 45°$) where hysteresis and stall were observed suggest that the transition Reynolds numbers should be an approximately continuous function of slant angle and that stall should occur for a reasonably wide range of slant angles at specific Reynolds numbers.

As a generalization of the previous statement, the flow regime map of figure 44 (a) is proposed to display the behaviors observed in the slanted cylinder wake for the data available in the literature, with the intent of guiding future studies on this geometry. Apart from the study from Britcher and Alcorn (1991), no other study in the survey intentionally detected the hysteresis threshold Reynolds numbers. The points collected in this study for only two slant angles suggest that the hysteresis window becomes narrower as ϕ is decreased, and therefore below a certain slant angle hysteresis as a function of Re_D should not be observed anymore. It is unclear, however, if the stall would still be observed at those lower Reynolds numbers for an arbitrarily low slant angle, which is the reason why the bottom-left part of the map is left blank in figure 44 (a). The shape of the dark-shaded hysteresis band is suggested based on the typical shape of a cusp-catastrophe - although its parameters cannot currently be estimated due to the sparsity of the data available. Therefore,

DISTRIBUTION A: Distribution approved for public release.

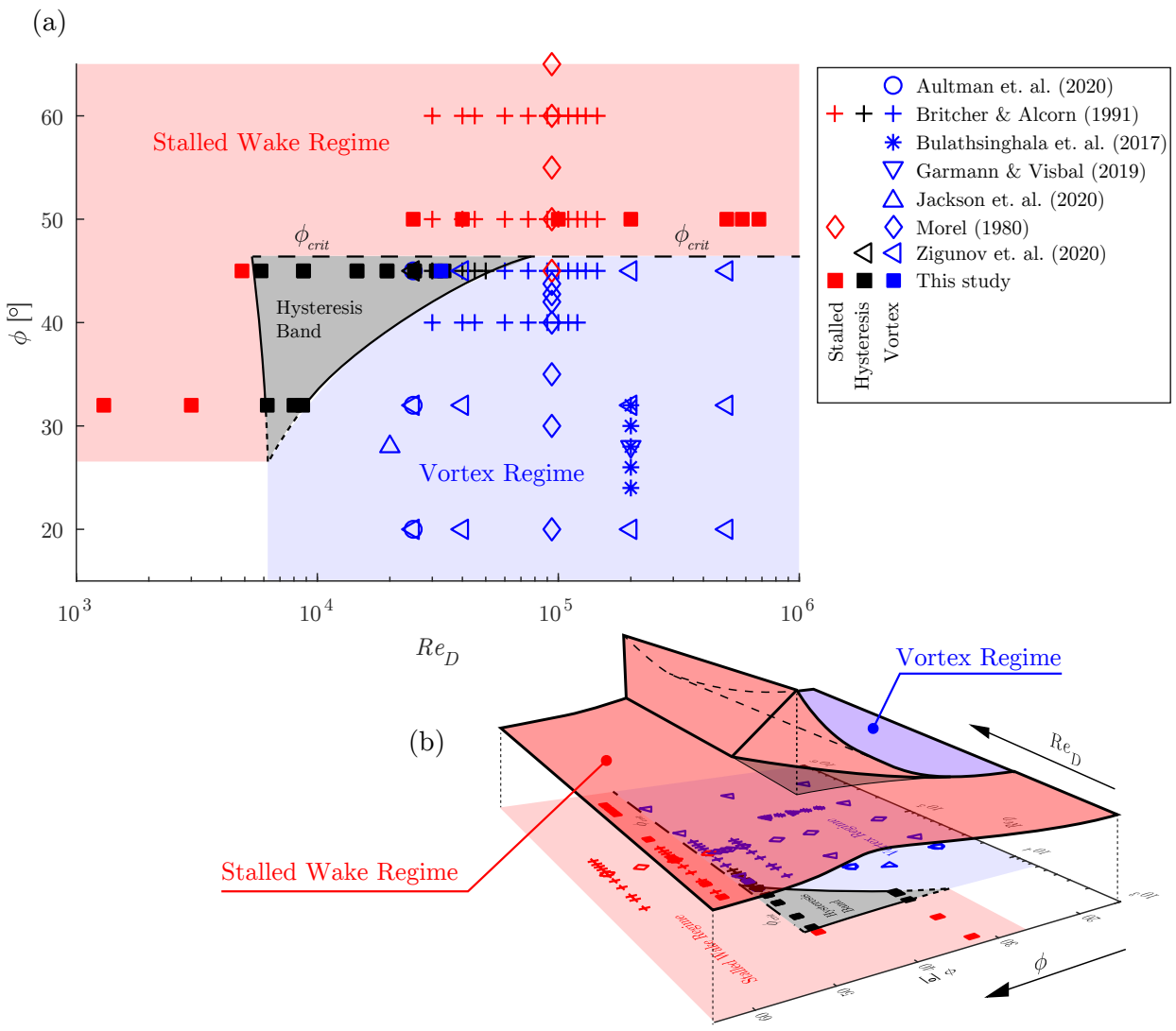


Figure 44: Flow regime map (a) based on the evidence available in the literature for the wake of the slanted cylinder afterbody. Black symbols (hysteresis) indicate both flow regimes have been observed. (b) Idealization of the proposed flow regime map as a cusp-catastrophe surface

the point where the two dashed lines meet is an extrapolation, and would require a directed study to precisely identify. This relationship with a cusp-catastrophe is more readily visualized with a surface of stable states of the dynamical system as sketched in figure 44 (b). The cusp-catastrophe shape occurs in the shaded black zone, where the surface "folds" onto itself and two distinct stable states are possible given a combination of the free parameters Re_D and ϕ. Varying Re_D, in this case, is observed to cause the catastrophic transitions at the edges of the fold.

On the upper part of figure 44 (a), it is proposed that for sufficiently large $\phi > \phi_{crit}$ the stalled wake regime would be present regardless of the Reynolds number value, which would not follow the classical cusp-catastrophe model. This suggestion is based on the observation of the red square

DISTRIBUTION A: Distribution approved for public release.

data point at $\phi = 50°$, $Re_D = 6.8 \times 10^5$, which exhibited the stalled wake flow regime at the upper limit of the facility used in the current study. The discontinuity line at ϕ_{crit} is, however, not completely understood. Morel (1980) reported different hysteresis ϕ_{crit} values for different runs, which based on the results presented in this study is possible if the free stream acceleration rate of the wind tunnel was not carefully controlled. It is also possible that there might be hysteresis effects in the ϕ direction, in which case the dashed line at ϕ_{crit} would also show a hysteresis band. Verifying this hypothesis, however, would require a model that changes its slant angle continuously during run time, which would be more feasible in a computational study.

5.1.4 Dynamic behavior of the wake in the hysteresis window

Vortex pair characteristics

A closer look at the wandering behavior of the vortex pair during the vortex regime is obtained in this section. TR-PIV was performed at a single spanwise plane ($z/D = 1.75$) with a stereoscopic PIV configuration. Vortex core tracking was performed by finding the peak of the Γ_1 quantity described by Graftieaux, Michard, et al. (2001) to reduce the data set. The trend in vortex wandering amplitude as a function of Reynolds number is displayed in Fig. 45 by examining the standard deviation of the tracked vortex core y location (y_{std}). It suggests that at Reynolds numbers greater than $Re_D > 1 \times 10^5$ the wandering amplitude is stable (about $y_{std} \approx 0.01D$). As the Reynolds number is decreased, the wandering amplitude increases rapidly, especially in the hysteresis window.

The data set shown in Fig. 45 is limited in record length ($t = 0.8$ s) due to the parametric scan nature of the experiment, which means statistics might not be converged for the lower Reynolds number values as the time scales of the phenomenon become longer. The record length corresponds to $\tau_D = 3.3$ convective times at the lowest Reynolds number ($Re_D = 6000$) acquired. Nevertheless, the trend of rapidly increasing vortex wandering amplitude is clearly observed inside the hysteresis zone with decreasing Re_D. A reasonable interpretation based on this data is that the increased wandering eventually is sufficient to disrupt the topology of the vortex-dominated wake and enable the separation bubble to open.

The vortex core statistics at this region also show interesting trends. Figure 46 (a) shows the vortex core mean radius a and the distance between the two mean core centers b as a function of Reynolds number. The core radius is defined by the second order moment of vorticity:

$$a^2 = \frac{1}{\Gamma} \int_S |\vec{x} - \vec{x}_c|^2 \omega_z dS \tag{14}$$

Where $|\vec{x} - \vec{x}_c|$ is the distance between any point in the planar domain and the tracked core. The integration domain S was the same circle where the circulation $\Gamma = \int_S \omega_z dS$ was calculated, which was expanded around the core until convergence of $\pm 2\%$ was attained. As observed in figure 46 (a), the core radius increases with decreasing Reynolds number. The core radius becomes ≈60% larger just before stall when compared to its value at the highest Reynolds number case examined ($Re_D = 2 \times 10^5$). The distance between cores b also decreases significantly when approaching

DISTRIBUTION A: Distribution approved for public release.

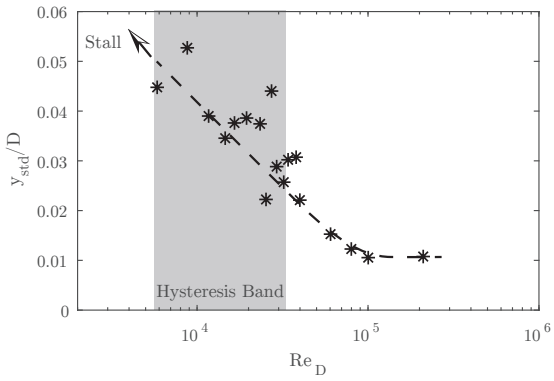


Figure 45: Vortex core wandering amplitude as measured by the core y-location standard deviation, as a function of slowly decreasing Reynolds number for $\phi = 45°$

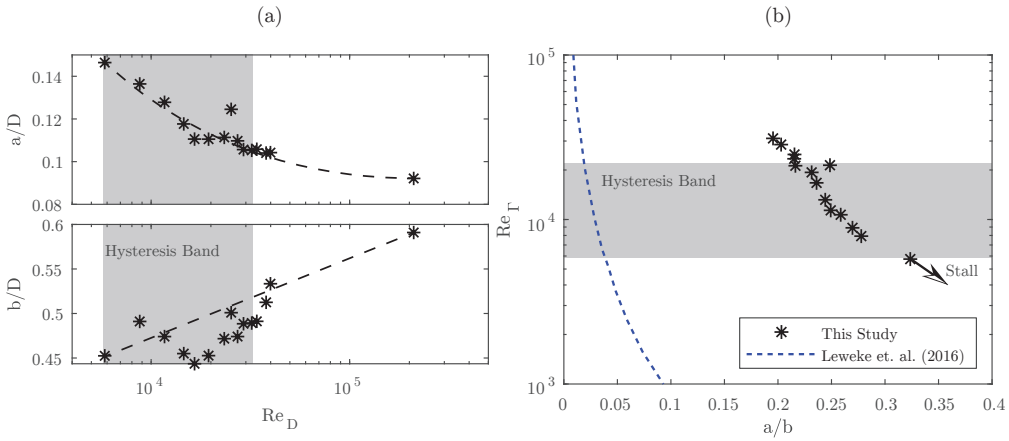


Figure 46: (a) Vortex core radius a and distance between cores b as a function of Re_D for $\phi = 45°$. (b) Ratio a/b as a function of vortex Reynolds number Re_Γ compared with the elliptic instability boundary (Leweke, Le Dizes, et al., 2016) showing the vortex pair is in the unstable regime

stall. Just before stall, the ratio a/b is very high ($a/b = 0.32$), which is probably related to the large wandering amplitude observed in figure 45. In figure 46 (b), the ratio a/b is plotted against the vortex Reynolds number $Re_\Gamma = \Gamma/\nu$ and compared to the elliptic stability boundary proposed for two long vortices (Leweke, Le Dizes, et al., 2016), showing that the vortices produced by this flow are far beyond the stability boundary.

Modal behavior of the two wake states

Further insight can be obtained through modal decomposition of the many PIV planes captured in the S-SPIV reconstructions displayed in Figure 42. For each plane captured, the Proper Orthogonal Decomposition (POD) algorithm (Berkooz, Holmes, et al., 1993) was applied to extract the most energetic modes presented by the flow field. The data matrix inputted to POD contained the three components of the velocity vectors V_x, V_y, V_z obtained at each SPIV plane. The planes were

DISTRIBUTION A: Distribution approved for public release.

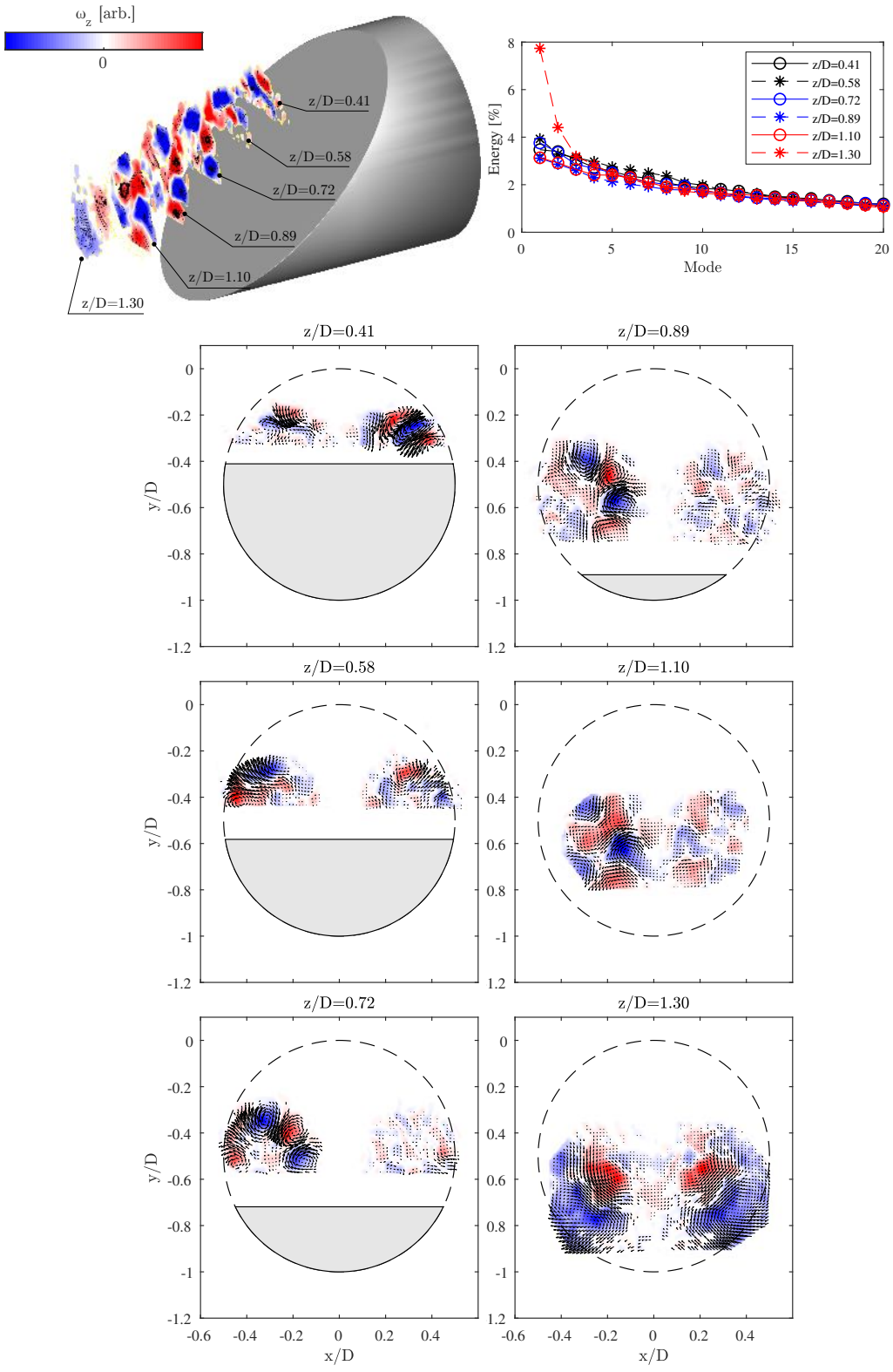


Figure 47: Most energetic POD mode at different SPIV planes for $\phi = 45°$ and $Re_D = 25000$ in the **vortex** regime. 3D view only showing left vortex for clarity.

DISTRIBUTION A: Distribution approved for public release.

analyzed separately, since there was no synchronization of data acquisition across planes.

Figure 47 shows the first mode of these spanwise slices at several planes for the vortex state of this wake. Cell blanking was used in the three-dimensional view for $x > 0$ and low ω_z values to avoid occlusion. The slices are plotted as vector fields colored by ω_z in a symmetric red-white-blue color map, to clarify the position of the coherent structures highlighted by POD. These coherent structures present a consistent mode shape across independently analyzed planes, indicating some of the spatial coherence in the streamwise direction can also be inferred from this data set. Between $z/D = 0.41$ and $z/D = 0.89$, coherent structures that are likely produced by the shear layer at the sides of the cylinder appear to join the main vortex as satellite vorticity pockets that orbit the vortex core. This is further confirmed by modes 2-4 of this data set (shown in Figure 48), which show structures with the approximately the same spatial wavelength and a phase shift or symmetry across the center plane, and by the more widespread modal energy distribution between 3% and 4% for these first modes. A change in modal behavior occurs about $z/D = 1.10$, where the principal mode switches to a helical mode of the vortex, with azimuthal wavenumber $m = 2$. This azimuthal wavenumber is lower than what would be expected from the spacing of the coherent structures at $z/D = 0.89$ (either $m = 3$ or $m = 4$). The azimuthal wavenumber of the principal POD mode is further reduced to $m = 1$ at $z/D = 1.30$, which has already been observed in the past by others (Bulathsinghala, Jackson, et al., 2017) closer to the trailing edge of the model. The presence of the vorticity pocket train was also observed in some downstream stations in the work of Bulathsinghala, Jackson, et al. (2017), however the connection with the shear layer produced at the edge of the slanted surface was not considered. The more detailed evidence of this data set suggests that, at least within the slanted surface extent, the structures produced by the shear layer are the ones that wrap around the vortex core and cause the vortex to wander. It is reasonable to assume that the wandering of the vortex pair observed in the far field, fundamentally related to the $m = 1$ mode, is likely to be related to a non-linear interaction of these shear layer structures.

In the stalled regime, however, the dynamics that POD captures in its most energetic modes are different. As shown in Fig. 49, the more upstream planes show a most energetic mode with coherent structures also related to the shear layer that forms at the edge where the slanted surface and the cylindrical section connect, however these coherent structures maintain themselves confined to a shallow region. These structures present a spanwise oscillation that is observed as pockets of opposite vorticity sign, suggesting waves like the Kelvin-Helmhotz instability develop a three-dimensional oscillation, perhaps due to the variation in the streamwise starting location of the shear layers in this flow. On the most downstream sections $z/D \geq 1.16$, a single pair of opposite polarity vorticity pockets are observed, in contrast with the vortex mode - where two pairs are observed. Examination of the vector fields of the first POD modes suggests these energetic modes are related to the shear layer produced closer to the trailing edge of the slanted surface and are similar to the mode shapes encountered in bluff body wakes where wake shedding occurs (Pavia, Varney, et al., 2019).

It is also worth noting that the modal energy content observed in the vortex regime of Figure 47 stays constant in the most upstream stations until the vortex pair is free to interact. This is in stark contrast with the stalled regime (Figure 49), where the energy content of the more energetic modes

DISTRIBUTION A: Distribution approved for public release.

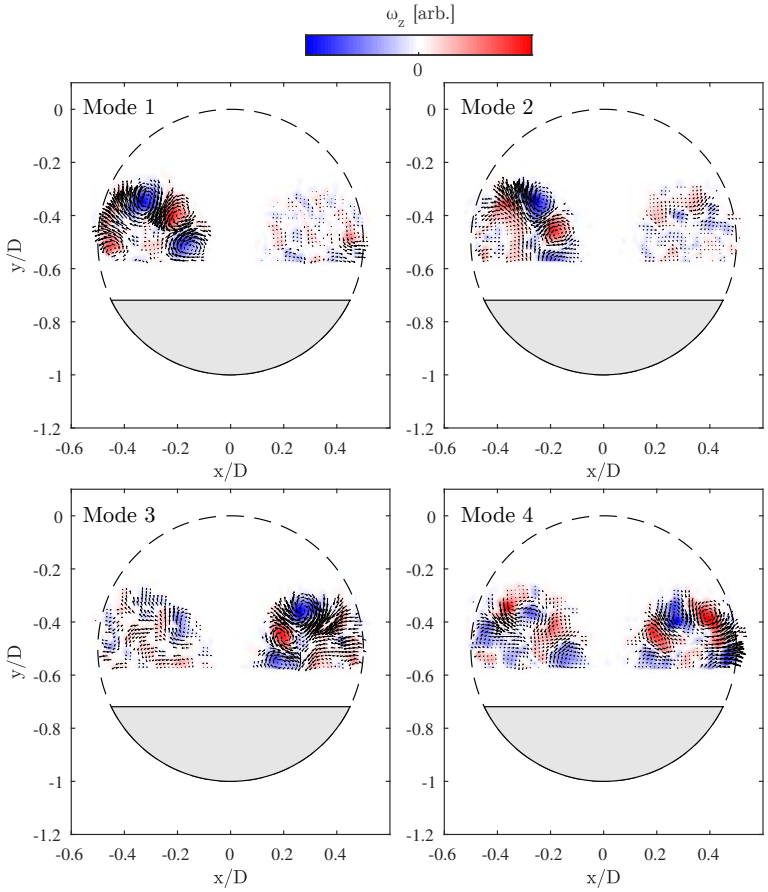


Figure 48: Most energetic 4 POD modes at $z/D = 0.72$ for $\phi = 45°$ and $Re_D = 25000$ in the vortex regime show symmetry pair and convective pairs for the same kind of shear layer structure. Other planes between $0.41 < z/D < 0.89$ show similar pairs.

starts very high ($\sim$10%) at the most upstream stations and goes down to about 3% as it approaches the trailing edge. At the more downstream planes, however, the most energetic mode suddenly increases again in energy content ($\sim$8%), due to the strong shedding produced by the trailing edge shear layer. This indicates the stalled state is much richer and more widespread in modal content near the slanted surface. It is likely, however, that a three-dimensional analysis of the modal content of this flow, performed with fully three-dimensional flow data, would highlight modes related to the bluff body wake shedding similar to the modes shown for $z/D \geq 1.16$ in Figure 49. This strong shedding of the bluff body wake is possibly related to the eventual reattachment of the separation bubble and transition to the vortex regime, as will be further explored in Section 5.1.4.

Transient behavior at wake state transition

Thus far, the present study presented compelling evidence of the wake stall hysteresis. Most of the analysis presented relied on time-averaged quantities and statistics. However, time-resolved, high speed PIV (TR-PIV) can be employed to improve the understanding of this phenomenon by

DISTRIBUTION A: Distribution approved for public release.

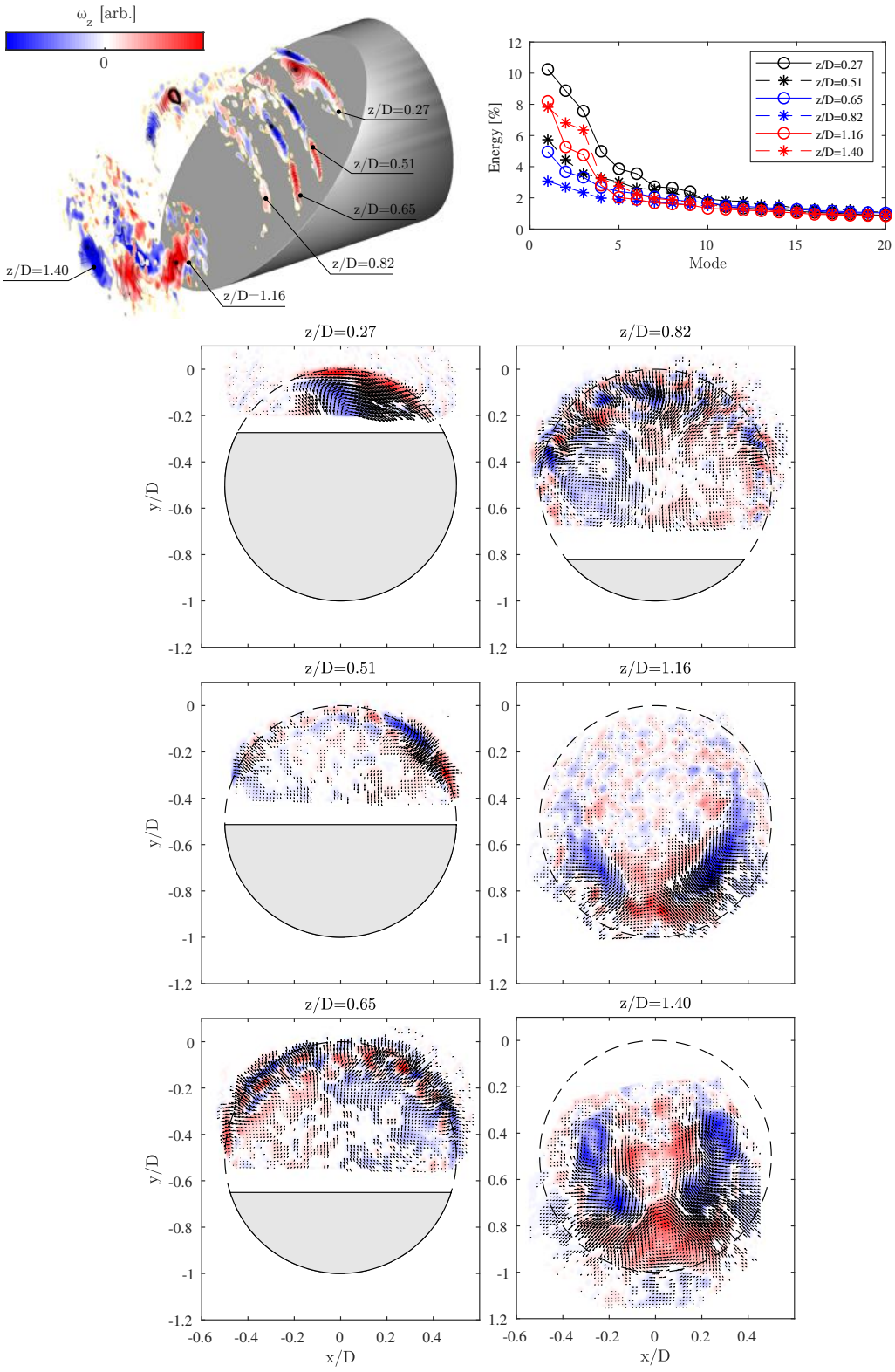


Figure 49: Most energetic POD mode at different SPIV planes for $\phi = 45°$ and $Re_D = 25000$ in the **wake** regime.

DISTRIBUTION A: Distribution approved for public release.

observing the transient behavior in this flow field as the transition occurs. This section will discuss observations of the transition transients in both directions (i.e., from the stalled regime to the vortex regime and vice-versa).

Transition from stalled state to vortex pair state

Starting with the wake regime for $\phi = 45^{\circ}$, the wind tunnel was slowly accelerated until the approximate Reynolds number where transition was about to be observed ($Re_D \approx 30000$). A 5 second long, 5 kHz TR-PIV capture at the center plane ($x/D = 0$) was started and the free stream velocity was slightly increased. The acceleration was measured from the PIV snapshots at a location far from the model to be about $dV_\infty/dt = 0.03$ m/s^2. The flow, as expected, transitioned to the vortex regime and, as seen from the PIV plane, an attachment of the separation bubble was observed.

Figure 50 presents the key snapshots that summarize the observations of this transient experiment. The time was normalized by the convective time ($\tau_D = tV_\infty/D$) and the reference time $\tau_D = 0$ was defined as the moment when the low-pass filtered velocity measured at a PIV probe location close to the trailing edge (shown as "p" in figure 50 (f) and plotted in figure 50 (g), blue trace) became positive and the transient behavior started. This criterion appears to have captured the onset of the transient behavior. The low-pass cutoff frequency of the 4$^{\text{th}}$ order digital Butterworth filter was chosen to be $St_{cutoff} = 0.25$, primarily seeking to eliminate correlation noise.

The first snapshot in figure 50 (a) shows a representative flow field before the transition, showing the instantaneous stalled wake flow topology. The spatial growth of the shear layer instability at the center plane is observed as it moves downstream, producing a large scale mixing zone very close to the trailing edge of the slanted surface. At the onset of transition in figure 50 (b), it was observed that the trailing edge z velocity component becomes slightly more positive ($V_z/V_\infty > 0.1$) than the historical values. Given the limitations in PIV measurements due to the reflections produced by the laser sheet on the surface, it is very likely that one of the requirements for transition of this wake is that the streamwise velocity near the trailing edge surface must be positive.

Further observation of the raw PIV time series at the trailing edge of the model indicates the presence of an increasingly fast, clockwise rotating vortical structure just prior to reattachment. This structure is of a length scale that is of the order of the correlation window size used to obtain the vector fields, and unfortunately cannot be observed successfully through PIV vector field processing but is visible to the naked eye. This structure is sketched in figure 50 (b) in the inset detail, and is observed to shed from the trailing edge just prior to the start of the reattachment process, about $\tau_D = 8.6$.

The progression shown in Fig. 50 (c)-(e) shows the catastrophic event that follows the "attachment" of the shear layer observed in Fig. 50 (b). The flow regime observed in Fig. 50 (b) appears to be the incipient point which triggers a cascade of rapid flow evolution after attachment of the upper shear layer, resulting in the closure of the separation bubble followed by a rapid shrinking in the bubble size. In about 15 convective times, the separation bubble size stabilizes to the condition shown in Fig. 50 (f). The full extent of the catastrophic transition took about 30 convective times, as is evidenced by the blue time trace in Fig. 50 (g). The plot in Fig. 50 (g) also shows the free

DISTRIBUTION A: Distribution approved for public release.

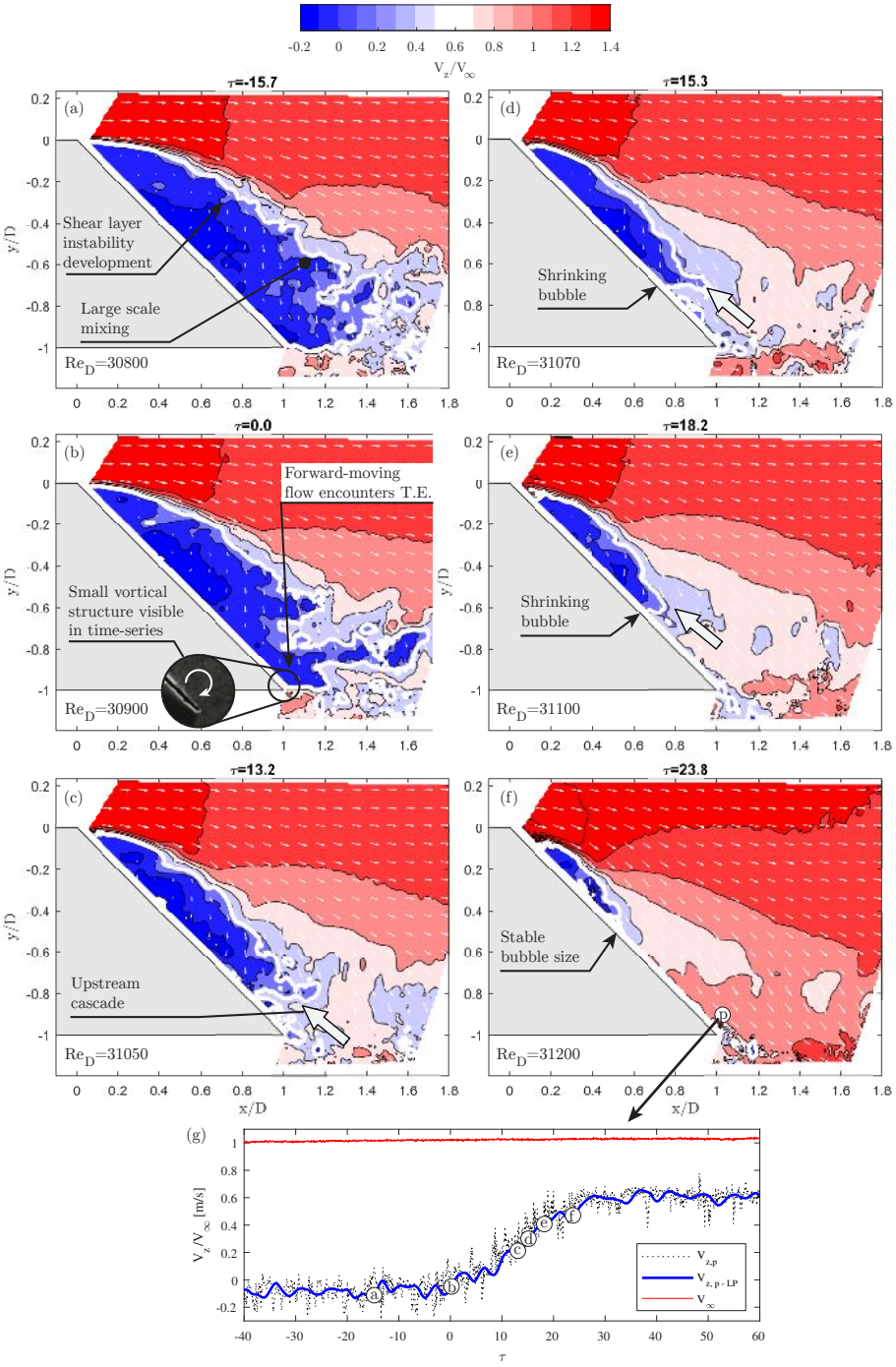


Figure 50: Transient flow evolution as seen by a planar PIV plane located at the center plane ($x/D = 0$). (a) to (f) show relevant snapshots of the development of the flow. (g) shows the time trace of a velocity probe located at (p), displayed in (f). Thick white line shows a contour of $V_z/V_\infty = 0.3$ for reference.

DISTRIBUTION A: Distribution approved for public release.

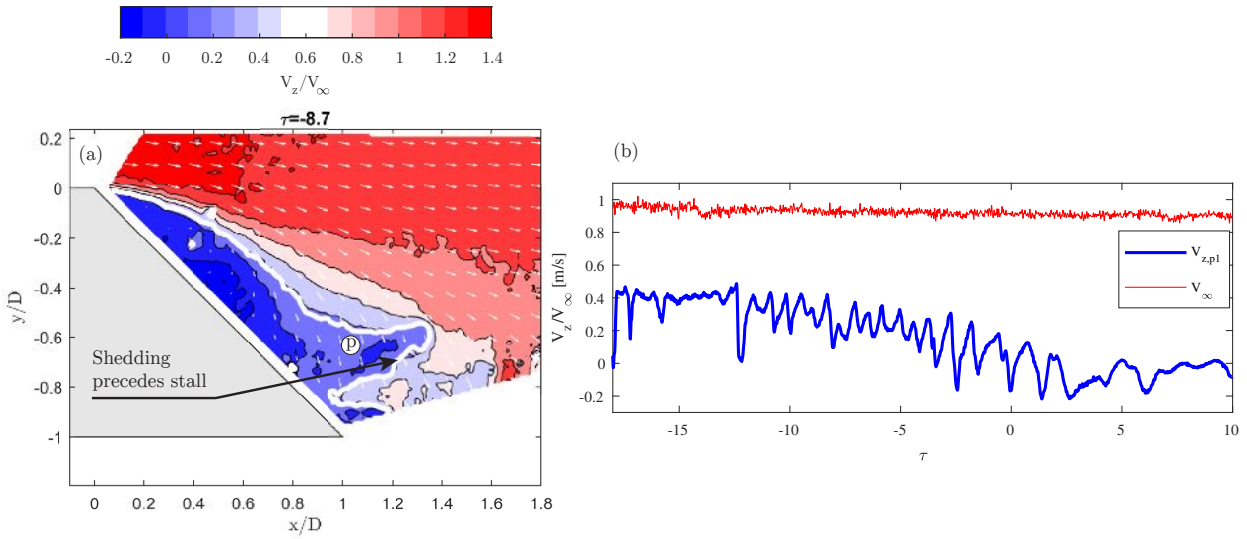


Figure 51: (a) Snapshot of the typical structure that is shed multiple times before the wake stall at $Re_D \approx 5000$. (b) Time series of V_z/V_∞ at the probe (p).

stream velocity as a red trace, which increased by $\sim 1.5\%$ during the transition.

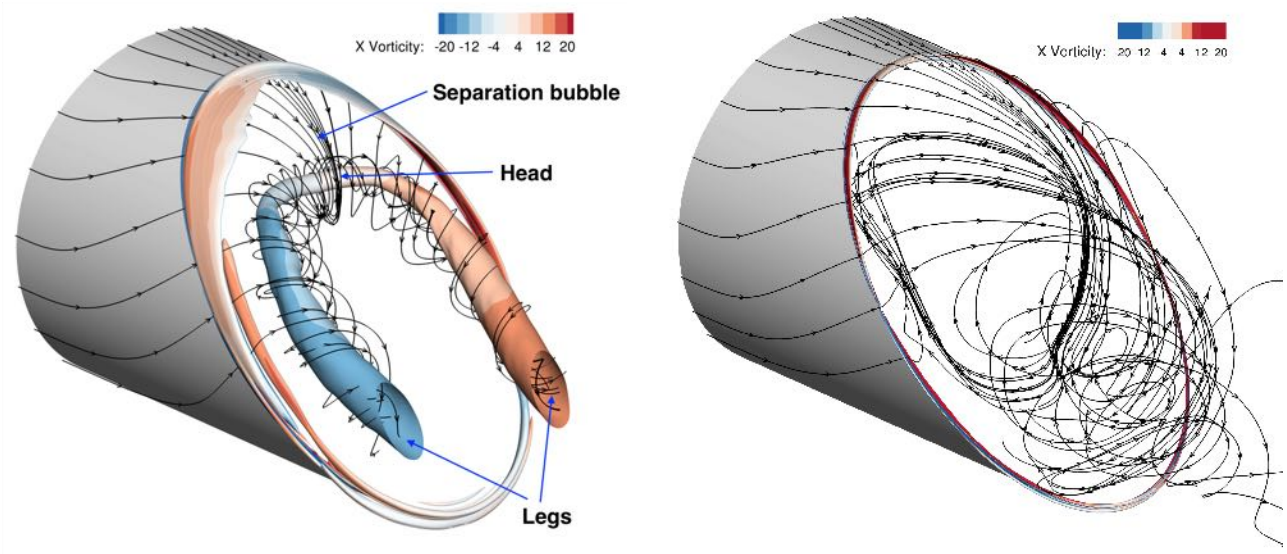
The sequence presented in Fig. 50 suggests that transition occurs when the shear layer generated at the upper leading edge successfully finds a reattachment point at the trailing edge. The boundary layer characteristics prior to separation, as well as the turbulence of the free stream, will determine the growth rate of the shear layer instability. As the shear layer becomes larger downstream, its increased entrainment makes it more likely that it will be able to close the separation bubble.

Transition from the stalled regime to the vortex pair regime

After forming the vortex pair regime, the free stream velocity was slowly reduced until just before the wake stalls at about $Re_D \approx 6000$. A 10 second long, 5 kHz TR-PIV recording at the center plane ($x/D = 0$) was started and the transition was triggered by reducing the Reynolds number to $Re_D \approx 5000$. A relevant snapshot is provided in Fig. 51 (a). The flow field initially displays a closed separation bubble region, indicative of the vortex pair regime. As time progresses, structures similar to the one depicted in Fig. 51 (a) are sequentially shed, with increasing amplitude. The shedding period before stall is about $\tau_{shed} \approx 0.7\tau_D$, rapidly increasing to $\tau_{shed} \approx 1.4\tau_D$ when the last event occurs. The original shedding period, $\tau_{shed} \approx 0.7\tau_D$, is consistent with the observed vortex wandering frequency for this model at many other Reynolds numbers (Zigunov, Sellappan, et al., 2020c) including a case in the hysteresis region ($Re_D = 25000$), suggesting the shedding of these structures is related to the vortex interaction. The time series of the raw PIV images, provided in Movie 4, indicate these bursts are out-of-plane motion, which could be related to the x direction wandering of the vortex pair.

The causes of the transition at this particular Reynolds number are not clear from the exami-

DISTRIBUTION A: Distribution approved for public release.



(a) Streamwise vortex wake

(b) Turbulent wake closure

Figure 52: 'Vortex' (a) and 'wake' (b) regimes behind for $\phi = 45°$, $Re = 25,000$. The vortical structures are shown through Q-criterion at $Q = 50$ and colored with streamwise vorticity. The 'head' and 'legs' of the large horseshoe-vortex are marked. Volume streamlines near the body wrap around the streamwise vortices in the vortex regime while they do not form coherent patterns in the wake regime. Note that the model in inverted for displaying the separation region near the upstream apex.

nation of the time series captured, due to the limitations of the PIV plane utilized. However, given the larger interaction of the vortex pair described in Section 5.1.4, it is very likely that it is this interaction that culminates in the stall event.

5.2 Computational Investigation

To anchor the description, and for subsequent reference, Figure 52 displays these two mean flow patterns, as obtained in the simulations that are the focus of the study.

The 3D-separation case, Figure 52(a), is comprised of a small separation bubble near the upstream apex and two streamwise vortices. On the other hand, the quasi-axisymmetric pattern, Figure 52(b) does not display the streamwise vortices, but rather has a large closed recirculating region as in axisymmetric base flows. The two regimes, as obtained from the computations, complement those discussed earlier from experiment, and are discussed in further detail below.

Other experimental studies have confirmed and further clarified hysteretic behavior. Xia and Bearman (1983) note that "the transition between the flow regimes may be extremely sensitive to the experimental arrangement and procedure." A noteworthy study by Britcher and Alcorn (1991) performed a repeatable Reynolds number sweep to confirm the hysteresis at $Re_D = 60,000$ based on diameter D and freestream velocity U_∞, and $\phi_{cr} = 45°$. The two regimes, denoted streamwise vortex wake and turbulent wake closure, respectively, were conjectured to be linked to the change in the state of the free-shear layer developing just downstream of the base. Very recent experiments

DISTRIBUTION A: Distribution approved for public release.

by Zigunov, Sellappan, et al. (2020a) also show the existence of the two regimes ('vortex pair' and 'separated wake') at the critical angle but at relatively low Reynolds number ($Re_D = 25,000$), with properties generally similar to those described by Morel (1980). For simplicity, we adopt the terminology 'vortex' and 'wake' respectively, based on the primary characteristic feature of each regime.

In addition to strikingly different mean states, the two regimes also display very different spectral behavior. Specifically, the regular frequencies observed in the wake regime are relatively low (Xia and Bearman, 1983) but increase as the upsweep angle is decreased from $\phi = 90°$, and are similar to vortex shedding in a bluff-body wake (Grandemange, Gohlke, et al., 2013). The vortex regime on the other hand is fundamentally different; fluctuations in the aft region have higher frequencies but display weak tones (Morel, 1980; Xia and Bearman, 1983).

Another observation of practical significance is that the wake regime exhibits dramatically lower drag. For example, both Morel (1980) and Britcher and Alcorn (1991) note a drop of about 50% in the drag coefficient, C_D, in the wake regime compared to that in the vortex regime. In addition to aircraft wakes, these phenomena are also very relevant for other transportation modes such as hatchback cars(Morel, 1978; Rao, Minelli, et al., 2018) and high-speed trains(Bell, Burton, et al., 2016). The upsweep angles in the military cargo fuselage are typically in the range of $7°$ to $28°$; however the effective upsweep may be much larger during aircraft maneuvers.

The two completely different regimes obtained at the same conditions, but with different histories, thus greatly affect the fundamental fluid dynamics associated with separation patterns, turbulence development and wake vorticity dynamics. The phenomenon of hysteresis in this configuration has to date been exclusively examined through the experimental campaigns cited above. The LES performed in the present work provides the first detailed numerical analysis of the problem; the resulting spatio-temporally resolved 3D data are used to facilitate a comprehensive elucidation of the flow characteristics and potential mechanisms. In addition to the full 3D flow, the numerical solutions are employed to examine sectional streamline projections, the pressure and turbulence fields in the two regimes.

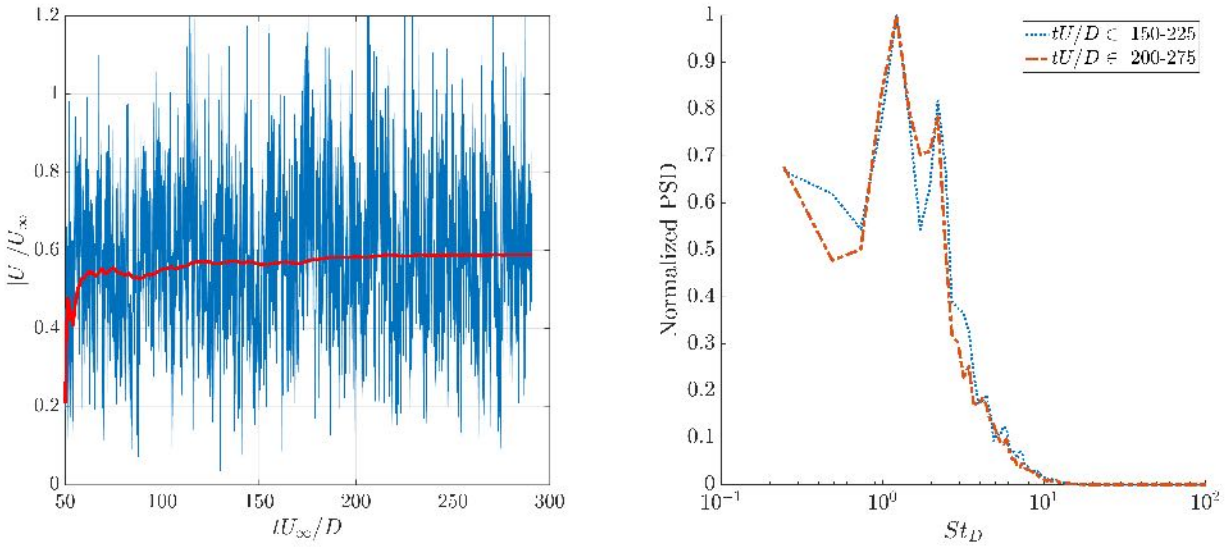
5.2.1 Hysteresis Simulation Procedure

Two different methods are used to provide confidence in the simulated hysteretic vortex and wake states at the chosen Reynolds number and critical angle. These are essentially three-dimensional counterparts of those employed by Singh and Mittal (2005) to reproduce the hysteretic behavior. The first set of simulations is motivated by the experiments of Morel (1980) and Xia and Bearman (1983), who found that for a fixed Reynolds number, lower slant angles yield the vortex regime, which transitions to the wake regime as the angle is increased. Thus, the first approach varies the angle at fixed Reynolds number ($Re_D = 25,000$) and the vortex regime is obtained by interpolating initial conditions from a lower upsweep simulation. Likewise, the wake regime is obtained by lowering the upsweep angle from a higher value, where the axisymmetric wake is the only solution. The second approach uses the observations of Britcher and Alcorn (1991) and Zigunov, Sellappan, et al. (2020a), who showed hysteresis with Reynolds number sweep. In this case therefore, starting from a vortex regime, the Reynolds number is reduced to $5,000$, where a wake regime is

DISTRIBUTION A: Distribution approved for public release.

Table 5: Computations performed in current hysteresis Study

Study	Parameter
ϕ-sweep ($Re_D = 25,000$)	$\phi \in$ [20° 32° 45° 50° 55° 90°]
Re_D-sweep ($\phi = 45°$)	$Re_D \in$ [5,000 10,000 15,000 20,000 25,000 50,000 1,00,000]



(a) (b)

Figure 53: Sample statistical stationarity results for vortex regime: (a) Time trace and sliding average at typical point probe (b) spectra of the signal at different time intervals.

observed, and then raised again gradually to obtain the desired wake state. Table 5 summarizes the different cases computed. Values in blue show conditions at which an asymptotic vortex regime is obtained, while red values indicate a wake regime. The results with both approaches yield the same statistically stationary (vortex or wake) regime.

For each state, care is taken to march the simulations for a long period of time ($> 200T_c, T_c = \frac{tU_\infty}{D}$) to ensure that the obtained state is statistically stationary. Figure 53 illustrates numerical convergence for a typical vortex case. The sliding average, Fig. 53(a) is tracked over the course of the simulation after initial transients and is seen to asymptote to a constant value. After statistical stationarity is achieved, the spectral content of the u-velocity at a representative point probe is very similar in two very different time windows (Fig. 53(b)).

Beyond this point, no evidence was observed of subsequent switching between one regime to the other or coherent asymmetry in the solution; as such, the flow did not exhibit bistability in the sense of random switching between two asymmetric states as reported for example in square-back Ahmed body type configurations (Grandemange, Gohlke, et al., 2013).

The above procedure is summarized in Fig. 54. Proceeding from the top left, the upsweep angle is increased from 20° (where the vortex regime is obtained) via 32° to 45°, constituting one of the two desired states. The properties of the vortex solution at 45° are very similar to those extensively

DISTRIBUTION A: Distribution approved for public release.

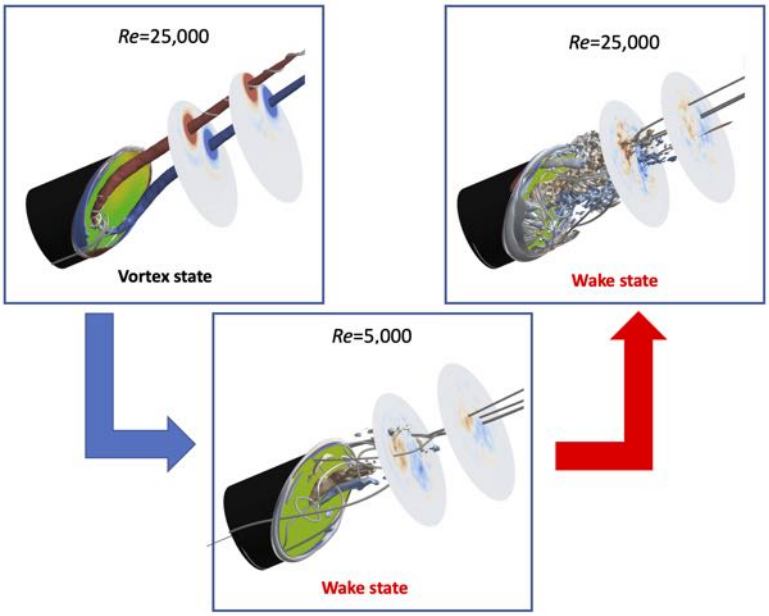


Figure 54: Afterbody flow exhibits hysteresis behavior at $45°$. Depending on the initial condition, either 'vortex' or 'wake' regime is recovered at $Re = 25,000$. Three-dimensional vortical structures are shown through Q-criterion at $Q = 5$ and colored with streamwise vorticity. Contours of streamwise vorticity at different sections in the downstream wake show the counter-rotating vortex pair in the vortex regime. Streamlines near the body indicate the separation pattern.

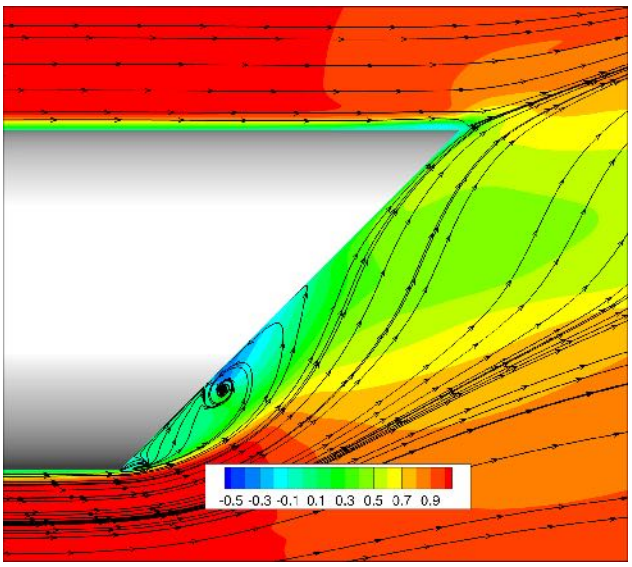
examined at lower upsweep angles (Bulathsinghala, Jackson, et al., 2017; Garmann and Visbal, 2019; Zigunov, Sellappan, et al., 2020a; Ranjan, Aultman, et al., 2020). As more clearly evident in Fig. 52(a), a small separation bubble forms near the upstream apex ($y/D = -0.5, z/D = 0.0$), with subsequent development of a vortex pair that can also be interpreted as the legs of a horseshoe-type vortex (Ranjan, Aultman, et al., 2020; Bulathsinghala, Jackson, et al., 2017; Garmann and Visbal, 2019). These eventually align with the freestream, and contain a prominent streamwise vorticity component.

The wake regime at the critical angle, obtained using two different ways, is shown in Fig. 54. One approach (from the bottom) reduces the Reynolds number of the $Re_D = 25,000$ vortex regime to $5,000$; this transitions the flow to a wake regime. When the Reynolds number is increased back to $25,000$, the flow remains in the wake regime in the asymptotic state. The other path, from the top right, obtains the same wake regime in a statistical sense, by reducing the angle from $90°$ via $55°$ and $50°$. Although not shown, starting the simulation at $45°$ from free-stream conditions everywhere leads to a wake regime; for a slanted-back Ahmed body, Conan, Anthoine, et al. (2011) found that the persistent of this state is three times more likely than the vortex regime.

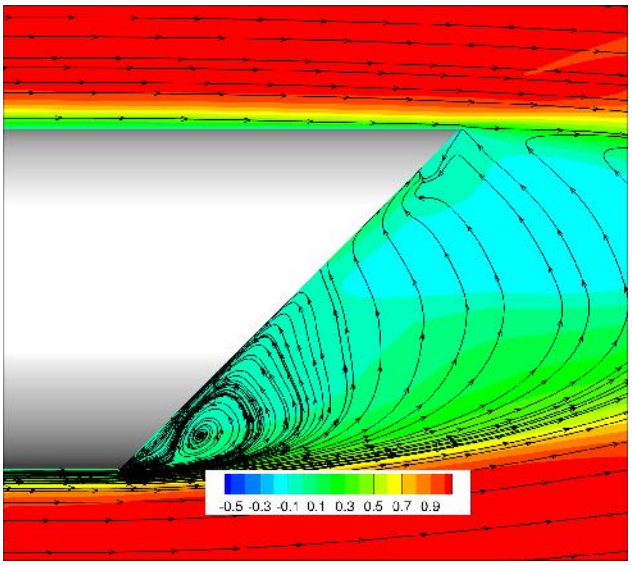
5.2.2 Kinematics of Vortex and Wake Regimes

The distinctions between vortex and wake regimes are now delineated by considering the various facets of the three-dimensional flowfield for each. Restricted symmetry plane ($z/D = 0$) stream-

DISTRIBUTION A: Distribution approved for public release.



(a) Vortex

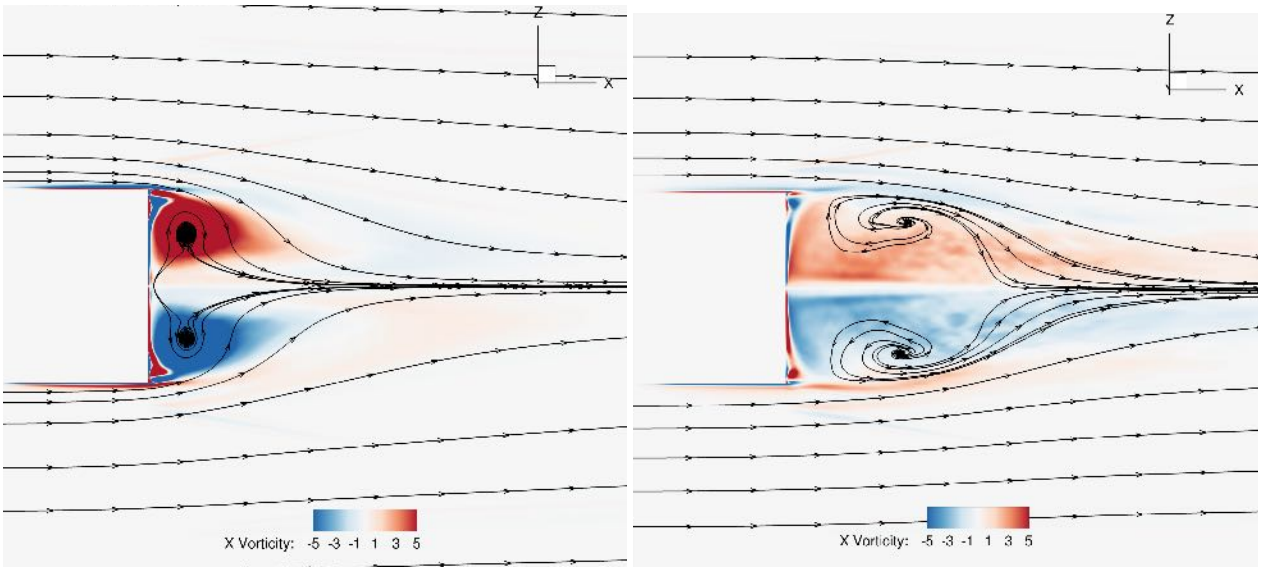


(b) Wake

Figure 55: Separation bubbles in 'vortex' and 'wake' regimes at the symmetry plane ($z = 0$). Contours of u-velocity are also shown. $\frac{u}{U_\infty} < 0.0$ represent separated flow region.

line patterns constitute an important projection of the flow, providing insights into the traces of key coherent structures. Figure 55(a) and (b) show the patterns for the two regimes, respectively. The boundary layer separates near the upstream apex for both regimes, however, the separation patterns downstream of the base are very dissimilar. Each regime displays a prominent focus, around which a "bubble" may be loosely identified. In three-dimensional flows, such a bubble is not closed; in this case, a focus is prominent, providing a mechanism for flow to leave the plane. However, the differences are easily apparent; while the bubble is relatively slender for the vortex regime, the

DISTRIBUTION A: Distribution approved for public release.



(a) Vortex (b) Wake

Figure 56: Comparison of vortex and wake regimes on xz-plane at $y/D = 0$. Contours of ω_x are shown at same levels for both the cases. Sectional streamlines are also plotted.

wake displays a much larger, rounded shape that encompasses the entire region beneath the base. The spiral associated with the vortex regime focus is relatively tightly wound, i.e., streamlines spiral more rapidly, and the focus essentially coincides with the cross-section of the head of the horseshoe vortex of Fig. 52(a). The location of this focus relative to the upstream apex depends on the upsweep angle as has been discussed in Ranjan, Aultman, et al. (2020).

The velocity magnitude is much lower in the wake regime, indicating a greater degree of stagnation (Fig. 55(b)). Similarly, the focus is further away from the surface, and restricted streamlines have a relatively more gradual trajectory towards it, with evidence of a limit cycle. On the other hand, the impingement of these streamlines on the surface near the middle of the slanted base is more orthogonal and may be related to drag considerations as below. This regime is characterized by large reversed flow bounded by the two detached shear layers from upstream and downstream apexes. In both regimes, the external flow passes over the recirculating region, being ultimately entrained in the vortex legs or constituting the wake, respectively.

The differences between vortex and wake regimes are also clearly evident in Fig. 56, which depicts streamlines restricted to the horizontal plane at the middle of the base ($y/D = 0.0$), together with streamwise vorticity. The streamlines are symmetric about the symmetry plane ($z/D = 0$), as anticipated. The penetration of the legs of the horseshoe vortex through this plane is associated with the two foci in Fig. 56(a); these regions display large coherent streamwise vorticity components, one negative and the other positive, that ultimately constitute the two streamwise vortices downstream. In contrast, the vortical region is larger in the wake case, but the organized component of vorticity is much weaker; here the streamlines bear greater similarity to those of the mean wake of a three-dimensional blunt-body(Grandemange, Gohlke, et al., 2013). Secondary and ter-

DISTRIBUTION A: Distribution approved for public release.

tiary vortices are evident near the surface – these are larger for the vortex regime and depend on the Reynolds number(Ranjan, Aultman, et al., 2020).

5.2.3 Upsweep Surface Flowfield and Drag Considerations

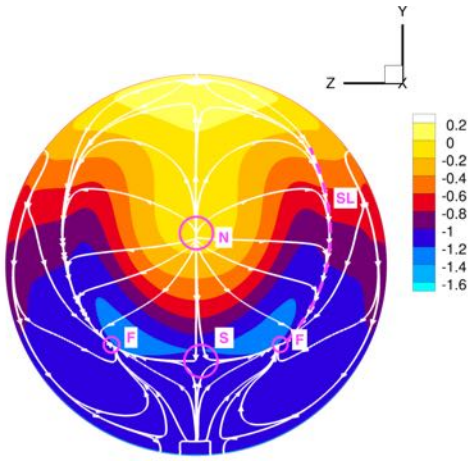
As noted in the Introduction, experimental hysteresis studies indicate that the drag is significantly lower in the wake regime(Morel, 1980; Britcher and Alcorn, 1991). The dynamics on the upsweep surface is now analyzed to examine this aspect. Fig. 57(a,b) superposes surface streamlines (effectively skin-friction lines) on each base pressure map. The streamlines display several lines of coalescence and divergence, typically indicating separation and attachment respectively, The surface pattern of the vortex regime has been extensively described in Ranjan, Aultman, et al. (2020). Streamlines are generally more upward oriented in the vortex regime, reflecting the stronger influence of the streamwise vortices. Some of the prominent features in the wake regime surface pattern, such as the presence of critical points (node **N**, two foci **F** and saddle **S**), are similar in a topological sense. This highlights difficulty in analyzing 3-D patterns from 2-D projections(Visbal, 1991). Nonetheless, key differences are evident, especially near the upstream apex, where the wake regime has a more axisymmetric surface pattern manifestation with separation lines relatively closer to the edges), and has the signature of the anticipated fully axisymmetric limit at 90° upsweep (see Fig. 54). For the vortex case, the saddle point (**S**) is farther away from the upstream apex, which corresponds to the focus in the symmetry plane streamlines (see Fig. 55) as discussed in Ranjan, Aultman, et al. (2020). The attachment lines, which are visible at low upsweep angles(Ranjan, Aultman, et al., 2020; Garmann and Visbal, 2019) are not evident in these flows, instead an unstable node (**N**) on the symmetry plane appears due to convergence of lines.

Contours of the base pressure coefficient $C_p = \dfrac{P - P_\infty}{0.5\rho_\infty U_\infty^2}$ in Figure 57 highlight the manner in which the wake regime achieves lower drag than the vortex regime. Although some key qualitative aspects of the distributions are similar to each other, significant quantitative differences are evident (necessitating the use of the different ranges in Figs. 57(a) and (b)). Specifically, C_p is always negative in the wake regime, while in the vortex case the flow achieves approximately free-stream pressure near the downstream apex ($y/D = 0.5$). Though the suction region in the vortex regime is smaller, its footprint is much stronger, *i.e.,* C_p values are much lower (minimum is -1.6) than the wake case. This very low value occurs beneath the core of the streamwise vortex near its inception ($y/D = -0.27, -0.17 < z/D < 0.17$, see Fig. 52(a)). Therefore, while the wake regime is characterized by larger but more uniform low-pressure regions, the vortex regime shows greater variations in pressure distributions on the base with localized pockets of very low pressure.

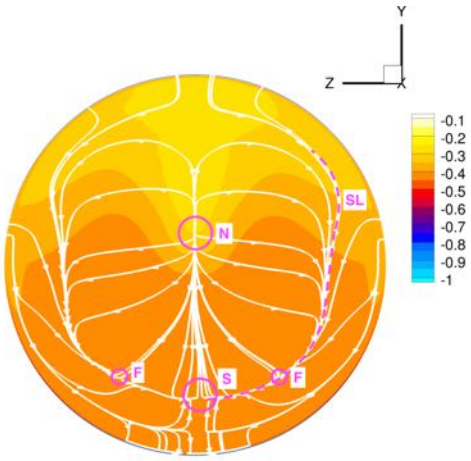
The difference in C_p between the two regimes is displayed in Fig. 57(c). Regions with positive ΔC_p are much smaller than those with negative ΔC_p. Thus, despite the earlier attachment, this disproportionate distribution of drag contribution is the direct cause for the larger drag in the vortex case. Since pressure taps are often employed in experimental measurements, a quantitative discussion of individual arrays is presented, to connect these measurements to the overall flow structure. Figure 58 compares pressure coefficients along several lines.

C_p values on the vertical line ($z/D = 0.0$) between the two apexes, Fig. 58(a), highlight the relatively uniform (flat) nature ($C_p \approx -0.4$) of the wake. In contrast, the vortex regime,

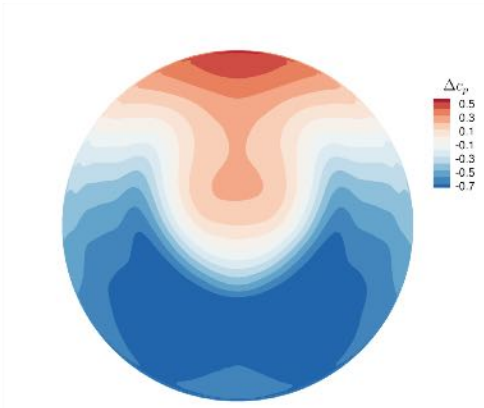
DISTRIBUTION A: Distribution approved for public release.



(a) Vortex



(b) Wake



(c) ΔC_p (vortex-wake

Figure 57: Wall pressure coefficient (C_p) in 'vortex'(a) and 'wake'(b) regimes. Difference in these, (c), shows a large region of $\Delta C_p < 0.0$ thus explaining higher drag in the vortex regime. Surface streamlines in the two regimes are also shown in (a) and (b) with several critical points marked. N-Node, S-Saddle, F-Focus, SL - Separation line.

displays a large variation from substantial suction in the footprint of the vortex head ($Cp \approx -1.2$ at $y/D = -0.21$), to about 0.2 near the upstream apex (an effective pitch down moment). The plateau in $-0.5 < y/D < -0.21$ in the vortex case corresponds to the separation bubble shown in Fig. 55(a). Comparing the C_p plots at different vertical locations ($-0.4 < y/D < 0.4$) in Figs. 58(b,e), the profiles of C_p do not vary much for the wake regime with $-0.4 \lesssim C_p \lesssim -0.3$. For this reason, Morel (1980) compared this regime with two-dimensional and axisymmetric base flows. On the other hand, the vortex regime has large variations across all vertical locations. At $y/D = -0.4$, where the flow is separated in both the regimes, profiles of both the cases are uniform across the span, but a much lower C_p is evident in the vortex case. The stark difference between base pressure in the region ($-0.5 < y < -0.28$) where flow in both regimes are separated but no inception of vortex can be explained by separation patterns shown in Fig. 55. Parezanović and

DISTRIBUTION A: Distribution approved for public release.

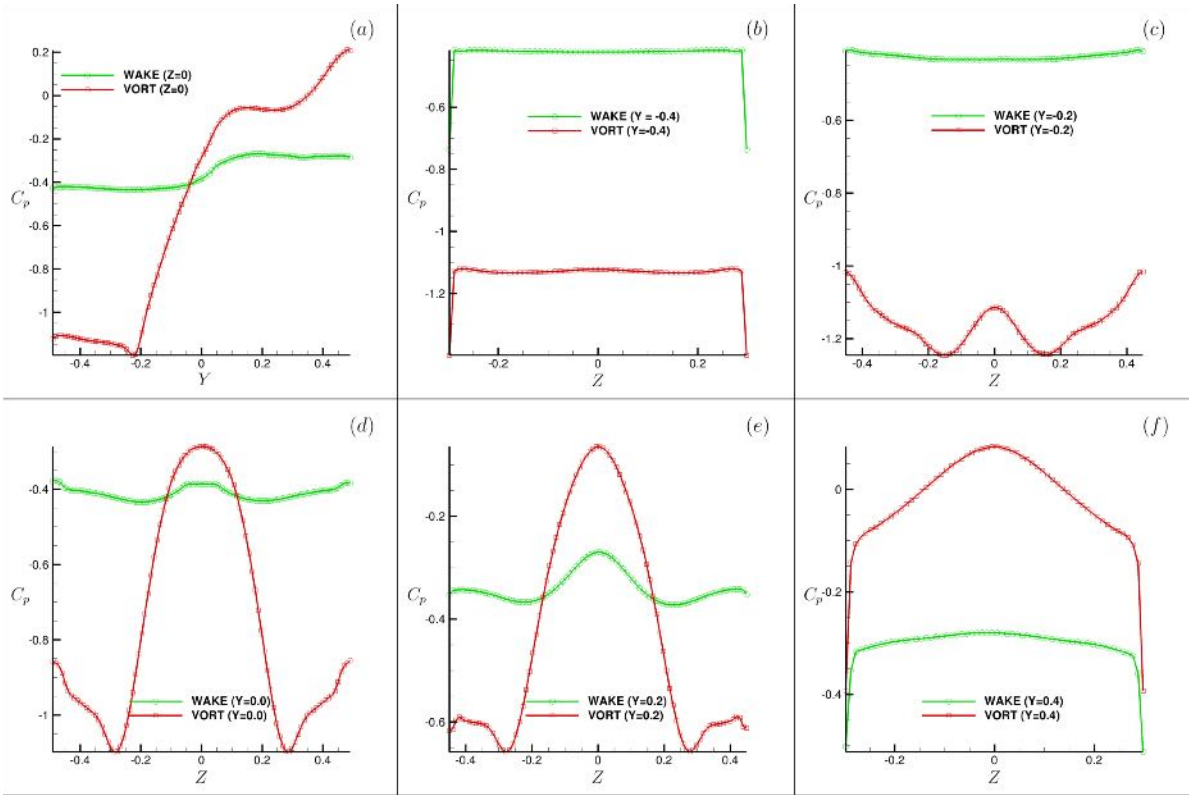


Figure 58: Wall pressure in 'vortex' and 'wake' regimes at different locations. (a) variation in the vertical direction at the symmetry plane ($Z \equiv z/D = 0.0$), (b-e) spanwise variation at locations $Y \equiv y/D = 0.0, \pm 0.2, \pm 0.4$.

Cadot (2012) have argued that the size of the separation length is a key parameter in determining the base pressure. A longer separation bubble, such as in wake regime, leads to less curvature of detached streamlines and thus higher base pressure, whereas the reverse holds in the vortex regime with a larger upward streamline deflection and higher suction.

At $y/D = -0.2$ in Fig. 58(c), the C_p profile in the vortex regime shows a drop at $z/D = \pm 0.18$; this corresponds to the pressure footprint of the cores of rolled-up streamwise vortices. As they grow along the upsweep surface, these vortices also diverge from the symmetry plane, as manifested in Fig. 58(d). Thus, the dips in C_p curves at this location ($y/D = 0.0$) are further outboard ($z/D = \pm 0.28$). The elliptic base places constraints that restrict the maximum spread of the vortex legs and therefore the spanwise locations of local pressure minima at the next horizontal cut ($y/D = 0.2$) remains unchanged. At the next location, $y/D = 0.4$, the vortices lift off the surface and no local high suction regions are observed. Slight spanwise variation of C_p in the wake regime at locations ($y/D = 0.0, 0.2$) are due to the diffused vorticity field as shown in 56(b).

An estimate the influence of the local pressure field on the drag may be made by noting that the primary effect on vehicle drag, assuming the upstream region is not influenced, is associated

DISTRIBUTION A: Distribution approved for public release.

with the differences in base pressure. The base pressure drag coefficient, C_{D_B}, is defined as:

$$C_{D_B} = \frac{\int_A (P_\infty - P)\, \mathrm{d}A}{0.5\rho_\infty u_\infty^2 A_p} \tag{15}$$

where $\mathrm{d}A$ is the component of elemental area vector parallel to the axis, and A_p is the projected area of the base. Therefore, the difference in drag coefficient due to the change in regimes is given by:

$$\Delta C_{D_B} \equiv C_{D_{BV}} - C_{D_{BW}} = -\frac{\int_A \Delta C_p \mathrm{d}A}{A_p} \tag{16}$$

where subscripts V and W correspond to vortex and wake regimes respectively. The distribution of ΔC_p is shown in Fig. 57(c). Integrating this field and normalizing based on the above expression yields a drag difference of $\Delta C_{D_B} = 0.17$. This large disparity in drag may be a concern for designers as the existence of hysteresis at $45°$ in certain Reynolds number ranges may yield potentially unanticipated drag relative to the design point. At lower angles relevant to aircraft, control techniques such as the use of splitter plates or flaps to enforce a wake-like regime may hold significant drag-reduction-associated benefits (see *e.g.,* Beaudoin and Aider (2008) and Bulathsinghala, Wang, et al. (2019)).

5.2.4 Turbulence and Spectra

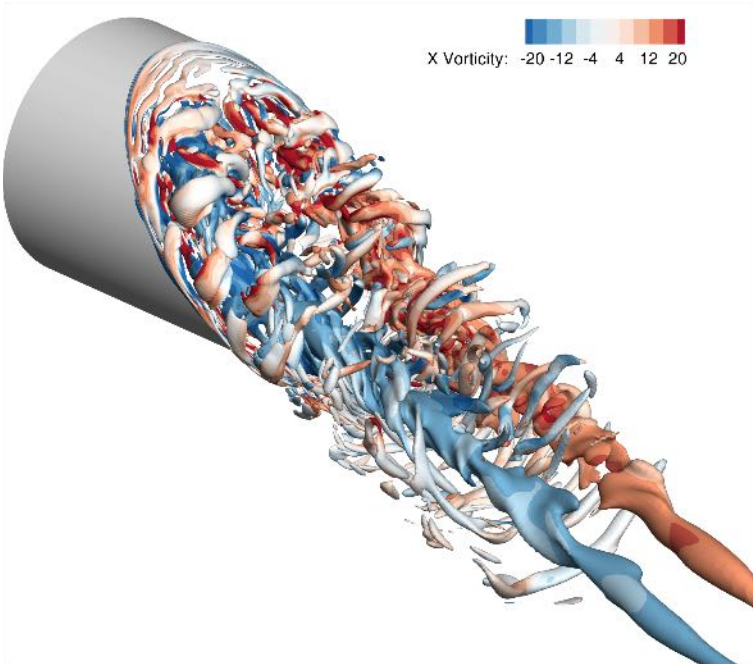
The major differences in the mean flow described above have significant consequences on the unsteadiness. For illustration, representative instantaneous flowfields are shown in Fig. 59 with Q-criterion isolevels at $Q = 50$, colored by streamwise vorticity for both regimes. The longitudinal vortex pair is clearly evident in the vortex regime, with opposing vorticity signs as in the mean. The mutual interaction of these gives rise to meandering of the vortex core in space, which has been examined in detail in Ranjan, Robinet, et al. (2020). In contrast, the wake regime displays an expected disorganized structure with vortex formation due to rollup of detached shear layers.

These differences in flow behavior manifest in the observed spectra. Raw u-velocity fluctuations from several probe points placed in the separated region are shown in Figure 60 for the two regimes. The vortex regime clearly displays visual evidence of higher frequency and amplitude content relative to the wake regime. A closer examination of time-signals suggests intermittent in-phase behavior in both the regimes.

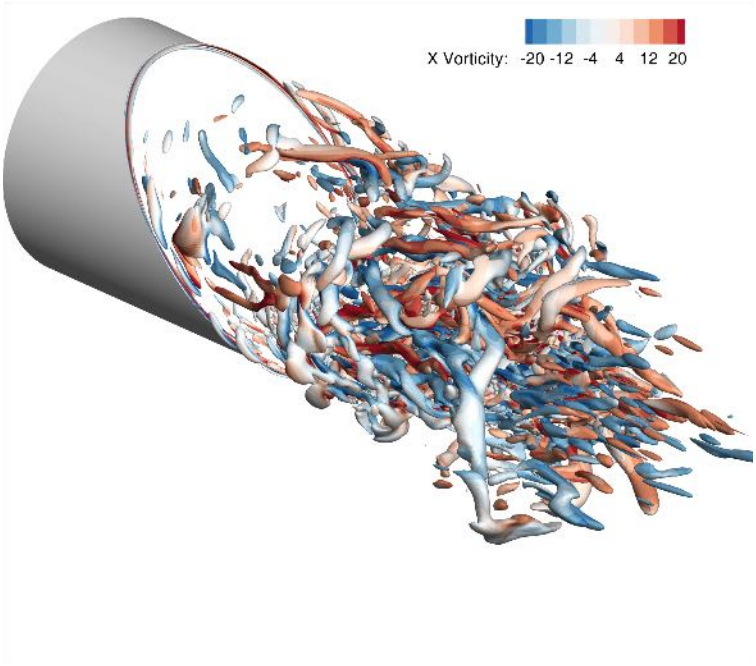
The spectral signatures of these signals are shown in Figure 61. The vortex regime is characterized by a prominent frequency at $St_D = 1.22$, which is evident in all probes. This value agrees with that reported by Morel (1980) for the vortex regime in the range $35° \geq \phi \geq 42°$. In the wake regime on the other hand, a much lower frequency is observed ($St_D = 0.1536$); this is consistent with the raw signal data of Fig. 60(b). This low-frequency unsteadiness is typical of shedding observed in bluff body wakes(Grandemange, Gohlke, et al., 2013). Harmonics of the fundamental frequency, albeit of lower amplitude, are also observed in the wake spectrum.

High amplitude fluctuations in the velocity manifest in high mean turbulence kinetic energy (TKE) in the vortex region. The TKE, defined as $k = 0.5(\overline{u'^2} + \overline{v'^2} + \overline{w'^2})$, on a plane parallel to the base at an axial distance of $\Delta x/D = 0.011$ from it, is shown in Fig. 62 for both vortex and

DISTRIBUTION A: Distribution approved for public release.



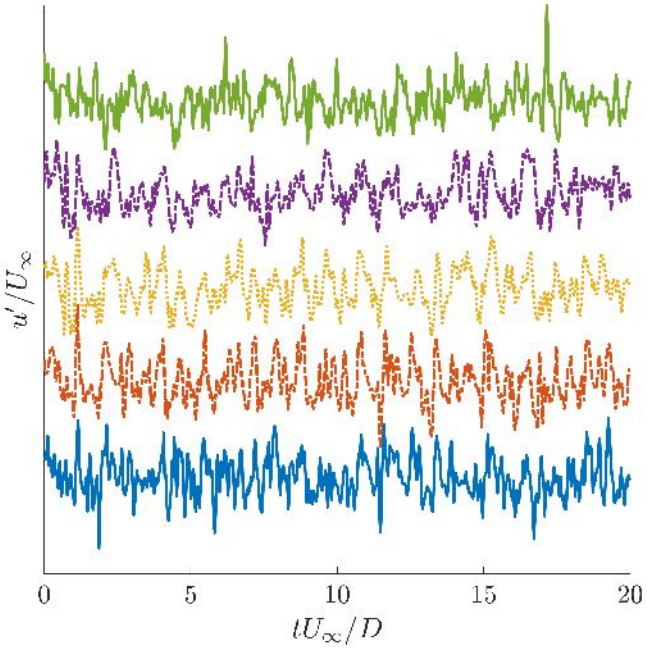
(a) Vortex



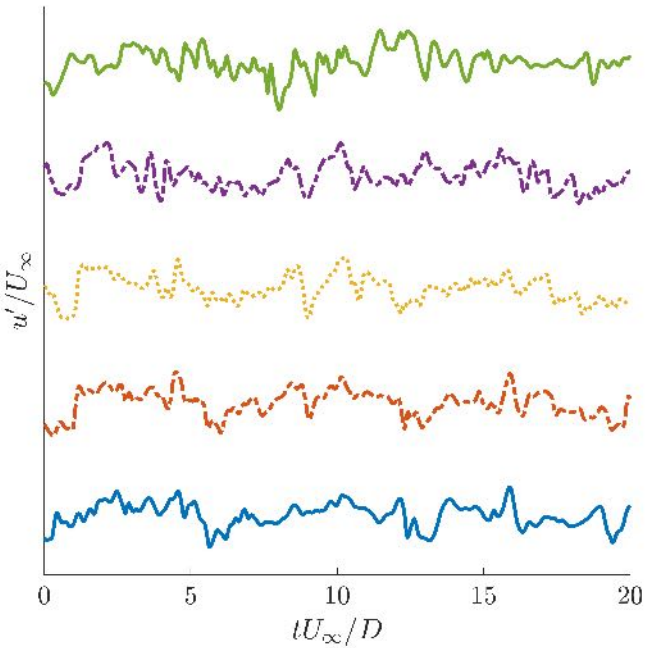
(b) Wake

Figure 59: Instantaneous snapshots in 'vortex' and 'wake' regimes shown through Q-criterion at $Q = 50$.

DISTRIBUTION A: Distribution approved for public release.



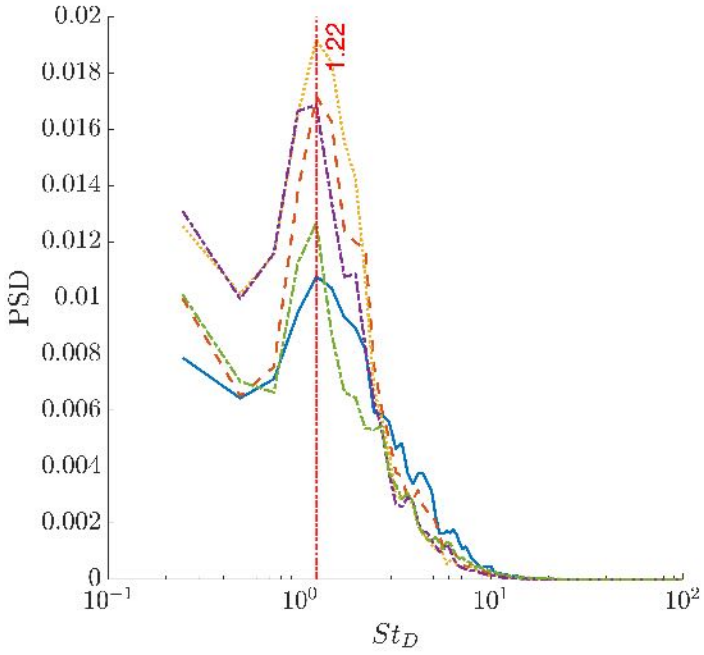
(a) Vortex



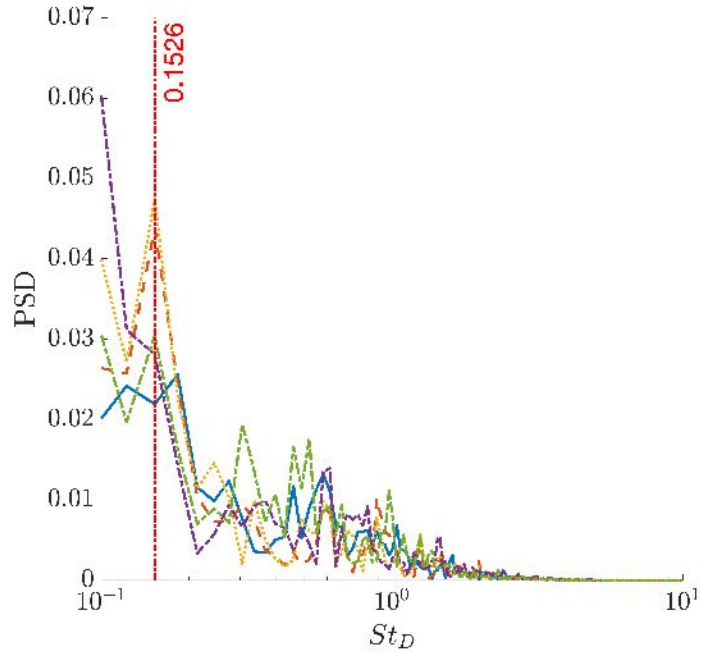
(b) Wake

Figure 60: Fluctuations in u-velocity from five point probe signals close to the base. The signals are shifted in vertical axis for displaying purpose. Time axis is shifted by 260 characteristic times.

DISTRIBUTION A: Distribution approved for public release.



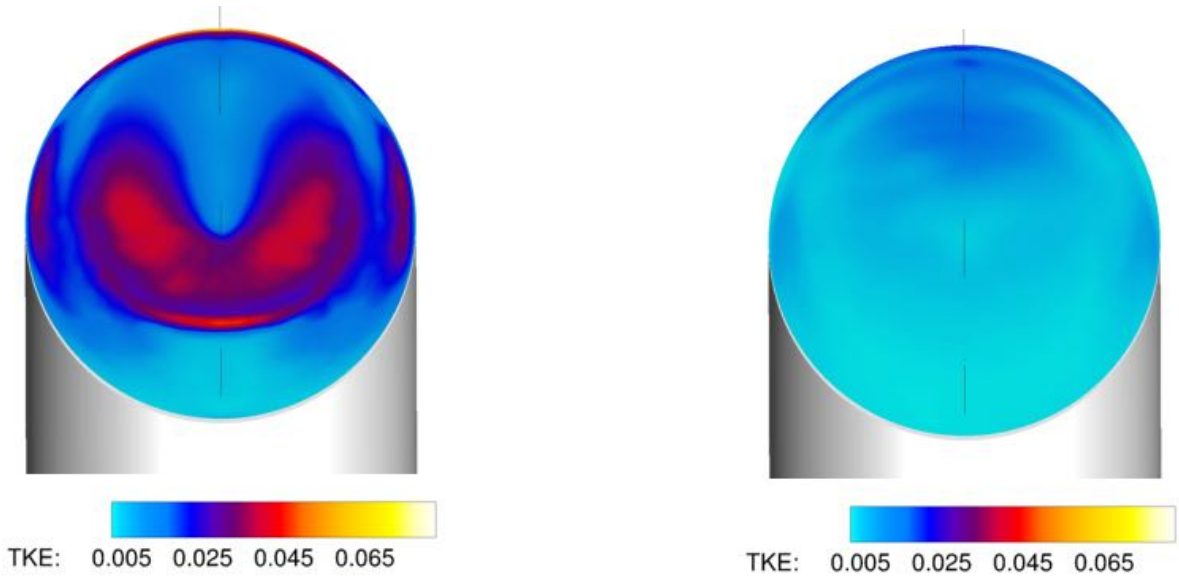
(a) Vortex



(b) Wake

Figure 61: Shedding frequency in 'vortex' and 'wake' regimes. Higher frequency of oscillations is observed in the vortex regime.

DISTRIBUTION A: Distribution approved for public release.



(a) Vortex (b) Wake

Figure 62: Turbulence kinetic energy distribution behind the base surface.

wake regimes at the same contours levels. The vortex regime exhibits a kidney-shaped structure with a very high TKE content, primarily from $\overline{v'^2}$ and $\overline{w'^2}$, in the region of the development of vortices until they move away from the surface. This higher production of turbulence indicates a larger energy contribution into the flow by the body. On the other hand, the TKE levels are an order of magnitude lower in the wake regime and are almost uniformly distributed. Therefore, the physical mechanism behind much higher drag in the vortex regime is consistent with the higher mean turbulent kinetic energy supplied into the streamwise vortices during their development.

In the context of wingtip vortices, Zeman (1995) found that vortical structures suppress the Reynolds shear stress and therefore the vortex-core growth rate is controlled only by molecular viscosity; as such, vortex turbulence decays with distance. Figure 63 shows the distribution of normal and shear stresses on the yz-plane near the vortex pair at the location $X/L = 2.0$. The normal stresses, figure 63(a-c) are symmetric about the mid-plane as expected. $\overline{v'v'}$ and $\overline{w'w'}$ are almost equal in magnitude (maximum non-dimensional value is 0.08) and considerably larger than $\overline{u'u'}$. Also, the distributions of $\overline{v'v'}$ and $\overline{w'w'}$ are elliptic in nature, with major axes oriented in the respective directions of the fluctuations. The shear stresses (figure 63(d-f)) are an order-of-magnitude smaller than the normal stresses and hence are plotted on a different scale. Reynolds shear stress mediates the extraction of energy from the mean flow by turbulence, and therefore in all the stresses, the peak is off-center due to zero turbulence production at the centerline of the vortex (Dghim, Ferchichi, et al., 2020; Zeman, 1995). The structure of in-plane shear stress, $\overline{v'w'}$, shows four lobes, similar to those obtained in Zeman (1995) for a turbulent wing tip vortex in the farfield region, using both Reynolds stress closure model as well as through experiments. The structures of correlating in- and out-plane shear stresses, $\overline{u'v'}$ and $\overline{u'w'}$ have additional noteworthy features.

DISTRIBUTION A: Distribution approved for public release.

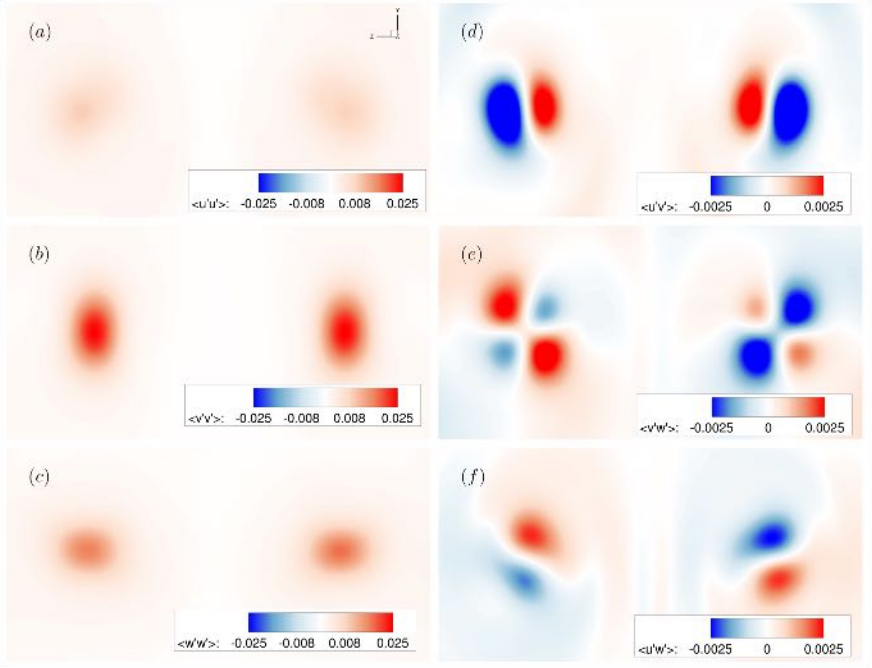


Figure 63: isolines Reynolds stresses at $X/L = 2.0$ in yz-plane. (a): $\langle u'u' \rangle$; (b): $\langle v'v' \rangle$; (c): $\langle w'w' \rangle$; (d): $\langle u'v' \rangle$; (e): $\langle v'w' \rangle$; (f): $\langle u'w' \rangle$.

These stresses indicate the strain in the field due to fluctuations in the axial velocity. Briefly, these stresses show two-lobe structures similar to $|m| = 1$ elliptic modes (Kerswell, 2002). These manifestations are associated with displacements of vortex cores as discussed later. The shear stresses are anti-symmetric with respect to the mid-plane due to the counter-rotating nature of vortices.

5.3 Summary

This portion of the research effort investigated the main flow features of the stalled regime of the slanted cylinder afterbody. A connection with the better-known vortex regime was made. A detailed examination of the topology aspects of the stalled regime and the hysteresis behavior present is this wake was provided. The phenomenon of stall hysteresis was successfully reproduced in this work with much greater detail through direct particle image velocimetry measurements and three-dimensional flow reconstructions using the S-SPIV technique. The lessons learned in this work may be useful to understand a broader class of bluff body flows that exhibit the same behavior.

The stall hysteresis was observed for $\phi = 45°$ between $6200 < Re_D < 32500$. Previously, this hysteresis phenomenon was only observed for $\phi = 45°$, however in this study evidence is also shown that stall hysteresis is present for a much lower slant angle of $\phi = 32°$ at a lower Reynolds number between $5000 < Re_D < 8700$. These two observations lead to the conclusion that stall hysteresis is an intrinsic characteristic of this wake at low Reynolds numbers at other slant angles, displaying a similar behavior to thick aerofoils at lower Reynolds numbers. A flow regime map

DISTRIBUTION A: Distribution approved for public release.

is suggested, compiling the observed flow states in this and past studies. Some regions of the flow regime map, at the lower Reynolds numbers and smaller slant angles, are still not completely understood and require further investigations to characterize.

A more careful study of the transient behavior of the wake during flow transition with time-resolved PIV reveals that the formation of the vortex pair regime is preceded by the interaction of the shear layer produced by the leading edge with the surface of the trailing edge, causing the closure of the separation region and forming a rapidly shrinking separation bubble. The stall of the wake at the lower bound of the hysteresis window, on the other hand, seems to be related to an increased interaction of the vortex pair that causes intense wandering, which might culminate in the shedding of the vortex pair prior to the wake stall.

High-fidelity simulations were also brought to bear on the problem. The three-dimensional data guides a comprehensive description of regime change, including the practical aspect of drag disparity. In this description, the two statistically stationary states, representing the "vortex" and "wake" regimes, were established at $Re_D = 25,000$ in two independent ways, using initial conditions based on sweeps of Reynolds number as well as base slant angles. The vortex regime is characterized by a large horseshoe structure with downstream oriented legs (vortex pair) while the wake regime displays turbulent wake closure. Mean sectional streamlines on the symmetry plane highlight the relatively tightly wound vortex profile in the vortex regime, but a large bulbous separation region in the wake regime. A similar analysis of a horizontal section shows the prominence of mean streamwise vorticity in the vortex regime. The base pressure distribution in the vortex regime shows large variation between the upstream and downstream apexes compared to much more uniformly distributed pressure in the wake regime, which is similar to axisymmetric base flows. This manifests in much higher base drag in the vortex case despite higher recovery. An analysis of the unsteady flow reveals highly coherent structures in the instantaneous flow of the vortex regime, as well as much higher frequencies and amplitudes of the fluctuation components. The higher drag in the vortex regime is consistent with the interpretation that the flow requires additional energy to sustain the streamwise vortices during their initial development downstream of the base. Although the $Re-$ and ϕ-sweeps both lead to the hysteresis, the simulations indicate that the sensitivity of the former variation is also influenced by the more rapid turbulent breakdown of the separating shear layer. Overall, despite the high upsweep angle, the vortex regime bears similarity to those observed in military cargo aircraft afterbodies, while the wake regime more closely resembles the bluff-body wakes in automotive applications.

A substantial reduction in the drag in the wake regime also suggests control objectives to restrict the formation of the streamwise vortex by guiding the separated streamlines away from the base to inhibit growth of the streamwise vorticity. Passive techniques such as obstructions typically employed in the wake of bluff-bodies may not be optimal. In any case, a reasonable estimate of drag reduction due to regime change may require several parameter considerations in addition to Mach and Reynolds numbers, such as upsweep angle, forebody and afterbody geometries, edge bluntness, upstream disturbances and free-stream turbulence, and ground proximity. Base edge curvature is more representative of realistic configurations; since the separation location is no longer localized at the sharp edge, the unsteadiness and hysteresis properties may change motivat-

DISTRIBUTION A: Distribution approved for public release.

ing further exploration.

6 Unsteady Vortex Motion

As noted earlier, the motions associated with vortex meandering are considerably broader than those observed specifically in the configuration of figure 21 and include, for example, wingtip (Del Pino, Lopez-Alonso, et al., 2011) and delta-wing vortices (Ma, Wang, et al., 2017). A consensus regarding underlying mechanisms in all these flows that sustain the displacement of vortex cores during meandering remains elusive. For example, some early efforts (Corsiglia, Schwind, et al., 1973) ascribe meandering phenomena in wind tunnels to the disturbance environment *i.e.,* free-stream turbulence effects in the test environment. This attribution was motivated by the fact that some experiments on wingtip vortices (Baker, Barker, et al., 1974) observed coherent side-to-side motions, similar to those associated with wandering at zero angle of attack *i.e.,* when no vortices are formed. More recent experimental efforts (Devenport, Rife, et al., 1996; Beresh, Henfling, et al., 2010) have observed that wandering amplitude increases with downstream distance, which is indicative of the possible existence of an instability mechanism.

Simplified situations with theoretical vortex models have greatly aided in developing a better understanding of the instability mechanism. Antkowiak and Brancher (2004) deduced the transient amplification of a disturbance to Lamb-Oseen vortex as being associated with the Orr mechanism as well as vortex induction. Other efforts have incorporated complications associated with external strain and the presence of a wake on the stability of the flow. The Batchelor vortex model that includes the effects of axial velocity, for example, has been fruitfully employed in some recent studies. At high swirl and Reynolds numbers, Parras and Fernandez-Feria (2007) connected the stability of these vortices to the dynamics of actual large-aircraft vortices. Through rigorous spatial stability analysis, they showed that at very high Reynolds number, absolute instabilities are present only in the presence of an axial velocity. Edstrand, Davis, et al. (2016) and Edstrand, Schmid, et al. (2018) used temporal and spatial stability analyses of a model Batchelor vortex resembling a tip vortex behind a NACA0012 wing. A key finding was the presence of marginal elliptic stability (Kerswell, 2002) as a possible mechanism for meandering. This was also confirmed by Cheng, Qiu, et al., 2019, who examined the problem at a range of Reynolds numbers and angles-of-attack in water tunnel experiments and performed corresponding linear stability analyses of a fitted Batchelor vortex model. Optimal perturbation analysis by Navrose, Brion, et al. (2019) for a trailing vortex system concluded that random perturbations near the wing surface, with relatively low initial energy, can non-linearly trigger vortex displacement.

While illustrative, studies on wake vortices modeled on isolated constructs of vortex models, may not fully represent the dynamics of vortex pairs, which could be either co- or counter-rotating (Fabre, Jacquin, et al., 2002; Leweke, Le Dizes, et al., 2016). The temporal stability results of Hein and Theofilis (2004) on a pair of Batchelor vortices exhibiting long-wavelength (Crow) instability, found stronger modification of the instability characteristics for the vortex pair system relative to the isolated vortex. For wingtip vortices, the vorticity dynamics of an isolated vortex, especially those occurring at short wavelengths, can be a good representative of counter-rotating vortex pair, because the individual vortices are well separated, typically by the wingspan. On the other hand, the afterbody counter-rotating vortices, such as those under consideration, are

DISTRIBUTION A: Distribution approved for public release.

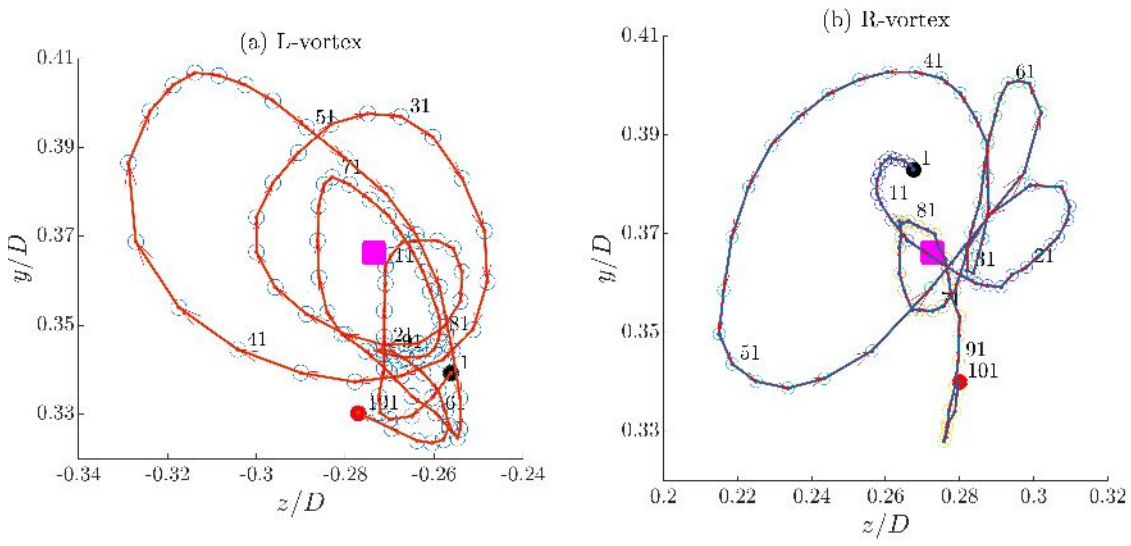


Figure 64: Phase-portrait of instantaneous vortices at $X/L = 2.0$. The location of the mean vortex is shown as the large filled square. Black and red circles respectively indicate the beginning and end of the trajectory.

much closer to each other as they both are formed on the same slanted cylinder surface. Hence, it is imperative to consider both the vortices in stability studies. Such efforts, which consider both vortices in the pair, are scarce due to much higher computational cost than a single vortex, although some exceptions have been reported (Jugier, Fontane, et al., 2020). For the current afterbody configuration, interactions between the afterbody vortices in the pair were postulated to be related to low-frequency ($St_D \sim 0.4$, where St_D is the Strouhal number based on diameter) oscillations observed in experiments (Zigunov, Sellappan, et al., 2020c). However, a rigorous stability analysis to confirm this conjecture is not available. The stability analysis in the present work, § 6.2, is therefore conducted by considering both vortices in the pair, each modeled as a Batchelor vortex. The analysis is performed at a downstream location, where a good description of the mean vortex can be obtained without much interference of the shear layer.

6.1 Meandering of Streamwise Vortices

6.1.1 Phenomenology

The motion of each vortex is now discussed by examining their behavior at location $X/L = 2.0$, where the immediate effects of the base region have diminished. The definition of vortex meandering follows Green and Acosta (1991) who characterize it as the fluctuation of the vortex core with time at a specific downstream location. The locus of vortex cores in time is presented in the form of a phase portrait in figure 64. The trajectory of each core using 100 snapshots, separated by a non-dimensional time $\Delta t = 0.025$, is shown on the crossflow (yz) plane. The initial and final positions of each core are marked with black and red circles, and the position of the mean vortex core is shown as a large magenta square. While the core of the **L**-vortex meanders in the

DISTRIBUTION A: Distribution approved for public release.

clockwise direction, the meandering trajectory of the **R**-vortex is counter-clockwise. The sense of rotation is the same as the swirl of the vortex, similar to observations on delta wings (Gordnier and Visbal, 2005). The instantaneous location of each vortex core deviates significantly from the mean, with $\Delta d_{max}/D = 0.05$, where Δd_{max} is the maximum displacement of instantaneous core location from the mean. In order to quantify this phenomenon, the meandering amplitude a_m, defined as the average of distance between instantaneous core (z_i, y_i) and mean core locations (z_c, y_c), is measured:

$$a_m = \sqrt{\frac{1}{N}\sum_{i=1}^{N}(z_i - z_c)^2 + (y_i - y_c)^2} \tag{17}$$

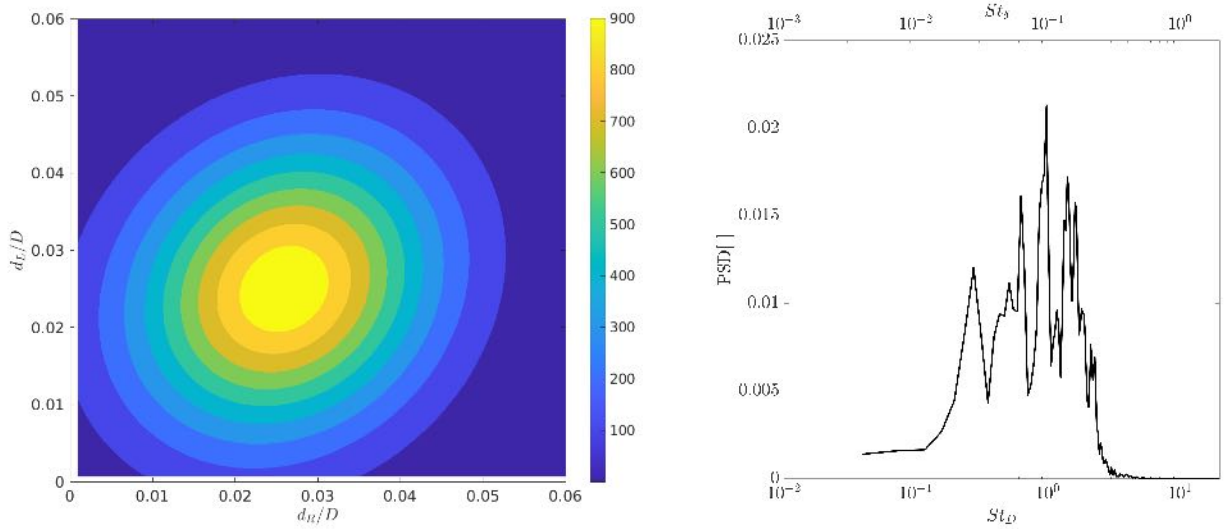
a_m values are 0.0288 and 0.0282 for **L** and **R** vortex, respectively. Similar values of the amplitude for both the vortices indicate their statistically analogous behavior despite seemingly random motion.

In order to estimate the correlation between meandering in the two vortices, we compute the correlation coefficient, $\mathbb{R}$, between **L** and **R** vortex by using the displacements of instantaneous cores from their respective mean positions. Smaller values of this coefficient indicate lower influence of the vortices on one another. The correlation coefficient thus obtained by considering $3{,}000$ instantaneous vortices is $\mathbb{R} = 0.1622$. This value is very near to that reported by Jackson, Wang, et al. (2015), but slightly higher than that of Bulathsinghala, Jackson, et al. (2017). According to Jackson, Wang, et al. (2015), these observations are rather independent of the streamwise location. To further probe the nature of the correlation, the Gaussian joint probability distribution function (JPDF) is plotted in figure 65(a).

The maximum probability of the interaction between the two vortices is observed at $d_L/D = d_R/D \simeq 0.028$. Since the mean vortex centers are separated by $b/D \simeq 0.06$, a reasonable inference is that the interaction may only become important when the instantaneous vortices are closest to the symmetry plane. The JPDF diminishes as the vortices move away from the symmetry plane. Although the above analysis suggests the effects of vortices on one-another are weak, these calculations do not include the crucial axial velocity component that can play a significant role in determining the instability mechanism responsible for the meandering of these vortices as discussed in § 6.2.

The frequency of the meandering motion at this location is characterized using the spectral signature of the instantaneous vortices at the mean vortex core location. Figure 65(b) shows the power spectral density (PSD) of fluctuations of v-velocity for the **R**-vortex using a long time-series signal, $tU_\infty/D > 60$. The signal shows a frequency band in Strouhal number based on diameter $St_D \equiv fD/U_\infty \in [0.3\ 2.0]$, with several low ($St_D \simeq 0.3, 0.6$) and high ($St_D \simeq 1.0, 1.4, 1.6$) frequency peaks. The maximum spectral energy is observed at $St_D \simeq 1.0$. Though not shown for brevity, similar frequency content is also obtained for the **L**-vortex. High-frequency peaks in the range $St_D \in [1.4\ 1.6]$ were also observed in the LES studies at high Reynolds number (Garmann and Visbal, 2019), whereas Zigunov, Sellappan, et al. (2020c) reported strong tones at low-frequency, $St_D \simeq 0.4$, in addition to the high-frequency peaks for a range of Reynolds num-

DISTRIBUTION A: Distribution approved for public release.



(a) (b)

Figure 65: Characterization of streamwise vortices at $X/L = 2.0$. (a) Gaussian joint PDF of instantaneous vortices. (b) Spectral content in vortex core fluctuations using Welch PSD for the **R**-vortex. Non-dimensional frequencies are shown based on the cylinder diameter, $St_D = \frac{U_\infty D}{\nu}$ as well as vortex core diameter, $St_\delta = \frac{U_\infty \delta}{\nu}$.

bers. Zigunov, Sellappan, et al. (2020c) postulated the high-frequency content to be related to the shear layer downstream of the body, while the low-frequency fluctuations were conjectured to be related to interactions between the cores as observed in several vortex meandering studies (Edstrand, Davis, et al., 2016; Devenport, Rife, et al., 1996). Detailed stability analyses of vortex pair are performed in §6.2 to investigate the vortex-vortex interactions, including effects on underlying frequency content as well as their correlation.

6.1.2 Coherent Structures

The phenomenon of meandering is associated with the motion of coherent structures constituting the vortex (Devenport, Rife, et al., 1996). One approach to educe these is with proper orthogonal decomposition (POD) using the method of snapshots as introduced by Sirovich (1987). For a given unsteady flowfield, the technique extracts modes with the largest energy content, which are often related to the coherence in the flow. The POD decomposition of time snapshots, represented by $\vec{q}(\vec{x}, t)$, is given by:

$$\vec{q}(\vec{x}, t) = \vec{\bar{q}}(\vec{x}) + \sum_{i=1}^{\infty} \sqrt{\Lambda_i} \vec{\Phi}_i(\vec{x}) \vec{a}_i(t) \tag{18}$$

where $\vec{\bar{q}}(\vec{x})$ is the mean flow. $\vec{\Phi}_i(\vec{x})$ and $\vec{a}_i(t)$ represent the i^{th} orthonormal spatial mode and its time-coefficient respectively. Λ_i is the energy associated with the i^{th} POD mode.

The role of coherent structures during the development of streamwise vortices is analyzed

DISTRIBUTION A: Distribution approved for public release.

first, as this provides a perspective of the meandering process downstream. This analysis is thus performed at different streamwise sections along the upswept base. $3{,}000$ snapshots, sampled every 100 iterations, are collected, for an effective time-step $\Delta t_{\text{POD}} = 0.025$. Results performed for each vortex in isolation indicate very similar spatial dynamics due to flow symmetry. For brevity, results from only **R**-vortex are presented here.

The first two most energetic modes are shown along with the mean vortex in Figure 66 at three different sections along the ramp, namely at $X/L = 0.2$, 0.6 and 1.0. At $X/L = 0.2$, figure 66(a), where the mean vortex is in a nascent stage and fed by the shear layer, the first mode qualitatively resembles the mean field (Bulathsinghala, Jackson, et al., 2017). This indicates the prominence of fluctuations in both the vortex as well as the shear layer.

Proceeding downstream, at $X/L = 0.6$ in figure 66(b), where the mean vortices have become nearly axisymmetric, but are still attached to the surfaces, both POD modes display a vortex dipole-like structure around the time-averaged vortex. However, the presence of a shear layer in the POD modes effectively diffuses these structures. Further downstream, towards the edge of the base, at $X/L = 1.0$ in figure 66(c), the vortex dipoles are clearly discernible near the vortex core for both POD modes. Smaller structures near the periphery of the cylinder display the shear layer emanating from the top. The influence of the shear layer on the vortex persists for some distance in the wake, complicating the overall flow dynamics.

In order to isolate the vortex dynamics and the role of large-scale coherent structures in the overall meandering process, detailed analysis is performed at a location relatively far downstream, $X/L = 2.0$. Since the instantaneous meandering motions of the two vortices in the pair are very different, as shown in figure 64, the vortices are considered separately for this component of the analysis. Figure 67(a) and (b) show the spatial structures of the first two POD modes as obtained from a decomposition of the **L** and **R** vortices separately and then plotting them together. The vortex dipoles are more distinctly defined compared to those observed at $X/L = 1.0$ in figure 66(c), while the shear layer component is very small.

The energies (Λ_i) of the first 20 most energetic modes are shown in figure 67(c,d) for the **L** and **R** vortex respectively. Both vortices show similar energy distribution among the modes. The first mode has nearly double the energy of the second, but together, these two modes contain almost 35% of the total energy. Furthermore, 80% of the flow field can be reconstructed by only considering the first 10 modes. Although first two modes differ in energy content, they may together be considered as paired helical modes with azimuthal wave number ($|m| = 1$), as in the Batchelor vortex results of Edstrand, Davis, et al. (2016).

The movement of each vortex core in the plane depends on the alignment of the vortex dipoles compared to the mean vortex as illustrated in figure 68. The inclination angles of vortex dipoles in the first and second POD modes are defined as α_1 and α_2, as shown in the figure, and double-sided arrows depict the oscillation axis of vortex core due to these individual dipoles. The dipole increases the vorticity in one half of the time-averaged vortex while decreasing it in the other half, thus causing the displacement, which is governed by the inclination of the dipole. In the simulation, α_1 and α_2 are approximately 16° and 106° for the left vortex, while for the right vortex, they are -16° and -106° suggesting that the coherent structures are also symmetric to each other. A 90°

DISTRIBUTION A: Distribution approved for public release.

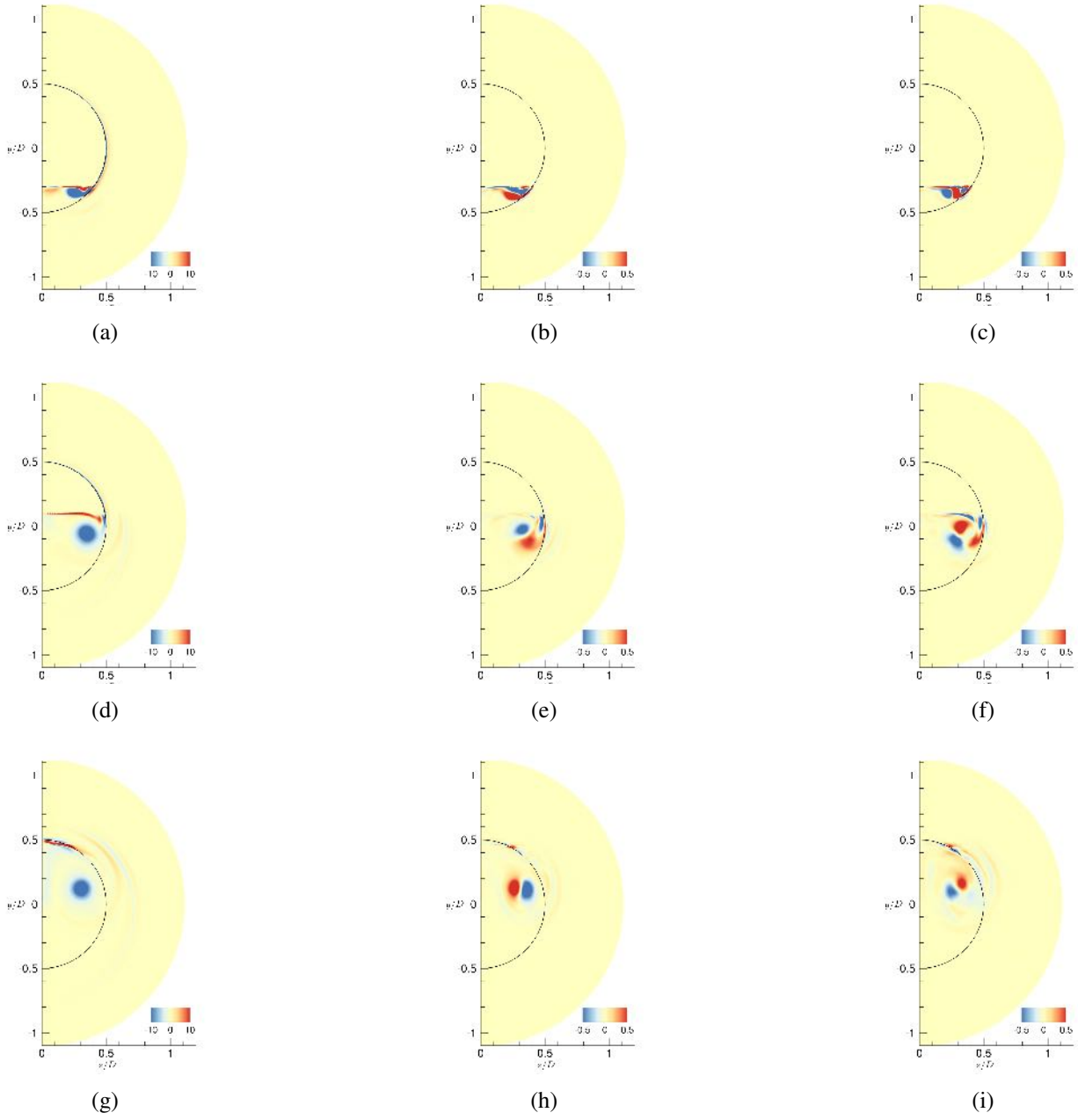
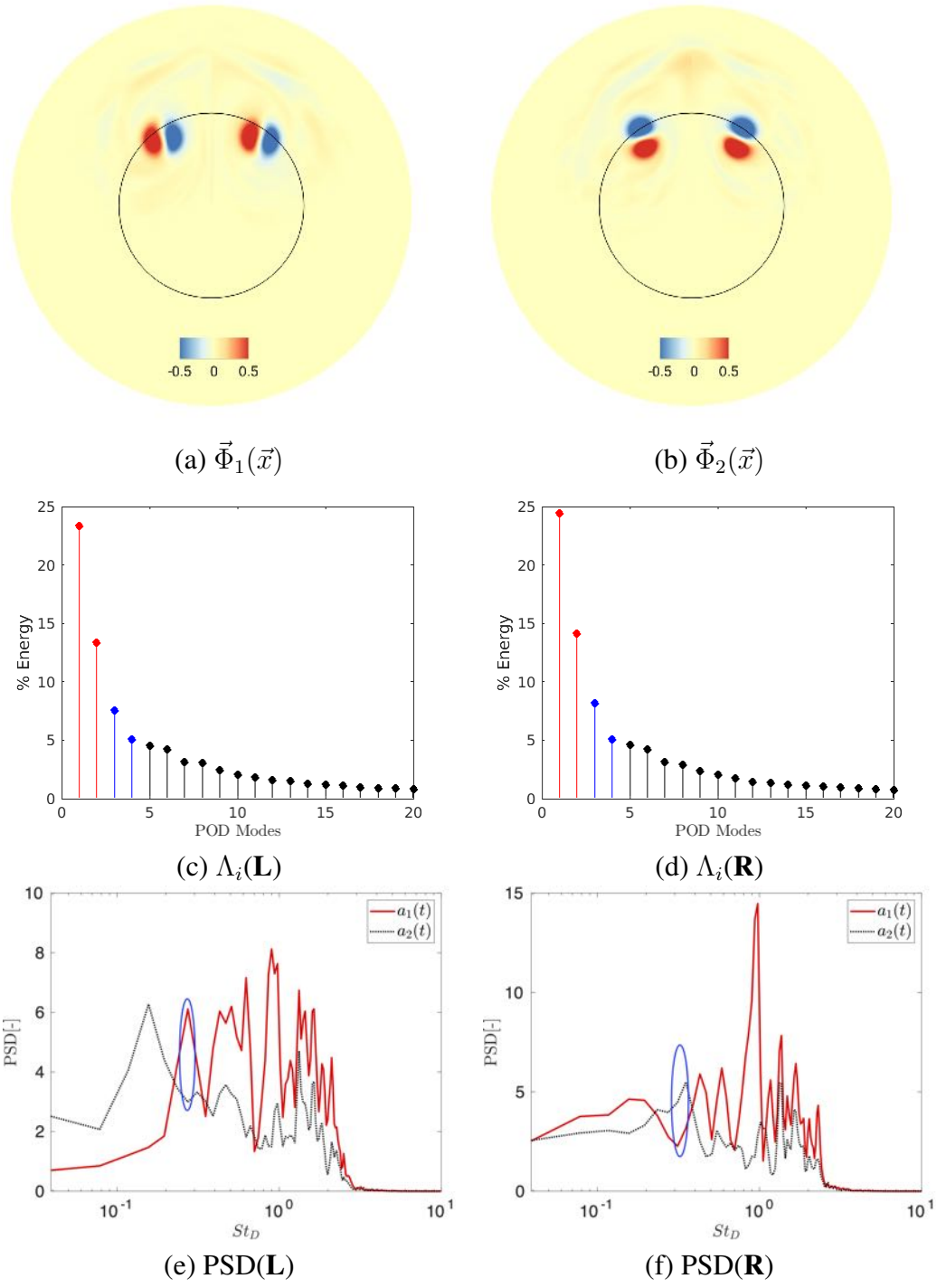


Figure 66: From left to right, mean flow as well as first two most energetic POD modes are shown through streamwise vorticity at different locations within ramp. Semi-circle indicates the boundary of the cylinder body.

difference between the inclination angles, $|\alpha_1 - \alpha_2|$, for both vortices, confirm that these modes are orthogonal to each other.

The temporal dynamics of these modes are examined in figures 67(e) and (f), by considering the power spectral density (PSD) of the **L** and **R** vortex respectively. Modes for both the vortices show spectral energies largely distributed in $St_D \in [0.3\ 2.0]$ as also observed in the analysis

DISTRIBUTION A: Distribution approved for public release.



(a) $\vec{\Phi}_1(\vec{x})$ (b) $\vec{\Phi}_2(\vec{x})$

(c) Λ_i(**L**) (d) Λ_i(**R**)

(e) PSD(**L**) (f) PSD(**R**)

Figure 67: Dominant two POD modes at $X/L = 2.0$. Structures of mode 1(a) and 2(b). Energy content in dominant modes for **L** and **R** vortices (c,d). The spectral content of time-coefficients in first two modes for both the vortices (e,f). Blue ovals in (e,f) highlight the peaks around $St_D \simeq 0.3$, which are later obtained from stability analysis (section 6.2.3) as being associated with unstable modes.

DISTRIBUTION A: Distribution approved for public release.



(a) POD Mode1 (b) POD Mode 2

Figure 68: Sketch depicting spatial displacement of vortex cores due to the leading POD modes.

of point probe data (figure 65(b)). The first POD mode for both the vortices show a peak at $St_D \simeq 1.0$, while the second POD mode has more spectral energy at low-frequencies. Because of the difference in energies (Λ) of the two modes in flow, the overall motion of the vortex core is seemingly random as shown in Fig. 64. However, the high energy content of leading modes in the flow can be exploited to reconstruct meandering phenomena using a low-rank model as presented in § 7.1.

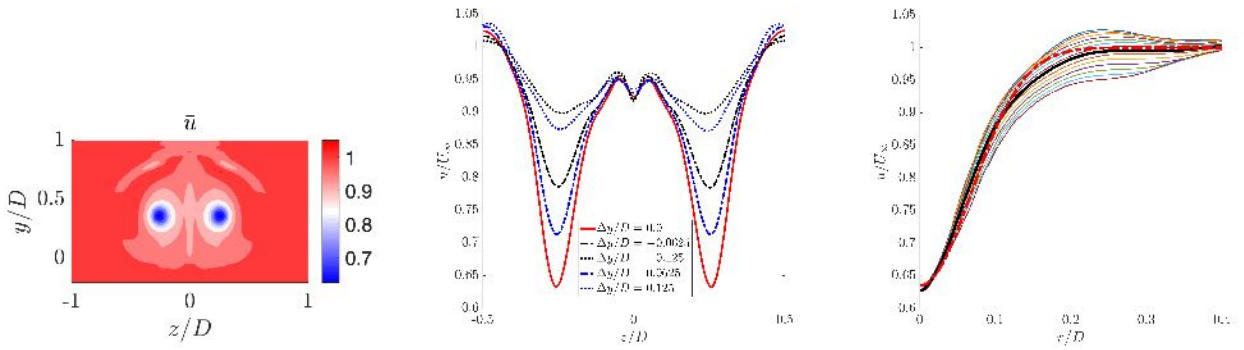
6.2 Linear Stability Analysis

Linear stability analysis is now employed to provide insights into the physical mechanism of meandering by extracting the underlying modal structures, frequencies and wavenumbers that form the basis for the observed phenomena. Jacquin, Fabre, et al. (2001) have observed that the cooperative interactions between the vortices affect the similar frequency range as meandering. Two typical instabilities of interest due to the mutual induction between counter-rotating vortex pairs are those designated elliptic and Crow. The former is of short-wavelength and incurs an internal deformation of the vortex cores with a wavy displacement of the vortex center (Widnall, Bliss, et al., 1971; Tsai and Widnall, 1976; Sipp and Jacquin, 2003). This instability thus can be viewed as a resonance between two normal modes of a vortex and an external strain field induced by the neighboring vortex. The Crow instability (C. Crow, 1970), on the other hand, is three-dimensional, in which perturbations displace the vortices locally as a whole without any change in their core structure; the observed wavelengths are large compared to the core radius. This instability can be observed in aircraft tip vortices (Leweke and Williamson, 1998).

A rough estimate of the features of these instabilities, if present, can be obtained by considering the characteristic length scales in the vortex pair, namely the core radius δ and the inter-vortical separation b; their ratio, δ/b, indicates the relative distance between the vortices. Values obtained in the current simulations, reported in Table 4, are consistently between 0.1 and 0.2 at all streamwise locations. According to Leweke, Le Dizes, et al. (2016), these lie in the range that can trigger both long and short wave instabilities, though Reynolds number considerations are also important.

The instabilities existing in the flowfield are now investigated in detail through a linear stability analysis. The mean vortex pair is first matched to a theoretical vortex model, and both temporal and spatial stability analyses are performed. Analyzing a fitted model vortex is advantageous because it offers the flexibility to extend the domain arbitrarily without compromising effects due to bound-

DISTRIBUTION A: Distribution approved for public release.



(a) (b) (c)

Figure 69: Axial velocity distribution at a streamwise location $X/L = 2.0$. (a)$\bar{u}$ contours. (b) Wake-like behavior shown by velocity distributions at different vertical locations measured from the vortex center. (c) Fitting of axial velocity from simulations to the Batchelor vortex. The thick black line indicates the azimuthally averaged axial velocity, and the red dashed line indicates the axial velocity in the fitted Batchelor vortex. Note the vortex in the simulation is recentered at (0,0) after interpolating to the cylindrical coordinate system.

aries. This also facilitates the examination of the long-wavelength Crow instability, if present. The possibility of a global mode is not examined as it is beyond the scope of the present study. Parallel flow is assumed in the streamwise direction; this is a reasonable assumption since the streamwise variation of the mean flow is relatively small at distances sufficiently downstream of the body such as those considered here. As such, stability characteristics of the vortices predicted with parallel flow assumption provide a reasonable description of the meandering phenomena (Edstrand, Schmid, et al., 2018).

6.2.1 Theoretical Vortex Model

Afterbody vortices, such as the ones of interest, are characterized by two components: swirl and strain. While the swirl effect is accounted through the radially varying in-plane velocity field, the axial velocity provides the strain field. The mean vortical field at location $X/L = 2.0$ was shown earlier in figure 22, while the mean axial velocity distribution in the vortex is shown in figure 69(a). As expected, the velocity is minimum at the center of the vortex and increases along the radial direction, eventually reaching free-stream values about 10 core radii (δ) away from the center. The quantitative profiles in figure 69(b) at different vertical locations show typical wake-like behavior. An important point to note is that the magnitude of $\bar{u}$ never reaches the free-stream value between the vortices because of their relatively close proximity to each other. This motivates the use of a vortex pair as opposed to an isolated **L** or **R** vortex for the present analysis.

Wake vortices have been modeled with different theoretical models that contain their characteristic information. Vortex models used in the literature for analyses of wingtip or similar vortices include the Batchelor or q-vortex (Edstrand, Davis, et al., 2016), Lamb-Oseen vortex (Antkowiak and Brancher, 2004), Lamb–Chaplygin vortex (Jugier, Fontane, et al., 2020), Rankine vortex (La-

DISTRIBUTION A: Distribution approved for public release.

caze, Birbaud, et al., 2005) and Moore-Saffman vortex model (Feys and Maslowe, 2016). Among these, the Batchelor and Moore-Saffman models account for axial flow and hence are more realistic in providing the dynamics of interest in this work. We employ the Batchelor model to match the individual vortex in the current streamwise vortex pair as the role of the axial velocity in the stability mechanism may be crucial. Although this model vortex is typically expressed in cylindrical coordinates, we analyze them in the Cartesian system to account for the two vortices in the pair. In this system, the velocity components for the Batchelor vortex can be written as (Paredes, Theofilis, et al., 2011):

$$u = 1 - \gamma(x) \exp\left(\frac{-r^2}{\delta(x)^2}\right) \tag{19a}$$

$$v = -\frac{\kappa}{r^2}(z - z_c)\left(1 - \exp\left(\frac{-r^2}{\delta(x)^2}\right)\right) \tag{19b}$$

$$w = \frac{\kappa}{r^2}(y - y_c)\left(1 - \exp\left(\frac{-r^2}{\delta(x)^2}\right)\right) \tag{19c}$$

where (y_c, z_c) is the center of the vortex as defined earlier and $r^2 = (y - y_c)^2 + (z - z_c)^2$. The quantity $\delta(x)$ corresponds physically to the dimensionless local vortex core radius. $\gamma(x)$ is the axial velocity defect and κ is a swirl strength parameter.

For the current analysis, one vortex is first matched to the model, and the other anti-symmetric vortex is then placed at the separation distance b. The simulation results are first interpolated on a cylindrical grid and the axial velocity u is then azimuthally averaged to obtain the parameters for the fitted Batchelor vortex. Edstrand, Davis, et al. (2016) have found that stability results are insensitive to the averaging process. Figure 69(c) shows the radial variation of axial velocity at different azimuthal locations. The azimuthally averaged vortex velocity as well as the fitted Batchelor vortex model are also shown.

Figure 70 compares the velocity fields in mean **R**-vortex obtained directly from simulations with those of the fitted vortex used for stability analysis. All the three velocity components considered in the model show good match with the LES data. The parameters of this matched Batchelor vortex are $\delta = 0.0972, \gamma = 0.365, \kappa = 0.07$, to obtain a non-dimensional swirl parameter $q = \kappa/(\delta\gamma) = 1.9731$. This value of q is much smaller than the $q = 4.41$ obtained for trailing edge vortex in Edstrand, Davis, et al. (2016). The present parameters correspond to a Reynolds number based on the core radius as $Re_\delta \equiv U_\infty \delta/\nu \simeq 2{,}500$, which is much lower compared to $Re_\delta = 27,200$ used in the stability study of wingtip vortices (Edstrand, Davis, et al., 2016).

6.2.2 Stability Approach

Most stability studies in the literature consider an isolated vortex and efforts on vortex pairs separated by a relatively small distance, and in the presence of an axial flow, are relatively rare. The latter problem presents substantial computational challenges as the domain becomes significantly larger (Hein and Theofilis, 2004). To ease the computational burden, temporal stability analyses are performed for a given wavenumber range while spatial analysis at the most unstable frequency is used to further confirm the results. Further, incompressible linearized Navier-Stokes equations

DISTRIBUTION A: Distribution approved for public release.

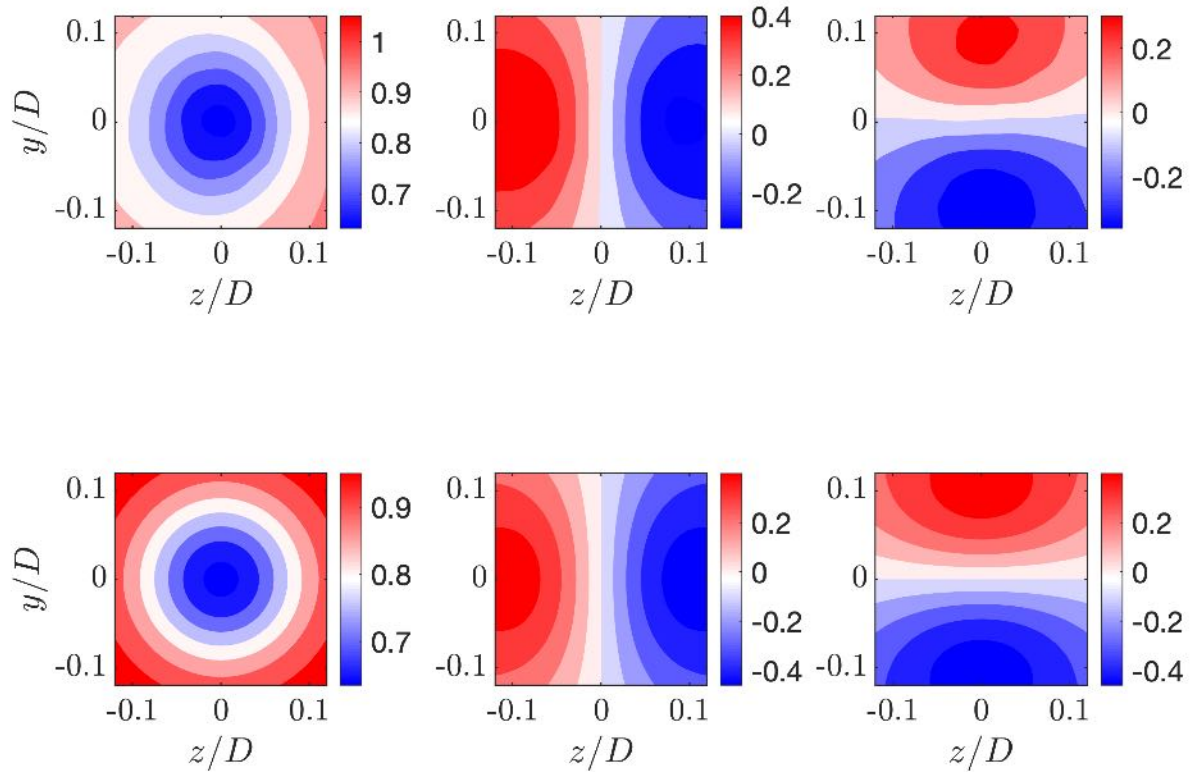
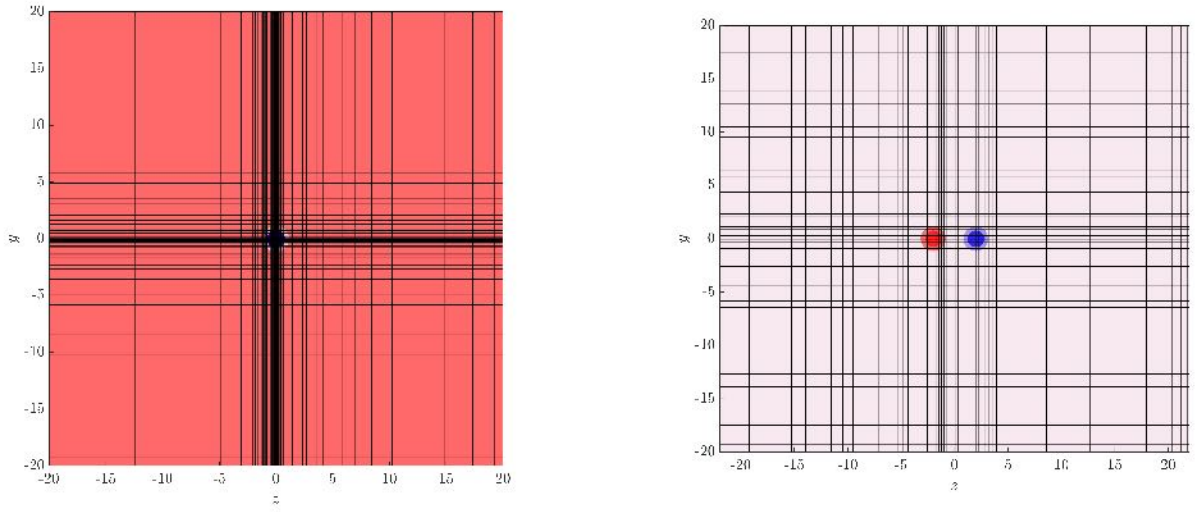


Figure 70: Top: **R**-vortex from the simulation. Bottom: Theoretical Model (Batchelor vortex). U, V, W velocity components are shown from left to right. Note the **R**-vortex in simulation is centered to (0,0) to compare with the fitted Batchelor vortex.

are considered for the eigenvalue analysis instead of compressible equations as the latter increases the linear operator size significantly due to an extra variable. This is acceptable because of the low Mach regime considered and a comparison with the fully compressible formulation is given below to ensure confidence. Consistent with the simulations, a spanwise coordinate system is used in which two inhomogeneous spatial directions, y and z, are resolved simultaneously, while the axial direction, x, is considered to be locally homogeneous. The resulting eigenvalue problems along with boundary conditions for both temporal and spatial analyses are summarized in Section 6.3 – further details may be found in Ranjan, Unnikrishnan, et al. (2021).

Hein and Theofilis, 2004; González, Gómez-Blanco, et al., 2008 have described the importance of choosing a sufficiently large domain for solving the eigenvalue problem, and a suitable grid discretization scheme to resolve the vortex core and wake regions adequately, while ensuring proper treatment of the relatively innocuous farfield. Because of the large domain, whose size scales as $y_\infty/\delta \approx 20$, $z_\infty/\delta \approx 20$ (Edstrand, Schmid, et al., 2018; Hein and Theofilis, 2004; Paredes, Theofilis, et al., 2011), finite difference schemes are not generally a preferred choice because of the large number of grid points required in the farfield region. Hein and Theofilis, 2004 use a mapping

DISTRIBUTION A: Distribution approved for public release.



(a) Isolated vortex $(72 \times 72, c = 0.975)$ (b) Vortex pair $(100 \times 100, c = 0.75)$

Figure 71: Spatial discretization for stability analysis.

ζ_j of Chebyshev collocation points $\eta_j \in [-1;\ 1]$ such that:

$$\zeta_j = \zeta_\infty \frac{\tan \frac{c\pi}{2}\eta_j}{\tan \frac{c\pi}{2}} \tag{20}$$

where ζ_∞ is the farfield boundary. The stretching parameter $c \in (0,\ 1]$ defines the clustering of grid points near the vortex core. Higher c provides more clustering near the vortex core while imposing a relatively coarser grid away from the core. This distribution of points will be referred to as the CHEB-TANH grid. Figure 71(a) shows a typical grid clustering for $\delta = 1, y/\delta \in [-20\ 20], z/\delta \in [-20\ 20], N_y = N_z = 72, c = 0.975$, ensuring that the vortex at the center is adequately resolved.

For a vortex pair, the choice of discretization scheme requires more care than for a single vortex, because of their separation along the z-axis connecting their centers. The domain used for the two vortex system is $y/\delta \in [-20;\ 20], z/\delta \in [-20 - b/2;\ 20 + b/2]$, where b is the separation between vortices as defined earlier. Naturally, for similar accuracy, the number of grid points required is much higher than the single vortex case, as the stretching parameter, c, in the CHEB-TANH needs to be relaxed to encompass both the vortices. Figure 71(b) shows a representative grid clustering for $c = 0.75$, resolving both the vortices as well as the spacing between them.

Table 6 shows validations for both temporal and spatial stability codes used in the study. For the temporal approach, the classical q-vortex at $q = 0.475, Re = 100, k = 0.418$ is chosen; this problem was first examined by Mayer and Powell (1992) and subsequently used for validation in several studies (Hein and Theofilis, 2004; Paredes, Theofilis, et al., 2011; Edstrand, Schmid, et al., 2018). The results for the unstable mode are reported along with the reference results from Paredes, Theofilis, et al. (2011). Excellent convergence is obtained with the mapped CHEB-TANH discretization, even for a slightly smaller domain in $[-15\ 15]$ and moderate grid size. The stretch-

DISTRIBUTION A: Distribution approved for public release.

Domain	Diff. Scheme	Resolution	Temporal	Spatial
Paredes	FD10		0.028353+0.009617i	0.543-0.185i
$[-15\ \ 15]$	CHEB-TANH	40×40	0.028337 + 0.009607i	0.5534-0.1839i
$[-20\ \ 20]$	CHEB-TANH	60×60	0.0283321 + 0.0096043i	0.549-0.18i
$[-15\ \ 15]$	FD6	101×101	0.028533 + 0.009980 i	
$[-15\ \ 15]$	FD6(C)	101×101	0.028225 + 0.010024 i	

Table 6: Validation of stability analyses techniques. The temporal analysis is performed for a q-vortex with parameters $q = 0.475, Re = 100, k = 0.418$. The spatial analysis is performed for the Batchelor vortex ($\kappa = 0.8, \gamma = 0.8, \delta = 1$) at $\omega = 0.86$ and $Re = 3000$. Temporal analysis using compressible formulation, FD6(C), at low Mach number ($M = 0.1$) yields leading modes close to those obtained with fully incompressible code.

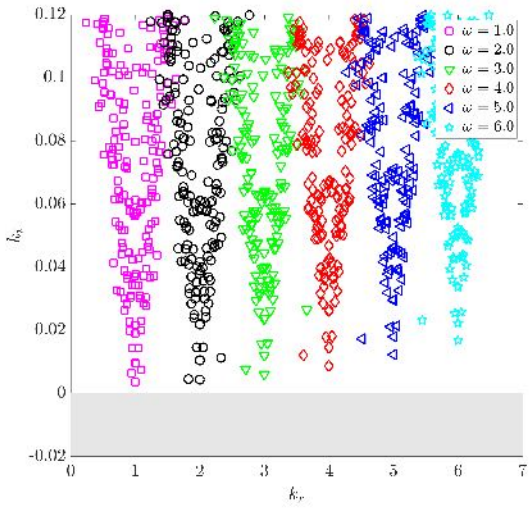
ing parameter in this discretization is fixed at $c = 0.975$, ensuring that the vortex at the center is adequately resolved. A good match is also obtained with the sixth-order finite difference (FD6) approach albeit at a higher resolution. The table also includes a result when a fully compressible stability solver is used for the same q-vortex analysis at a low Mach number ($M = 0.1$). Comparing the results between incompressible and compressible solvers with similar grid and numerical schemes, we note only a minor difference of about 1% in the frequency and 0.44% in the growth rate.

For the spatial code validation, the Batchelor vortex study by Paredes (2014) at $\kappa = 0.8, \gamma = 0.8, \delta = 1, Re = 3000$ is used for reference. In table 6, results for $m = 1, \omega = 0.86$) are compared against the values reported in Paredes, 2014. Even with a moderate 40×40 grid, the frequency obtained in the current study is within 2% of the reported value; the comparison improves with increase in grid size. For the subsequent results for current afterbody vortices, CHEB-TANH grid is employed.

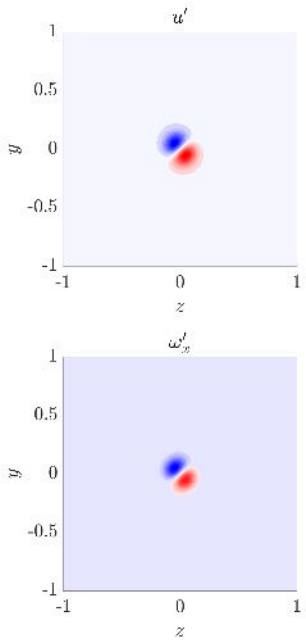
6.2.3 Stability Analysis of Afterbody Vortices

The stability dynamics of the afterbody vortices are now delineated. Before showing the dynamics of the vortex pair, we first discuss the stability characteristics of an isolated vortex. The fitted Batchelor vortex described in §6.2.1 is used for this study. Figure 72(a) shows results from spatial analyses of this vortex for input frequency varying from $\omega = 1$ to $\omega = 6$. A 60×60 grid with $c = 0.975$ is used for these analyses. As seen from the figure, the vortex is stable for the entire frequency range $\omega \in [1.0\ 6.0]$. The vortex becomes increasingly more stable as the frequency is increased. For input frequency $\omega = 1$, the least stable mode is obtained at $k \equiv k_r + ik_i = 0.9346 + 0.0025i$. Note that the positive value of k_i in the spatial analysis indicates a decaying mode (see Section 6.3). The spatial structure of this mode is shown in Fig. 72(b). Both the axial velocity and vorticity fluctuations show dipole structures indicating the $|m| = 1$ elliptic mode discussed earlier. This mode is typically observed to be the dominant instability mechanism in wake vortices (Edstrand, Davis, et al., 2016).

DISTRIBUTION A: Distribution approved for public release.



(a) Spatial analysis for $1.0 < \omega < 6.0$



(b) Least stable mode at $\omega = 1$ ($k = 0.9346 + 0.0025i$)

Figure 72: Eigenspectrum from spatial analyses of an isolated vortex for a range of frequencies(a). Shaded portion indicates the region of growing modes ($k_i < 0$). The least stable mode at $\omega = 1$ shows $m = 1$ elliptic instability (b).

6.3 Governing linear stability equations

The incompressible Navier-Stokes equations in non-dimensional form are given by:

$$\nabla.\vec{u} = 0 \tag{21}$$

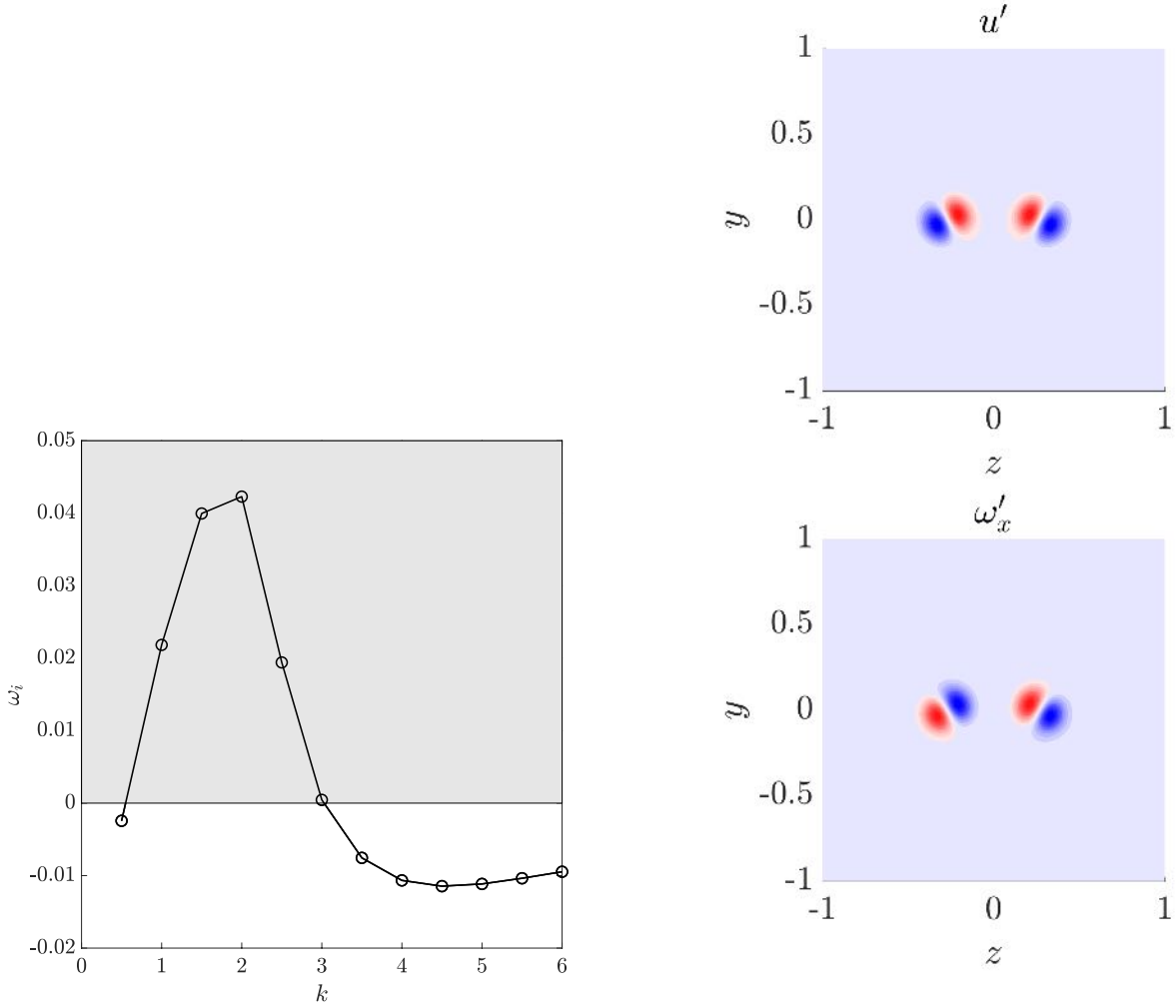
$$\frac{\partial \vec{u}}{\partial t} + (\vec{u}.\nabla)\vec{u} = \nabla p + Re^{-1}\nabla^2\vec{u} \tag{22}$$

where $\vec{u} = \{u, v, w\}^T$. The flow field is decomposed into a basic state $(\vec{\bar{u}}, \bar{p})$ and perturbations $(\vec{u'}, p')$, with the former satisfying equations (21). The equations governing linear perturbations are then:

$$\nabla.\vec{u'} = 0 \tag{23}$$

$$\frac{\partial \vec{u'}}{\partial t} + (\vec{u'}.\nabla)\vec{\bar{u}} + (\vec{\bar{u}}.\nabla)\vec{u'} = \nabla p' + Re^{-1}\nabla^2\vec{u'} \tag{24}$$

DISTRIBUTION A: Distribution approved for public release.



(a) Temporal analysis for $0.0 < k < 6.0$

(b) Unstable mode at $k = 2$

Figure 73: Eigenspectra from temporal analyses of the vortex pair for a range of wavenumbers (a). Shaded portion indicate the region of growing modes ($\omega_i > 0$). Structure of the fastest growing mode at all wavenumbers is shown in (b).

where the small non-linear terms, $(\vec{u'}.\nabla)\vec{u'}$, are ignored. For stability analysis, a modal form of the perturbations is assumed, with homogeneity in the x-direction

$$\{u', v', w', p'\}(x, y, z, t) = \{\tilde{u}, \tilde{v}, \tilde{w}, \tilde{p}\}(y, z)e^{i(kx-\omega t)} \tag{25}$$

DISTRIBUTION A: Distribution approved for public release.

where the quantities with tilde($\tilde{\bullet}$) are two-dimensional amplitude functions. Substituting this in the perturbation equations (23), the stability equations are obtained:

$$\Bigg(\underbrace{\begin{bmatrix} \mathcal{L} & \overline{U}_y & \overline{U}_z & 0 \\ 0 & \mathcal{L}+\overline{V}_y & \overline{V}_z & D_y \\ 0 & \overline{W}_y & \mathcal{L}+\overline{W}_z & D_z \\ 0 & D_y & D_z & 0 \end{bmatrix}}_{\mathbb{A}_0} + k \underbrace{\begin{bmatrix} i\overline{U} & 0 & 0 & i \\ 0 & i\overline{U} & 0 & 0 \\ 0 & 0 & i\overline{U} & 0 \\ i & 0 & 0 & 0 \end{bmatrix}}_{\mathbb{A}_1} + k^2 \underbrace{\begin{bmatrix} IRe^{-1} & 0 & 0 & 0 \\ 0 & IRe^{-1} & 0 & 0 \\ 0 & 0 & IRe^{-1} & 0 \\ 0 & 0 & 0 & 0 \end{bmatrix}}_{\mathbb{A}_2}$$
$$- \omega \underbrace{\begin{bmatrix} i & 0 & 0 & 0 \\ 0 & i & 0 & 0 \\ 0 & 0 & i & 0 \\ 0 & 0 & 0 & 0 \end{bmatrix}}_{\mathbb{B}} \Bigg) \begin{bmatrix} \tilde{u} \\ \tilde{v} \\ \tilde{w} \\ \tilde{p} \end{bmatrix} = 0 \tag{26}$$

where

$$\mathcal{L} \;=\; \overline{V} D_y + \overline{W} D_z - \frac{D_{yy} + D_{zz}}{Re}. \tag{27}$$

D_y, D_{yy} etc. represent first and second-order differentiation matrices. I is the identity matrix.

For the temporal analysis, the real wavenumber k is specified, while $\omega = \omega_r + i\omega_i$ is a complex quantity denoting the circular frequency, ω_r, and growth rate, ω_i. The generalized eigenvalue problem, following equations (26), is then:

$$\mathbb{A}\tilde{\vec{q}} = \omega \mathbb{B} \tilde{\vec{q}}. \tag{28}$$

with $\tilde{\vec{q}} = \{\tilde{u}, \tilde{v}, \tilde{w}, \tilde{p}\}^T$ and $\mathbb{A} = \mathbb{A}_0 + k\mathbb{A}_1 + k^2\mathbb{A}_2$.

For spatial stability analysis, the streamwise wavenumber $k = k_r + ik_i$ represents the complex eigenvalue, with $k_i < 0$ indicating spatial exponential growth, and ω is a real specified circular frequency. In this case, equations (26) present a quadratic eigenvalue problem:

$$(\mathbb{A}_0' + k\mathbb{A}_1 + k^2\mathbb{A}_2)\tilde{\vec{q}} = 0 \tag{29}$$

with $\mathbb{A}_0' = \mathbb{A}_0 - \omega\mathbb{B}$.

Although the problem can be solved directly, the quadratic eigenvalue problem can become very expensive for large matrices. Therefore, it is converted into a linear eigenvalue problem by using the companion matrix technique (Tisseur and Meerbergen, 2001). The matrix size of this spatial eigenvalue problem is therefore 75% higher than the temporal approach due to the padding of three auxiliary variables at every grid point. For both temporal and spatial analysis, distant farfield boundaries are used to allow for homogeneous Dirichlet boundary conditions for all perturbation variables except for pressure, for which the Neumann boundary condition is appropriate.

DISTRIBUTION A: Distribution approved for public release.

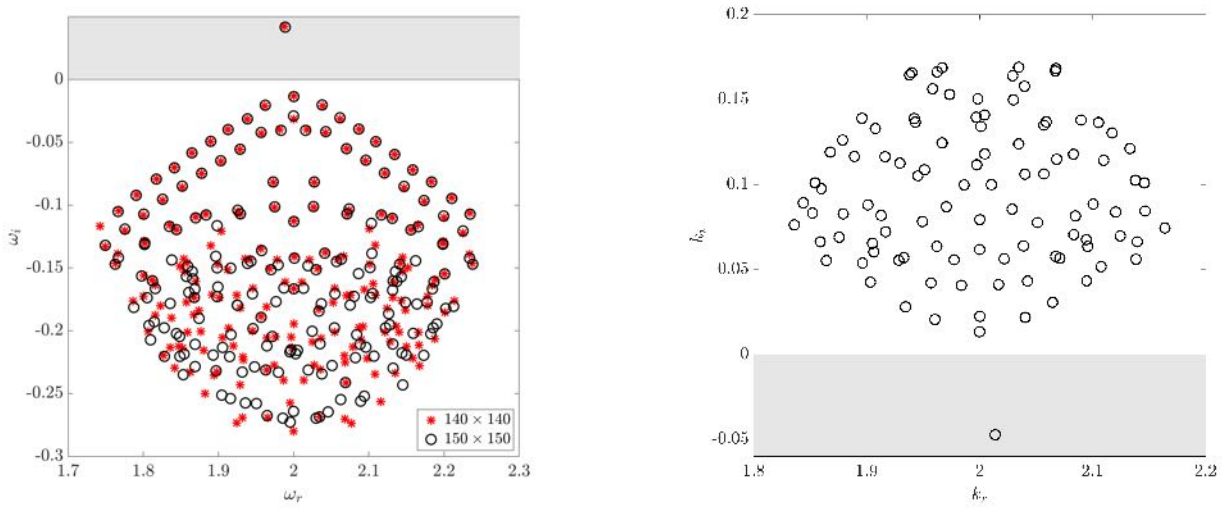
The eigenvalue problems are solved using the iterative Arnoldi (Arnoldi, 1951) algorithm. Further, the shift-and-invert approach (Lehoucq, Sorensen, et al., 1998) in the Arnoldi algorithm is used to obtain faster convergence to desired eigenvalues. A large Krylov dimension ($k = 100$) is chosen to ensure that the relevant unstable eigenspectrum around the shift value is captured.

Now we consider the change in stability characteristics due to the presence of a counter-rotating vortex next to the above stable vortex. Following the results of Section 4.2.3, the counter-rotating vortices are separated by $b/\delta = 5.6132$. As alluded to earlier, this relatively large separation between the vortices increases the computational requirement enormously because the stretching parameter needs to be relaxed to as low as 0.75, with a corresponding increase in the grid size to ensure sufficient accuracy. The parallel spatial analysis, performed above for the isolated vortex, is natural for the study of the vortex pair also, since it directly provides the wavenumber at which the flow can become unstable. However, since the grid size required for vortex pair is significantly larger (up to 150×150) than that for an isolated vortex, we use a temporal approach with wavenumber variation to extract the least stable wavenumber.

The temporal analysis results for a streamwise wavenumber sweep of $k \in [0.5\ 6.0]$ is shown in Fig. 73(a). These results are obtained by using a 140×140 CHEB-TANH grid that gives a dense matrix of $78{,}400 \times 78{,}400$. The vortex pair displays unstable eigenmodes at wavenumbers $1.0 \leq k \leq 3.0$, with growth rate increasing between $k = 1.0$ and $k = 2.0$. As the input wavenumber increases beyond $k = 2.0$, the modes become less unstable and only stable modes are recovered for $k > 3.0$. For the subsequent analyses, we focus on the wavenumber $k = 2.0$ at which the fastest growing modes are recovered. Figure 74(a) shows the convergence of dominant modes in the eigenspectrum at this wavenumber as obtained by performing the analysis on a finer 150×150 grid. Both grids recover most unstable modes at $\omega \equiv \omega_r + i\omega_i = \pm 1.988 + 0.0417i$ (note only the positive frequency ω_r mode is shown). The phase speed of this mode is $c_r \equiv \omega_r/k = 0.9940$. In order to confirm that spatial analysis also recovers similar instabilities, we show the eigenspectrum from this approach at input frequency $\omega = 2.0$ in figure 74(b). Note that the matrix size for the spatial problem is very large ($137{,}200 \times 137{,}200$) for a similar grid size of 140×140 and solving this eigenvalue problem with a Krylov size of 100, requires about 140 gigabytes of the physical system memory. The spatial analysis recovers an unstable mode at $k \equiv k_r + ik_i = \pm 2.0138 - 0.0473i$ as shown in the unstable region ($k_i < 0$) in figure 74(b). The phase speed of this mode, $c_r \equiv \omega/k_r = 0.9932$, is very similar to that obtained from the temporal analysis earlier. The recovery of analogous instabilities in both spatial and temporal approaches further validates present observations.

The structure of this mode as obtained from both temporal and spatial approaches is very similar as shown in figure 73(b). The shape exhibits a dipole form representing the $|m| = 1$ elliptic mode for both vortices in the pair, as observed in POD analysis. This dipole is extracted in both the axial velocity and vorticity fluctuations, but it is symmetric about the mid-plane ($z = 0$) in the former, but anti-symmetric in the latter. This is consistent with the symmetry of the mean flow. The inclination of the dipole with respect to the horizontal axis, α_1 (see sketch 68), is about $30°$, which is higher than that observed in POD mode 1. This suggests that the interaction of the downstream shear layer with the vortices, as well as non-linearities present in the flow, modifies

DISTRIBUTION A: Distribution approved for public release.



(a) Temporal ($k = 2$)

(b) Spatial ($\omega = 2$)

Figure 74: Eigenspectra from temporal(a) and spatial(b) analyses of the afterbody vortex pair. Both approaches show analogous instabilities at a phase speed of about 0.99.

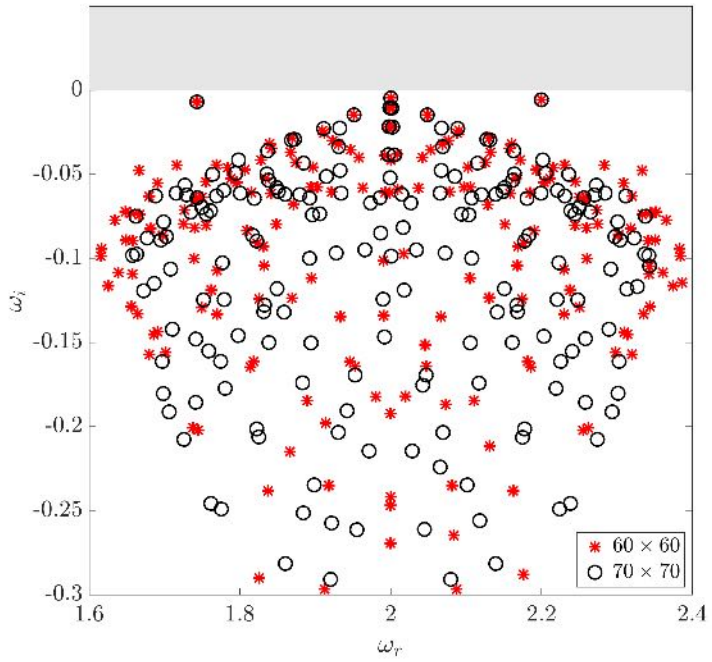
these structures and introduces high-frequency content as evident in the spectral signatures of the POD modes (figure 67(e,f)).

The frequency of the most unstable mode as obtained from the temporal analysis is $\omega \simeq 1.988$, or equivalently $St_D \simeq 0.32$. This low-frequency was observed in the vortex flowfield (figure 65(b)) as well as in the POD modes (figure 67(e,f)). As mentioned earlier, in the experimental work of Zigunov, Sellappan, et al. (2020c) this low-frequency was observed and was conjectured to be related to fluctuations due to interactions of cores. The present stability analysis confirms this hypothesis and establishes meandering as a low-frequency phenomenon in afterbody flows in similarity with vortices in aircraft wakes (Jacquin, Fabre, et al., 2001).

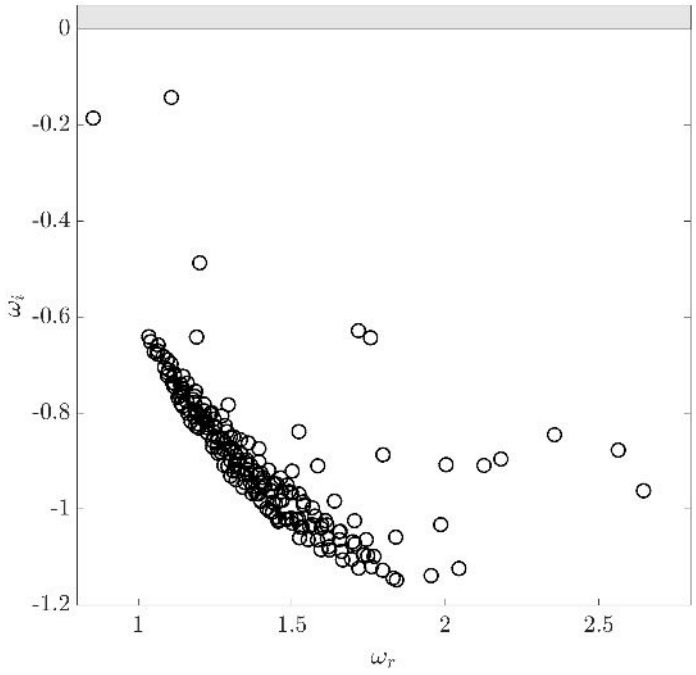
To further confirm the role of the interaction between the vortices as a necessary mechanism for the recovery of unstable modes, we perform the temporal stability analysis for an isolated vortex with the same swirl and strain as in each individual vortex in the pair. Figure 75(a) shows the result from this analysis along with grid convergence for the dominant modes as obtained with two grids. Unlike in the two-vortex system, all modes recovered in this analysis are decaying. The least stable modes are found at $\omega = \pm 2.0001 - 0.0047i$ exhibiting dipole structures for both vorticity and axial velocity, which is similar to that shown in figure 72(b).

The external strain field is influenced by the neighboring vortex, and is accounted for in the stability calculations through the axial velocity component. The correlation analysis of section 6.1.1, based on the phenomenological description of instantaneous vortex cores on a sectional plane, indicates only weak influence of the vortices on one another. That analysis, however, did not include the axial velocity component, whose role in destabilizing the vortices is now clarified. A stable vortex can become unstable even without the presence of axial flow (as in the Kelvin vortex) due to an elliptic instability of the core; however, the presence of an axial flow can make an otherwise

DISTRIBUTION A: Distribution approved for public release.



(a) Isolated vortex



(b) Vortex pair $(u = 0)$

Figure 75: Eigenspectra from temporal analysis at $k = 2.0$. (a) Isolated vortex with axial velocity. (b) Vortex pair with no axial velocity.

DISTRIBUTION A: Distribution approved for public release.

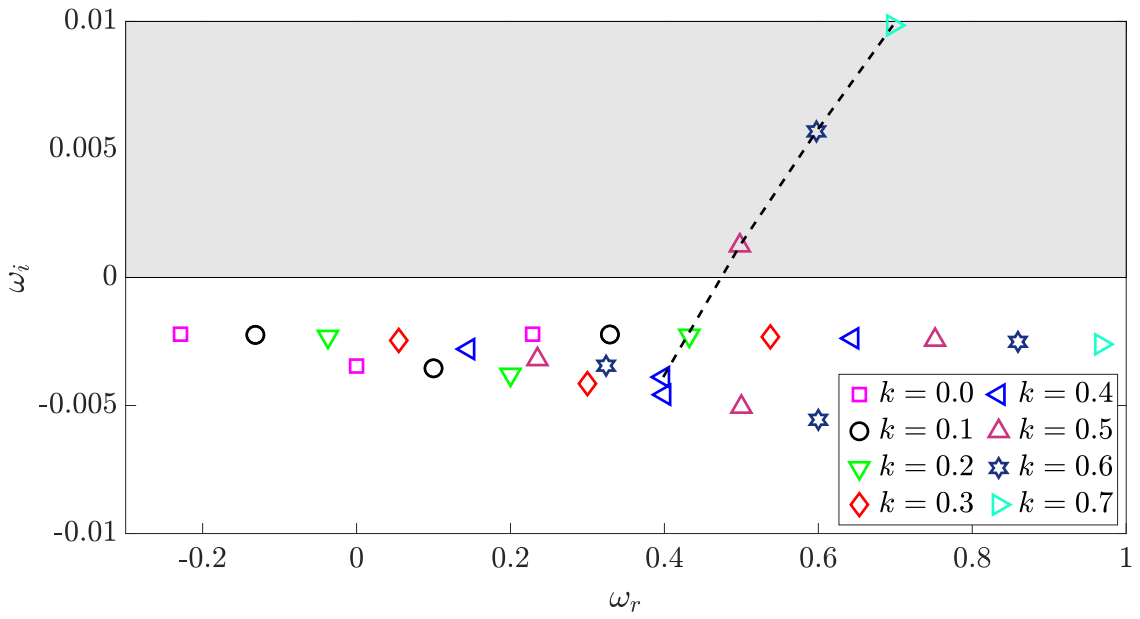


Figure 76: Eigenspectra from temporal analyses of the afterbody vortex pair at low wavenumbers. No unstable modes are recovered below $k = 0.5$.

stable vortex unstable (Lacaze, Birbaud, et al., 2005; Jacquin, Fabre, et al., 2005). In order to examine the effects of this strain, the temporal stability analysis was repeated on the afterbody vortex pair by setting the axial velocity to zero. The problem then becomes essentially similar to Rankine vortex models used in the literature to study elliptic instabilities (Kerswell, 2002). The eigenspectrum thus obtained is shown in figure 75(b). A key observation is that unlike the analysis with the axial velocity (figure 74(a)), no unstable mode is recovered in this calculation. Further, the modes are far removed from the zero axis. Although not shown, the shapes of dominant modes continue to show helical structures. The present analysis thus shows that it is necessary to consider a vortex model that includes the strain field in order to recover the correct instability behavior in afterbody vortices.

Finally, the possible presence of long-wavelength (small k) Crow instability in the flow is briefly investigated. The least stable mode at $k = 2$ in figure 73(b) is inclined at $30°$ to the horizontal. The Crow instability on the other hand typically manifests a $45°$ inclination in the structure (Brion, Dekerret, et al., 2008). To confirm this further at low wavenumbers, the temporal analysis was performed using a k-parameter sweep between 0.0 and 1.0 at increments of 0.1. Figure 76 shows the resulting eigenspectra for all these wavenumbers for the current vortex pair. No unstable mode is observed in the k-range of $[0.0\ 0.4]$, and the first unstable mode occurs at $k = 0.5$. The growth rate of modes continues to increase with wavenumber until $k = 2.0$ as discussed earlier. This indicates the absence of the Crow instability in this flow, although simulations with a longer domain may be necessary to establish this fact numerically. Further, the flow conditions that lead to a change in the non-dimensional swirl parameter or the Reynolds number may affect this observation, as discussed in Hein and Theofilis (2004). Another key parameter in the analysis that

DISTRIBUTION A: Distribution approved for public release.

determines the interaction between the two vortices is the separation distance, b/δ. If this distance varies substantially with the upsweep angle ϕ of the afterbody, the analysis needs to be repeated to examine the stability mechanism.

7 Reduced Model of Vortex Pair

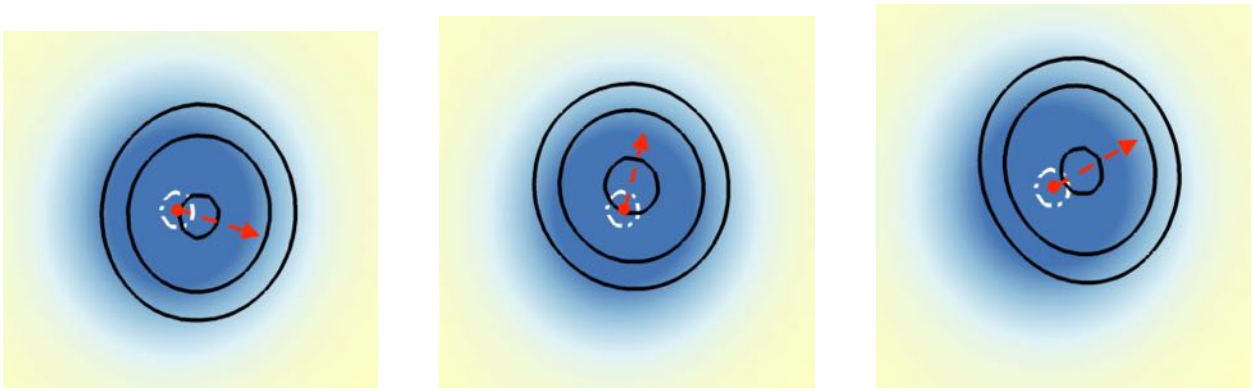
Although the causal dynamics is predicated on the underlying stability mechanisms and the corresponding stability modes, considerable insight may be obtained by post-processing the fully turbulent fluctuation field. Several models, as described above, are available to characterize the behavior of mean vortex fields, but those that capture the primary building block coherent structures underpinning the dynamics of meandering as well as shear layer are relatively scarce. A final contribution of the current work is therefore to propose a low-rank, large-scale fluctuating flowfield representation that describes the vortex meandering phenomenon. Such representations can be readily used to construct a reduced-order model (ROM) using Galerkin-projections (Rowley, Colonius, et al., 2004). Potential low-rank representation, and therefore the ROM of a complex turbulent flowfield, depends on the behavior of coherent structures, which are the next dominant flow features after the mean. These structures can be obtained from a suitable decomposition of the flowfield depending on the primary objective of the reduction. Among the flows of interest, Iungo, Santoni-Ortiz, et al. (2015) used selected dynamic mode decomposition (DMD) modes to construct a reduced-order model (ROM) for the downstream evolution and dynamics of wind turbine wakes. Similarly, Gupta and Wan (2019) used local linear stability modes of the time-averaged mean flow to develop a low-order model of wake meandering. Their model successfully predicts the increase in meandering amplitude and the advancement of the onset of meandering closer to the turbine.

In the current work, § 7.1, we employ the POD modes extracted in § 6.1.2 as a prelude to stability studies, to propose a low-rank representation for meandering. POD is an effective way to facilitate the construction of a physics-based low-rank approximation to meandering phenomena since it provides optimum convergence in extracting spatial modes and time-coefficients in terms of the time-mean energy of the flow (Aubry, 1991). The current low-rank approximation approach is similar to that used in some related flows such as Mula and Tinney (2015) for a spiraling vortex filament, or Karami, Hangan, et al. (2019) for tornado-like vortices. However, in the present study, we adopt a more rigorous validation by not only considering the accuracy of the spatial structures due to these models but also their ability to recreate the actual meandering motion. This study can thus be directly relevant to the control efforts directed at reducing meandering (Dghim, Ferchichi, et al., 2020). The models are examined at several streamwise locations downstream of the body to compare their performance.

7.1 Low-rank Representation

The characteristics of the POD and flow stability modes discussed above indicate the potential for a low-rank unsteady vortex meandering model using POD-based coherent structures. The reconstruction using a range of modes between m_1 and m_2, $\tilde{\vec{q}}_{m_1,m_2}(\vec{x},t)$, may be performed using

DISTRIBUTION A: Distribution approved for public release.



(a) $\tilde{\vec{q}}_{1,1}(\vec{x},t)$ (b) $\tilde{\vec{q}}_{2,2}(\vec{x},t)$ (c) $\tilde{\vec{q}}_{1,2}(\vec{x},t)$

Figure 77: Displacement of mean vortex core due to most energetic POD modes. Mean **R**-vortex ($\vec{\bar{q}}(\vec{x})$) is shown with flooded contours using the streamwise vortex at contour levels between -10 and 10. Broken white lines indicate the core. Reconstructed vortex cores ($\tilde{\vec{q}}_{m_1,m_2}(\vec{x},t)$) are shown in solid black lines. The red arrow shows the direction of movement of the mean vortex center due to superposition of first mode(a), second mode (b) as well as both first and second modes (c). In (a,b), the arrow directions are consistent with the alignment of modes, α_1 and α_2 in figure 68.

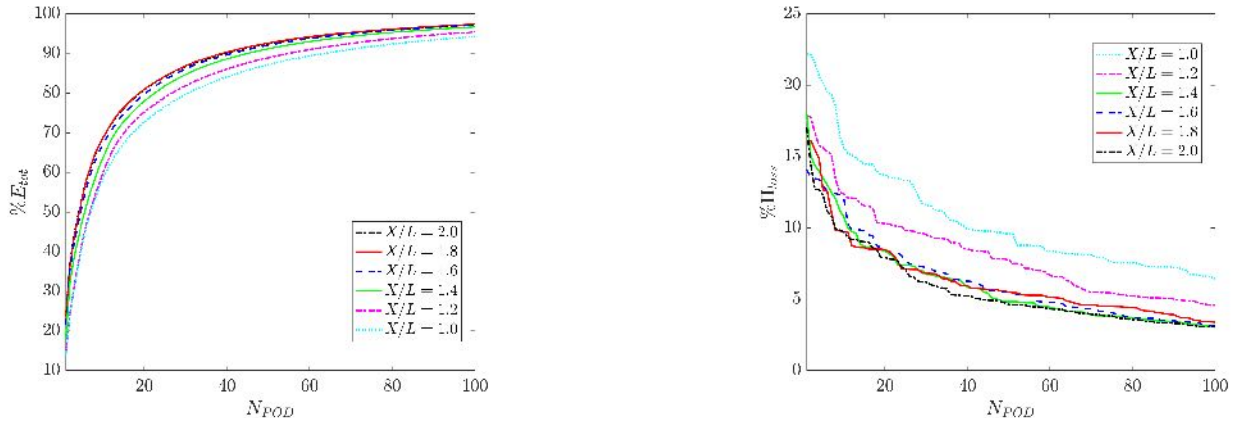
the definition of POD in equation (18) as:

$$\tilde{\vec{q}}_{m_1,m_2}(\vec{x},t) = \vec{\bar{q}}(\vec{x}) + \sum_{i=m_1}^{m_2} \sqrt{\Lambda_i}\vec{\Phi}_i(\vec{x})\vec{a}_i(t) \tag{30}$$

The influence of POD modes 1 and 2, as described in § 6.1.2, is examined first by adding them individually to the mean flow and reconstructing the solution. Subsequently, the combined effect of both helical modes is examined in reproducing meandering effects. Figures 77(a,b) show the displacement of the **R**-vortex core at $X/L = 2$ when the first two POD modes are added individually to the mean flow at a representative time. The reconstructed vortices display slightly non-axisymmetric structure due to the addition of these modes. Furthermore, the core, as estimated by the innermost black contour, is displaced from its mean position shown with a broken white contour. The displacement of the core is in the direction of the inclination of the dipoles shown earlier in figure 68. When the two modes are added, the effective displacement of the core from the mean position is shown in Figure 77(c).

The efficacy of a low-rank approximation may be evaluated by comparing the LES result with reconstructed spatio-temporal evolution of the vortex cores due to a small subset of modes, taking into account the different energy content of each mode. The rank-order of the approximation is a function of the streamwise location chosen since the intensity of meandering as well as the proximity of the separating shear layer can alter the properties of the POD modes (*e.g.,* compare leading modes at $X/L = 1.0$ and 2.0 in figures 66 and 67 respectively). The cumulative energy

DISTRIBUTION A: Distribution approved for public release.



(a) (b)

Figure 78: Comparison of energy of POD modes (a), and performance losses in reconstruction (b) at different streamwise locations.

content,

$$E_{tot} = \sum_{i=1}^{N_{POD}} \Lambda_i \tag{31}$$

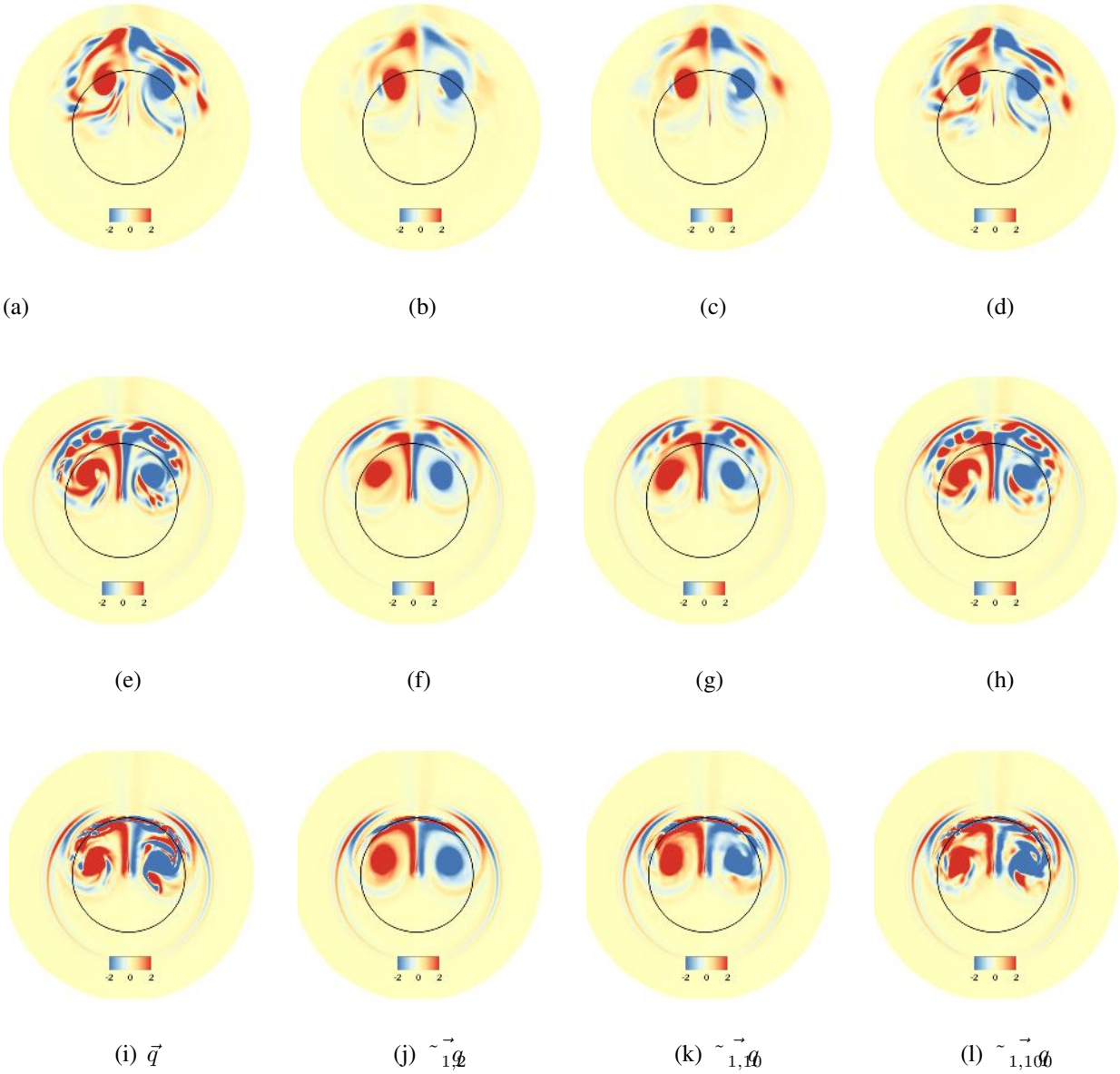
due to N_{POD} modes is shown in figure 78(a) for six locations downstream of the body at an interval of $\frac{\Delta x}{L} = 0.2$. The total energy contribution due to dominant modes gradually increases with the downstream distance, with nearly overlapping mode contributions for $X/L = 1.8$ and 2.0. Comparing the situation at $X/L = 1.0$ and 2.0, the first two modes contribute to about 24% and 37% of the total energy of flow respectively, while the first 100 modes respectively account for 97.3% and 94.3%.

The disparity in energy content of dominant modes at different locations is expected to affect the reconstruction of flowfields with these modes. Figure 79 compares the actual and reconstructed flowfields at three locations when 2, 10 and 100 modes are considered respectively. At the primary location of interest, $X/L = 2.0$ in Fig. 79(a), a reasonable description of the streamwise vortices is obtained with only the first two modes. These modes also contribute to the large-scale structures in the top shear layer away from the vortices. The next 8 modes primarily contribute to small-scale structures surrounding the vortices and the top shear-layer. When 100 of the total $3{,}000$ modes are used for reconstruction, the structure is very similar, qualitatively and quantitatively, to the LES result.

At locations closer to the body, $X/L = 1.4$ and 1.0, shown in Fig. 79(b) and (c) respectively, the first two modes contribute to the coherent structures of the vortices. However, due to high meandering intensity at these locations, the structures of the reconstructed vortices are significantly different from the LES snapshots. The addition of more modes improves the result as expected, with about 100 modes nearly reconstructing the complete flowfield with reasonable accuracy.

A performance loss parameter Π_{loss} is used to quantify the error in reconstruction, similar to

DISTRIBUTION A: Distribution approved for public release.



(a) (b) (c) (d)

(e) (f) (g) (h)

(i) $\vec{q}$ (j) $\tilde{\vec{q}}_{1,2}$ (k) $\tilde{\vec{q}}_{1,10}$ (l) $\tilde{\vec{q}}_{1,100}$

Figure 79: Reconstruction of flow fields using POD modes. The first two modes are major contributors to the coherent structures of the streamwise vortices. At locations closer to the body e.g., at $X/L = 1.0$ and $X/L = 1.4$, the meandering intensities are higher and therefore reconstructed vortices with just two modes differ significantly from the LES. In all three cases, 100 of the total $3{,}000$ modes reconstruct the complete flowfield to reasonable accuracy.

that used in Jovanović, Schmid, et al. (2014):

$$\Pi_{loss} = \frac{||\vec{q} - \tilde{\vec{q}}||_2}{||\vec{q}||_2} \tag{32}$$

DISTRIBUTION A: Distribution approved for public release.

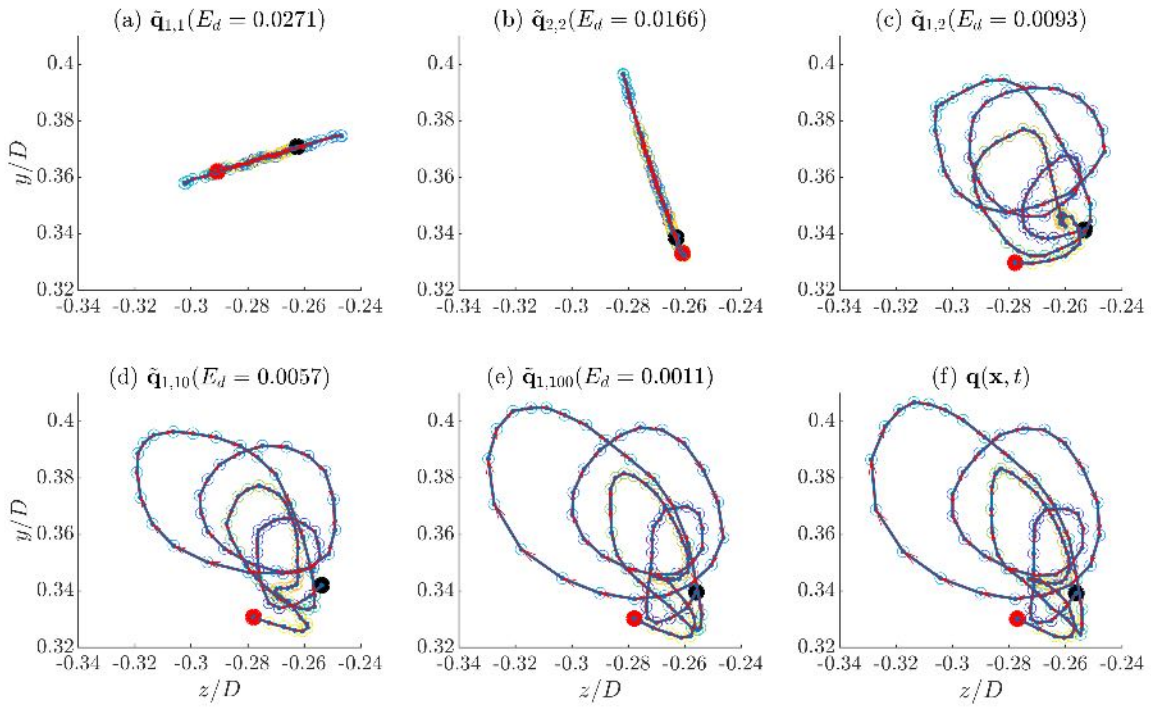


Figure 80: Meandering of the **L**-vortex using reconstructed flow fields. Black and red circles indicate the beginning and the end of the meandering trajectory.

Figure 78(b) displays these losses at six locations between $X/L = 1.0$ and 2.0. Even with only one POD mode, the maximum performance error is only 23% across all locations, further confirming the low-rank behavior of the flow. As expected, the losses are higher at locations near the body, with a difference of about 5% between $X/L = 1.0$ and 1.2. Away from the body, for example at $X/L = 2.0$, the loss is about 3% with 100 modes. At $X/L = 1.0$, this loss is slightly higher (8%). Further, as described above in the context of Fig. 79(a), the major factor contributing to error observations at the farthest location ($X/L = 2.0$) is the absence of finer structures in the first few modes; two modes by themselves recreate the streamwise vortices reasonably well.

The effects of low-rank approximation on the temporal dynamics at this location are now compared to the meandering observed in the LES field. As explained earlier, the reconstruction results in vortex motion that does not follow a preferred displacement direction but rather moves around in a manner that represents the meandering observed in the LES. The temporal displacement of the vortex cores at $X/L = 2.0$, when the effects of the leading modes are added are shown in figure 80 for the **L** vortex. The individual displacement due to the first and second modes considered separately are depicted in figures 80(a) and (b), respectively for 100 time-steps. These figures confirm that the motions of the core induced by mode 1 and 2, by themselves, lie along straight lines. The slopes of these lines, α_1 and α_2, are consistent with the structures of the vortex dipoles as described earlier in § 6.1.2.

Although the displacements due to the individual modes are relatively simple, their combined

DISTRIBUTION A: Distribution approved for public release.

effect is not. The trajectory of vortex cores due to both modes, shown in figure 80(c), are clearly very complex and are established due to the combination of two nearly straight lines in an effect similar to Lissajous curves (Fahy and Karioris, 1952) generated by a system of parametric equations. The combined displacement due to both these modes may be compared with the actual meandering motion shown in figure 80(f). Even when only the two dominant POD modes are considered, the result qualitatively reproduces the complex clockwise movement of the core, although the maximum displacement of core in the reconstructed flowfield is smaller than the original flowfield. The error in reconstruction may be characterized using the displacement from the vortex location in the root-mean-square sense as:

$$E_d = \sqrt{\frac{\sum_{i=1}^{N}((y_i - \tilde{y}_i)^2 + (z_i - \tilde{z}_i)^2)}{N}} \tag{33}$$

where y_i, z_i are the coordinates of the vortex center from the LES flowfield for snapshots $i = 1, 2..., N$. The tilde quantities $(\tilde{y}_i, \tilde{z}_i)$ represent the vortex centers in the reconstructed flowfield. These errors are also shown in Fig. 80. This error is 0.0271 and 0.0166 considering only the first and second mode respectively, and decreases to 0.0093 when both modes are added. When 10 modes are considered (Fig. 80(d)), the trajectory approaches the actual meandering path even further, and the error decreases to $E_d = 0.0057$. Further, when the vortex core movement is computed on a flowfield reconstructed with 100 modes (Fig. 80(e)), the core trajectory nearly mimics the complete meandering path. The addition of high-order modes mainly contributes to correcting the maximum displacement from the mean vortex, while the direction of the core movement is mainly dictated by only two modes.

In order to confirm that this observation also holds true for the **R** vortex, its reconstructed meandering motions are shown in figure 81(a-e). Consistent with the observations for the **L** vortex, linear displacements are observed due to the first and second POD modes in this vortex also, as shown in figure 81(a) and (b) respectively. The inclinations of the linear paths for this vortex are different from those obtained for **L** case of course, since they are aligned with displacements due to the individual modes of the **R** vortex. The displacement errors E_d due to these modes are comparable to each other. The combined displacement effect due to both modes, shown in figure 81(c), again mimics the actual meandering path (figure 81(f)), except for lower maximum displacements. The addition of 8 more modes brings the trajectory closer to the actual meandering path (figure 81(d)), and with a total 100 modes, the paths nearly overlap with each other (figure 81(e)). Although not shown, for locations closer to the body, the reconstruction error of the meandering path using these modes is slightly higher, as expected from their performance in reconstructing spatial structure (figure 79(b)). However, the key observation that they continue to exhibit low-rank behavior remains valid.

The reconstruction of the meandering path with only a few leading modes confirms the lower-dimensional dynamics and a smaller number of Lyapunov exponents in the dynamical system that characterize the chaos present in the system. Singler (2008) show that POD can be used in

DISTRIBUTION A: Distribution approved for public release.

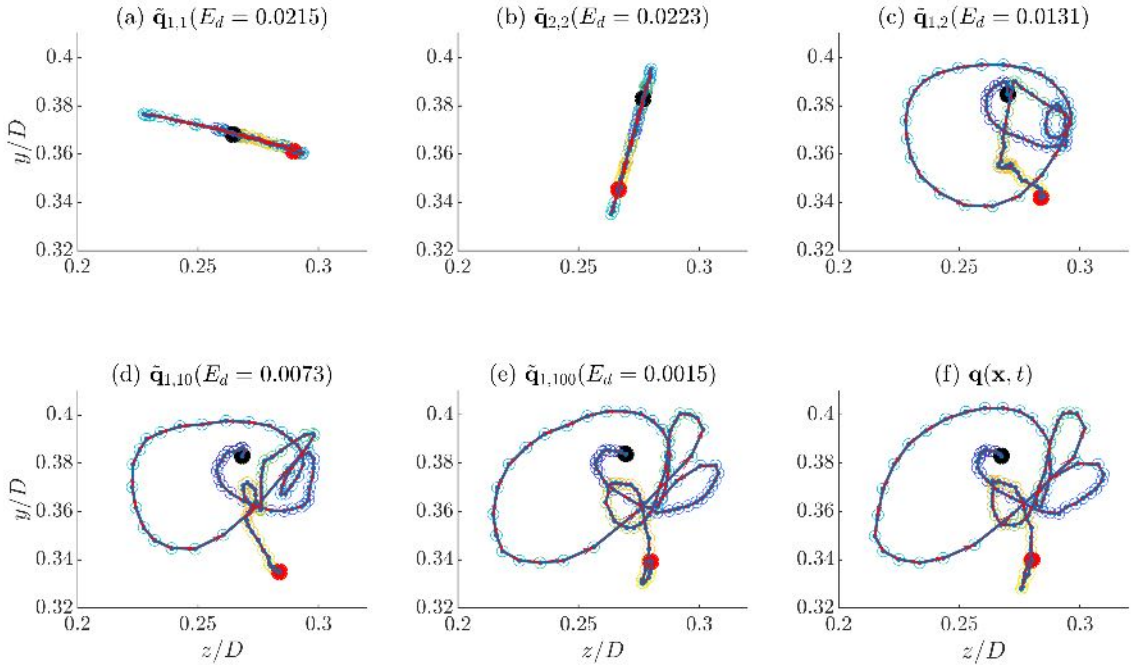


Figure 81: Meandering of **R**-vortex using reconstructed flow fields.

the manner above to compute approximate low-rank solutions of the Lyapunov equations. The solution of these equations can be used with standard methods to compute reduced-order models of linear systems either in a Galerkin-based (Couplet, Basdevant, et al., 2005) or a Galerkin-free approach (Shinde, Longatte, et al., 2016). This would constitute a significant step in ultimately determining control laws to modulate the meandering of vortices.

7.2 Summary

Relatively far downstream from the base, the wake vortices, while axisymmetric in the mean sense, exhibit low-frequency meandering in space and time. This motion is characterized by seemingly random displacement of the vortex cores, although the time trajectory of the displacement of the core shows a rotation sense commensurate with the swirl in the vortices. These complex phenomena are first analyzed through proper orthogonal decomposition (POD) at several locations on the ramp as well as downstream of the body. Near the base, the dominant structures show fluctuations in both the vortex and the shear layer. Downstream, however, the coherent structures are characterized by a pair of orthogonal helical modes with azimuthal wave number ($|m| = 1$). These two most energetic modes provide a first-order approximation of the displacement of the vortex cores, confirming that the meandering is primarily associated with changes in large-scale coherent structures. The instability mechanism underlying meandering is analyzed using a linear stability approach on the time-averaged streamwise vortex pair. The mean vortex obtained from the simulations is first matched to a suitable Batchelor vortex and then a counter-rotating model vortex is placed at an appropriate separation distance from the first vortex. Both spatial and temporal analyses confirm

DISTRIBUTION A: Distribution approved for public release.

the presence of an elliptic instability with the structures of the unstable modes being similar to those obtained from POD. The unstable modes are obtained at relatively low frequency with the presence of axial velocity as primary mechanism for instability.

Low-rank behavior is examined by considering different numbers of POD modes. Consideration of only the first or second mode generates temporal displacement of each core along a relatively straight line, which is very different from the actual meandering path. However, when both the modes are considered together, the effective trajectory recreated recovers the broad meandering motion. In the spatial reconstruction, these two modes alone capture the vortex cores reasonably well, while high-order modes further correct both spatial and temporal reconstructions to capture small scale features. Both spatial and temporal reconstruction errors diminish rapidly with the superposition of additional modes, especially in downstream regions. These low-rank observations of the complex meandering phenomena should facilitate the construction of a reduced-order model as a surrogate for the full dynamical system in flow control analyses.

8 Overall Summary

Detailed summaries for each aspect examined in this work are provided at the end of the corresponding section. Here we highlight the main points:

- The basic flow structure was characterized in terms of the a) formation of a separation bubble near the upstream apex of the base, b) inception and growth of streamwise vortices through an unstable vortex sheet c) interaction of shear-layer and vortices developing along the base, d) meandering of vortices downstream of the body.
- A comparative study of base pressure distributions at different upsweep angles provided insights into the mechanisms underlying base drag. As the upsweep angle is increased, the vortex pair strengths also increase until a limiting critical value ($\phi = 45°$) beyond which a wake regime is established.
- Hysteresis was demonstrated experimentally (Zigunov, 2020) as well as computationally (Ranjan and Gaitonde, 2020). In the former, the upsweep angle was fixed and the Reynolds number was increased and then decreased, whereas in the latter, the sweep angle was varied in like fashion. The vortex and wake regimes have a large drag disparity between them.
- For a given regime (vortex or wake) however, the effect of Reynolds number above $\sim 200,000$ is secondary.
- The behavior of the vortices downstream can be matched to an equivalent theoretical Batchelor vortex pair facilitating a more detailed study of flow stability. Two-dimensional stability analysis exposed an unstable mode responsible for breakdown and meandering; spectral analysis of the LES guided by this information revealed the corresponding mechanism for the low-frequency phenomenon.
- The different types of coherent structures in the flowfield were enumerated, and their characteristics were placed in context. In particular, some of the complex vortex dynamics was deconstructed into simpler mechanisms; for example, the meandering of vortices was shown to be primarily a result of the motions of first two elliptic modes of dipole shapes. Generalized techniques were developed to identify vortex cores and thus describe the meandering phenomena quantitatively as well as to verify the accuracy of low-order reconstruction using Proper Orthog-

DISTRIBUTION A: Distribution approved for public release.

onal Decomposition (POD) modes (Ranjan, Robinet, et al., 2020), with potential application to flow control (Zigunov, 2020).

A follow-on proposal has been submitted to build upon this understanding by examining the effects of:

- speed on wake dynamics at Mach 0.3 to 0.6.
- contoured fuselage edges on separation and vortex formation.
- open cargo bays without and with extended ramp-door.
- a genetic algorithm-informed experimental campaign using microjet actuators for drag reduction.

9 List of Publications from this Work

- Ranjan R., and Gaitonde D., "Hysteresis in Slanted-Base-Cylinder Afterbody Flows", Aerospace Science and Technology, Vol. 106, August 2020.
- Ranjan R., Aultman M., and Gaitonde D., "Mean Flowfield Evolution with Upsweep Angle in a Simulated Cargo Fuselage Aftbody", Journal of Aircraft, Vol. 57, No. 6. July 2020.
- Ranjan R., Robinet J.-Ch., and Gaitonde D.V., "Meandering of longitudinal wake vortices in slanted base afterbody flows", AIAA SciTech Paper 2020-1532, Jan 2020.
- Aultman M., Ranjan R., and Gaitonde D.V., "Effect of upsweep angle on the mean flowfield of a simulated cargo fuselage" , AIAA SciTech Paper 2020-1323, Jan 2020.
- Ranjan, R., Unnikrishnan, S., and Gaitonde, D. V., "A robust approach for stability analysis of complex flows using high-order Navier-Stokes solvers", Journal of Computational Physics, Vol. 403, October 2019.
- Ranjan, R., Unnikrishnan, S., Robinet, J-C. and Gaitonde, D.V., "Global transition dynamics of flow in a lid-driven cubical cavity." Theor. Comput. Fluid Dyn. 35, 397–418 (2021).
- Zigunov, F., Sellappan, P. and Alvi, F., "Reynolds number and slant angle effects on the flow over a slanted cylinder afterbody" , Journal of Fluid Mechanics, June 2020.
- Zigunov, F., Sellappan, P. and Alvi, F., "Flow topology of the slanted cylinder afterbody" , AIAA SciTech Paper 2019-1141, Jan 2019.
- Zigunov, F., Sellappan, P. and Alvi, F., "Dynamics of the slanted Cylinder afterbody vortices" , AIAA SciTech Paper 2020-1332, Jan 2020.
- Zigunov, F., Sellappan, P. and Alvi, F., "An empirical platform for optimal placement of open-loop microjet-in-crossflow actuators" , AIAA SciTech Paper 2021-1213, Jan 2021.
- Zigunov, F., Sellappan, P. and Alvi, F., "Beyond actuator line arrays in active flow control studies: lessons from a Genetic Algorithm approach" , Physical Review Fluids (Under Review).

References

Antkowiak, A. and Brancher, P. (2004). "Transient energy growth for the Lamb–Oseen vortex". *Physics of Fluids* 16.1, pp. L1–L4.

Arnoldi, W. E. (1951). "The principle of minimized iterations in the solution of the matrix eigenvalue problem". *Quarterly of Applied Mathematics* 9.1, pp. 17–29.

DISTRIBUTION A: Distribution approved for public release.

Aubry, N. (1991). "On the hidden beauty of the proper orthogonal decomposition". *Theoretical and Computational Fluid Dynamics* 2.5-6, pp. 339–352.

Baker, G., Barker, S., Bofah, K., and Saffman, P. (1974). "Laser anemometer measurements of trailing vortices in water". *Journal of Fluid Mechanics* 65.2, pp. 325–336.

Beam, R. and Warming, R. (1978). "An Implicit Factored Scheme for the Compressible Navier-Stokes Equations". *AIAA Journal* 16.4, pp. 393–402.

Beaudoin, J.-F. and Aider, J.-L. (2008). "Drag and lift reduction of a 3D bluff body using flaps". *Experiments in fluids* 44.4, p. 491.

Bell, J., Burton, D., Thompson, M., Herbst, A., and Sheridan, J. (2016). "Dynamics of trailing vortices in the wake of a generic high-speed train". *Journal of Fluids and Structures* 65, pp. 238–256.

Beresh, S. J., Henfling, J. F., and Spillers, R. W. (2010). "Meander of a fin trailing vortex and the origin of its turbulence". *Experiments in Fluids* 49.3, pp. 599–611.

Bergeron, K., Cassez, J.-F., and Bury, Y. (2009). "Computational investigation of the upsweep flow field for a simplified C-130 shape". *47th AIAA Aerospace Sciences Meeting including The New Horizons Forum and Aerospace Exposition*, p. 90.

Berkooz, G., Holmes, P., and Lumley, J. L. (1993). "The Proper Orthogonal Decomposition in the Analysis of Turbulent Flows". *Annual Review of Fluid Mechanics* 25.1, pp. 539–575.

Brion, V., Dekerret, H., Sipp, D., and Jacquin, L. (2008). "Optimal perturbation of a vortex sheet for fast destabilization of the trailing vortices". *38th Fluid Dynamics Conference and Exhibit*, p. 4182.

Britcher, C. and Alcorn, C. (1991). "Interference-free measurements of the subsonic aerodynamics of slanted-base ogive cylinders". *AIAA Journal* 29.4, pp. 520–525.

Bulathsinghala, D., Jackson, R., Wang, Z., and Gursul, I. (2017). "Afterbody vortices of axisymmetric cylinders with a slanted base". *Experiments in Fluids* 58.5, p. 60.

Bulathsinghala, D., Wang, Z., and Gursul, I. (2018). "Drag Reduction by Manipulation of Afterbody Vortices". *Journal of Aircraft* 55.6, pp. 2380–2391.

— (2019). "Modified near-wakes of axisymmetric cylinders with slanted base". *Aerospace Science and Technology* 86, pp. 351–363.

Bury, Y., Jardin, T., and Klöckner, A. (2013). "Experimental investigation of the vortical activity in the close wake of a simplified military transport aircraft". *Experiments in Fluids* 54.5, p. 1524.

C. Crow, S. (Dec. 1970). "Stability Theory for a Pair of Trailing Vortices". *AIAA Journal* 8, pp. 2172–2179.

Carter, D. L. (2017). "Legacy Transport Aircraft Drag Reduction Program". *35th AIAA Applied Aerodynamics Conference*, p. 4225.

Cheng, Z.-P., Qiu, S.-Y., Xiang, Y., and Liu, H. (2019). "Quantitative Features of Wingtip Vortex Wandering Based on the Linear Stability Analysis". *AIAA Journal*, pp. 2694–2709.

Claus, M., Morton, S., Cummings, R., and Bury, Y. (2005). "DES turbulence modelling on the c-130 comparison between computational and experimental results". *43rd AIAA Aerospace Sciences Meeting and Exhibit*, p. 884.

DISTRIBUTION A: Distribution approved for public release.

Conan, B., Anthoine, J., and Planquart, P. (2011). "Experimental aerodynamic study of a car-type bluff body". *Experiments in fluids* 50.5, pp. 1273–1284.

Corsiglia, V., Schwind, R., and Chigier, N. (1973). "Rapid Scanning, Three-Dimensional Hot-Wire AnemometerSurveys of Wing-Tip Vortices". *Journal of Aircraft* 10.12, pp. 752–757.

Couplet, M., Basdevant, C., and Sagaut, P. (2005). "Calibrated reduced-order POD-Galerkin system for fluid flow modelling". *Journal of Computational Physics* 207.1, pp. 192–220.

Coustols, E., Prudhomme, S., Mignosi, A., and Destarac, D. (1995). "Rear fuselage flow studies on a modern transonic transport aircraft". *Journal of Aircraft* 32.6, pp. 1183–1190.

Dallmann, U. (1988). "Three-Dimensional Vortex Structures and Vorticity Topology". *Fluid Dynamics Research* 3.1-4, pp. 183–189.

— (1983). "Topological Structures of Three-Dimensional Vortex Flow Separation". *AIAA Paper 83-1735*.

Del Pino, C., Lopez-Alonso, J., Parras, L., and Fernandez-Feria, R. (2011). "Dynamics of the wing-tip vortex in the near field of a NACA 0012 aerofoil". *The Aeronautical Journal* 115.1166, pp. 229–239.

Devenport, W. J., Rife, M. C., Liapis, S. I., and Follin, G. J. (1996). "The structure and development of a wing-tip vortex". *Journal of Fluid Mechanics* 312, pp. 67–106.

Dghim, M., Ferchichi, M., and Fellouah, H. (2020). "On the effect of active flow control on the meandering of a wing-tip vortex". *Journal of Fluid Mechanics* 896, A30.

Edstrand, A. M., Davis, T. B., Schmid, P. J., Taira, K., and Cattafesta, L. N. (2016). "On the mechanism of trailing vortex wandering". *Journal of Fluid Mechanics* 801.

Edstrand, A. M., Schmid, P. J., Taira, K., and Cattafesta, L. N. (2018). "A parallel stability analysis of a trailing vortex wake". *Journal of Fluid Mechanics* 837, pp. 858–895.

Epstein, R., Carbonaro, M., and Caudron, F. (1994). "Experimental investigation of the flowfield about an unswept afterbody". *Journal of Aircraft* 31.6, pp. 1281–1290.

Fabre, D., Jacquin, L., and Loof, A. (2002). "Optimal perturbations in a four-vortex aircraft wake in counter-rotating configuration". *Journal of Fluid Mechanics* 451, p. 319.

Fahy, E. F. and Karioris, F. G. (1952). "Geometrical and graphical representations of Lissajous figures". *American Journal of Physics* 20.3, pp. 121–123.

Feys, J. and Maslowe, S. A. (2016). "Elliptical instability of the Moore–Saffman model for a trailing wingtip vortex". *Journal of Fluid Mechanics* 803, pp. 556–590.

Gaitonde, D. V. and Visbal, M. R. (Aug. 1998). *High-Order Schemes for Navier-Stokes Equations: Algorithm and Implementation into FDL3DI*. Tech. rep. AFRL-VA-WP-TR-1998-3060. Air Force Research Lab Wright-Patterson AFB OH Air Vehicles Directorate.

— (Nov. 2000). "Pade-Type Higher-Order Boundary Filters for the Navier-Stokes Equations". *AIAA Journal* 38.11, pp. 2103–2112.

Gaitonde, D. (2010). "Mean Flowfield Structure of a Supersonic Three-Dimensional Base Flow". *Journal of Aircraft* 47.2, pp. 368–382.

Gaitonde, D. V. (2013). "Analysis of plasma-based flow control mechanisms through large-eddy simulations". *Computers & Fluids* 85, pp. 19–26.

DISTRIBUTION A: Distribution approved for public release.

Garmann, D. J. and Visbal, M. R. (2019). "High-Fidelity Simulations of Afterbody Vortex Flows". *AIAA Journal* 57.9, pp. 3980–3990.

Ghoreyshi, M., Bergeron, K., and Lofthouse, A. J. (2017). "Numerical Simulation of Wake Flowfield Behind the C-130 with Cargo Ramp Open". *Journal of Aircraft* 55.3, pp. 1103–1121.

González, L. M., Gómez-Blanco, R., and Theofilis, V. (2008). "Eigenmodes of a counter-rotating vortex dipole". *AIAA Journal* 46.11, pp. 2796–2805.

Gordnier, R., Visbal, M., Gursul, I., and Wang, Z. (2009). "Computational and Experimental Investigation of a Nonslender Delta Wing". *AIAA Journal* 47, pp. 1811–1825.

Gordnier, R. E. and Visbal, M. R. (2005). "Compact Difference Scheme Applied to Simulation of Low-Sweep Delta Wing Flow." *AIAA Journal* 43.8, pp. 1744–1752.

Graftieaux, L., Michard, M., and Grosjean, N. (2001). "Combining PIV, POD and vortex Identification Algorithms for the study of unsteady turbulent Swirling Flows". *Measurement Science and Technology* 12, pp. 1422–1429.

Grandemange, M., Gohlke, M., and Cadot, O. (2013). "Turbulent wake past a three-dimensional blunt body. Part 1. Global modes and bi-stability". *Journal of Fluid Mechanics* 722, pp. 51–84.

Green, S. and Acosta, A. (1991). "Unsteady flow in trailing vortices". *Journal of Fluid Mechanics* 227, pp. 107–134.

Gupta, V. and Wan, M. (2019). "Low-order modelling of wake meandering behind turbines". *Journal of Fluid Mechanics* 877, pp. 534–560.

Gursul, I., Gordnier, R., and Visbal, M. (2005). "Unsteady aerodynamics of nonslender delta wings". *Progress in Aerospace Sciences* 41.7, pp. 515–557.

Gursul, I. (2005). "Review of unsteady vortex flows over slender delta wings". *Journal of Aircraft* 42.2, pp. 299–319.

Haller, G. (2005). "An objective definition of a vortex". *Journal of Fluid Mechanics* 525, pp. 1–26.

Hein, S. and Theofilis, V. (2004). "On instability characteristics of isolated vortices and models of trailing-vortex systems". *Computers & fluids* 33.5-6, pp. 741–753.

Hoffmann, J. A. (1991). "Effects of freestream turbulence on the performance characteristics of an airfoil". *AIAA Journal* 29.9, pp. 1353–1354.

Holzäpfel, F. N., Strauss, L., and Schwarz, C. W. (2019). "Assessment of Dynamic Pairwise Wake Vortex Separations for Approach and Landing at Vienna Airport". *AIAA Aviation 2019 Forum*, p. 3178.

Hu, H., Yang, Z., and Igarashi, H. (2007). "Aerodynamic Hysteresis of a Low-Reynolds-Number Airfoil". *Journal of Aircraft* 44.6, pp. 2083–2086.

Iungo, G. V., Santoni-Ortiz, C., Abkar, M., Porté-Agel, F., Rotea, M. A., and Leonardi, S. (2015). "Data-driven reduced order model for prediction of wind turbine wakes". *Journal of Physics: Conference Series*. Vol. 625. 1. IOP Publishing, p. 012009.

Jackson, R., Wang, Z., and Gursul, I. (2019). "Control of Upswept Afterbody Vortices Using Continuous and Pulsed Blowing". *Journal of Aircraft*, pp. 1–17.

Jackson, R. W., Wang, Z., and Gursul, I. (2015). "Control of afterbody vortices by blowing". *45th AIAA Fluid Dynamics Conference*, p. 2777.

DISTRIBUTION A: Distribution approved for public release.

Jacquin, L., Fabre, D., Geffroy, P., and Coustols, E. (2001). "The properties of a transport aircraft wake in the extended near field-An experimental study". *39th Aerospace Sciences Meeting and Exhibit*, p. 1038.

Jacquin, L., Fabre, D., Sipp, D., and Coustols, E. (2005). "Unsteadiness, instability and turbulence in trailing vortices". *Comptes Rendus Physique* 6.4-5, pp. 399–414.

Jovanović, M. R., Schmid, P. J., and Nichols, J. W. (2014). "Sparsity-promoting dynamic mode decomposition". *Physics of Fluids* 26.2, p. 024103.

Jugier, R., Fontane, J., Joly, L., and Brancher, P. (2020). "Linear two-dimensional stability of a Lamb-Oseen dipole as an aircraft wake model". *Physical Review Fluids* 5.1, p. 014701.

Karami, M., Hangan, H., Carassale, L., and Peerhossaini, H. (2019). "Coherent structures in tornado-like vortices". *Physics of Fluids* 31.8, p. 085118.

Kerswell, R. R. (2002). "Elliptical instability". *Annual Review of Fluid Mechanics* 34.1, pp. 83–113.

Lacaze, L., Birbaud, A.-L., and Le Dizès, S. (2005). "Elliptic instability in a Rankine vortex with axial flow". *Physics of Fluids* 17.1, pp. 017101–017101.

Lehoucq, R. B., Sorensen, D. C., and Yang, C. (1998). *ARPACK users' guide: solution of large-scale eigenvalue problems with implicitly restarted Arnoldi methods*. SIAM.

Lele, S. (1992). "Compact Finite Difference Schemes with Spectral-like Resolution". *Journal of Computational Physics* 103.1, pp. 16–42.

Leweke, T., Le Dizes, S., and Williamson, C. H. (2016). "Dynamics and instabilities of vortex pairs". *Annual Review of Fluid Mechanics* 48, pp. 507–541.

Leweke, T. and Williamson, C. H. (1998). "Cooperative elliptic instability of a vortex pair". *Journal of Fluid Mechanics* 360, pp. 85–119.

Li, Y. and Wang, J. (2003). "Experimental studies on the drag reduction and lift enhancement of a delta wing". *Journal of Aircraft* 40.2, pp. 277–281.

Li, Z., Zhang, P., Pan, T., Li, Q., Zhang, J., and Dowell, E. H. (2018). "Catastrophe-Theory-Based Modeling of Airfoil-Stall Boundary at Low Reynolds Numbers". *AIAA Journal* 56.1, pp. 36–45.

Lienhart, H., Stoots, C., and Becker, S. (2002). "Flow and turbulence structures in the wake of a simplified car model (ahmed modell)". *New Results in Numerical and Experimental Fluid Mechanics III*. Springer, pp. 323–330.

Lockard, D. P., Brentner, K. S., and Atkins, H. L. (1995). "High-accuracy algorithms for computational aeroacoustics". *AIAA Journal* 33.2, pp. 246–251.

Lombard, J.-E. W., Moxey, D., Sherwin, S. J., Hoessler, J. F., Dhandapani, S., and Taylor, M. J. (2016). "Implicit large-eddy simulation of a wingtip vortex". *AIAA Journal* 54.2, pp. 506–518.

Lopera, J., Ng, T. T., Patel, M. P., and Stucke, R. (2007). "Forebody Geometry Effects on the Flow of a Blunt-Nose Projectile at High Alpha". *Journal of Aircraft* 44.6, pp. 1906–1922.

Ma, B.-F., Wang, Z., and Gursul, I. (2017). "Symmetry breaking and instabilities of conical vortex pairs over slender delta wings". *Journal of Fluid Mechanics* 832, pp. 41–72.

Mayer, E. W. and Powell, K. G. (1992). "Viscous and inviscid instabilities of a trailing vortex". *Journal of Fluid Mechanics* 245, pp. 91–114.

DISTRIBUTION A: Distribution approved for public release.

Morel, T. (1980). "Effect of base slant on flow in the near wake of an axisymmetric cylinder". *The Aeronautical Quarterly* 31.2, pp. 132–147.

Morel, T. (1978). "Aerodynamic drag of bluff body shapes characteristic of hatch-back cars". *SAE Transactions*, pp. 1270–1279.

Morgan, P. E. and Visbal, M. R. (2019). "Numerical Simulation of Transonic and Supersonic Flow Over a Wall-Mounted Hemisphere". *AIAA Aviation 2019 Forum*, p. 2921.

Morton, S. A., Vignes, B., and Bury, Y. (2006). "Experimental and computational results of a simplified C-130 shape depicting airflow influence on airdrop". *RTO MP-AVT-133 AC/323(AVT-133)TP/133*.

Mula, S. M. and Tinney, C. E. (2015). "A study of the turbulence within a spiralling vortex filament using proper orthogonal decomposition". *Journal of Fluid Mechanics* 769, pp. 570–589.

Navrose, Brion, V., and Jacquin, L. (2019). "Transient growth in the near wake region of the flow past a finite span wing". *Journal of Fluid Mechanics* 866, pp. 399–430.

Neal, D., Sciacchitano, A., Smith, B., and Scarano, F. (July 2015). "Collaborative framework for PIV uncertainty quantification: The experimental database". *Measurement Science and Technology* 26.

Pang, S. K., Ng, E. Y.-K., and Chiu, W. (2012). "Comparison of turbulence models in near wake of transport plane C-130H fuselage". *Journal of Aircraft* 50.3, pp. 847–852.

Paredes, P. (2014). "Advances in global instability computations: from incompressible to hypersonic flow". *Universidad Politécnica de Madrid: PhD Dissertation*.

Paredes, P., Theofilis, V., Rodriguez, D., and Tendero, J. (2011). "The PSE-3D instability analysis methodology for flows depending strongly on two and weakly on the third spatial dimension". *6th AIAA Theoretical Fluid Mechanics Conference*, p. 3752.

Parezanović, V. and Cadot, O. (2012). "Experimental sensitivity analysis of the global properties of a two-dimensional turbulent wake". *Journal of Fluid Mechanics* 693, pp. 115–149.

Parras, L. and Fernandez-Feria, R. (2007). "Spatial stability and the onset of absolute instability of Batchelor's vortex for high swirl numbers". *Journal of Fluid Mechanics* 583, pp. 27–43.

Pavia, G., Varney, M., Passmore, M., and Almond, M. (2019). "Three dimensional structure of the unsteady wake of an axisymmetric body". *Physics of Fluids* 31.2, p. 025113.

Perry, A. and Chong, M. (1987). "A Description of Eddying Motions and Flow Patterns Using Critical-Point Concepts". *Annual Review of Fluid Mechanics* 19, pp. 125–155.

Ranjan, R., Aultman, M., and Gaitonde, D. (2020). "Mean Flowfield Evolution with Upsweep Angle in a Simulated Cargo Fuselage Aftbody". *Journal of Aircraft* 57.6, pp. 1156–1169.

Ranjan, R. and Gaitonde, D. (2020). "Hysteresis in slanted-base-cylinder afterbody flows". *Aerospace Science and Technology* 106, p. 106138.

Ranjan, R., Robinet, J.-C., and Gaitonde, D. V. (2020). "Meandering of longitudinal wake vortices in slanted base afterbody flows". *AIAA Scitech 2020 Forum*, p. 1532.

Ranjan, R., Unnikrishnan, S., Robinet, J.-C., and Gaitonde, D. (June 2021). "Global transition dynamics of flow in a lid-driven cubical cavity". en. *Theoretical and Computational Fluid Dynamics* 35.3, pp. 397–418.

DISTRIBUTION A: Distribution approved for public release.

Rao, A., Minelli, G., Basara, B., and Krajnović, S. (2018). "On the two flow states in the wake of a hatchback Ahmed body". *Journal of Wind Engineering and Industrial Aerodynamics* 173, pp. 262–278.

Rowley, C. W., Colonius, T., and Murray, R. M. (2004). "Model reduction for compressible flows using POD and Galerkin projection". *Physica D: Nonlinear Phenomena* 189.1-2, pp. 115–129.

Sellappan, P., McNally, J., and Alvi, F. S. (July 2018). "Time-averaged three-dimensional flow topology in the wake of a simplified car model using volumetric PIV". *Experiments in Fluids* 59.8, p. 124.

Shinde, V., Longatte, E., Baj, F., Hoarau, Y., and Braza, M. (2016). "A Galerkin-free model reduction approach for the Navier–Stokes equations". *Journal of Computational Physics* 309, pp. 148–163.

Singh, S. and Mittal, S. (2005). "Vortex-induced oscillations at low Reynolds numbers: hysteresis and vortex-shedding modes". *Journal of Fluids and Structures* 20.8, pp. 1085–1104.

Singha, A. and Balachandar, R. (2011). "Structure of wake of a sharp-edged bluff body in a shallow channel flow". *Journal of Fluids and Structures* 27.2, pp. 233–249.

Singler, J. R. (2008). "Approximate low rank solutions of Lyapunov equations via proper orthogonal decomposition". *2008 American Control Conference*. IEEE, pp. 267–272.

Sipp, D. and Jacquin, L. (2003). "Widnall instabilities in vortex pairs". *Physics of Fluids* 15.7, pp. 1861–1874.

Sirovich, L. (1987). "Turbulence and the dynamics of coherent structures. I. Coherent structures". *Quarterly of Applied Mathematics* 45.3, pp. 561–571.

Smith, B., Yagle, P., and Hooker, J. (2013). "Reduction of aft fuselage drag on the C-130 using microvanes". *51st AIAA Aerospace Sciences Meeting including the New Horizons Forum and Aerospace Exposition*, p. 105.

Speth, R. and Gaitonde, D. (2013). "Parametric Study of a Mach 1.3 Cold Jet Excited by the Flapping Mode Using Plasma Actuators". *Computers & Fluids* 84, pp. 16–34.

Stepanov, R., Zherekhov, V., Pakhov, V., Mikhailov, S., Garipov, A., Yakubov, W., and Barakos, G. N. (2016). "Experimental Study of Helicopter Fuselage Drag". *Journal of Aircraft* 53.5, pp. 1343–1360.

Tisseur, F. and Meerbergen, K. (2001). "The quadratic eigenvalue problem". *SIAM Review* 43.2, pp. 235–286.

Tobak, M. and Peake, D. (1982). "Topology of Three-Dimensional Separated Flows". *Annual Review of Fluid Mechanics* 14, pp. 61–85.

Tsai, C.-Y. and Widnall, S. E. (1976). "The stability of short waves on a straight vortex filament in a weak externally imposed strain field". *Journal of Fluid Mechanics* 73.4, pp. 721–733.

Visbal, M. (1991). "Structure of Laminar Juncture Flows". *AIAA Journal* 29.8, pp. 1273–1282.

Wake, B. E. and Choi, D. (1996). "Investigation of high-order upwinded differencing for vortex convection". *AIAA Journal* 34.2, pp. 332–337.

Widnall, S., Bliss, D., and Zalay, A. (1971). "Theoretical and experimental study of the stability of a vortex pair". *Aircraft wake turbulence and its detection*. Springer, pp. 305–338.

DISTRIBUTION A: Distribution approved for public release.

Wieneke, B. (July 2015). "PIV uncertainty quantification from correlation statistics". *Measurement Science and Technology* 26.

Wortman, A. (1999). "Reduction of fuselage form drag by vortex flows". *Journal of Aircraft* 36.3, pp. 501–506.

Xia, X. and Bearman, P. (1983). "An experimental investigation of the wake of an axisymmetric body with a slanted base". *The Aeronautical Quarterly* 34.1, pp. 24–45.

Yaniktepe, B. and Rockwell, D. (2004). "Flow structure on a delta wing of low sweep angle". *AIAA Journal* 42.3, pp. 513–523.

Yeung, K. and Lee, K. (1999). "Particle image velocimetry study of wing-tip vortices". *Journal of Aircraft* 36.2, pp. 482–484.

Zeman, O. (1995). "The persistence of trailing vortices: a modeling study". *Physics of Fluids* 7.1, pp. 135–143.

Zigunov, F., Sellappan, P., and Alvi, F. S. (June 2020a). "Reynolds number and slant angle effects on the flow over a slanted cylinder afterbody". *Journal of Fluid Mechanics* 891.

Zigunov, F. (Nov. 2020). "Detailed flow field study of an upswept cylinder wake and experimental optimization using active flow control". PhD thesis.

Zigunov, F., Sellappan, P., and Alvi, F. S. (2020b). "Dynamics of the Slanted Cylinder Afterbody Vortices". *AIAA Scitech 2020 Forum*, p. 1322.

— (2019). "Flow topology of the slanted cylinder afterbody". *AIAA Scitech 2019 Forum*, p. 1141.

— (2020c). "Dynamics of the Slanted Cylinder Afterbody Vortices". *AIAA Scitech 2020 Forum*.

DISTRIBUTION A: Distribution approved for public release.